



UNIVERSITY OF SASSARI
PH.D. SCHOOL IN NATURAL SCIENCE
Via Muroni 25, I-07100 Sassari, Italy

*A Dissertation for the Degree of Doctor of Philosophy in Science and technology of mineral
and rocks of industrial interest presented at Sassari University in 2013*

XXVI cycle

**NEW GAMMA-RAY SPECTROMETRY METHODS FOR ESTIMATING K, U,
TH CONCENTRATIONS IN ROCKS OF THE SARDINIA BATHOLITH**

DIRECTOR:
Prof. Maro Curini Galletti

PhD. CANDIDATE:

Xhixha (Kaçeli) Merita

SUPERVISOR:

Prof. Oggiano Giacomo

CO-SUPERVISOR:

Dr. Mantovani Fabio

Table of content

ABSTRACT	5
RIASSUNTO.....	6
PART I	7
Introduction to radioactivity and radiation detection applied to geophysics	7
Chapter I.1	8
Basics of radioactive decay and the origin of natural radioactivity.....	8
I.1.1 Main radioactive decays	8
<i>I.1.1.1 Alpha decay</i>	9
<i>I.1.1.2 Beta decay</i>	10
<i>I.1.1.3 Gamma emission</i>	12
I.1.2 Law of radioactive decay	13
<i>I.1.2.1 The decay equation</i>	13
I.1.2.2 Radioactive decay series	14
I.1.3 Origin of natural radioactivity.....	17
<i>I.1.3.1 Cosmic radiation</i>	17
I.1.3.2 Primordial radionuclides and their distribution in rocks.....	18
Chapter I.2	23
Principles of gamma-ray spectrometry and instruments	23
I.2.1 Interaction of gamma-radiation with matter.....	23
I.2.1.1 Photoelectric absorption.....	23
I.2.1.2 Compton scattering.....	25
I.2.1.3 Pair Production	27
I.2.2 Germanium gamma-ray detector principles: MCA-Rad system	28
I.2.2.1 Semiconductor detectors	28
I.2.2.2 MCA-Rad system design	31
I.2.2.3 Efficiency calibration and validation	35
I.2.3 Scintillation gamma-ray detector principles: portable NaI(Tl) system	39
I.2.3.1 Scintillation detectors.....	39
I.2.3.2 A portable NaI(Tl): design set-up	43
I.2.3.3 Sensitivity calibration and validation.....	44
Chapter I.3	50
Basics of statistical analysis	50
I.3.1 Counting statistics	52
I.3.1.1 Counting distributions and sampling statistics	52

I.3.1.2 Counting decision limits	54
I.3.1.3 Propagation of uncertainty	55
I.3.2 Data analysis	55
I.3.2.1 Data distributions: exploratory data analysis	55
I.3.2.2 Uncertainty propagation using Monte Carlo method	61
PART II	63
New insights on the geological structure of N-E Sardinia (Corsica-Sardinia Variscan Batholith) revealed by gamma-ray spectrometry survey	63
Chapter II.1	64
Introduction and objectives	64
II.1.1 Variscan orogen of central Europe and the geological evolution of Sardinia	64
II.1.2 Current studies on natural radioactivity in European Variscan	69
II.1.3 Objectives of the study.....	71
Chapter II.2.....	73
Study of the distribution of natural radionuclides in Sardinian batholith.....	73
II.2.1 Geological setting of study area	73
II.2.2 Gamma-ray spectrometry survey measurements.....	82
II.2.2.1 In-situ gamma-ray spectrometry measurements	83
II.2.2.2 Laboratory gamma-ray spectrometry (MCA_Rad system) measurements	85
II.2.2.3 Comparison of results and characterization of rocks from Sardinia Batholith for their radionuclide content.....	86
II.2.3 The distribution of abundances of ⁴⁰ K, U and Th and ternary map	97
II.2.4 Preliminary study of radiogenic heat generation from upper crust.....	107
Chapter II.3.....	113
Discussions and conclusions	113
PART III.....	116
A new portable instrument for detailed in-situ gamma-ray survey	116
Chapter III.1	117
Introduction and objectives	117
III.1.1 State of art: in-situ γ -ray spectrometry	117
III.1.2 Objectives of the study	120
Chapter III.2	121
Cava-Rad system: a collimated instrument for in-situ gamma-ray measurements.....	121
III.2.1 Cava-Rad system: set-up design	121
III.2.2 Cava-Rad system: sensitivity calibration.....	123
III.2.3 Experimental validation of the sensitivity calibration method	129
Chapter III.3	137

Discussions and conclusions	137
References	139
Appendix A	152
The average SiO ₂ content in rocks of Sardinia	152
Appendix B.....	153
List of publications.....	153

ABSTRACT

In this PhD thesis are collected the results of a research project in the field of nuclear geophysics developed with the scientific collaboration between the Department of Natural and Territorial Sciences of the University of Sassari and the Department of Physics and Earth Sciences of the University of Ferrara. In particular, the research has focused on two main themes: the first part of the work has addressed the problem of the content of natural radionuclides in rocks as an instrument of their lithological characterization, geochemistry and orogenetic, while the second part deal with the realization of a collimated gamma spectrometer for in situ measurements.

The abundances of ^{40}K , U and Th in the Corsica-Sardinian Batholith in the N-E of Sardinia were investigated with 545 in situ gamma spectroscopy measurements with portable detectors NaI(Tl) and 167 measurements of natural radionuclides on rock samples using HPGe detectors. On the basis of the data obtained were processed high-resolution thematic maps of the distribution of radionuclides as well as radiometric ternary map, which show excellent agreement with the geological maps of the region.

The second part of the thesis describes a new portable and collimated NaI(Tl) spectrometer, which has been calibrated successfully using the FSA method with the NNLS constraint. The results of the measurements show good agreement with the measured concentrations with independent instruments (HPGe).

Keywords: Corsica-Sardinia Variscan Batholith; Gamma-ray spectrometry survey; Collimated NaI(Tl) detector; Natural radionuclides; Radiometric maps.

RIASSUNTO

In questa tesi di PhD sono raccolti i risultati di un progetto di ricerca nel campo della geofisica nucleare sviluppato grazie alla collaborazione scientifica tra il Dipartimento di Scienze della Natura e del Territorio dell'Università di Sassari e il Dipartimento di Fisica e Scienze della Terra dell'Università di Ferrara. In particolare l'attività di ricerca si è concentrata su due tematiche principali: nella prima parte del lavoro si è affrontato il problema del contenuto di radionuclidi naturali nelle rocce come proxy della loro caratterizzazione litologica, geochimica ed orogenetica, mentre nella seconda parte si è messo a punto uno spettrometro gamma collimato per misure in situ.

Le abbondanze di ^{40}K , U e Th nel Batolite Sardo Corso nel nord est della Sardegna sono state investigate con 545 misure di spettroscopia gamma in situ con rivelatori portatili NaI(Tl) e 167 misure di radionuclidi naturali su campioni di roccia utilizzando spettrometri HPGe. Sulla base dei dati ottenuti sono state elaborate mappe tematiche della distribuzione dei radionuclidi nonché mappe radiometriche ternarie ad alta risoluzione, le quali mostrano ottimi accordi con le carte geologiche della regione.

Nella seconda parte della tesi è descritto un nuovo spettrometro NaI(Tl) portatile e collimato, che è stato calibrato con successo usando il metodo FSA con il vincolo NNLS. I risultati delle misure mostrano ottimi accordi con le concentrazioni misurate con strumenti indipendenti (HPGe).

Parole chiave: Corsica-Sardinia Varisico Batolite; Indagine di spettrometria a raggi gamma; Rivelatore NaI(Tl) collimato; Radionuclidi naturali; Carte radiometriche.

PART I

Introduction to radioactivity and radiation detection applied to geophysics



Table of content:

Chapter I.1: Basics of radioactive decay and the origin of natural radioactivity

- I.1.1 Main radioactive decays
- I.1.2 Law of radioactive decay
- I.1.3 Origin of natural radioactivity

Chapter I.2: Principles of gamma-ray spectrometry and instruments

- I.2.1 Interaction of gamma-radiation with matter
- I.2.2 Germanium gamma-ray detector principles: MCA-Rad system
- I.2.3 Scintillation gamma-ray detector principles: portable NaI(Tl) system

Chapter I.3: Basics of statistical analysis

- I.3.1 Counting statistics
- I.3.2 Data analysis

Chapter I.1

Basics of radioactive decay and the origin of natural radioactivity

This chapter introduces the principles of radioactive decays (alpha and beta decays) and the mathematics of radioactive decay. Particular attention was made to primordial radionuclides together with their geochemical properties and typical concentrations in various rock types. Natural decay series of ^{238}U , ^{235}U and ^{232}Th are studied for the secular equilibrium of chain segments and implications in environmental gamma-ray spectrometry measurements.

I.1.1 Main radioactive decays

The **atom** is considered the smallest constituents of matter that distinguish their chemical properties that consist of a nucleus surrounded by **electrons**. The nucleus consists of positively charged **protons**, and uncharged **neutrons**; both called **nucleons**. In general, an assembly of nucleons, with its associated electrons, should be referred to as a **nuclide**. The diameter of an atom is of the order 10^{-10} m, and the diameter of a nucleus is of the order of 10^{-15} m. The nucleus is commonly identified by the notation:

$${}^A_Z X_N \quad (\text{I.1.1})$$

where X is the chemical symbol of the element, Z is the number of protons in a nucleus (called the **atomic number**) and defines the element (Z will also be the number of orbital electrons), N the number of neutrons in a nucleus and A is the **mass number** given as the total number of nucleons, $A = Z + N$. Known the relationship between Z , N and A and because the chemical symbol uniquely identifies the element (the atomic number as subscript is usually omitted), this notation is written simply as ${}^A X$.

Atoms of an element having the same atomic number but different numbers of neutrons (i.e. different mass numbers) are called **isotopes**. Isotopes have identical chemical properties, but different physical properties. The atomic nuclei of some isotopes have a surplus of energy, are unstable, and disintegrate to form more stable nuclei of a different isotope. This process is accompanied by the emission of particles or electromagnetic radiation, termed **nuclear radiation**. Nuclides with this feature are called **radionuclides**, and the process is called **nuclear** or **radioactive decay**.

Stable nuclides occur in a very narrow band in the N - Z plane (**Fig. I.1.1**) called **island of stability**. The heaviest stable element is bismuth ($Z = 83$, $N = 126$). The figure also shows the location of some high Z unstable nuclides – the major thorium ($Z = 90$) and uranium ($Z = 92$) nuclides.

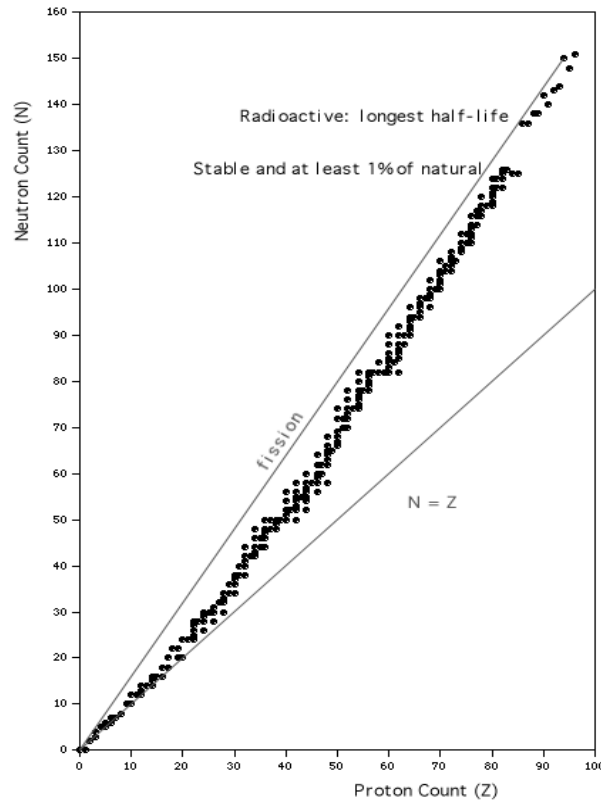


Figure I.1.1: chart of the nuclides (Figure from (G. R. Gilmore 2008) .

All other nuclei are unstable and decay spontaneously in various radioactive decay modes. The principal modes of radioactive decay are alpha and beta decay. Gamma emission frequently appears as a consequence of alpha or beta decay, being one of the de-excitation processes. The units of energy we use in gamma spectrometry are **electron-volts** (eV), where $1 eV = 1.602\ 177 \times 10^{-19} J$. Energies in the gamma radiation range are conveniently in keV .

1.1.1.1 Alpha decay

An **alpha particle**, α , is a highly energetic helium nucleus (${}^4_2He^+$) that is emitted from unstable heavy nuclei having high atomic numbers ($Z > 83$). Since the atomic number and mass numbers are conserved an alpha decay can be written schematically as:



where X and Y are the initial and final nucleus species. A typical example is the decay of the isotope of ${}^{226}Ra$ in ${}^{222}Rn$ (part of the ${}^{238}U$ decay chain):



where Q is the quantity of energy released, equal to the difference in mass between the initial nuclide and final products shared in a definite ratio because of the conservation of momentum. For the above example, $Q = 4.871 \text{ keV}$, is the energy shared between the Rn and the He , releasing a **mono-energetic alpha particle**.

In many cases, especially for lower Z radionuclides, the emission of an alpha particle takes the nucleus directly to the ground state of the daughter. However, for heavier nuclei, alpha decay can lead to excited states of the daughter. **Figure I.1.2**, the decay scheme of ^{226}Ra , shows gamma emission following alpha decay (5.55%), but even here it will be seen that most alpha transitions go directly to the ^{222}Rn ground state (94.45). The gamma radiation, 186.2 keV , is released as that excited state de-excites and drops to the ground state.

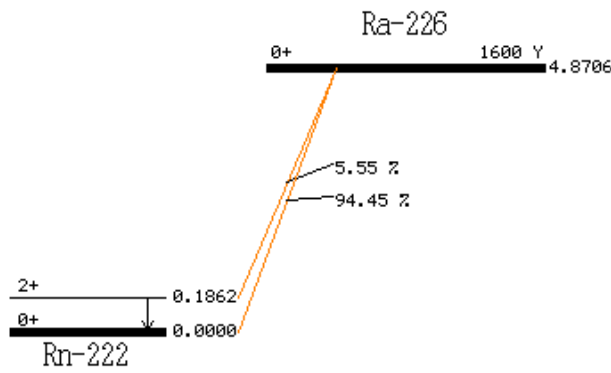


Figure I.1.2: a simplified decay scheme of ^{226}Ra in ^{222}Rn through a pure alpha decay (94.45%) or through an alpha-gamma decay (5.55%).

1.1.1.2 Beta decay

A **beta decay**, β , corresponds to transitions along an isobar, or line of constant A in the nuclide chart (**Fig. I.1.1**). A common transformation for neutron rich radionuclides is that neutrons are changing to protons ($n \rightarrow p + \beta^- + \bar{\nu}_e$), **beta minus decay**, or on the opposite side for neutron deficient radionuclides, protons are changing to neutrons ($p \rightarrow n + \beta^+ + \nu_e$), **beta plus decay**. The β^- and β^+ decays can be written schematically according to the conservations of the atomic number and mass numbers:



where β^- and β^+ are respectively the electron and the positron (anti-electron). The different notation between atomic electrons (e^-) and beta particles (β) is because the latter are emitted by radioactive nuclides

during radioactive decay. In these processes, is emitted another particle called **neutrino** (ν) and **anti-neutrino** ($\bar{\nu}$), but since the neutrino has no electrical charge, its inclusion in the decay process does not affect the identity of the other final particles. Anti-neutrinos (and neutrinos from β^+ decay) are theoretically crucial in maintaining the universality of the conservation laws of energy and angular momentum.

An example, of β^- decay is the transformation of ^{137}Cs to ^{137}Ba :



In this case, the decay energy, $Q = 1.176 \text{ MeV}$, is shared between the particles in inverse ratio to their masses in order to conserve momentum. The mass of ^{137}Cs is very large compared to the mass of the beta particle and neutrino and takes a very small, insignificant portion of the decay energy. Therefore, the beta particle and the anti-neutrino share almost the whole of the decay energy in variable proportions ranging from zero to 100%. For this reason, beta particles are not mono-energetic, as one might expect from the decay scheme, and their energy is usually specified as $E_{\beta\text{max}}$.

As for alpha decay, many beta transitions do not go to the ground state of the daughter nucleus (pure beta emitters), but to an excited state. For ^{137}Cs , some beta decays (5.60 %) go directly to the ground state of ^{137}Ba ; most (94.4 %) go into an excited nuclear state of ^{137}Ba (**Fig. I.1.3**). The gamma radiation, 661.7 keV, is released as that excited state de-excites and drops to the ground state.

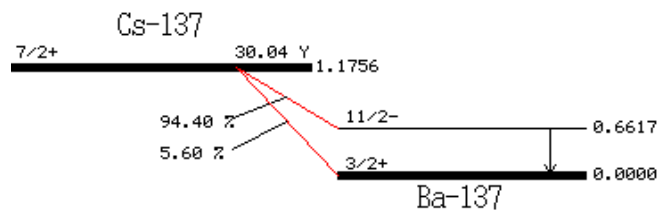


Figure I.1.3: a simplified decay scheme of ^{137}Cs in ^{137}Ba through a pure beta- decay (5.6%) or through a beta-gamma decay (94.4%).

As we emphasized, during this decay a positron (anti-electron), is emitted, and conservation issues are met by the appearance of a neutrino (**Eq. I.1.5**). Positron emission is only possible if there is a sufficiently large energy difference, that is, mass difference, between the consecutive isobaric nuclides. The critical value is 1022 keV, which is the combined rest mass of an electron plus positron, **electron / positron pair** (known as **pair production**). As with β^- decay, there is a continuous energy spectrum ranging up to a maximum value, and emission of complementary neutrinos. The positron has a short life; it is rapidly slowed in the matter until it reaches a very low, close to zero, kinetic energy, then the process of **annihilation** occurs. Both the positron and electron disappear and two photons are produced, each with energy equal to the electron mass, 511.00 keV. These photons are called **annihilation radiation** and the annihilation peak is a common

feature in gamma spectra, which is much enhanced when β^+ nuclides are present. To conserve momentum, the two 511 keV photons will be emitted in exactly opposite directions.

For neutron deficient nuclides close to stability island, where that energy is not available, the electron needed to convert the proton is captured by the nucleus from one of the extranuclear electron shells, most likely K shell being closest to the nucleus, indeed sometimes the process is called **K-capture**. The probability of capture from the less strongly bound higher shells (L, M, etc.) increases as the decay energy decreases. The process is known as **electron capture** decay and can be schematically given by **Eq. I.1.7**.



The ${}^{40}\text{K}$ (primordial radionuclide) is an example of both, a pure beta minus decay (89.28%) and electron capture (10.72%), which is followed by gamma emission, 1460.9 keV, (**Fig. I.1.4**).

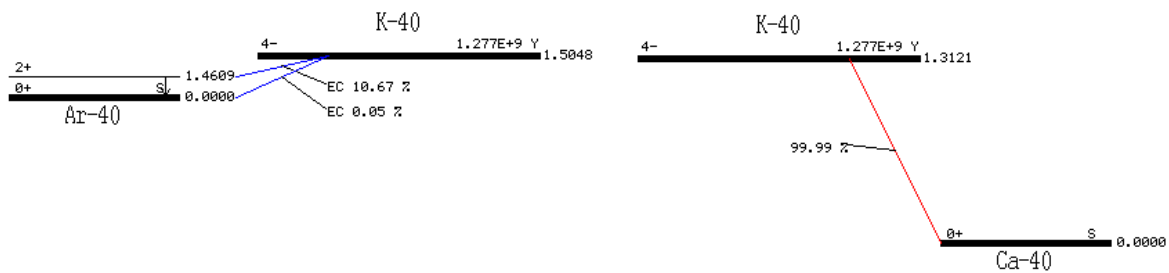


Figure I.1.4: a simplified decay scheme of ${}^{40}\text{K}$ composed by two branching: in ${}^{40}\text{Ca}$ through a pure beta- decay (89.28%) and in ${}^{40}\text{Ar}$ through an EC-gamma decay (10.67%).

The loss of an electron from the K shell leaves a vacancy there, which is filled by an electron dropping in from a higher, less tightly bound, shell. The energy released in this process often appears as an X-ray, in what is referred to as **fluorescence**.

I.1.1.3 Gamma emission

This is not a form of decay like alpha or beta, in that there is no change in the number or type of nucleons in the nucleus; there is no change in Z , N or A . Gamma-rays are monochromatic electromagnetic radiations that are emitted from the nuclei of excited atoms following radioactive transformations: they provide a mechanism of reaching the nuclei energetic stability. As shown above, gamma emissions usually follow alpha or beta decays since will often lead to excited states in the daughter nucleus. These transitions are known as isomeric transitions and the long-lived excited states, ${}^A X$, are called **isomeric states** or **isomers** (sometimes **metastable states**).



A process that often competes with gamma emission is **internal conversion**, in which the nucleus de-excites by transferring its energy directly to an atomic electron, which then appears as free electrons.

I.1.2 Law of radioactive decay

I.1.2.1 The decay equation

Radionuclides are, by definition, unstable and decay of one, or more, of the decay modes; alpha, beta-minus, beta plus or electron capture. The amount of a radionuclide in a sample is expressed in **Becquerel** – numerically equal to the rate of disintegration – the number of disintegrations per second. We refer to this amount as the **activity** of the sample. The rate of decay is directly proportional to the number of atoms of the radionuclide present in the source, i.e. the activity, A , is directly proportional to the number of atoms, N , of nuclide present:

$$A = -\frac{dN}{dt} = \lambda N \quad (\text{I.1.9})$$

The proportionality constant, λ , is called the **decay constant** (the probability per second that the emission takes place) and has the units of reciprocal time (s^{-1}). The reciprocal of the decay constant is the **mean lifetime**, τ , of the radionuclide, the average time which an atom can be expected to exist before its nucleus decays:

$$\tau = \frac{1}{\lambda} \quad (\text{I.1.10})$$

This time represents a decay of the source by a factor of e (i.e. 2.718). It is more convenient and meaningful to refer to the **half-life**, $t_{1/2}$, of the radionuclide – the time during which the activity decreases to half its original value:

$$t_{1/2} = \frac{\ln(2)}{\lambda} = \frac{0.693}{\lambda} \quad (\text{I.1.11})$$

Integrating the **Eq. I.1.9** lead to the exponential law of radioactive decay which relates the number of atoms ($N(t)$) at a time (t) and half-life ($t_{1/2}$):

$$N(t) = N_0 e^{-\frac{\ln(2)}{t_{1/2}} t} \text{ or } N(t) = N_0 e^{-\lambda t} \quad (\text{I.1.12})$$

where N_0 is the number of atoms at time $t = 0$. In practice, it is more useful to replace the number of atoms by activity, bearing in mind that activity is proportional to the number of atoms:

$$A(t) = A_0 e^{-\lambda t} \quad (\text{I.1.13})$$

The historical unit of activity has been the curie (*Ci*), defined as exactly 3.7×10^{10} *disintegrations / second*, which owes its definition to its origin as the best available estimate of the activity of 1 gram of pure ^{226}Ra . Although still widely used in the literature, the curie is destined to be gradually replaced by its SI equivalent, the Becquerel (*Bq*), defined as disintegration per second, thus:

$$1 \text{ Bq} = 2.703 \times 10^{-11} \text{ Ci} \quad (\text{I.1.14})$$

I.1.2.2 Radioactive decay series

The natural decay series of ^{238}U , ^{235}U and ^{232}Th are an example of natural radioactive decay series and therefore are briefly discussed in this section. Radioactive decay series (or chain) often occurs in a number of daughter products, which are also radioactive, and terminates in a stable isotope $A(\lambda_A) \rightarrow B(\lambda_B) \rightarrow C(\text{stable})$. Assuming that at time $t = 0$ we have N_{A_0} atoms of the parent element and no atoms of the decay product are originally present, the number of the parent nucleus decrease with time according to the **Eq I.1.12**.

$$N_A = N_{A_0} e^{-\lambda_A t} \quad (\text{I.1.15})$$

While the number of daughter nuclei increases (grow-up) as a result of the decays of the parent and decreases as a result of its own decay:

$$\frac{dN_B}{dt} = \lambda_A N_A - \lambda_B N_B \quad (\text{I.1.16})$$

The solution of the first order differential equation $(dN_B / dt) + \lambda_B N_B = \lambda_A N_{A0} e^{-\lambda_A t}$ is of the form $N_B = A e^{-\lambda_A t} + B e^{-\lambda_B t}$ and by substituting into the above equation with the initial conditions described above we find:

$$N_B = \frac{\lambda_A N_{A0}}{\lambda_B - \lambda_A} (e^{-\lambda_A t} - e^{-\lambda_B t}) \quad (\text{I.1.17})$$

From **Eq. I.1.15** and **Eq. I.1.17** can be calculated the relative activity ratio of the two species:

$$\frac{\lambda_B N_B}{\lambda_A N_A} = \frac{\lambda_B}{\lambda_B - \lambda_A} [1 - e^{-(\lambda_B - \lambda_A)t}]$$

- $\lambda_A \ll \lambda_B$: in the case when the half-life of nuclide A is much greater than the half-life of nuclide B , so the parent decays at constant rate we have:

$$\lambda_B N_B = \lambda_A N_{A0} (1 - e^{-\lambda_B t})$$

This equation expresses the **secular equilibrium condition**, where, as the time t becomes larger nuclei B decay at the same rate at which they are formed: $\lambda_B N_B = \lambda_A N_{A0}$. This result can also be immediately obtained from **Eq. I.1.16**, taking $dN_B/dt = 0$. For practical purposes, equilibrium may be considered established after the seven half-lives of daughter radionuclide (more than 99% of daughter nuclides grow-up) (**Fig. I.1.5**).

In the study of uranium decay chain through gamma-ray spectrometry techniques it is important to emphasize that some long lived radionuclides, e.g. ^{226}Ra , can be the head of decay chain segments which can be directly measured or through equilibrium grow-up conditions. In gamma-rays spectrometry measurements, ^{226}Ra can be directly measured through its gamma ray emitted, 186.2 keV (**Fig. I.1.2**). However, this shows some difficulties since generally it is recorded as a doublet with 185.7 keV from ^{235}U . Instead ^{214}Pb and ^{214}Bi are directly measured and ^{226}Ra is estimated under the equilibrium grown up condition, which is generally reached through radon tight containers within 26.7 days (**Fig. I.1.5**). While, thorium and its daughters are generally found in secular equilibrium. However, in ^{232}Th decay chain the two chain segments headed by ^{228}Ra (measured through ^{228}Ac) and ^{228}Th (measured through ^{212}Pb , ^{212}Bi and ^{208}Tl) reach the secular equilibrium in about one month.

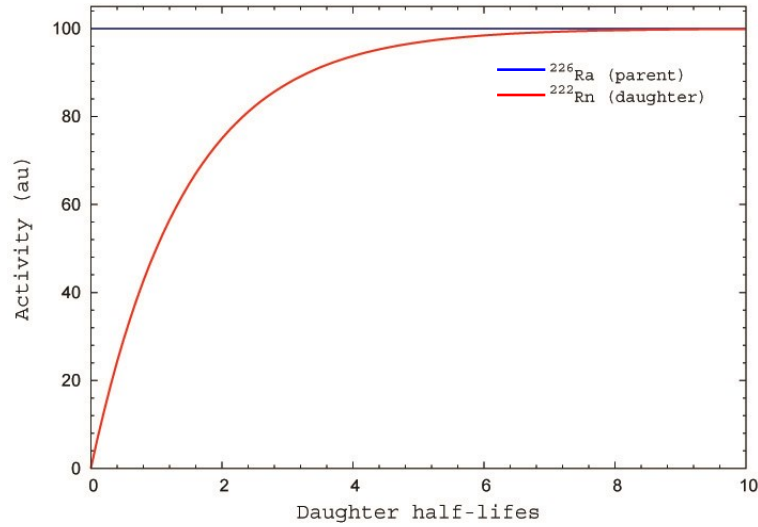


Figure I.1.5: secular equilibrium buildup of a very short-lived daughter (^{222}Rn of half-life 3.824 d) from a long-lived parent (^{226}Ra of half-life 1600 y). The activity (arbitrary unit) of the parent remains constant, while the activity of the daughter reaches secular equilibrium (more than 99%) just after seven half-lives.

- $\lambda_A < \lambda_B$: as the time t increases, the exponential term becomes smaller and the activity ratio (A_B/A_A) approaches the limiting constant value $\lambda_B/(\lambda_B - \lambda_A)$. The activities themselves are not constant, but the nuclei of type B decay (in effect) with the decay constant of type A . This situation is known as **transient equilibrium condition** (Fig. I.1.6).

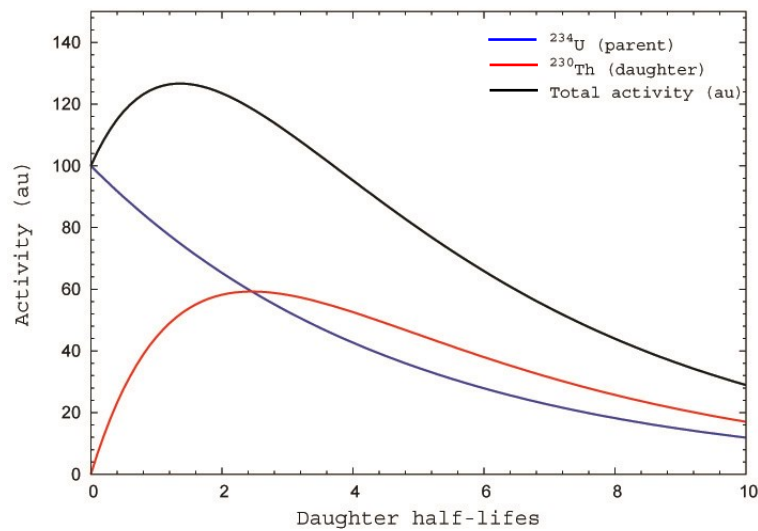


Figure I.1.6: transient equilibrium of the decay of ^{234}U (of half-life 2.45×10^5 y) to ^{230}Th (of half-life 7.54×10^4 y). The activity ratio daughter/parent approaches the constant value 1.48.

- $\lambda_A > \lambda_B$: in the case when the parent decay quickly, ($\lambda_A > \lambda_B$), and the daughter activity rises to a maximum and then decays with its characteristic decay constant, if t is so long the number of nuclei type A is small ($e^{-\lambda_A t} \approx 0$): $\lambda_B N_B \approx (\lambda_B \lambda_A N_A / \lambda_A - \lambda_B) e^{-\lambda_B t}$, which reveals that the type B nuclei decay approximately

according to the exponential law (**Fig. I.1.7**). An example of no equilibrium condition, is the nuclear fission product series containing ^{90}Sr which is largely studied for environmental radioprotection purposes:

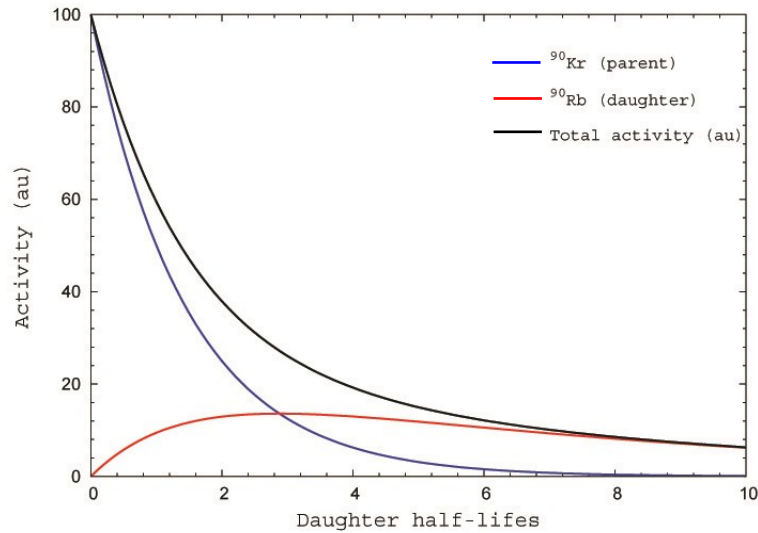
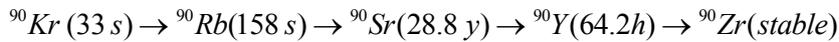


Figure I.1.7: no equilibrium: the growth and decay of ^{90}Rb (of half-life 158 s) from ^{90}Kr (of half-life 33.33 s). If ^{90}Kr is not continuously produced it will vanish quicker producing ^{90}Rb which in turn will vanish quickly respective ^{90}Sr having a much longer half-life and reaching secular equilibrium with its daughter ^{90}Y .

I.1.3 Origin of natural radioactivity

I.1.3.1 Cosmic radiation

The primary sources of **cosmic radiation** are the galaxies in outer space and secondary source is the Sun in our solar system (significant during maximum sun cycle activity). The galactic cosmic radiation coming at the upper atmosphere is made up of about 98% baryons and 2% electrons (**G. Reitz 1993**). It consists mainly of protons (87%) and to a lesser extent of helium ions (11%) and heavier ions (ranging from carbon to iron; 1%), with energies ranging from 10^2 MeV to more than 10^{14} MeV. In fact, the result of the cosmic radiation is a continuous bombardment of Earth's magnetosphere by a nearly isotropic flux of charged particles having different energies. However, only a part of the cosmic radiation actually reaches the surface of the Earth. Furthermore, charged particles are deflected from the Earth's magnetic field component that is perpendicular to the direction of particle motion. This means that the cosmic radiation is deflected more at the equator than near the poles producing a geomagnetic latitude effect of cosmic radiation.

The interaction of high-energy particles with atoms and molecules in the atmosphere (mainly nitrogen and oxygen), are the dominant mechanism of interaction resulting in a cascade of interactions and reaction products like secondary protons, neutrons and charged/uncharged pions (**D. R. Bartlett 2004**) together with

parents having very long half-life. The principal sources of environmental radioactivity monitoring interest are due to the presence of ^{238}U , ^{232}Th and ^{40}K in the Earth's crust. Generally, other major trace elements like ^{235}U and ^{87}Rb are present. The world average abundances of the continental upper crust for ^{238}U , ^{232}Th and ^{40}K are respectively $2.7 \mu\text{g/g}^1$, $10.5 \mu\text{g/g}$ and 2.3% (**R. L. Rudnick and S. Gao 2003**). In **Table I.1.1** are shown typical concentrations of ^{238}U , ^{232}Th and ^{40}K in different rock types.

Table I.1.1: K, U and Th content of some rock types (data from (**J. H. Schoen 2011**)).

Rock type	K (%)	U ($\mu\text{g/g}$)	Th ($\mu\text{g/g}$)
Intrusive			
Granite	2.75 - 4.26	3.6 - 4.7	19 - 20
Granitic rocks (average)	4.11	4.35	15.2
Granitic rocks	2.3 - 4.0	2.1 - 7.0	8.3 - 40
Biotite granite	3.4	4.0	15
Gabbro	0.46 - 0.58	0.84 - 0.90	2.70 - 2.85
Granodiorite	2 - 2.5	2.6	9.3 - 11
Diorite	1.1	2.0	8.5
Dunite	< 0.02	< 0.01	< 0.01
Dunite, pyroxenite	0.15	0.03	0.08
Peridotite	0.2	0.01	0.05
Extrusive			
Rhyolite	2 - 4	2.5 - 5	6 - 15
Trachyte	5.7	2 - 7	9-25
Alkali basalt	0.61	0.99	4.6
Plateau basalt	0.61	0.53	1.96
Andesite	1.7	0.8	1.9
Dacite	2.3	2.5	10.0
Liparite	3.7	4.7	19
Metamorphites			
Gneiss-Swiss Alps	0.32 - 4.7	0.9 - 24	1.2 - 25.7
Gneiss (KTB, Germany)	2.28 ± 0.17	2.6 ± 1.2	8.2 ± 2.0
Eclogite	0.8	0.2	0.4
Amphibolite Swiss Alps	0.11 - 2.22	0 - 7.8	0.01 - 13.7
Amphibolite	0.6	0.7	1.8

¹ Conversion of radioelement concentration to specific activity for 1% K = 313 Bq/kg; 1 ppm U = 12.35 Bq/kg and 1 ppm Th = 4.06 Bq/kg IAEA (2003). "Guidelines for radioelement mapping using gamma ray spectrometry data." IAEA-TECDOC1363.

NOTE: this coefficients are calculated for natural isotopic abundances of 99.2745% for ^{238}U , 100% of ^{232}Th and 0.0118% of ^{40}K .

Metabasite (KTB, Germany)	0.6 ± 0.5	2.5 ± 1.6	2.5 ± 1.6
Schist – Swiss Alps	0.39 – 4.44	0.4 -3.7	1.6 – 17.2
Quartzite	0.6	0.8	3.1
Marble	0.2	1.1	2.2
Sediments			
Carbonate	0.0 – 2.0	2.8 – 2.5	0.1 – 7.0
Limestone	0.3	1.6	1.8
Dolomite	0.4	3.7	2.8
Marl	0.8	2.8	2.5
Anhydrite	0.4	0.1	0.3
Salt	0.1	0.02	0.3
Sandstone	0.7 – 3.8	0.2 – 0.6	0.7 – 2.0
Graywacke	1.3	2.0	7.0
Shale	2.0	6.0	12.0
Common shales	1.6 – 4.2	2 - 13	3 - 47
Shale	2.7	3.7	12
Oli shale (Colorado)	< 4.0	up to 500	1 - 30
Black shale	2.6	20.2	10.9
North American Shale Composite (NASC) std.	3.2	2.66	12.3
Clay, N – Atlantic, Caribbean	2.5	2.1	11
Clay, unconsolidated, Pleistocene	1.9 – 2.5	1.1 – 3.8	5.7 – 10.2
Clay/silt, Tertiary	1.3 – 3.1	1.2 – 4.3	1.4 – 9.3

Potassium

Natural potassium comprises three isotopes (^{39}K , ^{40}K , ^{41}K) where ^{40}K is the only radioactive potassium isotope having a natural isotopic abundance of 0.0118%. The beta and electron capture decay modes of ^{40}K to ^{40}Ca (89.28%) and ^{40}Ar (10.72%) (**Fig. I.1.9**), respectively, the latter followed by the emission of a 1460.8 keV gamma ray, contribute significantly to the natural radioactivity. Potassium is a lithophile element and is monovalent under natural conditions. Its distribution in weathered rocks and soils is determined by the break-up of these host minerals. Potassium is soluble under most conditions and during weathering is lost into solution. In rocks it is concentrated mainly in felsic rocks as alkali-feldspars and micas, while mafic and ultramafic rocks contain the lowest concentration.

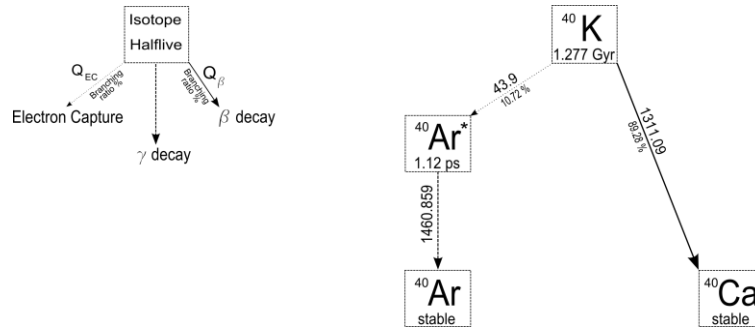


Figure I.1.9: potassium decay modes (Figure from (G. Fiorentini, M. Lissia et al. 2007)).

Uranium

Natural uranium is mainly constituted by ^{238}U , ^{235}U and ^{234}U created in the ^{238}U decay chain, having natural isotopic ratios 99.2745%, 0.730% and 0.0055%, respectively. The decay chain of ^{238}U includes 8 alpha decays and 6 beta decays respectively (Fig. I.1.10), often associated with gamma de-excitation of nuclei.

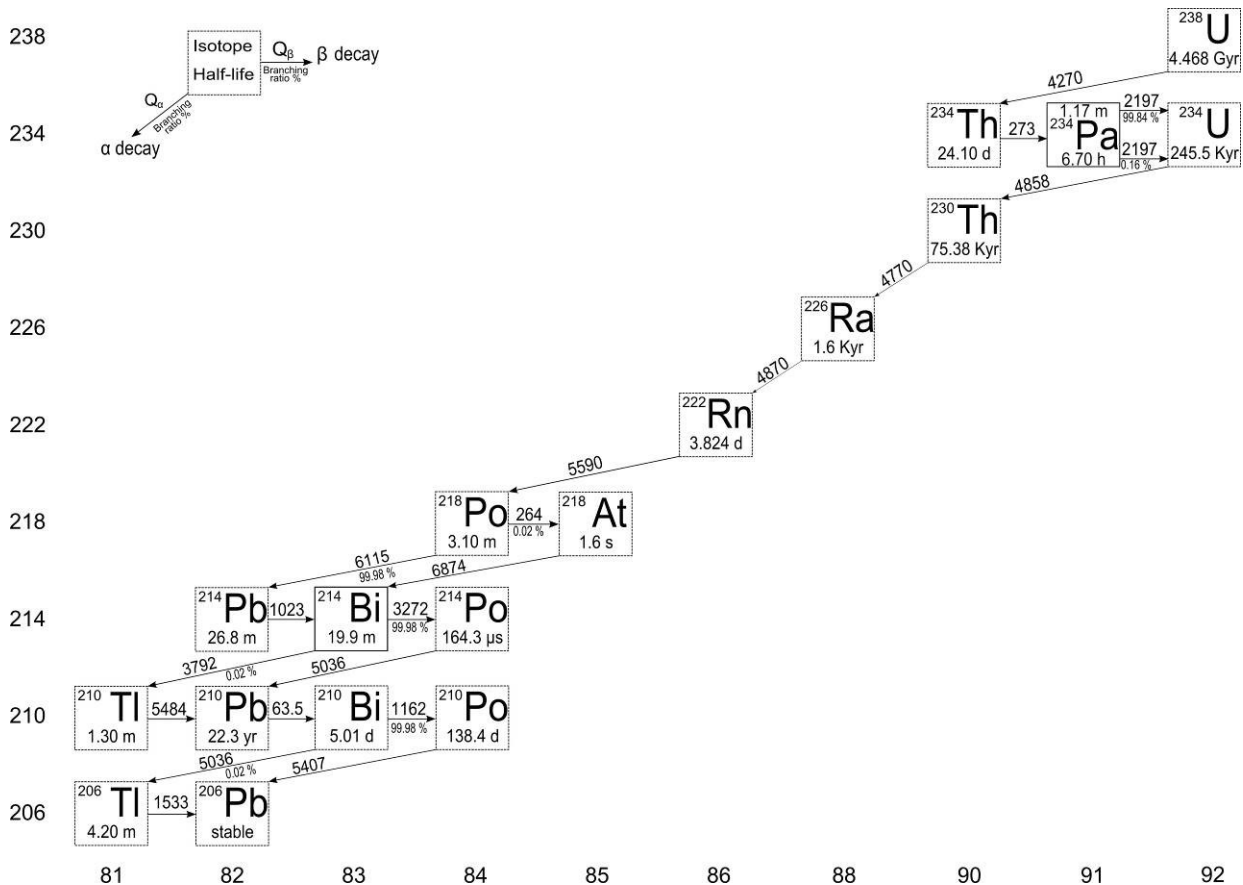


Figure I.1.10: uranium decay chain (Figure from (G. Fiorentini, M. Lissia et al. 2007)).

Uranium has four oxidation states U^{3+} , U^{4+} , U^{5+} and U^{6+} , where the most important are the tetravalent state and hexavalent state. The occurrence and the behavior of uranium in aqueous environment, is governed principally by the oxidation-reduction processes. Under oxidizing conditions uranium exits in the hexavalent

state (uranyl, U^{6+}) and forms carbonate, phosphate or sulphate complexes that can be very soluble, while under reducing conditions, exists in the tetravalent state (uranous, U^{4+}) which is insoluble. Uraninite (UO_2) is a common uranium mineral present as minute intrusions in the rock forming minerals in granites, hydrothermal veins or sedimentary rocks. The accessory minerals as zircon, monazite, apatite, allanite and sphene are common in igneous and metamorphic rocks, since for example zircon and monazite are the most resistant to weathering.

Thorium

Natural thorium has only one primordial isotope that of ^{232}Th having a natural isotopic ratio of 100%. The decay chain of ^{232}Th includes 6 alpha decays and 4 beta decays respectively (**Fig. I.1.11**), often associated with gamma de-excitation of nuclei. There are shorter-lived thorium isotopes in all three natural decay chains, as follows: ^{234}Th (24.1 d half-life) and ^{230}Th ($7.54 \cdot 10^4$ y half-life) in the ^{238}U chain; ^{228}Th (1.9 y half-life) in the ^{232}Th chain; and ^{231}Th (1.06 d half-life) in the ^{235}U chain.

Thorium occurs in the tetravalent (Th^{4+}) oxidation state and is insoluble except at low pH (near-neutral), or in the presence of organic compounds such as humic acids (**D. Langmuir and J. S. Herman 1980**). At near-neutral pH and in alkaline soils, the precipitation of thorium as a highly insoluble hydrated oxide phase and the co-precipitation with hydrated ferric oxides can, with sorption reactions, are two important mechanisms for the removal of thorium from solution. Because of sorption and precipitation reactions and the low solution rate of thorium-bearing minerals, thorium concentrations in natural waters are generally low. Thorium is a constituent of accessory minerals as zircon, monazite, allanite, xenotime, apatite and sphene.

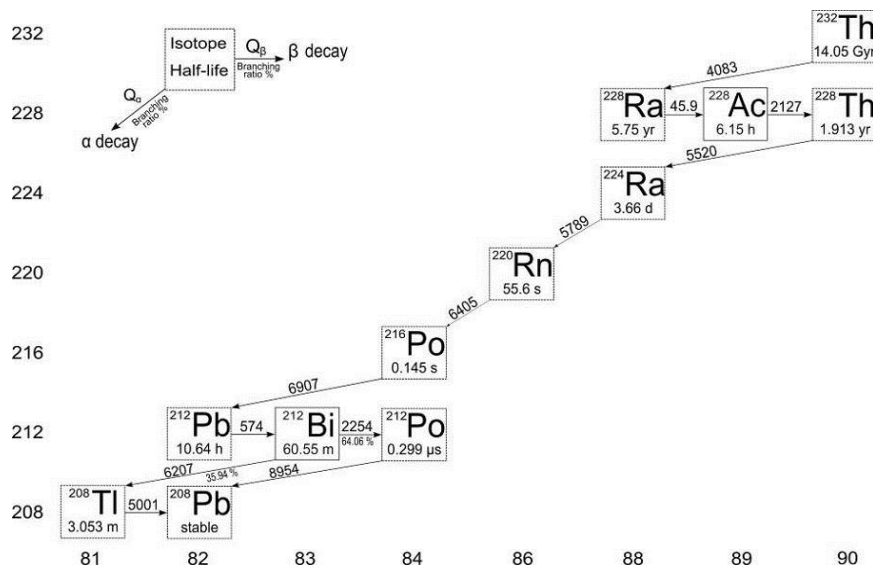


Figure I.1.11: thorium decay chain (Figure from (**G. Fiorentini, M. Lissia et al. 2007**)).

Chapter I.2

Principles of gamma-ray spectrometry and instruments

In this paragraph will recall the mechanisms of interaction of gamma radiation with matter in order to do an interpretation of the features within a gamma spectrum due to interactions within the detector and surroundings. The most important interaction processes for radiation measurements are **photoelectric absorption**, **Compton scattering** and **pair production**. In all three cases, partial or complete transfer of the gamma-ray photon energy to electron energy occurs, generating free electrons, and as these electrons are slowed down on their path through the matter they create electron-ion or electron-hole pairs. The discussion will be focused on gamma-ray spectrometry using semiconductor and scintillation detectors and instruments used in this study: in particular MCA-Rad system (**G. Xhixha, G. P. Bezzon et al. 2013**) – **Appendix B5** and portable NaI(Tl) system (**A. Caciolli, M. Baldoncini et al. 2012**).

I.2.1 Interaction of gamma-radiation with matter

I.2.1.1 Photoelectric absorption

Photoelectric absorption occurs during the interaction of the gamma-ray photon with one of the atomic bounded electrons. The electron may be ejected from its shell (**Fig. I.2.2a**), usually the most inner K-shell, if the gamma-ray energy is greater than the binding energy of that shell. If sufficient energy is not available to eject a K electron then L or M electrons will be ejected instead. This gives rise to sharp discontinuities (K, L or M edges) in the photoelectric absorption curves to the binding energies of the K, L and M electron shells. The gamma ray result totally absorbed and the electron gain a kinetic energy, E_e , given by:

$$E_e = E_\gamma - E_b \quad (\text{I.2.1})$$

where E_γ is the gamma-ray energy and E_b the energy binding the electron in its shell. (Generally, in order to conserve momentum when an electron is ejected a very small amount of energy must be retained by the recoil atom. This is very small and can be ignored for all practical purposes.) The atom is left in an excited state with an excess energy of E_b and recovers the equilibrium either by redistribution of the excitation energy between the remaining electrons in the atom (this can result in the release of other electrons, Auger electrons, which transfer a further fraction of gamma-ray energy to the detector) or by filling the vacancy left by the photoelectron by an outer shell electron (higher energy) giving rise to the emission of a characteristic X-ray called **X-ray fluorescence** (**Fig. I.2.2b**). This X-ray may then in turn undergo photoelectric absorption, perhaps emitting further X-rays and so on until all the energy of the gamma-ray is absorbed.

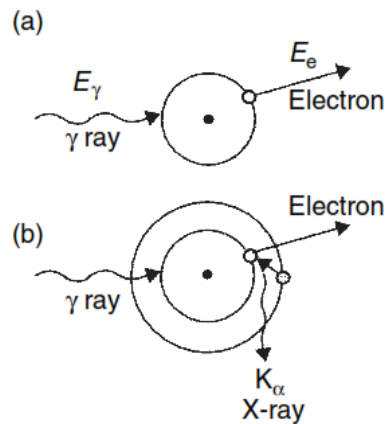
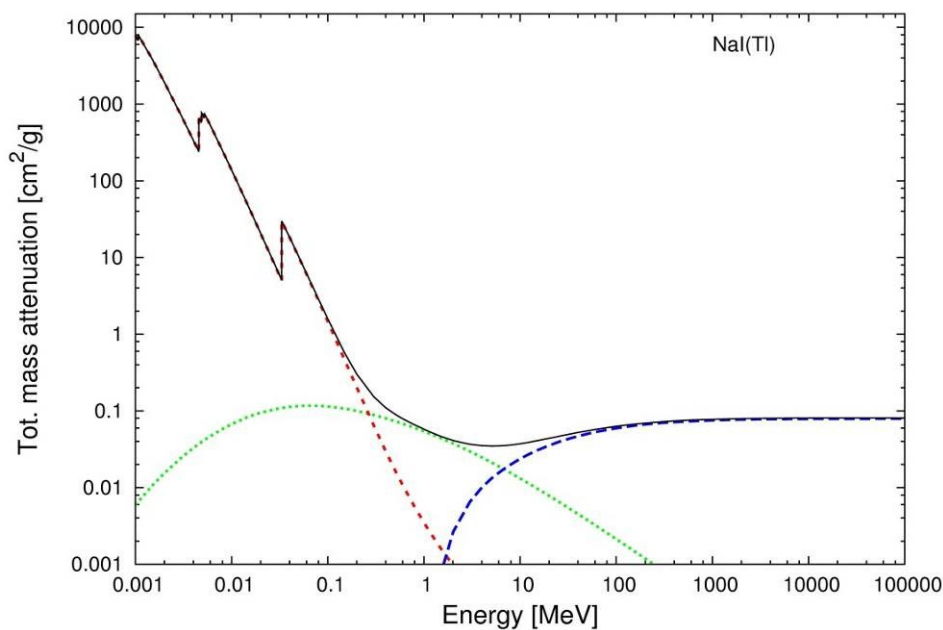


Fig. I.2.2a: (a) the mechanism of photoelectric absorption, and (b) the emission of fluorescent X-rays.

The energy level from which the electron is ejected depends upon the energy of the gamma-ray. The most likely to be ejected is a K electron. If sufficient energy is not available to eject a K electron, then L or M electrons will be ejected instead. This gives rise to the discontinuities in the photoelectric absorption curves. These **absorption edges** occur at the binding energies corresponding to the electron shells. For example, in the curve for germanium (**Figure I.2.3**) the K absorption edge occurs at 11.1 keV. For sodium iodide, there are two K edges, one corresponding to the iodine K electron at 33.16 keV and the other (very low) to the sodium K electron at 1.07 keV (**Figure I.2.3**). Similar edges corresponding to L and other less tightly bound electrons can be seen at lower energies of NaI(Tl), corresponding to iodine L electron at 5.18 keV, 4.85 keV and 4.55 keV. The L electron shell has three sub-levels and this is reflected in the shape of the L edge.



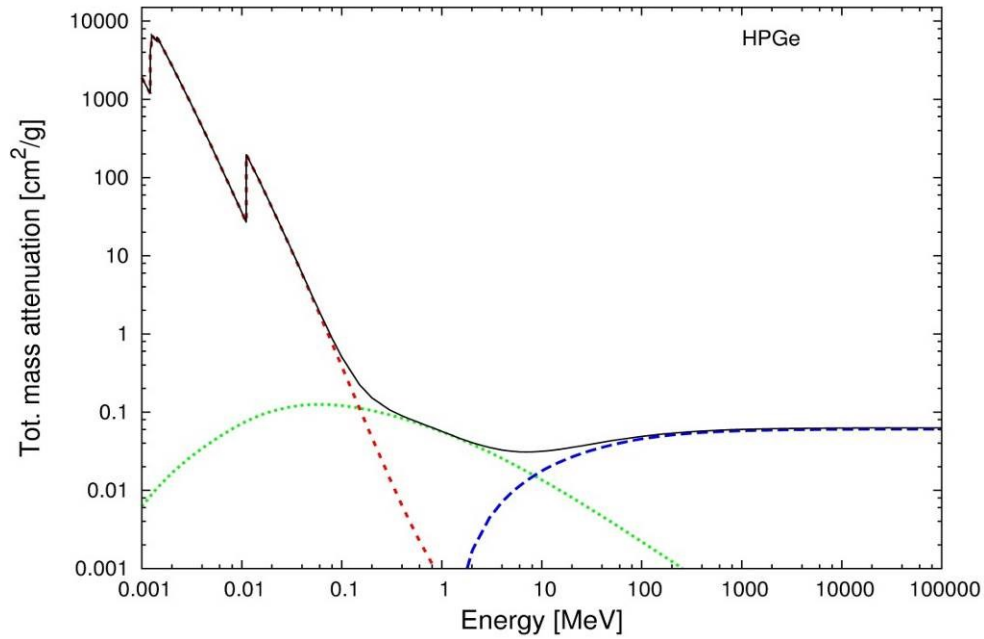


Figure I.2.3: attenuation coefficient of NaI(Tl) (top) and HPGe (bottom) as a function of gamma-ray energy: Compton scattering (dotted green), Photoelectric effect (dashed red), Pair production (dashed blue) and total attenuation (black).

The probability that a photon will undergo photoelectric absorption, expressed as a cross section, τ , increase by increasing the atomic number (Z) of the absorber and decreasing the gamma-ray energy (E) according to a complex relationship:

$$\tau \approx \frac{Z^n}{E_\gamma^m} \quad (I.2.2)$$

where n and m are within the range 3 to 5 depending upon energy. The photoelectric attenuation coefficient, μ_{PE} , can be derived from the related cross section in the following manner:

$$\mu_{PE} (m^{-1}) = \tau \times \rho \times \frac{N_A}{A} \quad (I.2.3)$$

where ρ is the density of the absorbing material, A its average atomic mass and N_A Avogadro's number.

I.2.1.2 Compton scattering

Compton scattering (**Fig. I.2.4**) is a direct interaction of the gamma-ray with an electron, transferring only a part of the incident gamma-ray energy to the kinetic energy of the recoil electron is given by the following equation:

$$E_e = E_\gamma - E'_\gamma \quad (1.2.4)$$

or

$$E_e = E_\gamma \left[1 - \frac{1}{1 + E_\gamma (1 - \cos \theta / m_0 c^2)} \right] \quad (1.2.5)$$

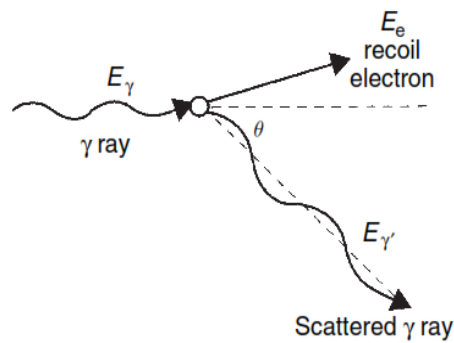


Figure I.2.4: the mechanism of Compton scattering.

The fraction of energy absorbed in any interaction is a function of incident gamma-ray energy, E_γ , and scattering angle, θ . Showing that for forward scattering gamma-rays, $\theta = 0^\circ$, no energy are transferred to the detector and at backscattering gamma-rays, $\theta = 180^\circ$ a maximum portion of energy is transferred to the recoil electron, known as **Compton edge** (Fig. I.2.5).

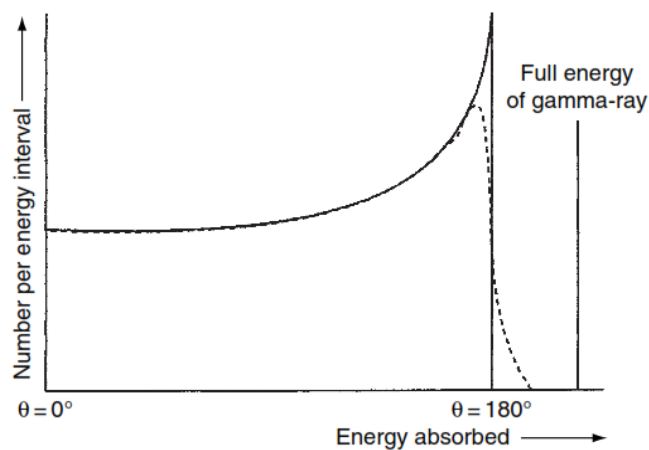


Figure I.2.5: energy transferred to the absorber by Compton scattering related to scattering angle.

The Compton scattering absorption cross section, often given the symbol σ , is related to atomic number of materials and the energy of the gamma-ray:

$$\sigma \approx Z \times E_{\gamma}^{-1} \quad (1.2.6)$$

Using an analogous relationship to that of **Eq.1.2.3** we can calculate a Compton scattering attenuation coefficient, μ_{CS} :

$$\mu_{CS} (m^{-1}) = \sigma \times \rho \times \frac{Z}{A} N_A \quad (1.2.7)$$

This relationship can be further simplified by taking into account the fact that over a large part of the periodic table the ration A/Z is reasonably constant with a value near to 2. This implies that the probability of Compton scattering at a given gamma-ray energy is almost independent of atomic number but depends strongly on the density of the material. Moreover, the mass attenuation coefficient, μ_{CS} / ρ , is approximately constant, at a particular energy.

1.2.1.3 Pair Production

Unlike photoelectric absorption and Compton scattering, pair production results from the interaction of the gamma-ray with the atom as a whole. The process takes place within the Coulomb field of the nucleus resulting in the conversion of gamma-ray into an electron-positron pair. This process is energetically possible at gamma-rays rather more than 1022 keV (twice the rest mass of an electron, 511 keV). In principle, pair production can also occur under the influence of the field of an electron, but the probability is much lower and the energy threshold is 2 times greater (2044 keV), making it negligible as a consideration in gamma spectrometry. The electron and positron created share the excess gamma-ray energy equally, losing it to the detector medium as they are slowed down.

$$E_e = E_{\gamma} - 2m_0c^2 \quad (1.2.8)$$

The annihilation of an electron-positron pair generally does not occur until the energy of the positron is reduced to near thermal energies, releasing the two 511 keV annihilation photons. This is likely to happen within 1 ns of creation of the pair and, taking into consideration the fact that the charge collection time of typical detectors is 100 to 700 ns, the annihilation can be regarded as instantaneous with the pair production event. If pair production occurs inside a detector, the 511 keV photons may be both absorbed or one or both escape depending on incident gamma-ray energy and detector size. The escape peaks therefore are formed at photopeak energies less 511 keV and 1022 keV. The complete sequence the events is described in **Figure 1.2.6**.

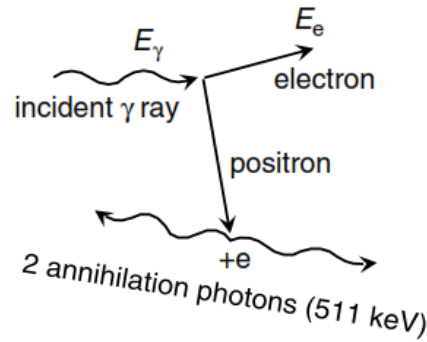


Figure I.2.6: the mechanism of pair production.

No simple expression exists for the probability cross section of pair production per nucleus, κ , but its magnitude varies approximately as the square of the absorber atomic number.

$$\kappa \approx Z^2 f(E_\gamma, Z) \quad (\text{I.2.9})$$

The variation of κ with atomic size is dominated by Z^2 term, the function $f(E, Z)$ is slightly dependent on Z and increases continuously with energy from the threshold 1022 keV so that at energies greater than 10 MeV pair production is the dominant mechanism of interaction. The attenuation coefficient, μ_{pp} , is calculated in a similar manner to the photoelectric attenuation coefficient (Eq. I.2.3).

I.2.2 Germanium gamma-ray detector principles: MCA-Rad system

I.2.2.1 Semiconductor detectors

Solid semiconductor materials (germanium or silicon) are widely used for gamma-ray and charge particle detection. In a free atom the electrons are disposed in precisely determined energy levels, while combining a solid structure broadens the energy levels into energy bands, each of which can contain a fixed number of electrons. The uppermost occupied energy band, known as the **valence band**, in a germanium crystal (IV valence atom) participate in covalent bounds showing a filled valence band and an empty **conduction band** (Fig. I.2.7). In an insulator or semiconductors the conduction band, the higher energy band, is separated by a forbidden region, **band gap** or **energy gap**, which width is the principal difference between them.

For an electron to migrate through the material it must gain sufficient energy to jump from the valence band across the band gap, E_g , into the conduction band. In an insulator this gap is of more than 5 eV, compared with about 1 eV in semiconductors. Thermal excitation at room temperature (with a probability given by Eq. I.2.10) makes that the conduction band is always populated by a small number of electrons and the application of a reasonable electric field (few kilovolts), will cause a current flow.

$$p(T) = CT^{3/2} e^{-\frac{E_g}{2kT}} \quad (\text{I.2.10})$$

where T = absolute temperature, E_g = energy bandgap, k = Boltzmann constant and C = proportionality constant characteristic of the material. For practical gamma-ray detectors, in order to reduce the noise (background) current (or leakage current), the semiconductor materials are cooled using liquid nitrogen (LN₂) or mechanical closed-cycle refrigerators, for example based on the Joule-Thomson effect (high-pressure gas, typically nitrogen at 100 atm, is expanded in a capillary tube to provide the cooling), which can reach temperatures as low as 77 K.

When an electron occupies the conduction band a vacancy is left behind, which is effectively positively charged and referred to as a **hole**. As a consequence a valence electron may fill the vacancy left (creating in this process a new hole), the hole appears to migrate through the crystal. Although semiconductor materials provide a ready means by which the electron-hole pairs can be collected, in a practical detector this must be accomplished within a reasonable time (few tens of ns). The time taken for each charge carrier to reach its destination, the charge collection time, will depend upon the distance it must travel (depletion depth, d) and the speed at which it travels. If an electric field, E , created by a bias voltage, V_b , is applied across the detector an additional **drift velocity** will be added parallel to the direction of the field. For each entity we can define their **mobility**, μ , given by:

$$\mu_{e,h} = \frac{v_{e,h}}{E} \quad (\text{I.2.11})$$

where $v_{e,h}$ = drift velocity of the electron or hole and E = electric field strength.

The mobilities of electrons and holes are different, although in germanium this difference is only about 15%. At low-to-moderate field intensity the mobility is almost constant but at high field intensity the drift velocity does not increase proportionately with field and eventually reaches a **saturation velocity** (in semiconductors the saturation velocity is of the order of 10^7 cm/s). The fact that the mobility decreases with increasing temperature is yet another justification, in addition to reducing thermal excitation across the band gap, for operating germanium detectors at low temperature.

In order to control the electrical conduction in semiconductor materials, small amount of materials is added, called **dopants** and having III or V valence atoms. Germanium is a four valence atom and in a crystal will form four covalent bonds with neighboring germanium atoms, each equally contributing electron to the bonding between them. For V valence impurities, such as arsenic or phosphorus, will have one electron in excess and the impurity atom will be a **donor atom** sitting on a donor site and will introduce discrete **donor states** just below the conduction band. Because there is an excess of negative charge carriers (electrons) this material is called **n-type** germanium. Alternatively, for III valence impurities, such as gallium or boron, will have one hole in excess and the impurity atom will be an **acceptor atom** sitting in an acceptor site and will

introduce discrete acceptor states just above the **valence band**. Because there is an excess of positive charge carriers (holes) this material is called **p-type** germanium. The effect of this process is a narrower band gap and a higher conductivity.

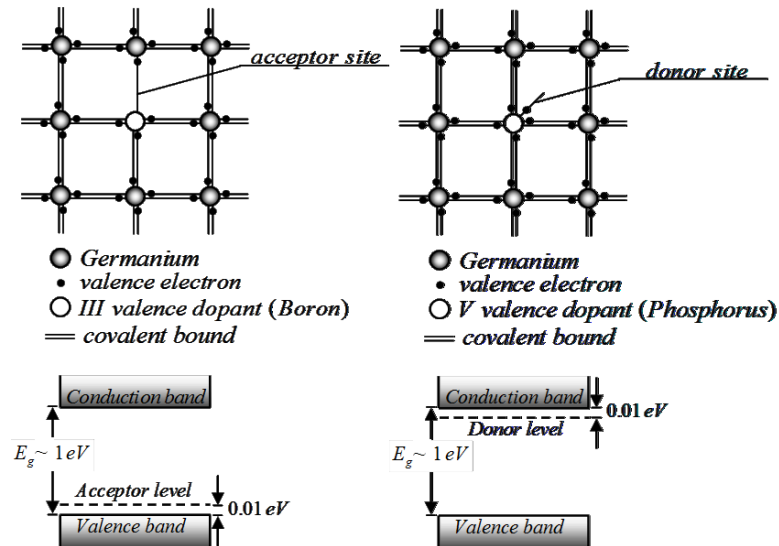


Figure I.2.7: (a) Representation of an acceptor impurity, boron, (left) occupying a substitution site in a germanium crystal and the corresponding acceptor levels created in the p-type germanium bandgap. (b) Representation of an acceptor impurity, phosphorus, (right) occupying a substitution site in a germanium crystal and the corresponding acceptor levels created in the n-type germanium bandgap.

Semiconductors for gamma-ray spectrometry

The semiconductor gamma-ray detector depends upon the electronic redistribution which occurs when p-type and n-type semiconductor materials are brought into appropriate thermodynamic contact (p-n junction). As these dissimilar semiconductor materials diffuse under the thermal influence, the electrons from the n-type material can move across the junction into the p-type material and combine with holes; in the vicinity of the physical junction of the two materials, the charge carriers are neutralized, creating a region called **depleted region**, the active element of the detector. The migration of the charge carriers gives rise to a negative space charge in p side and a positive space charge in n side which will create a potential barrier called the **contact potential** (about 0.4 V high in germanium) which eventually stops further migration. Generally because there is a marked difference in the doping levels, the depletion region will not extend equal distances into both sides. The depletion region can be effectively increased if a positive voltage (few kilovolts) is connected to the n side of the junction (**Fig. I.2.8**). Because the positive voltage is connected to the negative type semiconductor this is called **reverse biased junction**. This because the p-n junction will readily conduct current when voltage is applied in the “forward” direction, but it will conduct very little current when biased in “reverse” direction. In practice gamma-ray detectors are not constructed by placing

different types of semiconductor materials in contact but by conversion of one face of a block of germanium to the opposite semiconductor type by evaporation and diffusion or by ion implementation.

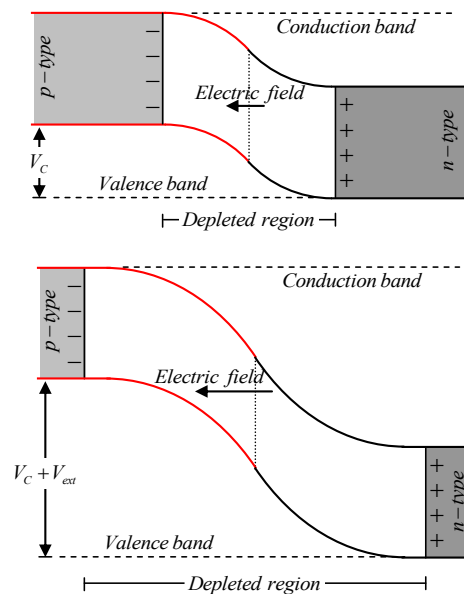


Figure I.2.8: (Top) When n-type and p-type materials are brought into contact, electrons and holes near the junction can recombine to create a region that is depleted of charge. (Bottom) Under reverse bias, the depleted region becomes larger and the magnitude of the electric field increases.

The interaction of a gamma-ray with the semiconductor material (depleted region) will produce relatively high energy primary electrons, which redistribution give rise to cascade of electron-hole pairs. In the presence of an electric field they will migrate up (electrons) or down (holes) the field gradient where the amplitude of electrical pulse created (number of electron-hole pairs) is directly proportional to the gamma-ray energy absorbed. **High-purity germanium** (abbreviated as **HPGe**, containing a level of impurity of less than 1 part in 10^{12}) is the most common detector material, where its higher atomic number than silicon makes it practicable to use it for the detection of higher energy gamma radiation.

I.2.2.2 MCA-Rad system design

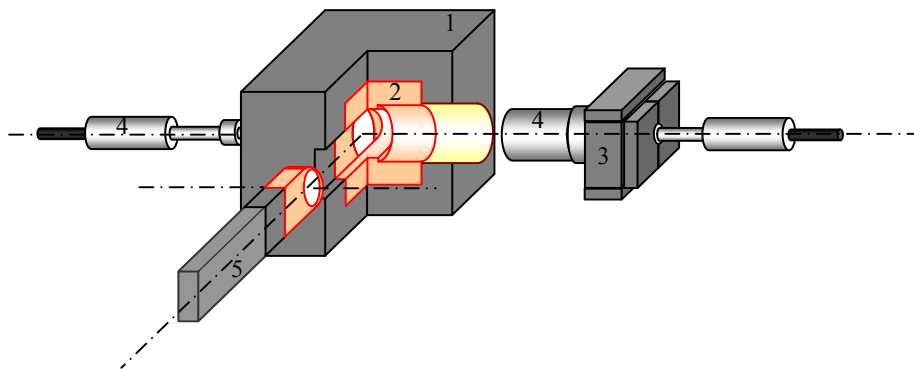
The core of the MCA_Rad system (G. Xhixha, G. P. Bezzon et al. 2013) – Appendix B5 consist in two vertical p-type HPGe gamma-ray spectrometers (Table I.2.2) facing each other at about 5 cm apart (Fig. I.2.10a and Fig. I.2.10b).

Table I.2.2: the features of the two detectors used in the project design of MCA_Rad system.

Description	Detector A	Detector B
Detector type (ORTEC®)	cylindrical coaxial p-type	cylindrical coaxial p-type
HPGe crystal net volume (cm ³)	234.4	292.84
HPGe crystal base surface (cm ²)	65.00	56.58
HPGe crystal length (cm)	5.43	7.96
End-cup type	1.5 mm Al	1.5 mm Al
Relative efficiency (⁶⁰ Co gamma-ray at 1332 keV)	60%	67%
FWHM at 1332 keV (⁶⁰ Co)	1.67 keV	1.84 keV
FWHM at 122 keV (⁵⁷ Co)	0.77 keV	0.82 keV
Peak shape (FWTM/FWHM) for ⁶⁰ Co	1.9	1.9
Peak shape (FWFM/FWHM) for ⁶⁰ Co	2.4	2.6
Peak-to-Compton ratio (⁶⁰ Co gamma-ray at 1332 keV)	81:1	83:1
HPGe cooling system	electro-mechanical	electro-mechanical
Positive High Voltage (kV)	4.8	2.0

The figures represent values measured by the manufacturer.

The two detectors are controlled by individual integrated gamma spectrometers for the digital signal processing using commercial software for spectra acquisition. The new cooling technology which uses mechanical coolers permits to simplify the management of the system, however, a similar system was developed also for LN₂ cooled HPGe detectors.



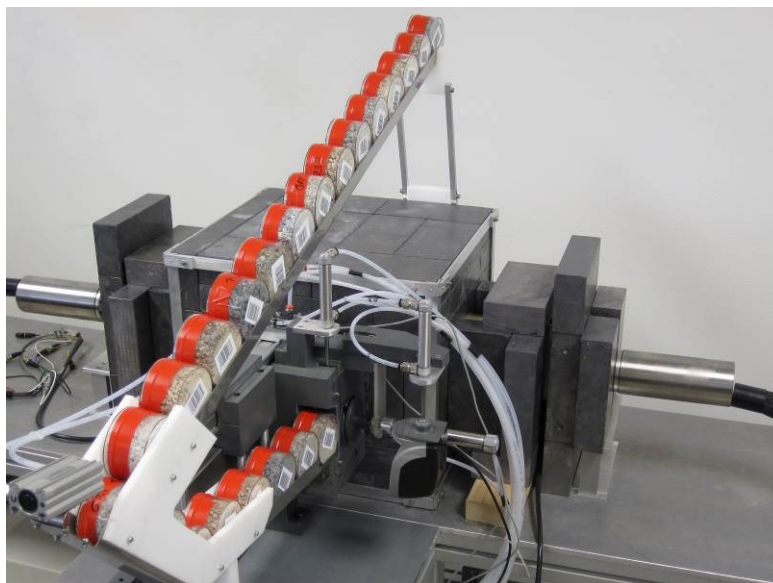


Figure I.2.10: (a) schematic design of the MCA_Rad system. 1) The main lead shielding construction (20 cm x 25 cm x 20 cm). 2) The core copper shielding (10 cm x 15 cm x 10 cm). 3) The rear lead shielding construction. 4) HPGe semiconductor detectors. 5) The mechanical sample changer. (b) view of MCA_Rad system.

A 10 cm thick lead outer house and a 10 cm thick oxygen free copper inner house shields the detector assembly leaving an empty volume dedicated hosting the sample container (cylindrical polycarbonate box of 75 mm in diameter and 45 mm in height (180 cm³ of useful volume)). In order to reduce the X-rays and high energy beta particles coming from the sample, the end-cup windows of the detectors are further shielded with a tungsten (W) alloy sheet of 0.6 mm. A 10 mm thick bronze cylinders and walls of about 10 cm of lead are also used to shield the rear part of the system (**Fig I.2.10**). Therefore the MCA-Rad system background is reduced by two orders of magnitude respect to unshielded detectors (laboratory background). The knowledge of background spectra is required in order to detect any potential residual contaminations and for background corrections. In **Table I.2.3** we calculate the limit of detection and the minimum detectable activity (discussed later in **section I.3.1.2**) for the background spectra of the MCA-Rad system.

Table I.2.3: characterization of MCA_Rad system background (Bckg. Lab. without shielding and Bckg. MCA-Rad with shielding) expressed in count per hour (cph) for the most intense energetic lines and the corresponding detection limit L_D in counts (Eq. I.3.21) for 95% confidence interval (CI) and minimum detectable activity (MDA) in Bq/kg (Eq. I.3.22).

Parent Nuclide	Daughter Nuclide	Energy (keV)	I (%)	Bckg. Lab. (Counts)	Bckg. MCA-Rad (Counts)	$L_D(5\%)*$ (Counts)	MDA* (Bq/kg)
^{238}U	$^{234\text{m}}\text{Pa}$	1001.0	0.837	180 ± 13	8 ± 1	21	22.16
	^{214}Pb	351.9	35.8	9704 ± 40	31 ± 2	49	0.50
	^{214}Pb	295.2	18.5	5165 ± 37	13 ± 2	51	0.35
	^{214}Bi	609.3	44.8	10273 ± 34	44 ± 1	32	0.49
	^{214}Bi	1764.5	15.36	2801 ± 16	27 ± 1	13	1.97
	^{214}Bi	1120.3	14.8	3022 ± 21	17 ± 1	23	1.67
	^{214}Bi	1238.1	5.86	1152 ± 17	9 ± 1	19	3.58
^{232}Th	^{228}Ac	911.2	26.6	5050 ± 26	27 ± 1	27	0.94
	^{228}Ac	968.9	16.2	3045 ± 21	17 ± 1	24	1.38
	^{228}Ac	338.3	11.3	3014 ± 33	7 ± 2	51	1.47
	^{212}Pb	238.6	43.3	12984 ± 52	100 ± 2	62	0.46
	^{212}Bi	727.3	6.58	1463 ± 21	10 ± 1	31	3.00
	^{208}Tl	2614.5	99	4857 ± 20	64 ± 1	9	1.58
	^{208}Tl	583.2	84.5	6579 ± 30	42 ± 1	33	0.71
^{40}K	-	1460.8	10.7	24947 ± 47	151 ± 1	19	5.53

* Values calculated for typical background (with shielding) spectra of 1h counting time.

The MCA_Rad system is a standalone low-background gamma-ray spectrometer fully automated for normal working processes including automatic samples changer and spectrum analysis. The mechanical automation consists of a set of compressed air driven electro-pneumatic valves programmed under Agilent VEE graphical language environment using an Agilent 34970A Data Acquisition Switch Unit. The Agilent 34970A consists of a three-slot mainframe with a built-in 6 1/2 digit digital multimeter with specialized plug-in modules.

The sample container is barcode labeled, which allow the sample identification through a barcode scanner and permitting the match with the job batch file. The software receives by the operator an input file with the relevant information about the slot of samples: acquisition live time, spectra file name, sample weight, sample description and barcode. Up to 24 samples can be charged in a slider moving on gravity and further introduced at the inner chamber through an automatic “arm” made of copper, lead and plastic closing the lateral hole of the housing and matching with the main shield material. Furthermore the program control the spectrum acquisition procedure automatically generating and running a job file (commonly used by

commercial software) which contain relevant information containing the duration of acquisition live time and spectra nomination codes. At the end of the each measurement the procedure is repeated until whether no more samples are detected by the bar-code reader or an error is detected in the sample change procedure generating a batch file used to automatically analyze the spectra.

1.2.2.3 Efficiency calibration and validation

The absolute photopeak efficiency (ε_p) for the MCA_Rad system (**G. Xhixha, G. P. Bezzon et al. 2013**) - **Appendix B5** has been determined by using standard point sources method, and producing the calibration curve. Two low activity point sources with complex decay schemes are used (**P. De. Felice, A. Fazio et al. 2006**): a certified ^{152}Eu source, with an activity of 6.56 kBq in 1995, known with an uncertainty of 1.5% and a ^{56}Co homemade source, that has been normalized relative to ^{152}Eu by calculating the activity of the 846.8 keV (^{56}Co) gamma line. The ^{56}Co source is used in order to extend the efficiency calibration for gamma energies up to 3000 keV.

The spectra obtained are corrected for:

- **coincidence summing**, C_{CS} , on each individual detector, produced by the complex decay scheme of the sources. The correction due to coincidence summing is studied by following the method described in (**P. De. Felice, P. Angelini et al. 2000**) and obtained as a relationship between the single total efficiency (ε_t), the single apparent absolute photopeak efficiency (ε_p^{app}) and isotope decay data:

$$C_{CS(i)} = \left[1 - \frac{\sum_j P_{ij} P_i P_j \varepsilon_j}{I_{\gamma i}} \right] \left[1 + \frac{\sum_{k,m} P_{tkm} P_k P_m \varepsilon_k^{app} \varepsilon_m^{app}}{I_{\gamma i} \varepsilon_i^{app}} \right] \quad (1.2.16)$$

where P_{ij} is the probability of coincident transitions (i, j); P_i is the probability of photon emission in transition i ; I_{γ} is the photon emission probability; ε_i is the apparent full energy peak efficiency and ε_j is the total apparent efficiency (obtained by estimating the peak-to-total ratio (P/T) using the empirical approach described by (**A. Cesana and M. Terrani 1989**) and recalling the relationship $\varepsilon_p^{app} / \varepsilon_i = P / T$). The decay coefficients for ^{152}Eu were calculated from decay data taken from (**BIPM-5 2004**), while those for ^{56}Co were taken from (**E. Tomarchio and S. Rizzo 2011**) and (**P. Dryàk and P. Kovàr 2009**).

- differences between the **geometry** of the point sources and the sample shape, C_G . The effect of volume geometry can be described in terms of the effective solid angle developed analytically by (**L.**

Moens, J. De Donder et al. 1981) within less than 2% of uncertainty between numerical and experimental calculations. The geometrical factor (**Fig. I.2.14**) for MCA_Rad system is deduced from a set of measurements using a ^{56}Co and ^{57}Co point sources placed at different radial distances (center, middle and lateral) from the detector axis at different planes, reconstructing the sample geometry using the formula:

$$C_G(E_i) = \frac{\bar{\Omega}_x}{\Omega_{ref}} \approx \frac{1}{R_{ref}(E_i)} \sum_{j=1}^N \frac{[R_x(E_i)]_j}{N} \quad (\text{I.2.18})$$

where $R_x(E_i)$ is the net count rate in the standard spectrum collected in different positions (j) and $R_{ref}(E_i)$ is the net count rate in the standard spectrum collected in the reference positions (center).

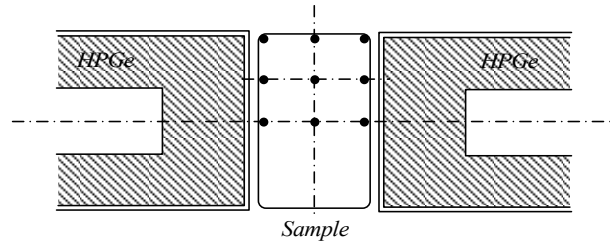


Figure I.2.14: experimental measurement configuration for the calculation of geometrical correction factor.

The geometrical correction factor is obtained as a function of energy by fitting a third order polynomial as a function of energy:

$$C_G(E) = \sum_{i=0}^4 a_i \left(\frac{E}{E_0} \right)^i \quad (\text{I.2.19})$$

where $E_0 = 1$ keV is introduced to make the argument dimensionless and a_i are the fitting coefficients ($a_0 = 0.8678$, $a_1 = 0.1098$, $a_2 = -0.0541$, $a_3 = 0.0077$).

- **self-attenuation**, C_{SA} , of gamma-rays within the sample volume. The gamma-ray attenuation correction C_{SA} is calculated for different kind of samples taking into account their differences in density by a simplified expression deduced by (**H. N. Cutshall, L. I. Larsen et al. 1983**) and (**P. J. Bolivar, M. Garcia-Leon et al. 1997**):

$$C_{SA} = \frac{1 - \exp(-\mu_l t)}{\mu_l t} \quad (\text{I.2.20})$$

where $\mu_l = \mu \rho$ (cm^{-1}) is the linear mass attenuation coefficient, μ ($\text{cm}^2 \text{g}^{-1}$) is the mass attenuation

coefficient, ρ (g cm^{-3}) is the sample density and t (cm) is the sample effective thickness (which in our case is the half thickness of the sample container). The mass attenuation coefficient is strongly Z dependent in the energy range below few hundred keV while for higher energies the trend is smoother and it depends mainly on energy. We can parameterize the mass attenuation coefficient as a function of energy. We used the XCOM 3.1 database, which is available on-line and developed by the Nuclear Institute of Standards and Technology (NIST). For various rocks forming minerals, the average mass attenuation coefficient was deduced with a standard deviation of less than 2% in the energy range 200 – 3000 keV. Finally the self-attenuation correction factor was given as a function of gamma-ray energy and sample density through the relationship:

$$C_{SA}(E, \rho_s) = \exp[b_0 + b_1 \ln(E) + b_2 \ln(E)^2] \rho_s \quad (\text{I.2.22})$$

where b_i ($b_0 = 1.2609$, $b_1 = -0.2547$, $b_2 = 0.0134$) are coefficients determined by fitting this function.

Then the absolute efficiency is fitted for the energy range from 200 keV to 3000 keV using the function given by (F.G. Knoll 1999) (Fig. I.2.13):

$$\varepsilon(\%) = (b_0 E / E_0)^{b_1} + b_2 \exp(-b_3 E / E_0) + b_4 \exp(-b_5 E / E_0) \quad (\text{I.2.17})$$

where E (keV) is the gamma-ray energy; $E_0 = 1$ keV is introduced to make dimensionless the argument of the exponential dimensionless and b_i are the fitting parameters (where $b_0 = 1.38$, $b_1 = 1.41$, $b_2 = 22.97$, $b_3 = 5.43$, $b_4 = 6.61$ and $b_5 = 0.44$).

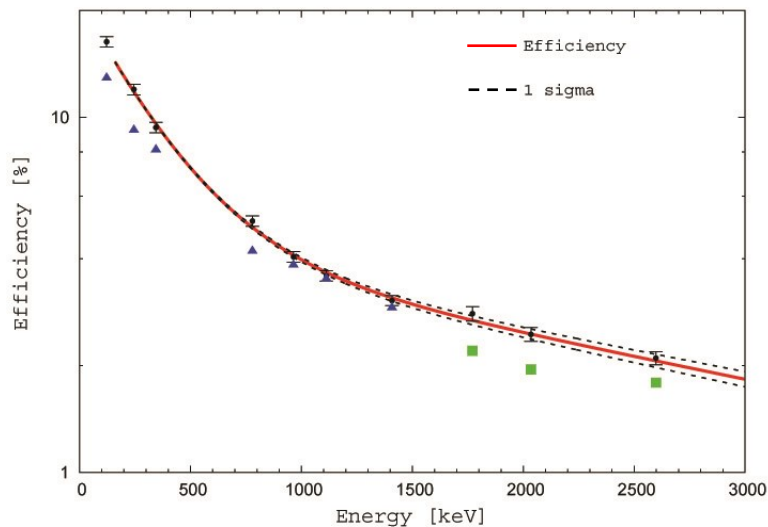


Figure I.2.13: absolute efficiency curve of MCA_Rad system. It is obtained by fitting ¹⁵²Eu (triangle) and ⁵⁶Co (circle) energies with Eq. I.2.17 performing the best fit (in red). Dashed curves represent \pm one sigma uncertainty interval.

The uncertainty budget for the calibration procedure is reported in **table I.2.4**. Considering the uncertainties due to geometrical and self-attenuation correction factors as systematic errors, the overall uncertainty about the absolute efficiency of the MCA_Rad system is estimated to be less than 5%.

Quality control and validation

The applicability of the MCA_Rad system as well as the method quality control was cross checked using certified reference materials containing concentrations comparable to NORM values. Three reference materials certified within 95% of confidence level prepared in the powder matrix (240 mesh) containing ^{238}U (IAEA RGU-1) $4940 \pm 30 \text{ Bq kg}^{-1}$, ^{232}Th (IAEA RGTh-1) $3250 \pm 90 \text{ Bq kg}^{-1}$ in secular equilibrium and ^{40}K (IAEA RGK-1) $14000 \pm 400 \text{ Bq kg}^{-1}$ are used. The sample boxes were filled with the reference materials, after were dried at 60°C temperature, hermetically sealed and then left undisturbed for at least 3 weeks in order to establish radioactive equilibrium in ^{226}Ra decay chain segment prior to be measured.

In **Table I.2.5** we report the specific activity calculated for the principal gamma lines used to estimate the isotopes of uranium and thorium decay chain and for potassium using the formula:

$$A (\text{Bq} / \text{kg}) = \frac{R}{\varepsilon I_\gamma m} C_{SA} C_G C_{CS}^* \quad (\text{I.2.23})$$

where R is the measured count rate (background corrected), ε is the absolute efficiency, I_γ is the gamma line intensity, m is the mass of the sample, C_{SA} is the correction factors for self-absorption, C_G is the geometrical correction factor and C_{CS}^* is the coincidence summing correction factor (calculated using the same approach as described above for the specific decay chains of the uranium and thorium). The results have an overall relative discrepancy of less than 5% among certified central values within the reported uncertainty.

Table I.2.5: In the sixth column we report the activity concentrations (in Bq kg⁻¹) calculated for the main energetic lines used for ²³⁸U and ²³²Th decay chains and for ⁴⁰K together with respective statistical uncertainties. The reference material activities certificated by the IAEA are shown in the seventh column. The correction coefficients C_{CS}^{*} and C_{SA} are referred to coincidence summing and self-absorption respectively.

Parent Isotope	Daughter Isotope	E (keV)	C _{CS} [*]	C _{SA}	Activity (Bq kg ⁻¹)	Certified Reference Material Activity (Bq kg ⁻¹)
²³⁸ U	^{234m} Pa	1001.0	1.000	1.24	4875 ± 48	4940 ± 30
	²¹⁴ Bi	609.3	1.190	1.32	4872 ± 4	
	²¹⁴ Pb	351.9	1.002	1.42	4773 ± 3	
²³² Th	²²⁸ Ac	911.2	1.024	1.24	3092 ± 4	3250 ± 90
	²¹² Pb	238.6	0.990	1.48	3246 ± 2	
	²¹² Bi	727.3	1.056	1.27	3389 ± 9	
	²⁰⁸ Tl	583.2	1.298	1.31	3342 ± 4	
⁴⁰ K	-	1460.8	-	1.21	14274 ± 71	14000 ± 400

I.2.3 Scintillation gamma-ray detector principles: portable NaI(Tl) system

I.2.3.1 Scintillation detectors

Inorganic crystals: NaI(Tl)

As described above, in semiconductor detectors the primary electrons produced by the gamma-ray interaction lose their energy by creating secondary electron-hole pairs, which after collected by the detector produce an electrical signal. In scintillation detectors the primary ionization of the detector is broadly the same but the collection process differs somewhat. The scintillation mechanism in inorganic materials depends on the energy states determined by the crystal lattice of the material, rather than a molecular effect as it was the case for organic scintillators.

According to the energy band structure (discussed in **paragraph I.2.1**), the primary electron produced by the gamma-ray interaction raises secondary electrons to the conduction band leaving holes in the valence band. In some cases the energy given to the electron may not be quite sufficient to raise it to the conduction band, remaining electrostatically attracted from the hole and giving rise to an extra band just below (**exciton band**), but continuous with, the conduction band (**Fig. I.2.17**). If the electrons are allowed to de-excite by falling back to the valence band they will emit electromagnetic radiation. If this radiation is in, or near, optical wavelengths it can be detected by a photomultiplier or other photosensitive devices.

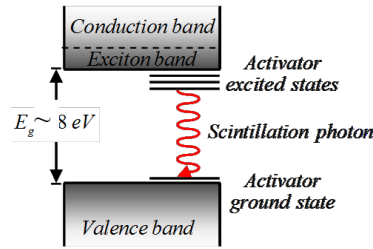


Figure I.2.17: energy band structure of an activated crystalline scintillator.

However, as it happens, the band gap of sodium iodide is large and photons emitted by de-excitation of electrons directly from conduction band would be far outside the visible range, making their detection very difficult. Not only that but the bulk of the material would absorb the emitted photon before they reached the photomultiplier. These two problems are solved by using an **activator**, which in the case of sodium iodide (NaI) it would be the thallium. The introduction of 0.1% of the impurity produces defect lattice sites which give rise to extra levels within the forbidden band between the valence and conduction bands (**Fig. I.2.17**). The ground state of this activator sites lies just above the valence band and the excited site just below the conduction band. When an electron-hole pair is formed the hole may migrate to a nearby activator site and the electrons in the conduction band within the excited activator states. This means that the photon energy released when these levels de-excite will be lower and the electromagnetic radiation will be of a longer wavelength. It turns out that the emission wavelength is, in general, longer than the absorption wavelength (Stoke's shift) not matching the absorption characteristics of the scintillators.

Not all the energy absorbed from the gamma-ray will be re-emitted as scintillation photons. There are several parameters characterizing scintillators. The **scintillation efficiency** is defined as:

$$\text{scintillation efficiency} = \frac{\text{average number of emitted photons}}{\text{absorbed energy}} \quad (\text{I.2.24})$$

The **scintillation yield** is defined as:

$$\text{scintillation yield} = \text{total energy of the emitted light} = h\nu (\text{scintillation eff.}) \quad (\text{I.2.25})$$

where $h\nu$ = energy of the emitted photons. The NaI(Tl), which is the most efficient crystal in terms of light output, will only release about 12% of the total. The rest of the energy is retained as lattice vibrations or heat.

The mean life, or lifetime, of an excited activator depends on the emission type. There are two types of light emission: **fluorescence (luminescence)** and **phosphorescence**. Fluorescence corresponds to prompt light emission (ns \rightarrow μ s) in the visible or near visible wavelength range and is temperature independent. Phosphorescence corresponds to light emitted over a longer period of time (μ s \rightarrow ms, even hours depending on the material) with longer wavelengths compared to fluorescence and is temperature dependent. It can often be a significant source of background light or “**afterglow**” in scintillators. A third possibility exists when an

electron is captured at an activator site: certain radiation less transitions are possible between some excited states formed by electron capture and the ground state, in which case no visible photon results. Such processes are called **quenching** and present loss mechanisms in the conversion of the particle energy to scintillation light. In practice, only fluorescence, characterized by fast light emission, is useful for the detection of particle or nuclear radiation.

Scintillator detectors have an advantage over HPGe semiconductor detectors in that they can operate at room temperature, and indeed the light output from NaI(Tl) is at a maximum at room temperature range. Relative efficiency is given to the conversion efficiency relative to NaI(Tl), since this is the most used scintillator material showing excellent performances. However, NaI(Tl) exhibits several drawbacks: it is brittle sensitive to thermal gradients and thermal shock, it is hygroscopic and therefore must be encapsulated at all times. Furthermore, it shows small impurities of internal radioactive contamination due to potassium, which is chemically similar to sodium, however the detector manufacture can reach sodium iodide purity as less than 0.5 $\mu\text{g/g}$ of potassium. The most notable property of NaI(Tl) is its excellent yield. Its response to electrons (and gamma rays) is close to linear over most of the significant energy range.

Detection of the scintillation light

The output from the scintillation crystal is a quantity of light which is measured converting it into an electric signal. Conventionally this is done by a photomultiplier tube (PMT). The general configuration of a scintillation detector is shown in **figure I.2.18**.

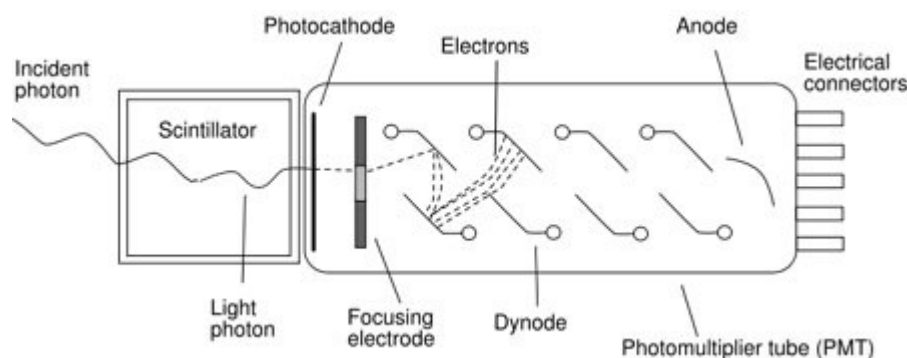


Figure I.2.18: schematic diagram of a scintillation detector comprising scintillation crystal optically coupled to a photomultiplier.

When light passes through an interface there is a potential for losses by reflection at the interface. Light which is incident on the surface at more than the critical angle, θ_C , will be totally internally reflected and if the angle is less than the critical angle almost all the light will be transmitted: a small amount will be reflected back (Fresnel reflection). For this reason in order to reduce transmission losses to a minimum, the refractive indices should be as near as possible equal to the scintillation material refractive indices.

$$\theta_C = \sin^{-1} \left(\frac{n_{med}}{n_{det}} \right) \quad (1.2.26)$$

where n_{det} = refractive indices of the detector material and n_{med} = refractive indices of the coupling medium.

The light photons strike a light sensitive layer, the **photocathode** having a low energy barrier to the release of photoelectrons from its surface, causing it to emit a photoelectron, via the photoelectric effect (Einstein equation):

$$E_e = h\nu - \varphi \quad (1.2.27)$$

where E_e = kinetic energy of the emitted electron, $h\nu$ = energy of incident scintillation light and φ = work function.

The photocathode materials are Na₂K₂Sb activated with cesium (called multialkali coating) and K₂CsSb activated by oxygen and cesium (called bialkali coating). The type of photocathode is chosen to have an overlap between its peak spectral response and the characteristic wavelength of maximum emission of the incoming light. In **figure 1.2.19** compares the emission spectrum of various scintillator materials with the photocathode response of two common photomultipliers. Not every photon striking the photocathode will produce a photoelectron: the quantum efficiency of a photocathode material (defined as the number of photoelectrons per incident photon) might be 20-30% in the optimum photon energy. In NaI(Tl) it takes about 26 eV of energy absorbed by the detector to produce one photon, which by taking into account the quantum efficiency as well, this means that it takes about 100 eV of gamma-ray energy to create the primary electron signal at the photocathode (compared to 2.96 eV at germanium detectors). This has implications for detector resolution, 6% (80 keV) for 3x3" at 1332 keV for NaI(Tl) compared with 0.15% (2 keV) for typical germanium detector.

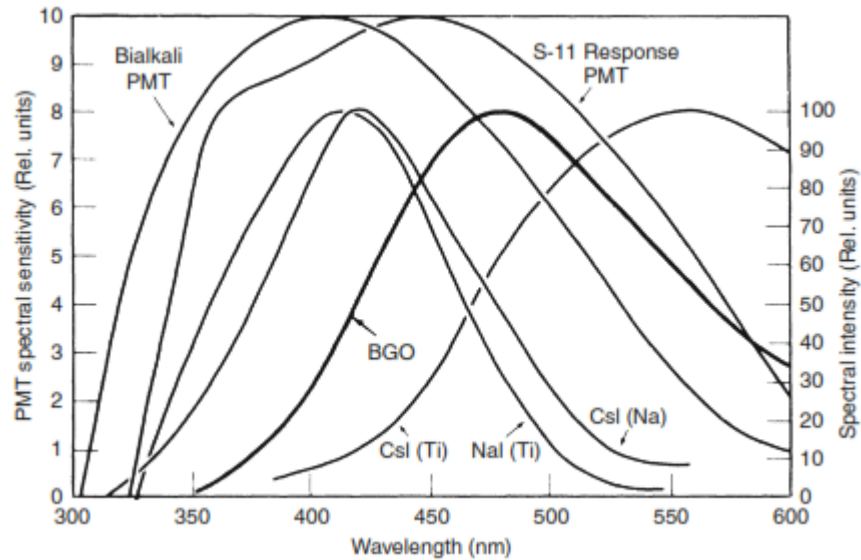


Figure I.2.19: the emission spectra of several common inorganic scintillators. Also shown are the response curves for two widely used photocathodes.

The photoelectrons are focused electrostatically onto the first of series of electron multiplier stages called **dynodes**, amplifying thus the signal. The multiplication factor, the ratio of the numbers of secondary and primary electrons, depends upon the potential difference between each consecutive pair of diodes (about 80-120 V) and the number of stages (about 10-12). The incident electron must be able to create electrons within the dynode with the energy of at least equal to the band gap (2-3 eV for typical dynode coating, beryllium or magnesium oxides or Cs_3Sb). However, the multiplication factor is less than predicted due to dispersion out of the surface and due to low energy. The gain factor of a photomultiplier with N stages would be:

$$\text{gain} = (k \times m)^N \quad (1.2.28)$$

where $(k \times m)$ is the gain factor for a single stage, k is the coefficient that accounts losses and m is the multiplication factor. If we take a typical value for m of 5 and assume k is near to 1 this gives an overall multiplication of about 10^7 for ten stages. The amplified signal is then collected at the anode and passed out to the measurement circuit.

I.2.3.2 A portable NaI(Tl): design set-up

The core of ZaNaI_1.0 system is composed by a NaI(Tl) crystal with a cubic shape of a volume of 1 liter (10.16 cm x 10.16 cm x 10.16 cm) and energy resolution of 7.3% at the 662 keV (^{137}Cs), 5.2% at 1172 and 1332 keV (^{60}Co). The NaI(Tl) detector is mounted in a backpack (**Fig. I.2.20**) and accurately folded with shock resistant materials in order to prevent it from possible damages in the field. The detector is coupled with a photomultiplier (PMT) base with integrated bias supply, preamplifier and digital multichannel

analyzer (MCA). The data outputs are transmitted to a portable notebook via USB communication. Auxiliary equipment's like USB communication GPS antenna (54 channels and 10 m accuracy) and a humidity and temperature sensor (10% accuracy) are used for positioning and weather condition measurement, respectively. The sampling period for GPS, humidity and temperature data is about 1 second while the sampling period of gamma-ray spectra depends on the acquisition modality ranging from a few seconds to a few minutes.

The data logging software are commercial in correspondence to the choice of the equipment's, while the analysis is based on self-programmed software based on Java environment. Position and gamma-ray records are combined to a Geo-referenced data log after off-line post-processing of the data. These data log formats are easily imported to GIS systems and Google Earth^(R) in order to produce radiation maps or logging points.



Figure I.2.20: configuration of ZaNaI_1.0 system set-up in a backpack.

I.2.3.3 Sensitivity calibration and validation

The portable scintillation detector was calibrated based on the selection of sites characterized by a prevalent concentration of one of the natural radionuclides (described in details in **(A. Caciolli, M. Baldoncini et al. 2012)**). All calibration sites (e.g. **Fig. I.2.21**) were selected using geological and Geomorphological considerations and further validated through laboratory measurements (a list of all the sites and the concentration of each isotope are reported in **Table I.2.9**). The in situ measurements can be affected by the specificity of the place, like the soil non-homogeneity, the ground morphology, the non-secular equilibrium in radioactive chains, the vertical distribution of ¹³⁷Cs, the presence of vegetation, moisture, etc.

One advantage of this calibration approach is the possibility to take into account radionuclides other than ^{40}K , ^{232}Th , and ^{238}U (as we mentioned above, in general a minimum of $k+1$ sites are needed, where k is the number of nuclides we want to be sensitive to). In our case a site with a prevalent concentration of ^{137}Cs has been included and used in the calibration (the CC2 site in **Table I.2.9**). As a matter of fact, after the Chernobyl accident, it is mandatory to take into account the ^{137}Cs signal in the spectrum analysis. The vertical migration of ^{137}Cs in soil of different types is rather slow, and the greater fraction of radionuclides is still contained in its upper layer (0 – 10 cm). On average, in the case of mineral soils, up to 90% of ^{137}Cs is found in the 0 – 5 cm layer; in the case of peaty soils, in which the radionuclide migration is faster, only 40-70% of ^{137}Cs is found in that layer (**UNSCEAR 2008**).

Thus, the compromising on choosing s calibration sites should be done according precise prescriptions:

- relatively uniform distribution of radionuclides in secular equilibrium with their products,
- plane area without any steps and large enough to be approximated as an infinite source (maximum 10 m radius (**L. Grasty, L. K. Kosanke et al. 1979a**),
- undisturbed areas: assuring relatively low ^{137}Cs vertical distribution
- uniform and relatively low and homogeneous soil moisture content and vegetable coverage.

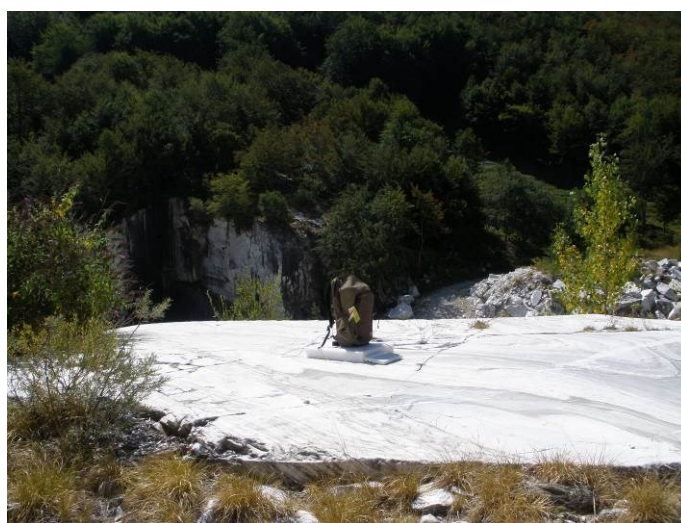


Figure I.2.21: example of a natural calibration site (GC1 see **table 3.3**).

The concentrations reported in **Table I.2.9** are the average of the measurements performed in the laboratory on the collected samples. This way the heterogeneity of each site is properly implemented by the errors which are dominated by the spread in the results of the collected samples in each calibration site. The number of calibration sites is greater than the number of investigating radioelements, as in our approach. This is mandatory in order to avoid artifacts in the sensitive spectra.

Table I.2.9: the average ($\pm 1\sigma$) of the distribution of natural radioisotope concentrations.

ID	Site type	K (%)	eU ($\mu\text{g/g}$)	eTh ($\mu\text{g/g}$)	Cs * (Bq/kg)
CA1	potassium	53.9 ± 0.7	< 1.0	6.0 ± 0.5	na
CC2	cesium	0.06 ± 0.02	0.7 ± 0.3	0.6 ± 0.7	61^{+100}_{-61}
GC1	background	0.07 ± 0.04	0.27 ± 0.08	1.14 ± 0.13	0.87 ± 0.04
GV1	mix	4.9 ± 0.6	7.5 ± 1.1	7 ± 1	31 ± 18
PM2	mix	2.26 ± 0.05	2.27 ± 0.18	10.7 ± 0.8	18 ± 9
RT1	uranium	0.10 ± 0.01	6.8 ± 1.1	1.74 ± 0.16	6 ± 5
SM1	mix	1.54 ± 0.14	1.6 ± 0.3	8.6 ± 0.6	26^{+37}_{-26}
SP2	thorium	2.92 ± 0.08	7.5 ± 0.4	39 ± 2	23 ± 2
ST2	thorium	7.8 ± 0.9	36 ± 5	124 ± 16	8 ± 4

* the activity concentrations of ^{137}Cs expressed in Bq/kg correspond to the samples of soil measured in the laboratory, showing as expected relatively high variability horizontal distribution but not considered for the overall characterization of the site since doesn't consider the vertical distribution.

Full spectrum analysis with non-negative least-square constrain (FSA-NNLS) method

The conventional approach of spectrum analysis recorded in-situ for studying the specific activity concentration is to calibrate broad spectral windows during the analysis for the main natural isotopes (**M. Verdoya, P. Chiozzi et al. 2009**); (**J. A. Desbarats and G. P. Killeen 1990**). Generally, these windows are chosen around the photopeaks of ^{40}K (1460 keV), of ^{214}Bi (1765 keV), and of ^{208}Tl (2614 keV). The concentration of ^{238}U and ^{232}Th are then evaluated detecting the γ -rays produced by ^{214}Bi and ^{208}Tl respectively. The assumption of secular equilibrium of the decay chains is required in order to use this approach. In addition to the above mentioned radionuclides, the three-window method has been extended to the measurement of ^{137}Cs by (A. J Cresswell, D. C. W. Sanderson et al. 2006) and (D. C. W. Sanderson, M. S. Baxter et al. 1989). The Windows analysis method is described in details in (**IAEA 2003**) and will not be discussed here.

The most important limit of this method is that it is blind to any unexpected signal (anthropic isotopes). Another limitation is the low accuracy for short time acquisitions and the physical restriction of poor intrinsic energetic resolution of NaI(Tl) detector. In particular, the Compton continuum around ^{137}Cs photopeak is generally very intense compared to the intensity of 662 keV γ -line. This translates into long acquisition times and costs. Moreover, the intrinsic energetic resolution of sodium iodide detectors prevents to resolve the triplet at the 583 keV (^{208}Tl), 609 keV (^{214}Bi), and 662 keV (^{137}Cs). This issue can be solved only by post processing the data. In any case as we mentioned above the windows analysis method requires a prior knowledge of the presence on site of such radioisotope.

A solution to the above mentioned limitations comes from the utilization of the full spectrum analysis (FSA) method. This method has been developed in different approaches (**M. Maucec, P. H. G. M. Hendriks et al. 2009**); (**P. H. G. M. Hendriks, J. Limburg et al. 2001**); (**B. R. S. Minty 1992**); (**D. J. Crossley and A. B. Reid 1982**); (**H. D. Smith, C. A. Robbins et al. 1983**) and was found to be a successful spectrum analysis tool. Indeed, the FSA encompasses almost the full energy spectrum, reducing the time required in order to reach an acceptable statistical uncertainty of a single measurement.

The spectra acquired in situ are processed by fitting them with a linear combination of the so-called fundamental spectra (of each investigated isotope) derived from the calibration procedure. The events registered in each channel in the measured spectrum, N , is then expressed as:

$$N(i) = \sum_{j=1}^4 C_j S_j(i) + B(i) \quad (1.2.29)$$

where $N(i)$ is the counts in the channel i , C_k are the concentration of the element k , $S_k(i)$ are the associated counts to the fundamental spectrum of the element k in the channel i , $B(i)$ are the counts in the channel i due to the intrinsic background and the index k stays for ^{40}K , ^{232}Th , ^{238}U , and ^{137}Cs .

The activity concentrations are deduced applying the least square algorithm for rectangular matrix and minimizing the reduced χ^2 according to the following equation:

$$\chi^2 = \frac{1}{n-5} \frac{\sum_{i=1}^n \left[N(i) - \sum_{j=1}^4 C_j S_j(i) - B(i) \right]^2}{\sigma_{N(i)}^2} \quad (1.2.30)$$

where the $N(i)$ is considered Poisson distributed (then $\sigma_{N(i)} = \sqrt{N(i)}$) and n is the number of channels in the spectrum used in the analysis.

As described in (**A. Cacioli, M. Baldoncini et al. 2012**), the χ^2 minimization without any further conditions, which is the base of the FSA method, can generate sensitive spectra having energy regions with negative events (**Figure I.2.22**). The presence of these nonphysical results introduces crosstalk effects in the analysis, leading to systematic errors. The NNLS (Non Negative Least Square) constraint; (**C. L. Lawson and R. J. Hanson 1995**); (**P. Désesquelles, T. M. H. Ha et al. 2009**); (**C. Boutsidis and P. Drineas 2009**), which forces the counts on each bin to be zero or positive, has been implemented for the first time in the FSA algorithm in order to avoid this problem (**M. Baldoncini 2010**).

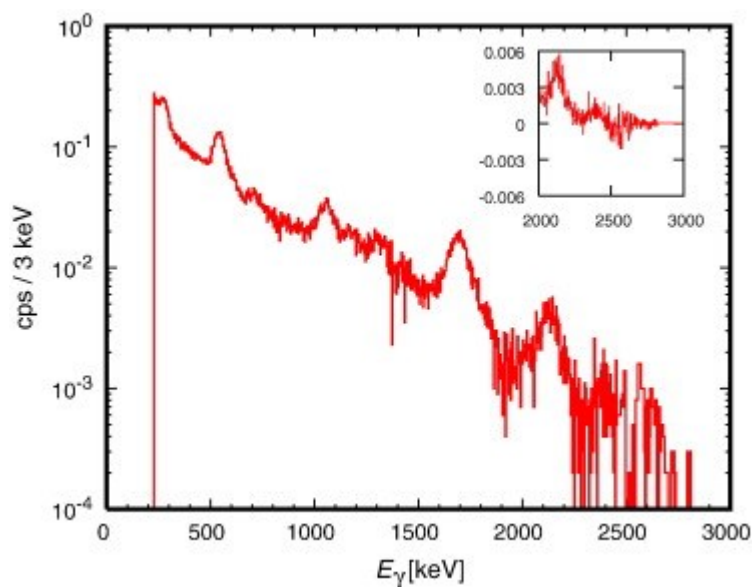


Figure I.2.22: the sensitive spectra of ^{238}U , obtained using the standard FSA method. The region where there are negative counts is emphasized in the box.

The sensitivity spectra calculated by the algorithm implementing the NNLS constrain are shown in **Figure I.2.23**. It can be seen directly a more comprehensive sensitivity spectrum. It has to be noted that the resolution of the sensitive spectrum resolution can be severely affected by gain mismatch and therefore an accurate calibration and check is always needed. Finally, residual correlations between isotopes are still present in the sensitive spectrum shape, due to the presence of all the radionuclides in most of the selected sites.

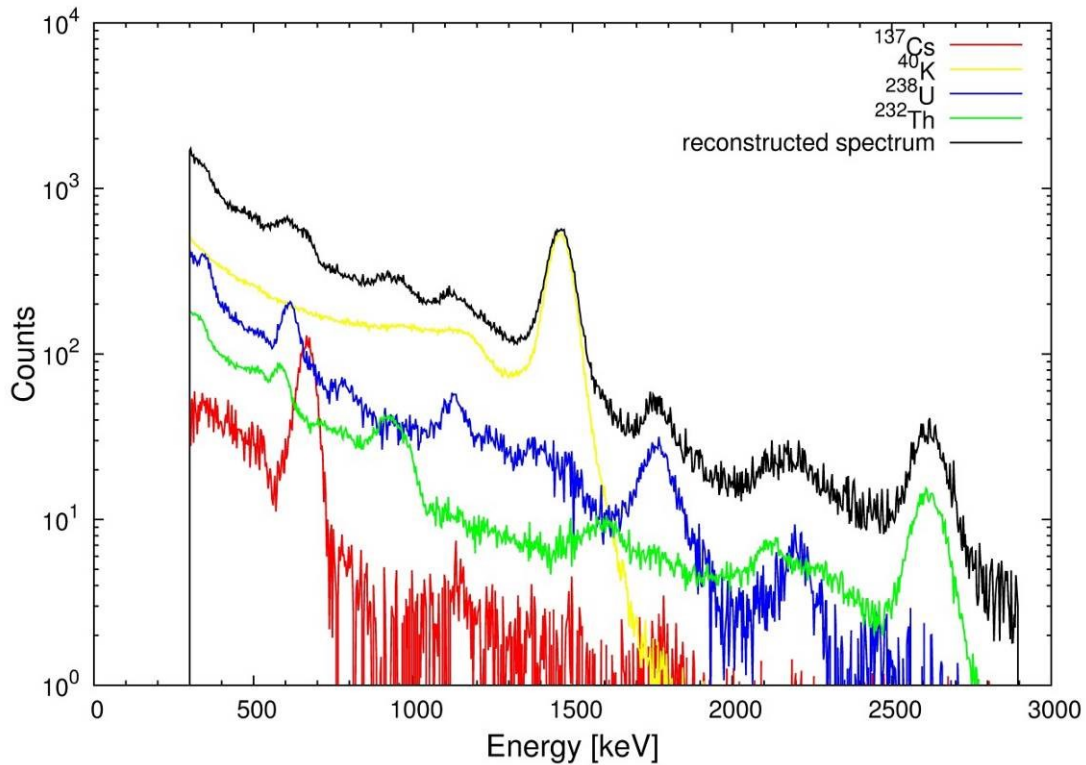


Figure I.2.23: the sensitive spectra obtained through the FSA with NNLS constrain and the reconstructed spectra.

Quality control and validation

The natural radioactivity of over 80 sites, where it has been investigated both by acquiring spectra in situ with the NaI(Tl) and by collecting samples for measurements with the MCA-Rad system. For each site the 10.16 cm×10.16 cm NaI(Tl) detector was used to perform 5 minutes ground measurements in-situ and analyzed using FSA-NNLS method. At each site one sample was collected in the position where the detector was grounded and four samples were collected on the side bisectors of a 2 m side square centered at the grounded position of the detector. The averages of the results obtained from measurements in laboratory for each site was used as a reference to be compared with the outputs of the two methods. The correlation coefficients for ^{40}K , ^{238}U and ^{232}Th are 1.06 ± 0.06 , 0.87 ± 0.12 and 0.94 ± 0.07 with a reduced χ^2 of 1.1 (discussed in details in (A. Cacioli, M. Baldoncini et al. 2012)).

Chapter I.3

Basics of statistical analysis

In this chapter, some fundamental statistical mathematics will be introduced as is necessary to understand the statistical nature of radioactivity counting and data analysis. Furthermore we briefly discuss the statistical aspects of counting parameters, the critical limits and the minimum detectable activity.

Let us assume we have m measurements, $x_1, x_2, x_3, \dots, x_m$, each of which is an estimate of a given parameter. The nature of the parameter and the shape of the distribution of the measurements does not concern us at the moment.. The distribution will have a value, $E(x)$, which we can expect our measurements to have. Thus:

$$\text{Expected value} = E(x) \quad (\text{I.3.1})$$

The difference between any particular value, x_j , and the **expected value** gives an idea of how well x_j estimates the investigated parameter. Taking into account the differences in all the measurements would give an idea of the overall uncertainty affecting the parameter estimate. The resulting factor is called **variance**, so that:

$$\text{var}(x) = \text{Expected value of } [x - E(x)]^2 \approx E\{[x - E(x)]^2\} \quad (\text{I.3.2})$$

A more convenient factor, which indicates the spread of the values about $E(x)$, is the **standard deviation**, σ_x . This is simply the square root of the variance:

$$\sigma_x = \sqrt{\text{var}(x)} \quad (\text{I.3.3})$$

The Standard deviation has a deeper meaning, in the sense that it has an obvious relationship with the expected value and the spread of the distribution. Calculating the ratio between the standard deviation and the distribution expected value gives the **relative standard deviation**, r_x , sometimes referred to as the **coefficient of variation**, which is often expressed as a percentage:

$$r_x = \frac{\sigma_x}{E(x)} 100 \quad (\text{I.3.4})$$

If we want to combine the results of two measurements, say x and y , then it is a straightforward matter to show that the following relationship holds:

$$E(x + y) = E(x) + E(y) \quad (\text{I.3.5})$$

$$E(xy) = E(x) E(y) + \text{cov}(x,y) \quad (\text{I.3.6})$$

The term $\text{cov}(x, y)$ is the **covariance** of x and y and is analogous to the variance:

$$\text{cov}(x, y) = E\{[x - E(x)][y - E(y)]\} \quad (\text{I.3.7})$$

Covariance is a measure of the interrelation, or correlation, between x and y . When there is no correlation, as is likely to be in all the cases discussed here, then $\text{cov}(x,y) = 0$.

$$\text{var}(x+y) = \text{var}(x) + \text{var}(y) \quad (\text{I.3.8})$$

$$\text{var}(x-y) = \text{var}(x) + \text{var}(y) \quad (\text{I.3.9})$$

$$\text{var}(xy) = E(y)^2 \text{var}(x) + E(x)^2 \text{var}(y) + 2E(x)E(y)\text{cov}(x, y) \quad (\text{I.3.10})$$

It can also be shown that, by making the covariance term negative, this relationship also holds for $\text{var}(x/y)$. More usefully, as we expect $\text{cov}(x,y) = 0$, we can rearrange **Eq. I.3.10** using relative standard deviations as follows :

$$r_{xy}^2 = r_{x/y}^2 = r_x^2 + r_y^2 \quad (\text{I.3.11})$$

Finally, if k is a constant then:

$$\text{var}(k) = 0 \text{ and } \text{cov}(k,x) = 0 \quad (\text{I.3.12})$$

$$E(k,x) = k E(x) \text{ and } \text{var}(k, x) = k^2 \text{var}(x) \quad (\text{I.3.13})$$

$$E(k+x) = k + E(x) \text{ and } \text{var}(k + x) = \text{var}(x) \quad (\text{I.3.14})$$

These relationships are valid whatever the distribution of our measured values is. When we make a radioactive count, our ultimate intention is to estimate the sample activity and a degree of confidence in that estimate of activity. Statistically we can achieve the former aim by identifying the measured counts, C , as the expected number of decays, $E(n)$, and relating the confidence limit to the variance $\text{var}(n)$. Both the expected value and the variance depend upon the form of the relevant statistical distribution and we can now move on to the particular case of the distribution of radioactive counts.

I.3.1 Counting statistics

I.3.1.1 Counting distributions and sampling statistics

Counting distributions

The **Poisson distribution** is used in statistics whenever the total number n of possible events is unknown. The distribution is described by the equation:

$$P(n) = \frac{[E(n)]^n}{n!} e^{-E(n)} \quad (\text{I.3.15})$$

$P(n)$ is the probability that a number of counts n will be observed given that the expected number of counts is $E(n)$. This distribution has, as might be expected, some similar properties to the **binomial distribution**. The variance of the distribution approximates that of a binomial distribution for $p \ll 1$:

$$\text{Var}(n) = E(n) \quad (\text{I.3.16})$$

In the Poisson case, the number of nuclei is unknown but large and p is very small. The **Gaussian** or **Normal distribution** is the specific case where the variance is equal to the expected value. This is the distribution one would expect if the differences between the observed and expected counts were solely due to chance. The similarity between the Poisson and Normal distribution is not surprising. When the expected number of counts is greater than 100, further mathematical approximations can be made to **Eq. I.3.15** which yields to the formula for a Gaussian distribution:

$$P(n) = \frac{1}{\sqrt{2\pi E(n)}} \exp\left\{-\frac{[n - E(n)]^2}{2E(n)}\right\} \quad (\text{I.3.17})$$

If we take a large number of measurements of the same parameter, we would find differences in the actual measured value from measurement to measurement. Indeed, each measurement is a sample of the infinite number of possible measurements we could make. These measurements will have a distribution and, of course, an expected value and a variance. If the difference between each measured value and the expected value is due purely to chance, then there is considerable evidence to suggest that the distribution will be Gaussian. In this case, the equation will have a form similar to the special case in **Eq. I.3.17**.

$$P(n) = \frac{1}{\sigma\sqrt{2\pi}} \exp\left\{-\frac{(x - \bar{x})^2}{2\sigma^2}\right\} \quad (\text{I.3.18})$$

that is, the probability of measuring a value x given a particular expected value, \bar{x} , and a standard deviation of σ (**Fig. I.3.1**). Suppose, we have m measurements, $x_1, x_2, x_3, \dots, x_m$. We can define the expected value, or **mean** or **average**, \bar{x} , of these measurements as:

$$\bar{x} = \frac{\sum_{i=1}^m x_i}{m} \quad (\text{I.3.19})$$

We can show that, as m becomes larger, then \bar{x} becomes a more precise estimate of the expected value. The mean \bar{x} is not the true value of the parameter, but a more reliable estimate of the true expected value. The width of the distribution of measured values gives an idea of the overall uncertainty of the measurements. The factor quantifying the width of a distribution is the variance, which is calculated as:

$$\text{var}(x) = \frac{\sum_{i=1}^m (x_i - \bar{x})^2}{m - 1} = s^2 \quad (\text{I.3.20})$$

where s is an estimated standard deviation, not to be confused with the true standard deviation of the distribution, σ , from which we have taken our sample. The denominator of **Eq. I.3.20**, $m - 1$, is referred to as the **number of degrees of freedom**. As already pointed out for the mean, the higher is the number of measurements m , the more precise is the estimate of the standard deviation.

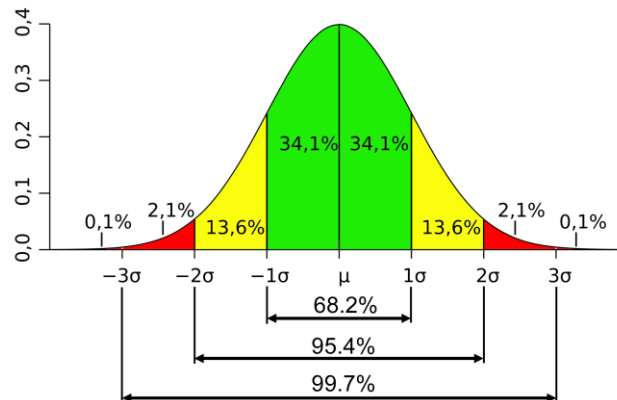


Figure I.3.1: an example of Gaussian distribution plotted as a function of the number of standard deviations from the mean..

It is becoming common to refer to a **standard uncertainty**, which is the uncertainty on a value at the level of one standard deviation.

If we refer again to the Normal distribution of all possible results of a particular measurement, then the uncertainty of the measurement must be related to the width of the distribution. In order to establish the

significance of a measurement, we must quote limits stating the degree of confidence that the true value lies somewhere within the identified ranges – hence the term ‘**confidence limits**’. The number of standard uncertainties we decide to quote to achieve our desired degree of confidence is called the **coverage factor**.

Table I.3.1 lists the degree of confidence associated with various coverage factors.

Table I.3.1: coverage factors and the associated degree of confidence

Coverage factor	Area within the confidence limits (%)
1.000	68.3
1.645	90.0
1.960	95.0
2.000	95.5
2.326	98.0
2.576	99.0
3.000	99.9

The confidence limit quoted in this manner may be referred to as the **expanded uncertainty**. If the distribution is skewed in some way, or if we are aware that the measurement was, for some reason, biased to high (or low) values, then the lower and upper confidence limits would not be identical.

I.3.1.2 Counting decision limits

As a good practice of gamma-ray spectrometry analysis, the **minimum detectable activity** (MDA) is calculated. The minimum detectable activity is a quantity answering the following question – ‘*What is the least amount of activity I can be confident of detecting?*’. This limit concerns the activity rather than the number of counts: it often equates to the activity equivalent of the **detection limit**, LD. The detection limit (LD) answers the following question – ‘*What is the minimum number of counts I can be confident of detecting?*’. Typically LD is that number of counts we expect to detect in 95 % of cases (assuming α is 0.05).

$$L_D = 2.71 + 4.65\sqrt{B} \approx 4.65\sqrt{B} \quad (\text{I.3.21})$$

where the approximation is admitted for the high number of counts. From this, we can calculate the MDA, which then becomes the activity we expect to detect in 95 % of cases.

The minimum detectable activity (MDA) for the blank test is calculated using the L_D , according to the formula (**Currie 1986**):

$$MDA = \frac{L_D}{\varepsilon I_\gamma t} \quad (\text{I.3.22})$$

where ε is the detector efficiency, I_γ is the gamma line intensity and t is the acquisition time.

I.3.1.3 Propagation of uncertainty

In the analysis of gamma ray spectrometry measurements we need to propagate the errors associated with the original data. If the errors are individually small and symmetric about zero, a general result can be obtained for the expected uncertainty associated with a given quantity calculated as a function of any number of independent variables. If x, y, z, \dots are direct measured quantities or related variables for which we know $\sigma_x, \sigma_y, \sigma_z, \dots$, then the standard deviation for any quantity u derived from these quantities can be calculated as:

$$\sigma_u^2 = \left(\frac{\partial u}{\partial x}\right)^2 \sigma_x^2 + \left(\frac{\partial u}{\partial y}\right)^2 \sigma_y^2 + \left(\frac{\partial u}{\partial z}\right)^2 \sigma_z^2 + \dots \quad (\text{I.3.23})$$

The **Eq. I.3.21** is generally known as the **error propagation formula**. Previously we discussed the results of this formula in addition, subtraction, multiplication and division (**Eq. I.3.8; Eq. I.3.9; Eq. I.3.11; Eq. I.3.12; Eq. I.3.13; Eq. I.3.14**). The variables x, y, z, \dots , must be chosen so that they are truly independent in order to avoid the effect of correlation (**Eq. I.3.10**).

I.3.2 Data analysis

I.3.2.1 Data distributions: exploratory data analysis

Counting statistics are well described by special cases of binomial distributions (Poisson or Gaussian distributions). The most widely used statistical methods in data analysis are all based on the assumption that the data show a normal or lognormal distribution. However, the distribution of geochemical data is usually skewed, having outliers and originate from more than one chemical process. In “*Normal and lognormal data distribution in geochemistry: death of a myth. Consequences for the statistical treatment of geochemical and environmental data*” **Reinmann and Filzmoser (2000)** emphasize that, when dealing with regional geochemical or environmental data, normal and/or lognormal distributions are an exception and not the rule. This has serious consequences for the further statistical treatment of geochemical and environmental data.

Log-normal distribution

The **log-normal distribution** is a continuous probability distribution of a random variable whose logarithm is normally distributed. The probability function of the lognormal variable x is defined by the following equation:

$$P(x) = \frac{1}{x\sigma\sqrt{2\pi}} \exp\left\{-\frac{[\ln(x) - \mu]^2}{2\sigma^2}\right\}, \quad x > 0 \quad (\text{I.3.24})$$

where μ and σ in logarithmic scale are called location parameter and scale parameter, respectively. Suppose we have m measurements $x_1, x_2, x_3, \dots, x_m$ and their logarithms $\ln(x_1), \ln(x_2), \ln(x_3), \dots, \ln(x_m)$. We can define the expected value in logarithmic scale, or **mean**, as:

$$\ln(\mu_g) = \frac{\sum_{i=1}^m \ln(x_i)}{m} \quad (\text{I.3.25})$$

which in the original scale corresponds to the **geometric mean**, μ_g :

$$\mu_g = \exp\left\{\frac{\sum_{i=1}^m \ln(x_i)}{m}\right\} \quad (\text{I.3.26})$$

The standard deviation in logarithmic scale is calculated as:

$$\ln(\sigma_g)^2 = \sqrt{\frac{\sum_{i=1}^m [\ln(x_i) - \ln(\mu_g)]^2}{m-1}} \quad (\text{I.3.27})$$

which in the original scale corresponds to the **geometric standard deviation**, σ_g :

$$\sigma_g = \exp\left\{\sqrt{\frac{\sum_{i=1}^m \ln(x_i/\mu_g)^2}{m-1}}\right\} \quad (\text{I.3.28})$$

Exploratory data analysis

The first step in our data analysis is to carefully study the distribution of the measured abundances of ^{40}K , ^{238}U , ^{232}Th in 712 samples. In order to have a first insight into the data structure, **figure I.3.2a, I.3.2b and I.3.2c** have shown the **frequency histogram** combined with the boxplot representation of abundances of ^{40}K , ^{238}U and ^{232}Th which gives a more direct indication of the presence of outliers (i.e. measurements

exceeding the median + 1.5 Inter Quartile Range (IQR)). It can be seen that the ^{40}K distribution shows negative skewness, while ^{238}U and ^{232}Th distributions show positive skewness and all distributions are strongly affected by outliers.

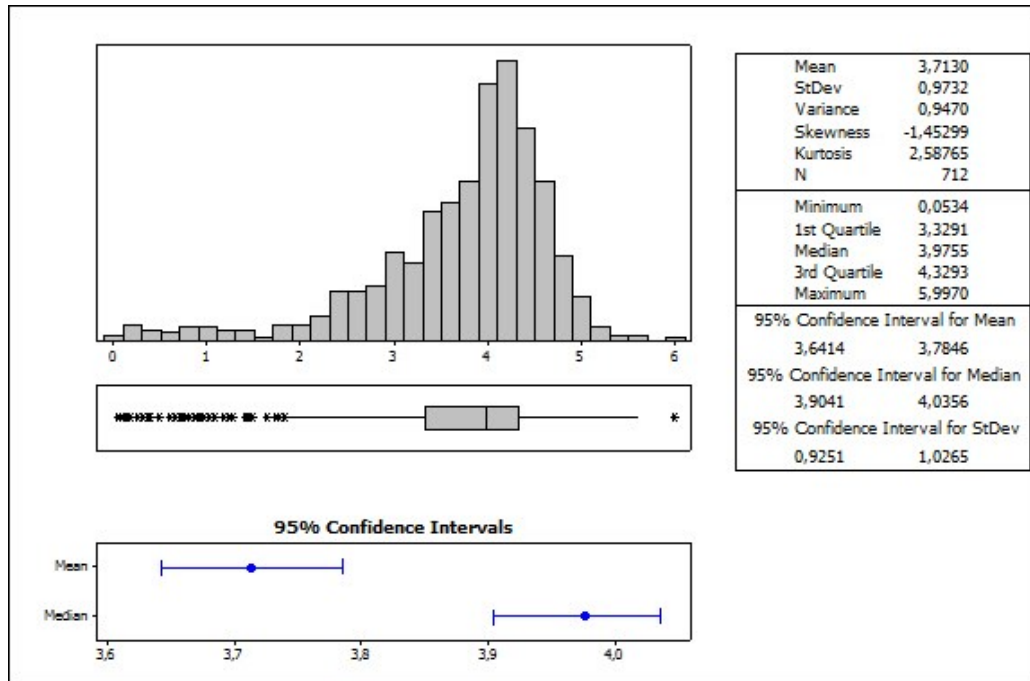


Figure I.3.2: (a) distribution of abundances of K (%) for 712 measurements.

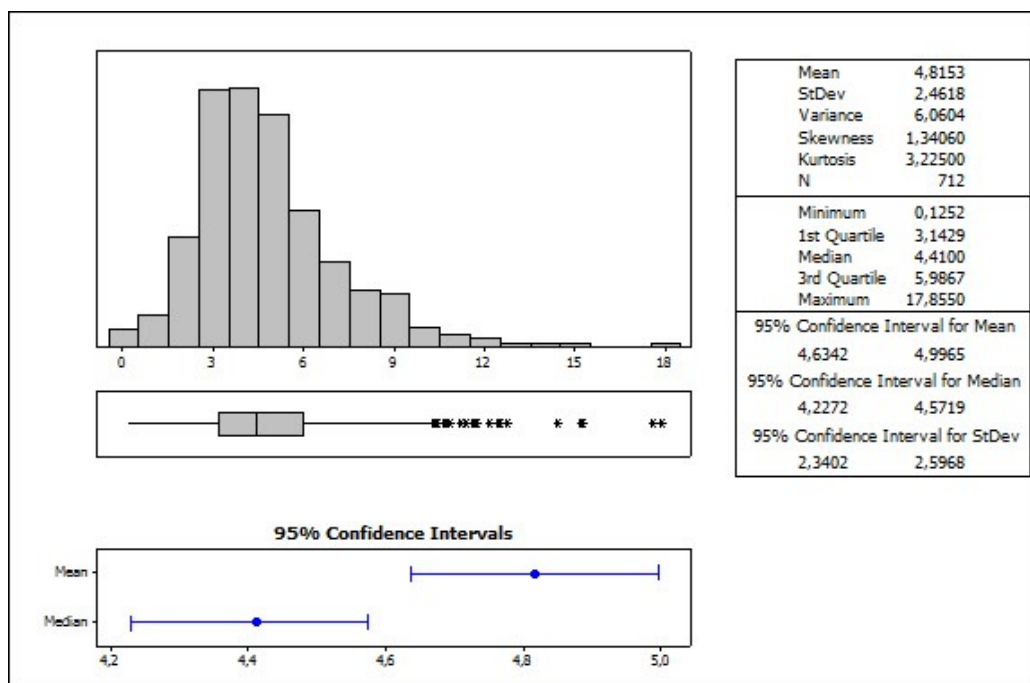


Figure I.3.2: (b) distribution of abundances of U ($\mu\text{g/g}$) for 712 measurements.

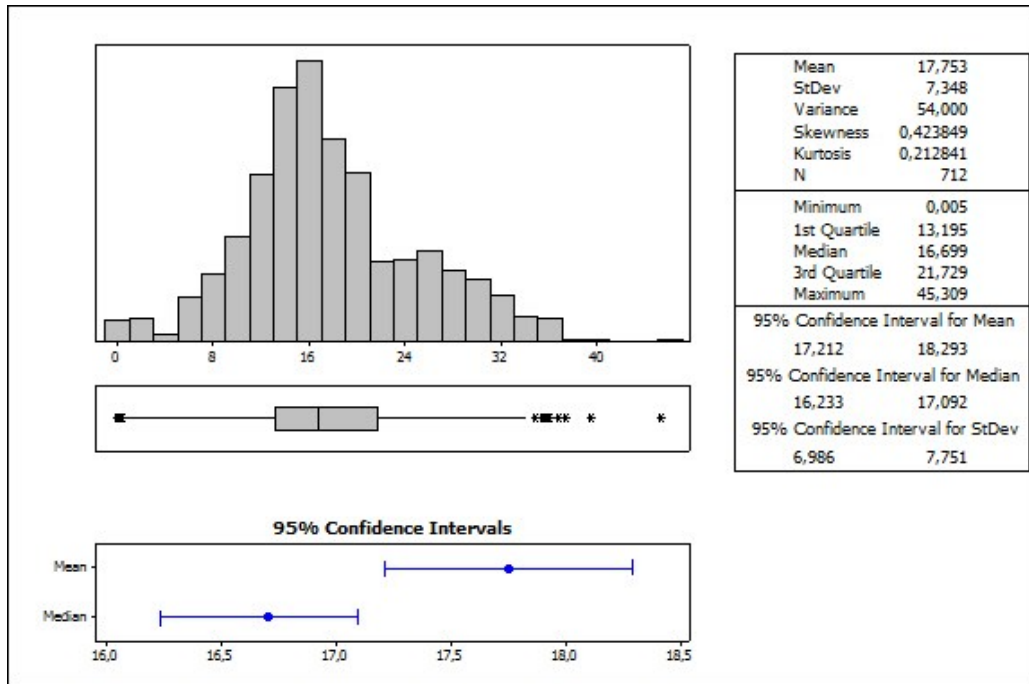


Figure I.3.2: (c) distribution of abundances of Th ($\mu\text{g/g}$) for 712 measurements.

Furthermore, we can graphically determine either a distribution is normal or lognormal according to a univariate statistics based on **percent-probability P-P plot**. In **Figure I.3.3** the P-P plots for ^{40}K , ^{238}U , ^{232}Th in 712 samples are shown. The data do not show either normal or lognormal distributions, therefore an a priori assumption about the distribution shape will lead to biased or faulty results.

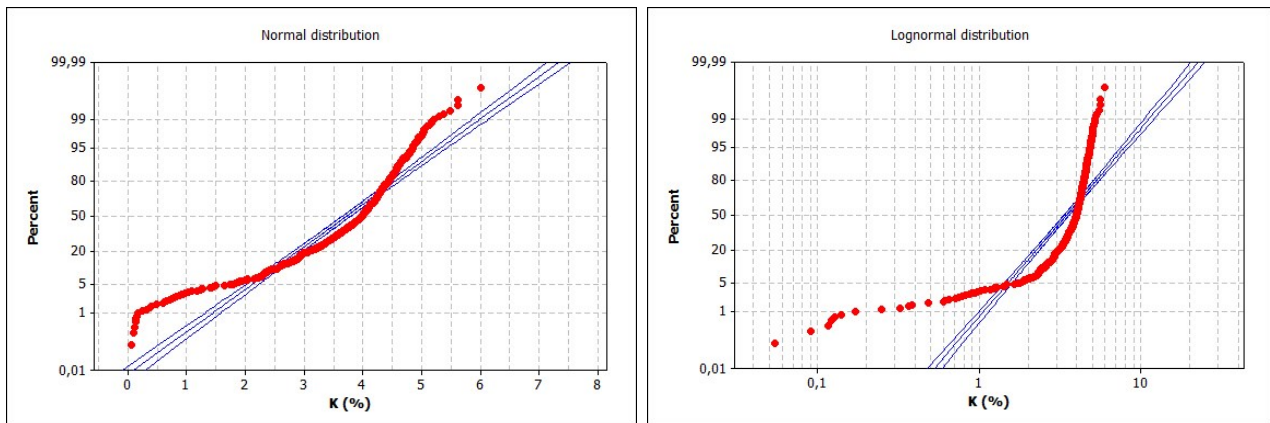


Figure I.3.3: (a) probability plot for K (%) (in red) compared either with theoretical normal and lognormal distributions (in blue).

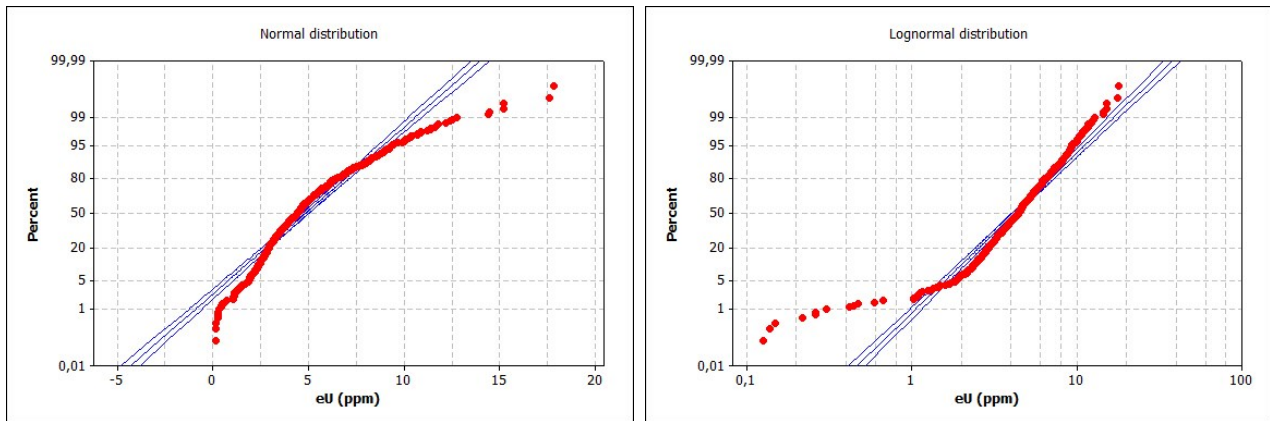


Figure I.3.3: (b) probability plot for U ($\mu\text{g/g}$) (in red) compared either with theoretical normal and lognormal distributions (in blue).

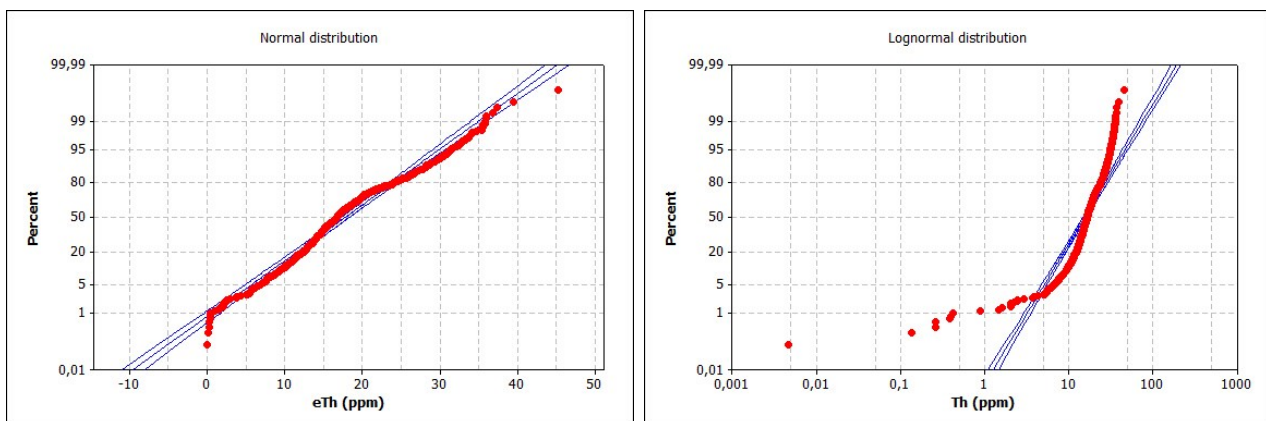


Figure I.3.3: (c) probability plot for Th ($\mu\text{g/g}$) (in red) compared either with theoretical normal and lognormal distributions (in blue).

Figure I.3.4 shows as a title of example the P-P plots for the concentration of ^{40}K , ^{238}U , ^{232}Th in monzogranites (336 samples) and granodiorites (84 samples). For monzogranites and granodiorites the distribution of ^{40}K is well described by normal distributions, for ^{238}U is well described by lognormal distributions, while for ^{232}Th the distribution is well described by a lognormal distribution in monzogranites and normal distribution in granodiorites.

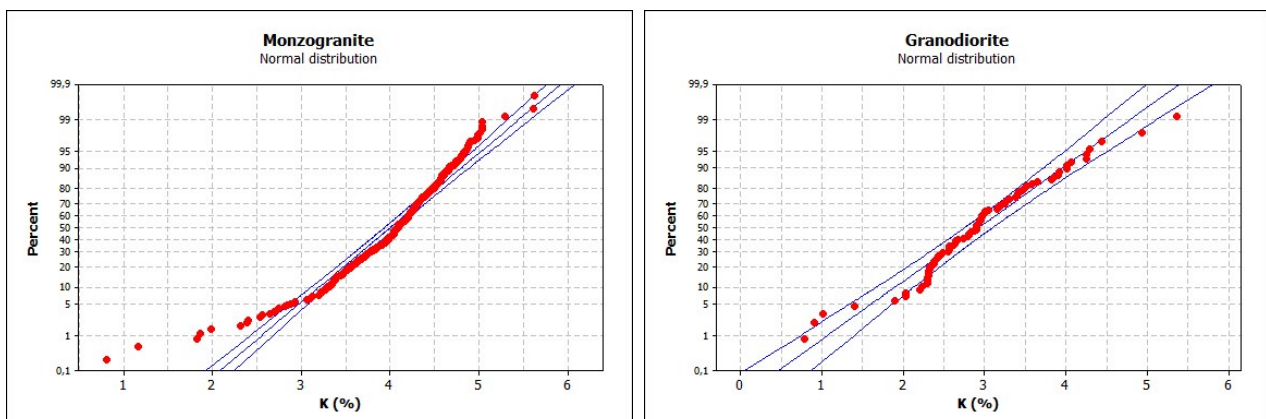


Figure I.3.4: (a) probability plot for ^{40}K (%) compared with normal distribution either in monzogranite and granodiorite rocks.

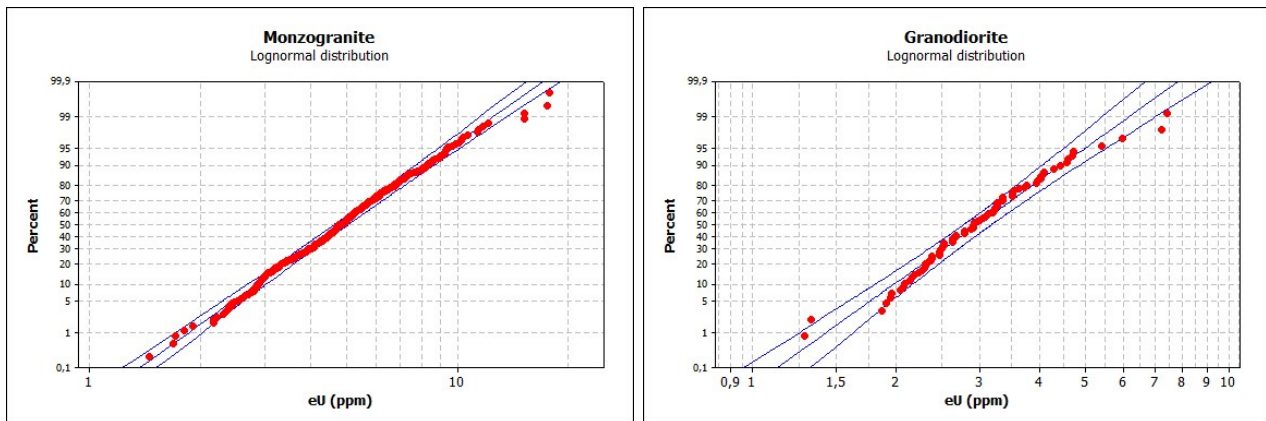


Figure I.3.4: (b) probability plot for ^{238}U ($\mu\text{g/g}$) compared with lognormal distribution either in monzogranite and granodiorite rocks.

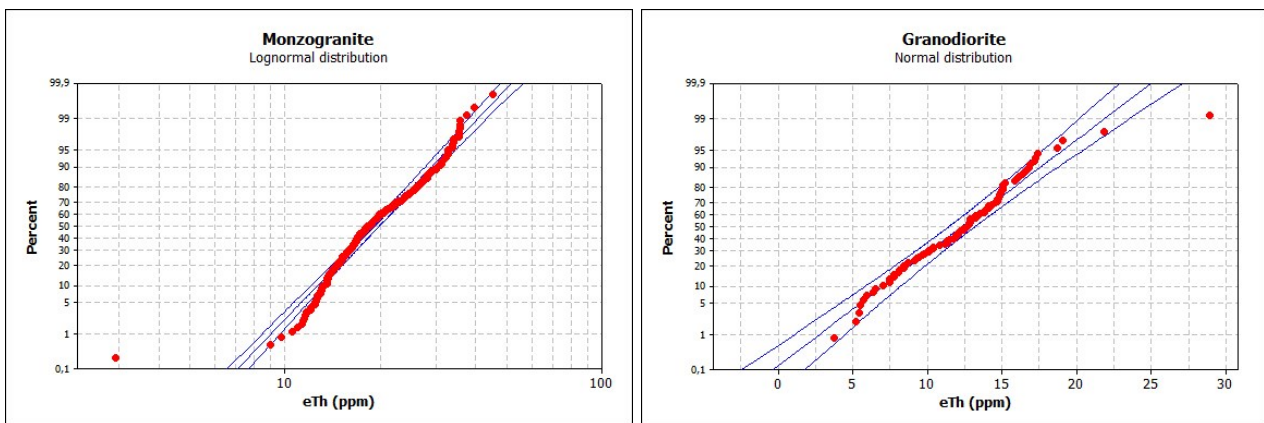


Figure I.3.4: (c) probability plot for ^{232}Th ($\mu\text{g/g}$) compared with lognormal distribution in monzogranite and normal distribution in granodiorite.

However, a more formal statistical test is applied to all data, the Kolmogorov-Smirinoff test, which provides a p-value that can be used as a figure of merit in order to decide whether or not the null hypothesis can be rejected. Usually, a p-value $p < 0.05$ is used to reject the null hypothesis of normal distributions. **Table I.3.2** summarizes the p-values calculated using Kolmogorov-Smirinoff test for the distribution of ^{40}K , ^{238}U and ^{232}Th abundances in different rock types investigated with a number of samples $N \geq 10$. For lithologies investigated with a statistic of $5 \leq N < 9$ we assumed a Gaussian distribution for each radionuclide abundance and we calculated the mean and standard deviation of each distribution; for $1 < N < 5$ we took the mean and maximum semidispersion.

Table I.3.2: The p-value calculated using Kolmogorov-Smirinoff test for raw data (Orig.) and logarithmic transformed data (Log.) for the rock types investigated with a number of samples of $N \geq 10$.

Rock type	No.	⁴⁰ K (%)		²³⁸ U (µg/g)		²³² Th (µg/g)	
		Orig.	Log.	Orig.	Log.	Orig.	Log.
Monzogranite	446	0.001	0	0	0.890	0	0.244
Granodiorite	87	0.165	0.035	0.056	0.711	0.837	0.175
Granite	21	0.779	0.083	0.073	0.456	0.847	0.220
Leucogranite	16	0.356	0.122	0.253	0.423	0.854	0.487
Sienogranite	11	0.955	0.954	0.824	0.863	0.411	0.255
Leuco-monzogranite	16	0.577	0.443	0.950	0.766	0.982	0.674
Amphibolite	12	0.971	0.909	0.649	0.371	0.327	0.750
Migmatite	25	0.978	0.869	0.332	0.768	0.676	0.620
Eclogite	11	0.676	0.916	0.328	0.926	0.183	0.331
Orthogneiss	13	0.848	0.867	0.348	0.870	0.480	0.965

According to the p-values determined applying the Kolmogorov-Smirnov test to our data sets, it is possible to observe that K and Th abundances generally follow a normal distribution. A common exception to this concerns eclogite and orthogneiss where the distribution was found to be lognormal. On the other hand U is generally studied using lognormal distribution.

I.3.2.2 Uncertainty propagation using Monte Carlo method

The uncertainty propagation formula (Eq. I.3.23) discussed above, can be applied when the errors are individually small and symmetric about zero. when dealing with lognormal distributions we have to consider that the uncertainties are asymmetrical, which implies that the uncertainty propagation formula cannot be applied. Therefore, the combination of uncertainties was estimated by Monte-Carlo simulation (JCGM, 2008). In particular, in order to obtain the standard deviation of the mean, matrices were generated in MATLAB® R2010b with 10^5 pseudo-random values. The individual measurement parameters have been used for each radionuclide, corresponding to mean and standard deviation for normal distributions and to location parameter and scale parameter for lognormal distributions. Fig. I.3.5a shows as a title of example the distribution of 10^5 pseudo-random values generated using the location parameter, $\mu = 1.575$, and scale parameter, $\sigma = 0.409$, obtained for ²³⁸U distribution in monzogranites transformed in logarithmic scale, which can be compared with the distribution of original data (Fig. I.3.5b).

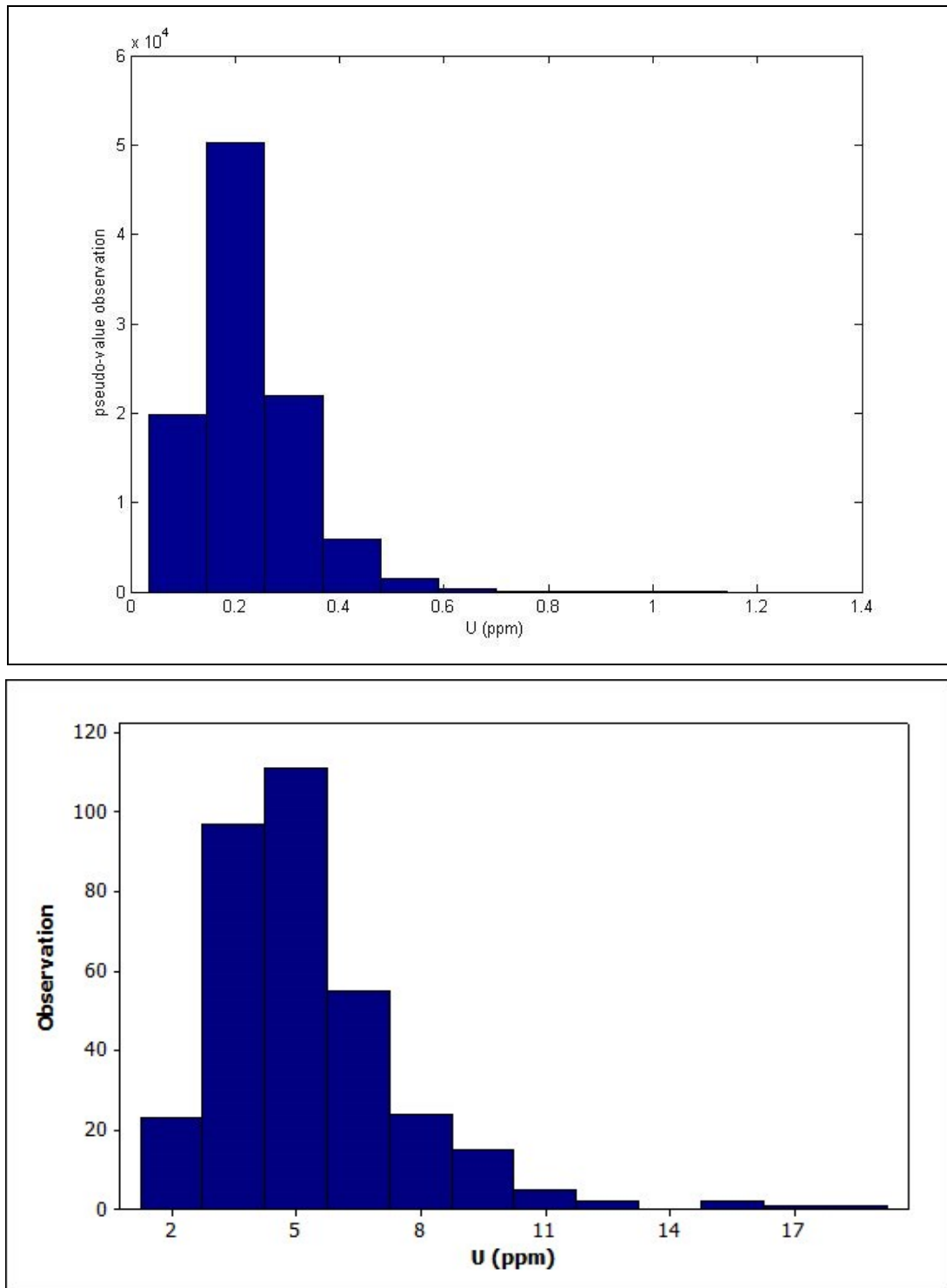


Figure I.3.5: (a) 10^5 pseudo-random values of ^{238}U in monzogranites generated using MATLAB® R2010b, compared with (b) the distribution of original data.

A simple code written in MATLAB® R2010b, then permits to propagate the uncertainties of variables obtained from the combination of K, U and Th, for example the radiogenic heat generation (**Eq. II.2.5**) or the ratios of Th/U, Th/K and K/U.

PART II

New insights on the geological structure of N-E Sardinia (Corsica-Sardinia Variscan Batholith) revealed by gamma-ray spectrometry survey

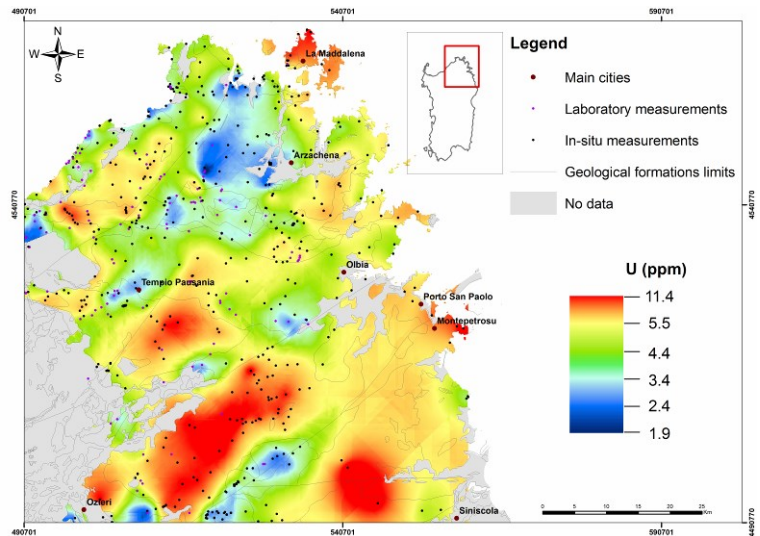


Table of content:

Chapter II.1: Introduction and objectives

- II.1.1 Variscan orogen of central Europe and the geological evolution of Sardinia
- II.1.2 Current studies on natural radioactivity in European Variscan
- II.1.3 Objectives of the study

Chapter II.2: Study of the distribution of natural radionuclides in Sardinian batholith

- II.2.1 Geological setting of study area
- II.2.2 Gamma-ray spectrometry survey measurements
- II.2.3 The distribution of abundances of ^{40}K , U and Th and ternary map
- II.2.4 Preliminary study of radiogenic heat generation from upper crust

Chapter II.3: Discussions and conclusions

Chapter II.1

Introduction and objectives

II.1.1 Variscan orogen of central Europe and the geological evolution of Sardinia

The Variscan belt in western Europe, was formed between 500 and 250 Ma as the result from the collision of two main continents, the Gondwana (African sector) to the south and the Baltica-Laurentia to the north (**P. Matte 2001**) (**Figure II.1.1**). The European Variscan belt is part of a large *Paleozoic* belt extending on both sides of the Atlantic, from the Ouachitas in the US and the Mauritanides in West Africa, to the Bohemian Massif in Czech Republic and Poland. The orogen is divided into three main zones. To the north the Rhenohercynian basin, which contains mainly low grade metamorphic rocks and basic igneous rocks, typical of extensional tectonic basins, can be traced from southern Ireland to Slovakia. The Saxothuringian zone in the south, which includes magmatic arc rocks, overthrust by nappes of deeper-water facies and crystalline. Further SE, is the Moldanubian zone complex, where SE-directed high- to medium-grade metamorphic sequences are found; this zone probably continues in the Variscan basement of the Alps. Following a continent–continent collision abundant late- to post-orogenic uraniferous leucogranites were emplaced into the upper continental crust from Spain and Portugal in the west to the Czech republic and Slovakia in the east.

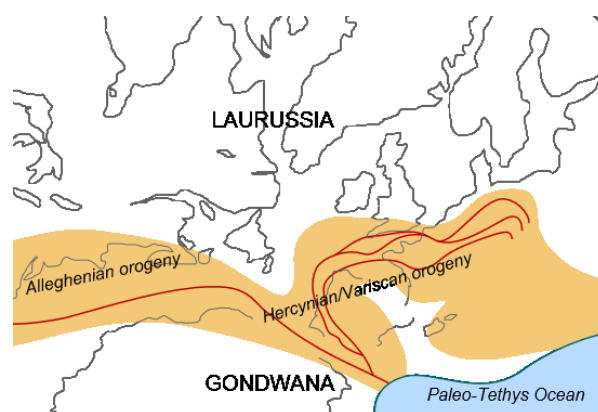


Figure II.1.1: Location of the Hercynian-Alleghenian mountain belts in the middle of the *Carboniferous* period after (**P. Matte 2001**). Present day coastlines are indicated in gray lines for reference.

The Variscan Europe belt outcrop in various massifs, where the geotectonic nomenclature and the zonation in these classical areas of Variscan evolution mirror the main Variscan tectonic structures. During the Variscan orogeny or Hercynian cycle, the central Europe was intruded by various kinds of granitoids before the Lower Permian, which changed during the evolution of Variscan orogeny. The schematic map of the major Variscan basements is shown in **Figure II.1.2**: Armorican Massif (France), French Massif Central

(France), Iberian Massif (Spain), Pyrenees, Iberian Massif (Portugal), Ossa Morena Zone (Portugal), Corsican-Sardinian batholith (Italy), Alps batholiths (Italy, Switzerland, Austria), Bohemian Massif (Germany, Czech, Austria, Poland), Vosges Massif (France) and Schwarzwald (Black forest) Massif (Germany) **Saxo-thuringian Zone**, Harz Massif (Germany), Ardennes-Rhenohercynian Massif (Germany), Lizard, Wales, South Ireland (South East England). Different genetic groups of granitoids can be distinguished (F. Finger, M. P. Roberts et al. 1997):

- *Late Devonian to early Carboniferous "Cordilleran" I-type granitoids* (ca. 370-340 Ma): these early Variscan granitoids are mainly tonalites and granodiorites. They often have hornblende and occur in association with diorites and gabbros. They form plutonic massifs in the Saxo-thuringian unit, in Central Bohemia and the intra-Alpine Variscides.
- *Early Carboniferous, deformed S-type granite/migmatite associations* (ca. 340 Ma): these occur in the footwall of a thick thrust in Southern Bohemia (Gfohl nappe) and seem to represent a phase of water-present, syn-collisional crustal melting related to nappe stacking.
- *Late Visean and early Namurian S-type and high-K, I-type granitoids* (ca. 340-310 Ma): these granitoids are mainly granitic in composition and particularly abundant along the central axis of the orogen (Moldanubian unit). This zone experienced a high heat flow at this time, probably as a consequence of post-collisional extension and magmatic underplating.
- *Post-collisional, epizonal I-type granodiorites and tonalites* (ca. 310-290 Ma): these plutons can be found throughout the Central European Variscides (Alpine-Carpathian chain). However, most of them occur in the Alps (near the southern flank of the orogen).
- *Late Carboniferous to Permian leucogranites* (ca. 300-250 Ma): Many of these rocks are similar to sub-alkaline A-type granites have been recognized in the Alps and Carpathians. Potential sources for this final stage of plutonism could have been melt-depleted lower crust or lithospheric mantle.

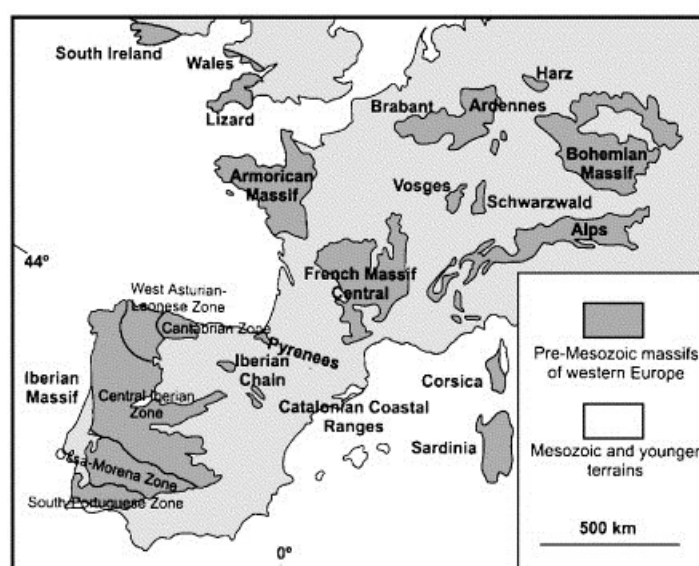


Figure II.1.2: simplified sketch map of European Variscan Massifs (after **Pin et al., 2002**): **Armorican Massif**, **French Massif Central**, **Iberian Massif**, Corsican-Sardinian batholith, Alps batholiths, **Bohemian Massif**, Vosges Massif, Schwarzwald (Black forest) Massif (**Saxo-thuringian Zone**), Harz Massif, **Ardennes-Rhenohercynian Massif**, Pyrenees and Lizard.

The last orogenic phases were dominated by strike-slip motion that was partially overlapped by an incoming high temperature (HT) to ultra-high temperature (UHT) metamorphism during overall post collisional extension (**G. Menard and P. Molnar 1988**); (**P. Conti, L. Carmignani et al. 1999**). The strike-slip phase occurred between ~325 and 310 Ma and is well documented in the Armorican Massif (**R. Tartese, G. Ruffet et al. 2011**), Maures-Esterel (**M. Corsini and Y. Rolland 2009**), Briançonnais basement (**M. Maino, G. Dallagiovanna et al. 2012**) and Corsica-Sardinia (**R. Carosi and Oggiano 2002**) (**R. Carosi and R. Palmeri 2002**); (**G. Di. Vincenzo, R. Carosi et al. 2004**). The South-European Variscan Realm (**P. Rossi, G. Oggiano et al. 2009**) is commonly considered as a reference example for ‘hot’ collisional chains, in which crustal anatexis, granite emplacement and high-T metamorphism all contributed to determine the tectonic style of the mountain belt (**A. G ebel, F. Roger et al. 2009**).

The present position of Sardinia and Corsica islands is due to a 30° anticlockwise rotation of the Corsica-Sardinia block away from Europe caused by the opening of the Western Mediterranean Ligurian - Provençal basin. The age of the rifting phase is dated to *Oligocene* (from 30 to 24 Ma) followed by a short *Early Miocene* oceanic accretion (ages ranging from 23 to 15 Ma). The largest part of Sardinia and Western Corsica islands are made up of a *Permo-Carboniferous* batholiths emplaced between 340 and 280 Ma into a Variscan basement which crops out more extensively in Sardinia than in Corsica (**R. Carosi, C. Frassi et al. 2006**).

The Variscan orogenic of the Corsica-Sardinia belt was formed during *Late Carboniferous* and *Permian* period was followed by magmatic intrusive and effusive activity and sedimentation into intercontinental and alluvial (**L. Cortesogno, G. Cassinis et al. 1998**). The main lithology complexes consist of:

- a) mainly *Palaeozoic* basement, poly-deformed and metamorphosed during the Variscan (Hercynian) Orogeny, then widely intruded by calc-alkaline granitoids;
- b) *Mesozoic* carbonate sequence, representative of sedimentary sequences which bounded the Southern Europe passive margin;
- c) *Cenozoic* volcano-sedimentary cover, consisting of marine shallow water carbonates, silicoclastic sediments, continental conglomerates as well as volcanic rocks represented by a calc-alkaline magmatism and by within plate basalts (**G. Oggiano and A. D. Pisa 2001**).

The geology in Sardinia is dominated by sedimentary, igneous and metamorphic *Palaeozoic* lithotypes, connected to the evolution of the Hercynian European Zone (**B. De. Vivo, M. Boni et al. 1997**). The main geological units of Sardinia are divided into: quaternary deposits, post-Hercynian covers (*Carboniferous Superior-Pliocene*), Hercynian basement (Intrusive complex) (*Carboniferous Superior-Permian*) and

Metamorphic Complex (*Precambrian-Lower Carboniferous*), and faults *Tertiary* (L. Carmignani, G. Oggiano et al. 2001) (**Figure II.1.3**).

The *Quaternary* deposit is largely represented by deposits with continental facies, while the subordinate marine deposits give rise to discontinuous outcrops of low thickness, and are attributed to the Tyrrhenian, being the only ones that provide a secure dating based on the content paleontology. The *Quaternary* deposits are divided into:

- Current deposits: gravel, sand, silt and sandy-clay of alluvial deposits.
- Continental and marine deposits: alluvial, colluvial, eolian, travertine, debris, beaches and beach ridges.
- Continental deposits, alluvial deposits, travertine and alluvial deposits of fossil fuels.
- Marine deposits, conglomerates, sandstones and beach bio-calcarenes (Panchina Auct.) (**L. Carmignani, P. Conti et al. 2001**).

The Variscan basement of northern Sardinia is divided in three main tectono-metamorphic complexes: the NW (Nurra and Asinara Island transect); the centre (SW Gallura and Anglona) and the NE (Baronie regions) of the island. (**R. Carosi, C. Frassi et al. 2005**).

- Nurra is characterized by a magmatic complex and a volcano-sedimentary *Ordovician* cover of internal volcanic products. The Variscan basement in the Nurra Peninsula is constituted by acid intermediate and basic metamorphic volcanic rocks. In different locations of the Gennargentu and Nurra were distinguished: a) acid metavolcanite (porphyries) and the products of their metamorphic reworking (metarose and quartzite to microcline). b) basic metavolcanites, intermediate and related meta-derivate of sedimentary reworking. The intermediate metavolcanites are mainly of andesites composition (**A. Di. Pisa, M. Attiglio et al. 1992**).

- Asinara Island is characterized by metamorphic evolution of metamorphic *Complex Hercynian* low and medium grade and *migmatitic Complex*, and is composed of *Late Hercynian* monzogranites, mica schists and paragneiss of intermediate P-T, mica schists and peragneiss of intermediate P-T with overprint of high T to low P, orthogneiss of Cala Reale, amphibolites with morb affinity, orthogenesis of Cala d'Oliva, migmatites and orthogenesis, amphibolites of the *Complex of Punta Scorno*.

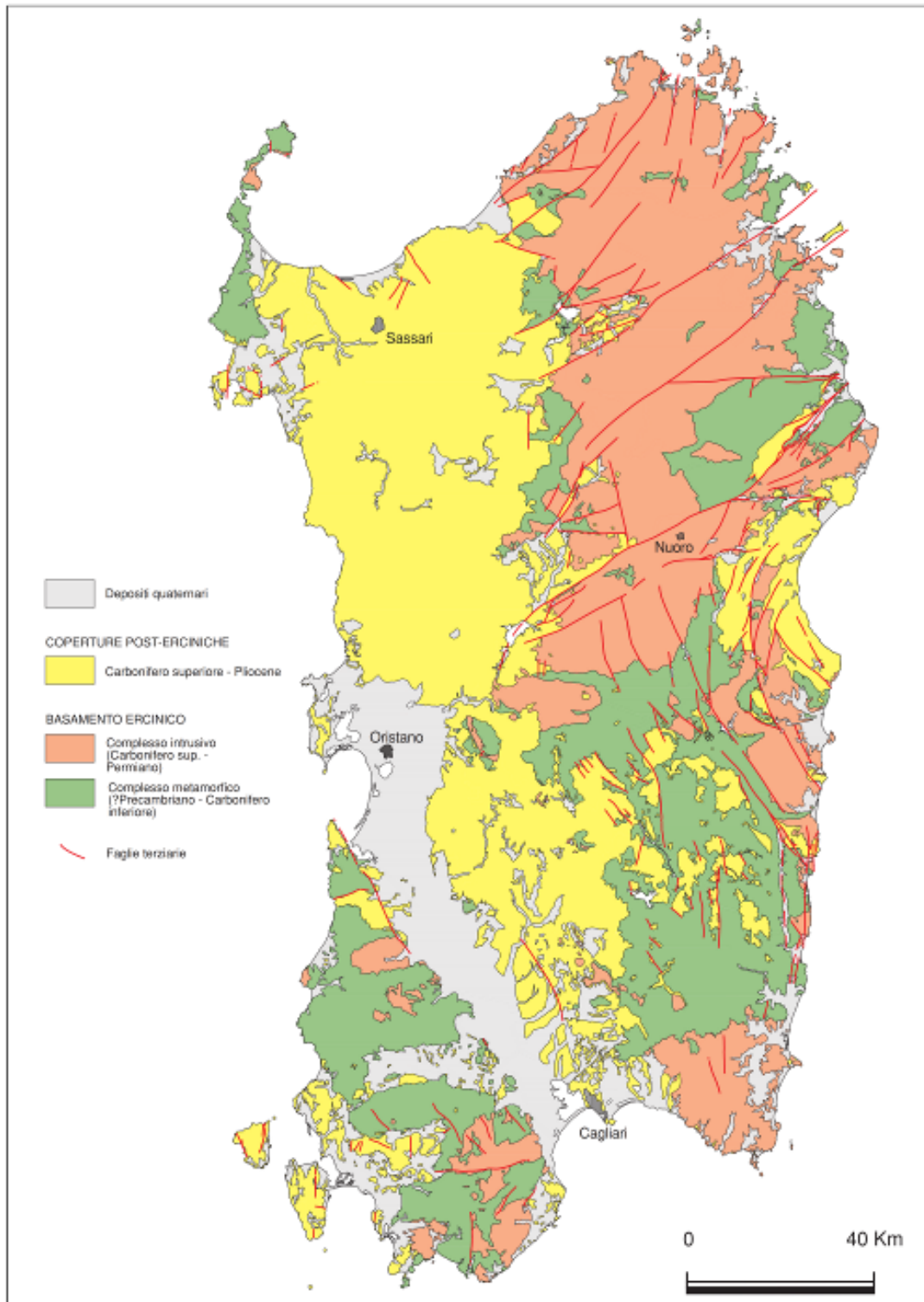


Figure II.1.3: the main geological units of Sardinia (after (L. Carmignani, G. Oggiano et al. 2001).

- Gallura (Sardinian batholith) is characterized by a Plutonic Complex of *Carboniferous-Permian*, and is composed of granitoids with different composition and ages that outcrops at the area of Porto Pollo-Barrabisa (Gallura), granitoids to cordierites, granodioritic and leucogranitic medium-grained intrusions, equigranulites, gabbro and gabbro-tonalitic masses, equigranular monzogranites, sodium syenites,

equigranular leucogranites and garnet leucogranites of an age of 300 ± 7 Ma (**P. Macera, S. Conticelli et al. 1989**).

- Baronia region is characterized by medium-grade metamorphic rocks in a greater continuity of outcrop; grade metamorphism increase rapidly towards the NE, and are composed of *Migmatic Complex* of the Sil + Ms + Sil + K-feldspar and eclogites sector, amphibolites with dikes of paragenesis in the granulite facies, mica-schist and paragneiss in amphibolites facies overprint and high temperature, and granitic orthogenesis granodioritic.

The *Post-Hercynian* Sardinia is covered by sediments and volcanic rocks of the *Upper Carboniferous-Permian*, *Mesozoic* and *Tertiary* age. The most representative formations are of *Miocene* age, and they emerge continuously from the Gulf of Cagliari and Sassari, comprising more than half of the outcrops of the covers post-Hercynian. They are composed of rhyolites and rhyodacite and intrusive volcanic porphyries rocks,. Mainly rhyolitic composition is of the complexes of ignimbritic-riodacitic associated with levels of tuffs. After the Hercynian evolution, the Sardinia, even out of the alpine orogenic, was found at the edge of two orogenic belts: the Pyrenees and the Apennines. Then it was marked, first at west and then at the east, by two oceanic evolution rifting: the opening of the Burdigalian Balearic Basin and the opening of the Tyrrhenian Sea in the south-central *Upper Miocene-Pliocene* (**L. Carmignani, P. Conti et al. 2001**).

II.1.2 Current studies on natural radioactivity in European Variscan

It is known that Variscan granitoids may contain a high concentration of natural radioelements mainly uranium, thorium and potassium. In particular, the distribution of uranium over Europe showed that the highest concentrations (> 4 mg/kg up to 53 mg/kg) occur over the Variscan orogen (**J. A. Plant, S. Reeder et al. 2003**), especially in areas into which late post-orogenic high radiogenic heat production (HHP) granites were emplaced. In particular, exposed crystalline basement rocks of the Variscides such as those of the North West Iberian Peninsula, Brittany and the Massif Central in France, the Black Forest of Germany, the Bohemian Massif of Germany and the Czech Republic and the Variscan rocks of Corsica and Sardinia. The occurrence of granite-related U deposits associated with Variscan granites is previously studied by (**M. Cuney 1987**) and by (**V. Ziegler and J. Dardel 1984**) in European Variscan.

The rare earth element (REE) distribution over Europe (**L. Fedele, J. A. Plant et al. 2008**) showed high values in Variscan crystalline massifs including the Iberian Massif and the Massif Central and Variscan blocks in eastern Europe showing medium to large negative Eu anomalies in the resulting Post-Archean Australian Shales (PAAS) or chondritic normalized REE patterns. The high values are all thought to reflect the presence of evolved igneous rocks. The distribution of high REE values is very similar to that of high uranium values described by (**J. A. Plant, S. Reeder et al. 2003**), which were also attributed to the presence of highly evolved leucogranites in the crust.

In (**B. Tourlière, J. Perrin et al. 2003**) the Armorican Massif of Brittany (France) was investigated by using of airborne gamma-ray spectrometry for kaolin exploration based on the potassium contrast between favourable host-rock such as a leucogranite and kaolin occurrence.

The knowledge of the radiogenic element (U, Th and K) distribution in granitic bodies is necessary to calculate the total heat production distribution within the upper crust. However, it is not sufficient, deep seismic reflection profiles of Hercynian crust are necessary to grossly divide the granodiorite, amphibolite facies and granulitic facies gneisses, since they are depleted in radiogenic elements in decreasing order. Granitic intrusions locally disturb the surface heat flow owing to their higher internal heat production and thermal conductivity (**J. L. Vigneresse and M. Cuney 1991**). They observed that the distribution of the radioelements in granites shows variations which reflect complex fractionation processes which vary from one granite to another and therefore cannot provide a viable model for bulk distribution of radioelements: in Granite Mt. Pluton (Wyoming) a 405 m deep borehole (from biotitic rich to leucocratic granite) showed a large variation in upper facies and lower facies of $7.0 \pm 0.7 \mu\text{W}/\text{m}^3$ and $3.0 \pm 0.9 \mu\text{W}/\text{m}^3$, respectively; in Precambrian granite (Illinois, USA) beneath a metasedimentary cover (660 m) a 1540 m deep borehole (from fine-grained facies with muscovite and biotite to a coarse-grained facies) showed a decrease from $23.0 \pm 3.0 \mu\text{W}/\text{m}^3$ to $20.4 \pm 0.9 \mu\text{W}/\text{m}^3$; in Eye-Dashwa Lakes Pluton (Ontario, Canada) a 1090 m deep borehole (from medium- to coarse-grained hornblende-biotite granite intrudes Archean tonalitic gneisses) showed values varying from $1.12 \pm 0.15 \mu\text{W}/\text{m}^3$ to $1.0 \pm 0.2 \mu\text{W}/\text{m}^3$. In Hercynian granites (320-350 Ma) in the Massif Central France, two boreholes 1000 m and 900 m deep into Auriat granite (biotite \pm muscovite pluton emplaced in medium-grade metamorphic rocks) showed no significant variation from $6.1 \pm 0.7 \mu\text{W}/\text{m}^3$ to $5.7 \pm 0.6 \mu\text{W}/\text{m}^3$. The second borehole (in a topaz-lepidolite albitic granite) showed an increase from 3.6 to $4.2 \pm 0.2 \mu\text{W}/\text{m}^3$ (mainly due to increase of U with depth) which remain constant $4.3 \pm 0.4 \mu\text{W}/\text{m}^3$.

The heat flow studies in the Variscan Iberian Massif showed that the highest values of higher values are obtained from granitic rocks ($2.5\text{-}3.5 \mu\text{W}/\text{m}^3$), whereas metasediments and basic rocks reach values of $1\text{-}2.5 \mu\text{W}/\text{m}^3$ and nearly zero, respectively (**M. Fernández, I. Marzàn et al. 1998**). Studies in the Avilla batholith (Iberian Massif) confirm high heat production ($2.5\text{-}3 \mu\text{W}/\text{m}^3$) and consider that the contribution of radiogenic heat and the fertility of source rocks would have been essential for anatexis (**F. Bea, P. Montero et al. 1999**). In (**A. Gerdes, G. Worner et al. 2000**), the HT-LP metamorphism present in South Bohemian Batholith (southern Moldanubian Zone) with the South Bohemian Batholith internal radiogenic heat production within thickened crust ($2\text{-}3 \mu\text{W}/\text{m}^3$). The same hypothesis was proposed by (**O. Lexa, K. Schulmann et al. 2011**) which proposed a significant enrichment of heat radiogenic elements in the lower crust ($\sim 4 \mu\text{W}/\text{m}^3$): HT-metamorphism could be a consequence of melt-induced rheological adjustments of thick orogenic roots. Variable and typically high radiogenic heat production usually between $4\text{-}10 \mu\text{W}/\text{m}^3$ are reported in the Variscan Erzgebirge (Germany) granites, depending on their chemical type and degree of fractionation (**A. Forster and H. J. Forster 2000**). In Corsican batholith (**M. Verdoya, W. Pasquale et al. 1998**) report the radiogenic heat production rate vary from $0.2 \mu\text{W}/\text{m}^3$ (basalts) to $4.2 \mu\text{W}/\text{m}^3$ (calc-alkaline granites).

However, most of models evidence a geodynamic scenario that led to thickening of the continental crust with increased internal radiogenic heating, but without simultaneous thickening of the mantle lithosphere.

Relatively high concentration of indoor radon is associated with particular types of bedrock (**J. D. Appleton and J. C. H. Miles 2010**). In the Czech Republic, the highest indoor and soil gas radon concentrations are associated with the Variscan granites (up to 10–20 $\mu\text{g/g}$ U in bedrock) of the Bohemian massif as well as Palaeozoic metamorphic and volcanic rocks and also with uranium mineralization (**I. Barnet, P. Pacherovà et al. 2008**). The highest radon in Germany occurs over the granites and Palaeozoic basement rocks (**J. Kemski, R. Klingel et al. 2009**). In France, some of the highest radon levels occur over peraluminous leucogranites or metagranitoids (8 $\mu\text{g/g}$ U in bedrock) in a stable Hercynian basement area located in South Brittany (**G. Ielsch, D. Thièblemont et al. 2001**). In Portugal, generally higher values of U (17 $\mu\text{g/g}$, in average) and Th (> 30 $\mu\text{g/g}$) together with soil-gas concentrations of radon are observed in several lithologies of granitic rocks from the Central Iberian Zone (Iberian Massif) (**M. E. P. Gomes, L. M. O. Martins et al. 2013**). In Corsican-Sardinian batholith is extensively studied where the average activity concentrations of ^{40}K , ^{238}U and ^{232}Th are 4 %, 5 $\mu\text{g/g}$ and 17 $\mu\text{g/g}$, corresponding to an average outdoor absorbed dose rate of 124 nGy/h (**A. Puccini, G. Xhixha et al. 2013**) – **Appendix B3**.

II.1.3 Objectives of the study

The objectives of this study are:

1. Characterization of the content of ^{40}K , U and Th in rocks from the Sardinia batholiths, by investigation with gamma-ray spectroscopy method. The study will focus the N-E Sardinia which geological structure is part of Corsica-Sardinia Variscan Batholith. This study will be performed by measuring rock samples in laboratory using MCA-Rad system (see **Section I.2.2.2**) and by performing measurements in-situ using a portable gamma-ray spectrometer (see **Section I.2.3.2**). The mean abundance of K, U and Th on the N-E Sardinia will be compared with the concentration in European Variscan belts.
2. Study of the correlation between the spatial distribution of radionuclides of ^{40}K , U and Th and principal geological formations in order to reveal new evidences on the geological structure of N-E Sardinia. Here will be realized the radiometric map of the concentrations of ^{40}K (%), ^{238}U and ^{232}Th in ($\mu\text{g/g}$) based on geostatistical methods.
3. Study of the geochemical properties of rocks in N-E Sardinia by means of radioelement ratios. Here will be realized the spatial distribution of of K/U, Th/U and K/Th based on geostatistical methods, in relation with geological formation.

4. Preliminary study of heat generated from rocks in N-E Sardinia and crustal heat production. The mean heat production of rocks from N-E Sardinia will be compared with the concentration in European Variscan belts.

Chapter II.2

Study of the distribution of natural radionuclides in Sardinian batholith

II.2.1 Geological setting of study area

The Autonomous Region of Sardinia (Italy) is the second biggest island in the Mediterranean Sea, after Sicily. The nearest land masses are: the Corsica Island (France), the Italian Peninsula, Sicily Island, Tunisia and Balearic Island. The surface of Sardinia Island is of about 24,090 km². In **Figure II.2.1** is shown the geographical position of Sardinia Island and the location of the study area.

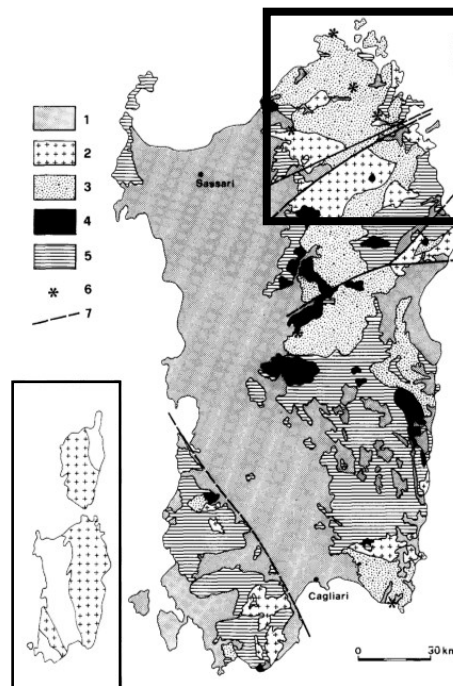


Figure II.2.1: Sardinia-Corsica Batholith: (1) sedimentary formation; Permian and post-Paleozoic volcanites; (2) leucogranites; (3) monzogranites; (4) tonalities and granodiorites; (5) metamorphic complex; (6) gabbro-dioritic masses; (7) faults (Figure from (G. Poli, C. Ghezzi et al. 1989)). With the black rectangle shows the study area.

The Corsica-Sardinia Batholith occupies an area of ca. 12000 km² emplaced during the complex tectono-metamorphic evolution in an interval of time of about 40 Ma (from about 320 to about 280 Ma). In the Sardinia-Corsica Batholith, was distinguished two main groups of complex: a magnesium-potassium of Viséan Namurian age, present only in northern Corsica, and a calc-alkaline complex essentially attributable to the Upper *Carboniferous-Lower Permian*, which constitutes almost all of granitoids of the southern Corsica and Sardinia (B. J. Orsini 1980).

The study area (**Fig. II.2.1**) is located in the north-eastern part of Sardinia and is part of the Hercynian basement, with a surface of about 4000 km². The Sardinia batholith is heterogeneous, consisting in seven complexes which differ in mineralogical composition and age (**Figure II.2.1**). In Sardinia, where there is only the calc-alkaline association, the radiometric ages and the relationships between the internal schistosity of the intrusion and the general structure of the chain, indicate that the deformation, even in solid state flow, of the intrusion, is put in relation to transtensive shear zones subsequent of the layers stacking, as into the Mt. Grighini (**G. Musumeci 1992**), or in any case in shear zones associated with a tectonic decompression, as in the low Gallura (**G. Oggiano and Di. Pisa 1988**); (**P. Macera, S. Conticelli et al. 1989**). Ultimately, it is to be assumed that the emplacement of the Sardinia-Corsica Batholith is due to extensional tectonics, related to the gravitational collapse of the Hercynian chain. This tectonics is certainly active in Sardinia from at least 308 Ma, the age of closure of muscovite metamorphic decompression related to the event of high T/P (**P. Macera, S. Conticelli et al. 1989**), and continued at least until Autunian, because this tectonic occurs with a regional metamorphism of high T / P, with the development of molassic deposits and with an active calc-alkaline volcanism. As a result, much of the calc-alkaline plutonic rocks of the Sardinia-Corsica Batholith must be considered to be coeval with sediment (at least the lower most part) than with the volcanics present in continental basins. In fact, some Autunian intrusion probably represents the effusive facies of the Plutonic Batholith. The character of the Sardinian calc-alkaline granitoid association was highlighted by time (**P. Di Simplicio, G. Ferrara et al. 1974b**); (**B. J. Orsini 1980**); (**A. Bralia, C. Ghezzi et al. 1981**); (**C. Ghezzi and J. B. Orsini 1982**); (**G. Poli, C. Ghezzi et al. 1989**).

The main intrusions show a great variety ranging from quartzodiorite, leucogranite up to two-mica, defining trend from calc-alkaline -trondjemitic to calc-alkaline -monzogranitic, in agreement with those defined by (**J. Lameyre and P. Bowden 1982**). The type calc-alkaline is also indicated by some mineral-petrographic characters such as friferous biotite with an evolutionary trend towards higher levels in Fe + Mn, amphibole-type (**B. J. Orsini 1980**.)

The proportions of the various terms of the calc-alkaline association, after (**B. J. Orsini 1980**), are schematized in **Figure I.2.2** for the mineralogical content;

- a) intermediate granitoids (60-65% SiO₂): tonalite and granodiorite, covering 6-7% of the total surface;
- b) felsic granitoids (65-75% SiO₂): granodiorite and monzogranite, covering 60% of total outcrop;
- c) ultra-felsic granitoids (75-78% SiO₂): monzogranite and leucogranite, covering 30% of total outcrop;
- d) mafic (basic) intrusive rocks (gabbro and gabbro-tonalite), covering 1% of total outcrop.

The granitoids in acidic composition (granodiorites and monzogranites) show greater inhomogeneity; instead leucogranites are more homogeneous, among which are not rare the intrusions peraluminose leucogranites.

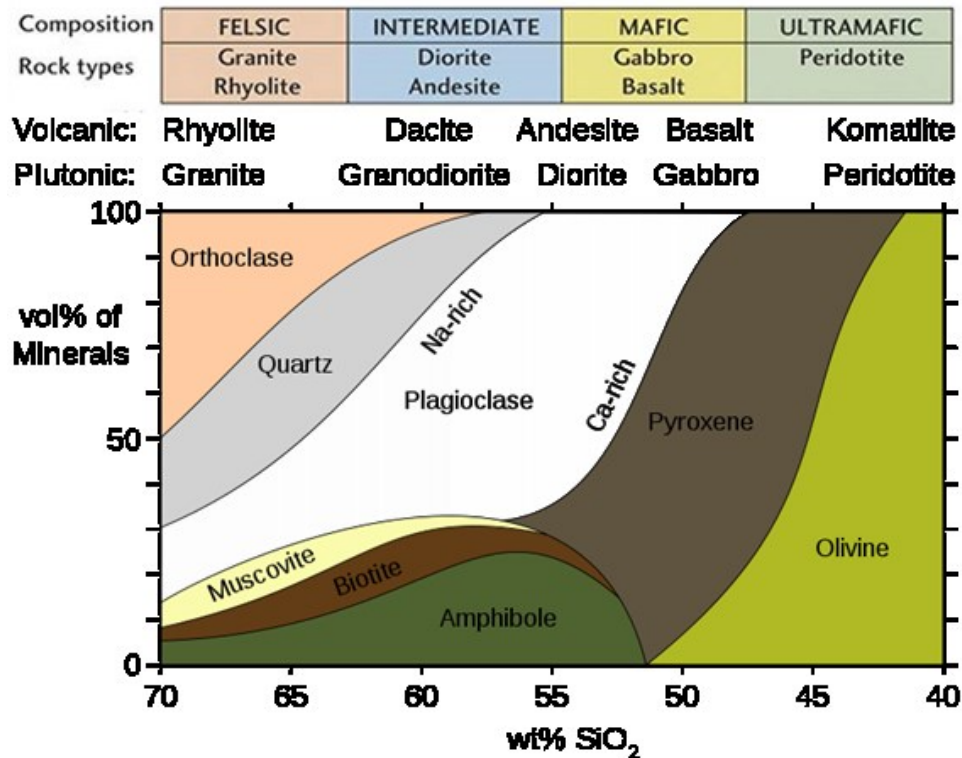


Figure II.2.2: basic classification scheme for igneous rocks on their mineralogy.

The main geological Complexes of North Sardinia Batholiths (**Figure II.1.3**) are:

I. Intrusive Complex:

(a) Upper Carboniferous-Permian pluton complex

Leucogranites (31). Outcrops extensively in all sector of the Sardinia basement. They are characterized by compositional homogeneity and the weakly oriented textures or almost isotropic. The dominant direction varies from NS to NE-SW (C. Ghezzi and J. B. Orsini 1982). The available radiometric ages range from 289 ± 1 Ma to 274 ± 9 Ma (A. D. Moro, P. D. Simplicio et al. 1975); (A. Cocherie 1978); (A. Cocherie 1985; F. Castorina and Petrini 1989). In some areas, are also reported to leucogranites inequigranular facies, which crop up continually in the massif of Mt. Limbara and Mt. Lerno (Gallura). It is a trend of leucocratic inequigranular granitoids, to which gives it a globular quartz porphyry base.. The biotite is present in modal proportion not exceeding 5%. The leucogranite, that emerge along the Oschiri valley and in the Olbia area, as St. Teresa-port (Gallura), differ from the previous grain ranging from medium to large and weaving inequigranular, highlighted with subhedral crystals of pink K-feldspar with centimeter size, locally disoriented along magmatic flow. The biotite crystallized in isolated individuals in size around 3 mm, is in modal proportions not exceeding 5%. The most extensive intrusion of leucogranites outcrops NW of Luras, and W in San Pantaleo Olbia (Gallura). They are characterized by a medium-grained equigranular texture, with K-feldspar equidimensional with sub-centimeter size, crystallized polycrystalline individuals rather than to the rock with characteristic pinkish color. The biotite, of a size not exceeding 2 mm, is in modal

proportions not exceeding 7%. The facies outcropping in Sarrabus it differ from the previous ones for the fine-grained and for the olo-leucocratic tendency resulting from the almost total absence of biotite. The leucogranite described above are clearly different from those outcropping in Punta Tepilora (Barony) for their peraluminose character which is manifested by the presence of garnet and muscovite (garnet leucogranites). It is compositionally a leucogranite with pinkish isotropic texture and medium-fine grain, characterized by the presence of a garnet red, with sizes up to 6-7 mm, and rare crystals of millimetric muscovite. The K-feldspar is pinkish in color and sometimes with pecilitic inclusions of biotite, which crystallizes even in individuals subhedral millimeter-sized, uniformly distributed and in modal proportions not exceeding 4%.

Equigranular to inequigranular Monzogranites and Sodic Sienites (32). These intrusive rocks are a variety of facies resulting from variations in either texture orientation, and grain variability. Equigranular Monzogranites abound in the area of Buddusò-Ala dei Sardi (**B. J. Orsini 1980**). They are leucocratic monzogranites, with equigranular texture and with planar fluidity not always well expressed. This lithotype is characteristic of the pearly gray color, a good color homogeneity and particle size interrupted by sporadic euhedral phenocrysts of white milk K-feldspar. Compared to non-eterogranular monzogranites , those equigranular are characterized by the low content of biotite. In the Olzai-Gavoi (Barbagia) and S Dorgali (Gulf of Orosei), the equigranular monzogranites have a leucocratic tendency, medium-fine grained and equigranular texture, with white sub-centimeter size K-feldspar crystallized in poly-crystalline elements. As regards **inequigranular monzogranite**, are to be mentioned the isolated masses including between Olzai and Irgoli (Baronie). It is characterized by a unimodal tendency rocks with the size of pinkish K-feldspar color, which varies between 3-5 cm. Locally is appreciable a moderate orientation along magmatic flow direction. At the core of the wide extensive intrusion of Tempio Pausania (Gallura), are found monzogranites with pink K-feldspar oriented with a large size (8-12 cm), but it does not represent more than 10% of the total K-feldspar. The most common lithotype of the monzogranites family, outcrops in continuity in the area of Nord of Tempio-Calangianus, up to Telti. It differs from the much smaller size of phenocrysts of which does not exceed 5-6 cm, keeping an average of around 3-3.5 cm. Also, unlike the previous, almost all of the K-feldspar is represented by euedral oriented phenocrysts. The extensive outcrop area between Aglientu and Arzachena (Gallura) is represented by well-differentiated rock types being more equigranular markedly from the previous and with a significant decrease in the size of K-feldspar, which often has a size comparable to that of plagioclase. The radiometric age determined by various authors have totaled around 280 Ma (**A. Cocherie 1985**); (**F. Castorina and Petrini 1989**). Along with monzograniti we remember the small stock of sodic syenites that develop in an E-W direction within the granodiorite Sarrabus (**P. Brotzu, L. Morbidelli et al. 1978**).

Equigranular granodiorites and equigranular tonalites (33). The granodiorite outcrops extensively in the Sardinian sector of the batholith, with most frequent intrusion in green schists metamorphic complex

fancies, whereas, are subordinated in the medium and high grade metamorphic complexes of NE Sardinia. They always have a strong anisotropy marked by the orientation of the biotite and by the mafic inclusions always included in these plutonites. Based on the structural characteristics, it can distinguish equigranular and inequigranular granodiorite with a monzogranitic trend, and granodiorite and tonalite. The equigranular granodiorites are characterized by a variable grain from medium coarse to medium-fine, with equigranular texture and a moderate magmatic orientation highlighted by a biotites orientation and by the mafic inclusion. The biotite, with dimensions of about 2 mm, is in modal proportions not exceeding 15%, the quartz, rarely subhedral, is in proportions not exceeding 20%. In the inequigranular granodiorites the grain is of medium to medium-fine texture and the inequigranular character is determined by the presence of K-feldspar pluricentimetric phenocrysts, whose distribution is inhomogeneous in the scale of the outcrop. Also here the fluidity of the magma is well marked from the orientation of biotite and of the K-feldspar as well as the numerous mafic inclusions. Between the mafic phases is observed, sporadically, green amphibole, while the biotite presents modal proportions between 15-20%. The tonalitic granodiorites are characterized by medium-large grain for the sporadic presence of crystals of white-pinky K-feldspar, with pluricentimetric size and pecilitiche inclusions of biotite.

Tonalites, Gabbro and gabbro-tonalitic masses (34). The tonalites outcrops mainly in the western sector of the batholith (zone of Trinity Agultu: Gallura, Ottana: Nuorese), with a granodioritic character, medium-grained and moderately inequigranular. They are characterized by an evident textural anisotropy marked by the alignment of all the minerals and of the abundant microgranular dark inclusion of dioritic-tonalitic composition. The biotite is in modal proportions not exceeding 25% and is often associated with a green amphibole in modal quantities not exceeding 5%. In the area of Busachi-Ortuero (Barigadu), in the area of Bitti-Lula (Barbagia) and Lanusei-Barisardo (Ogliastra), the tonalite are differentiate from the previous to the absence of an evident textural anisotropy and for the more markedly tonalitic character (**D'Amico 1960**); (**G. C. Negretti 1966**). West of Atzara (Mandrolisai), there are granodioritic tonalites with isotropic texture, medium-grained, with rare individuals inequigranular K-feldspar in size up to 1 cm. The biotite is in modal proportions not exceeding 20%, associated with rare amphibole. The quartz, with interstitial character, is estimated not to exceed 15%. The Gabbros and the gabbro-tonalitic masses are very rare in the Sardinia-Corsica Batholith, and constitutes small bodies almost always incorporated within plutonites more acid. The most important outcrops are at Punta Falcone, Bortigiadas (Gallura), Osidda (Barbagia Bitti) and Sarrabus.

Foliated granitoids (35). They are granitoids with different composition and age; are represented both peraluminous-leucogranites, with an age of emplacement of 300 ± 7 Ma (**P. Macera, S. Conticelli et al. 1989**), that granodiorites and tonalites. The main textural characteristic of a granite outcropping in the Porto-Pollo Barrabisa (Gallura), is an obvious evident foliation marked by bands of quartz, parallel of the metamorphic foliation.. The grain is heterogeneous and often there is a facies with centimetric plagioclase crystals with pecilitic inclusions of biotite. In the area of Bortigiadas (Gallura) there are tonalitic

granodiorites strongly oriented, characterized by the alignment of phenocrysts of plagioclase and quartz. The texture is sometimes gneissic, the grain varies from medium-fine to coarse. They differ from the previous ones by the absence of aluminous phases such as the muscovite and cordierite.

Anatectic granitoids (37). Leucogranites and granodiorites of anatectic origin, crop up in the Gallura, Barrabisa, S.Maria Island, Golfaranci, Aglona; Tarra Padedda; Mandrolisai, M.te Grighini.

(b) Upper Carboniferous-Triassic dike complex

The Sardinian basement shows many sub-volcanic events. The chronology of these sub-volcanic phenomena can be reconstructed by emplacement evidences. Many sills cut the granitoid batholiths and Permian Volcanics (**G. Traversa 1969**). The radiometric data indicate that the age of the Filoniane acidic events ranging from 268 ± 4 Ma to 298 ± 4 Ma (**C. Vaccaro, P. Atzori et al. 1991**). The direction of the dyke system is very variable and characteristic. In northern Sardinia are very common directions from NE-SW to NNE-SSW (up to NS at the northern end of the Gallura) In southern Sardinia, up to Southern Sarrabus, prevail instead directions NW-SE to NNW-SSE.

Acid dikes (28). Sills of granite porphyry, microgranitici, aplitici and pegmatite with isotropic texture, sometimes porphyritic with phenocrysts of alkali feldspar potassium, quartz, and more rarely biotite and muscovite dispersed in a groundmass granofirica.

Basic dikes (29). Filonian sills with basaltic composition, calcalkaline, transitional and alkaline.

Hydrothermal dykes (30). Dikes and subvolcanic bodies of prevailing quartz, often mineralised with sulphides, barite, fluorite, gold and silver, etc. Upper Carboniferous-Lower Triassic.

2. Metamorphic Complex (Inferior Precambrian – Carboniferous) connected with the Hercynian Collision.

The Stratigraphic evolution of the pre-Hercynian (? Precambrian-Lower Carboniferous) can be clearly described only in the central-southern Sardinia, mainly in the Internal nappes and the External nappes. Moving towards NE, metamorphism and deformation processes are increased and the reconstruction of the stratigraphy become very difficult. In Baronia, where the metamorphic rocks show the major continuity in outcrop, the metamorphic grade increases rapidly towards the NE; in a wide zone of about fifty kilometers the facies vary from the green schist to the amphibolite and migmatites. From SW to NE there are distinct zones: chlorite, biotite, garnet, staurolite to biotite +, biotite + kyanite and sillimanite + muscovite and sillimanite + K-feldspar. These characteristics are typical of metamorphism Barroviano. In northern area

(Gallura) the outcrops of metamorphic rocks are included in the mass of granite that here is the dominant lithotype. According to the geodynamic reconstruction (L. Carmignani, G. Oggiano et al. 2001), the Complex migmatitic derives from continental crust Armorican, moved on subducted Gondwaniano margin in which have been recognized: a) Hercynian metamorphic complex with dominant amphibolic facies b) greenschist and sub-greenschist facies Hercynian metamorphic complex subdivision Internal nappes and External nappes. The descriptions of these complexes are written in the legend of the map northern Sardinia. The two margins are separated by an important milonitica area, the Asinara–Posada line, which include portions of oceanic crust.

The study area includes also Quaternary deposits and sedimentary covers of less extended surface and not subject of this study. However, the detailed legend of north-eastern Sardinia Batholith map (**Fig. II.2.2**) is shown below.

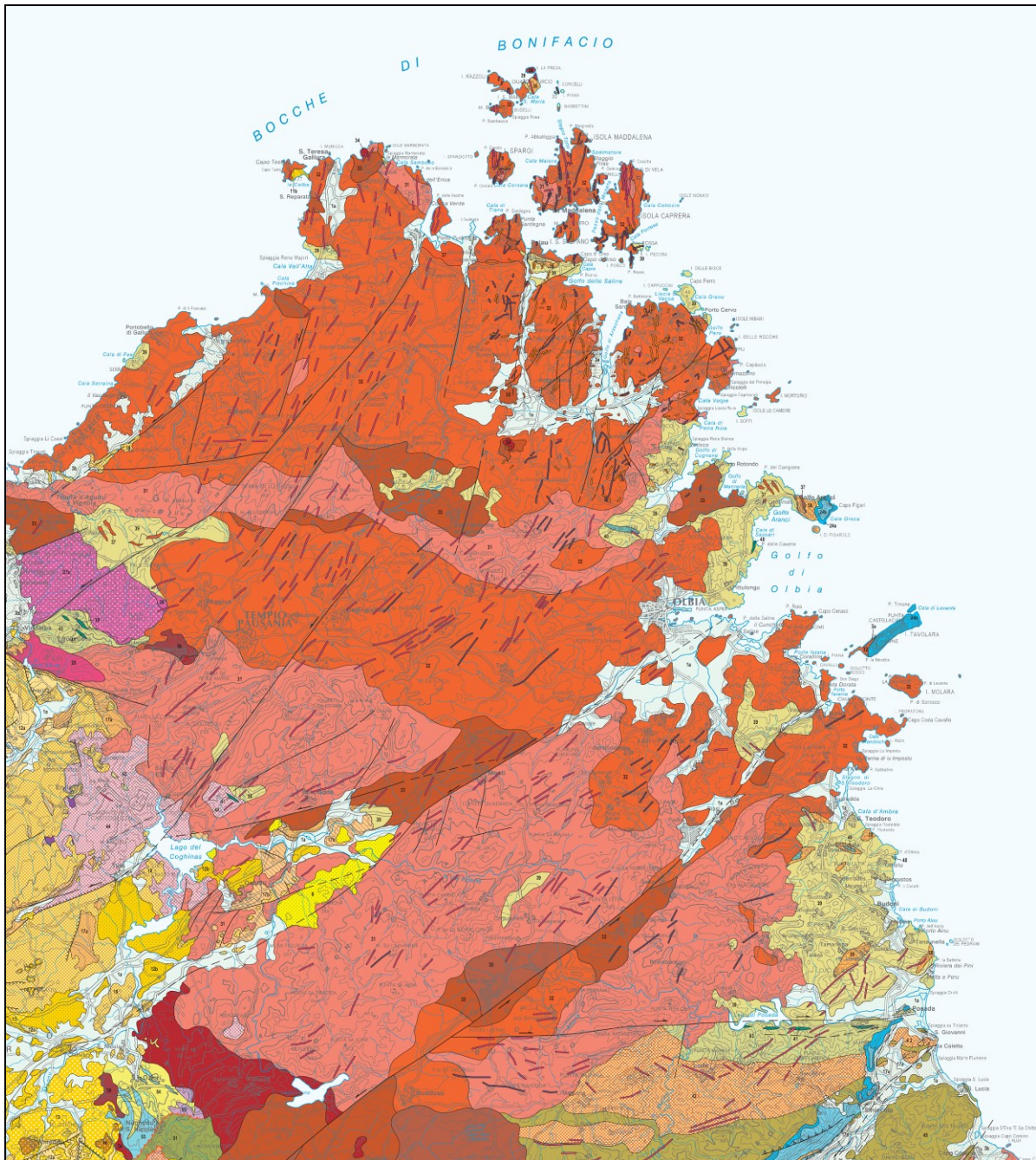


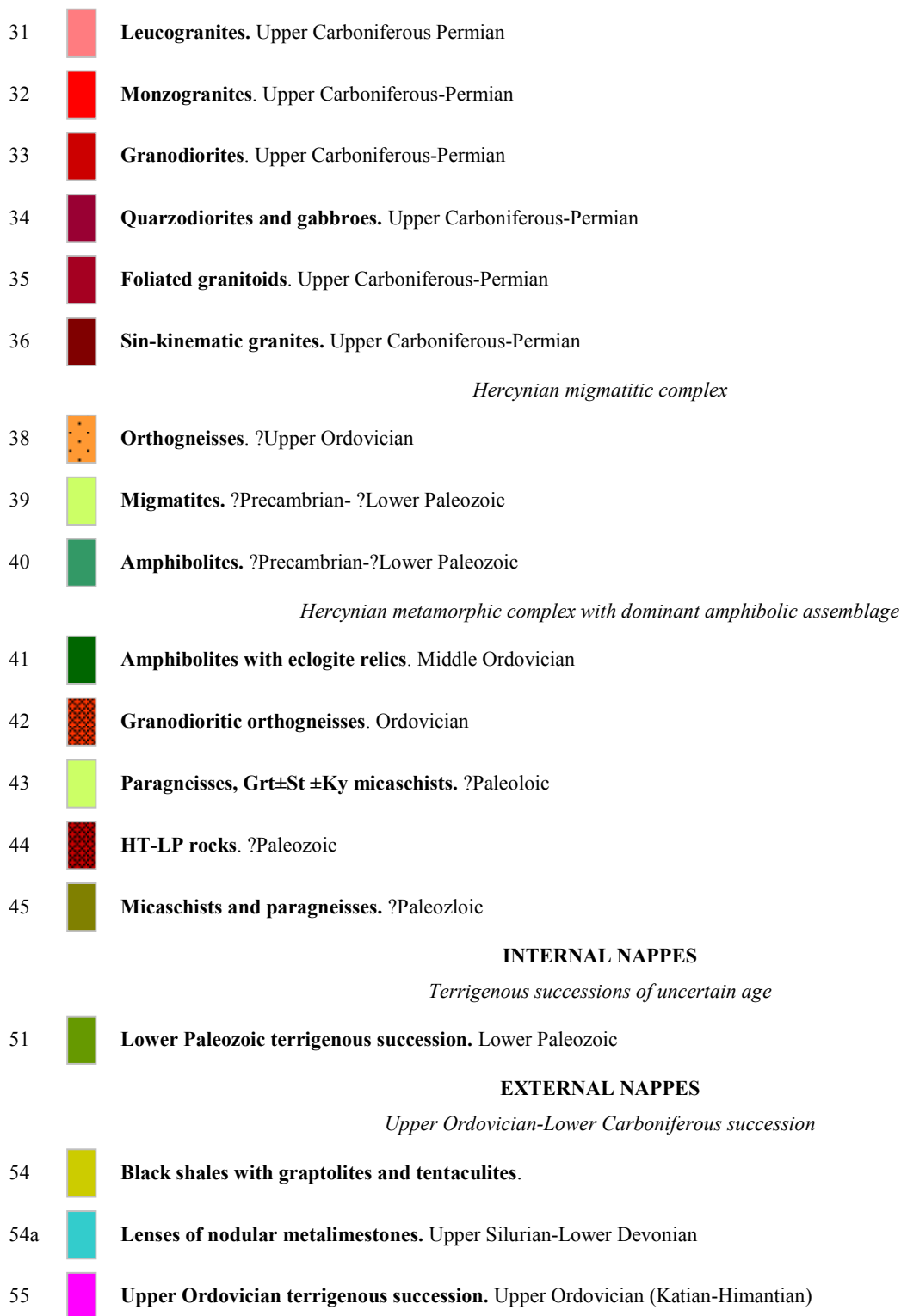
Figure II.2.2: The geological map of study area (L. Carmignani, G. Oggiano et al. 2012).

The simplified legend of the geological map is described below:

QUATERNARY DEPOSITS

- 1a  Marine to continental Holocene deposits. Holocene
- 3a  Ancient marine deposits.

- 3b  **Ancient continental deposits.** Pleistocene
- VOLCANIC AND SEDIMENTARY COVER**
- 4b  **Lava flows alkaline basalts.** Pliocene-Lower Pleistocene
Upper Miocene-Lower Pliocene sedimentary succession
- 8  **Marine deposits of the third Miocene sedimentary cycle.** Tortonian
Lower-Middle Miocene volcano-sedimentary succession
- 11a  **Littoral carbonatic deposits of the second Miocene sedimentary cycle.** Upper Burdigalian
- 11b  **Marine deposits of the second Miocene sedimentary cycle.** Upper Burdigalian Middle-Upper Langhian.
- 12a  **Epiclastites of the second Miocene sedimentary cycle.** Burdigalian.
- 15a  **Andesitic lavas of the second Miocene volcanic cycle.** Burdigalian.
Upper Oligocene-Lower Miocene volcanic-sedimentary succession
- 18  **Pyroclastic flows of the first Oligo-Miocene volcanic cycle.** Aquitanian-Burdigalian.
- 19c  **Acid lavas of the first Oligo-Miocene volcanic cycle.** Aquitanian-Burdigalian.
Paleogene marine to transitional successions
- 20b  **Continental deposits.** ?Middle-Upper Eocene-Oligocene
Mesozoic sedimentary successions - Upper Cretaceous marine successions
- 22b  **Middle-Upper Cretaceous succession of Western Sardinia.** Middle-Upper Cretaceous (Cenomanian-Campanian)
Middle Triassic-Lower Cretaceous marine and transitional successions
- 24a  **Middle-Upper Jurassic succession of Eastern Sardinia.** Middle-Upper Jurassic (Dogger-Malm)
- 24b  **Upper Jurassic succession of Eastern Sardinia.** Dogger – Malm
- 25  **Triassic succession.** Upper Triassic
Carbonatic shelf deposits of circalittoral to transitional environment: Middle Triassic
Upper Carboniferous-?Lower Triassic continental succession
- 26  **Volcano-sedimentary succession.** Westphalian D (?)-Autunian
- 27b  **Rhyolitic-dacitic volcanites.** Upper Carboniferous-Upper Permian-?Lower Triassic
- HERCYNIAN BASEMENT**
- Upper Carboniferous- Triassic dike complex*
- 28  **Acid dikes.**
- 29  **Basic dikes.**
- 30  **Hydrothermal dikes.** Upper Carboniferous-Lower Triassic
Upper Carboniferous- Permian plutonic complex



II.2.2 Gamma-ray spectrometry survey measurements

An area of about 4165 km² was investigated with at least one sample per approximately 6 km² in average by performing 545 in-situ measurements and by collecting 167 rock samples, which were after measured in the laboratory. In **Figure II.2.3** it shows the location of in-situ measurements and samples collected. In situ

measurements were performed using a portable NaI(Tl) detector (see **Section I.2.3.2**) and laboratory measurement were performed using the MCA-Rad system (see **Section I.2.2.2**), following the procedures described below.

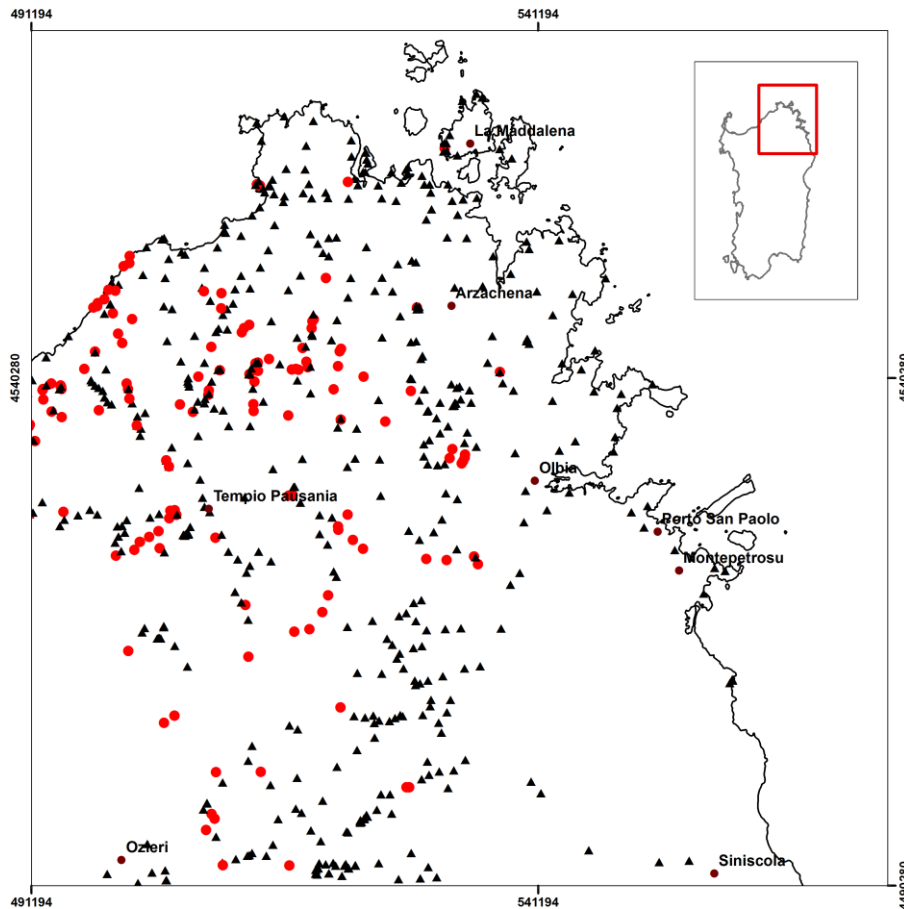


Figure II.2.3: the distribution of in-situ measurements (black triangle) and rock sample collected (red circles).

II.2.2.1 In-situ gamma-ray spectrometry measurements

In this survey over 545 outcrops were investigated by performing 5 minutes in-situ measurements each by placing the portable detector on the ground (**Fig. II.2.4**). A number of relevant precautions were taken to ensure the reliability of our measurements. To minimize the interference due to morphology, relatively flat outcrops were chosen, far from the sides of the outcrop and from man-made constructions. The portable NaI(Tl) detector was placed on bare rocks with no soil cover or vegetation. The measurements were never performed immediately after rainfalls and since the detector was placed on bare rocks the interference of moisture was considered negligible. The ^{238}U and ^{232}Th activity concentrations were calculated assuming secular equilibrium in the decay series. The main advantages of using in situ measurements are (a) quick feedback, (b) a large sample size, (c) immediate repeatability of the measurement and (d) low management costs.



Figure II.2.4: examples of the configuration of in-situ measurements using the portable NaI (TI) detector.

The spectra collected are then recalibrated energetically and analyzed to determine the concentration of ^{40}K , $e\text{U}$ and $e\text{Th}$ by using the full spectrum analysis with the non-negative least squares (FSA-NNLS) constraint described in **Section I.2.3.3**. As described in **Section I.2.3.3** the systematic uncertainty of the method is estimated to be 5 % for ^{40}K and 7 % for $e\text{Th}$ and 15% for $e\text{U}$, which gives the quality of in-situ measurements. In the case of 5-min in situ measurements on Sardinia Batholiths outcrops, the statistical uncertainties were < 10 % for ^{40}K , ^{238}U and ^{232}Th , respectively. The results are summarized in **Table II.2.1**.

Table II.2.1: characterization of investigating rock types for the abundances of K (%), U ($\mu\text{g/g}$) and Th ($\mu\text{g/g}$) within 1σ standard deviation. The statistical analysis was performed as described in **Section I.3.2**.

rock-type	No.	K (%)	U ($\mu\text{g/g}$)	Th ($\mu\text{g/g}$)
monzogranite	379	4.07 ± 0.56	$5.05^{+2.40}_{-1.61}$	$18.74^{+6.93}_{-5.04}$
granodiorite	59	2.92 ± 0.55	$3.08^{+0.90}_{-0.70}$	12.63 ± 3.26
migmatite	25	3.42 ± 0.60	$4.55^{+1.40}_{-1.07}$	13.10 ± 4.76
leuco-monzogranite	15	4.50 ± 0.43	7.68 ± 2.52	23.23 ± 8.58
granite	13	4.11 ± 0.61	$5.58^{+3.41}_{-2.12}$	15.29 ± 5.75
orthogneiss	8	3.82 ± 0.74	5.82 ± 2.62	15.19 ± 7.60
sienogranite	7	4.56 ± 0.32	7.78 ± 2.52	28.59 ± 3.06
monzo-granodiorite	6	3.54 ± 0.67	4.65 ± 1.76	14.03 ± 1.96
porphyry	6	4.54 ± 0.42	5.34 ± 1.60	19.93 ± 5.92
leucogranite	5	4.06 ± 0.49	5.45 ± 4.26	15.41 ± 9.93
meta-arenaria	5	3.30 ± 0.31	3.85 ± 1.07	14.41 ± 4.37
monzo-sienogranite	5	4.40 ± 0.26	8.65 ± 3.63	29.26 ± 2.98
quarzodiorite	4	1.17 ± 0.35	1.64 ± 0.76	5.01 ± 1.17
mica-schist	3	3.61 ± 0.59	5.24 ± 0.43	18.06 ± 0.78
eclogite	2	0.65 ± 0.05	1.05 ± 0.02	1.91 ± 0.32
marble	1 ^a	0.97 ± 0.02	1.08 ± 0.04	5.67 ± 0.21
sienite	1	3.64 ± 0.03	4.30 ± 0.08	19.86 ± 0.40
tonalite	1	2.15 ± 0.03	1.85 ± 0.05	9.27 ± 0.27

a – the uncertainty correspond to the statistical uncertainty of the measurement.

II.2.2.2 Laboratory gamma-ray spectrometry (MCA_Rad system) measurements

The specific activities of ^{40}K , ^{238}U and ^{232}Th were measured in 167 representative rock samples by using a high-purity germanium (HPGe) gamma-ray spectrometer (MCA-Rad system, see **Section I.2.2.2**). Each rock sample was crushed, homogenized (less than 2 mm fine grain size) and constant weight dried at 110°C temperature (**Fig. II.2.5**). Then, each sample was sealed in a 180 cm^3 cylindrical polycarbonate container (which is the calibration geometry, see **Section I.2.2.3**). After sealing, each container was left undisturbed for at least four weeks before spectrum acquisition: this step provides enough time to establish secular equilibrium between ^{226}Ra and ^{222}Rn , as described in **Section I.1.2.2**. As described in **Section I.2.2.3** the efficiency of the MCA-Rad system is estimated with an overall uncertainty of 5%, which gives the quality of the measurements. In laboratory measurements are do 1 hour per each sample the statistical uncertainties were $< 5\%$ for ^{40}K , ^{238}U and ^{232}Th , respectively. The results are summarized in **Table II.2.2**.



Figure II.2.5: Laboratory sample measurement with fully automated MCA-Rad system.

Table II.2.2: characterization of investigating rock types for the abundances of K (%), U ($\mu\text{g/g}$) and Th ($\mu\text{g/g}$) within 1σ standard deviation. The statistical analysis was performed as described in **Section I.3.2**.

rock-type	No.	K (%)	U ($\mu\text{g/g}$)	Th ($\mu\text{g/g}$)
monzogranite	67	3.79 ± 0.77	4.14 ± 1.64	19.57 ± 6.09
granodiorite	28	2.93 ± 1.32	$2.77^{+1.41}_{-0.94}$	$10.79^{+6.25}_{-3.97}$
amphibolite	12	1.56 ± 0.70	2.11 ± 0.71	$8.01^{+2.90}_{-2.14}$
leucogranite	11	4.10 ± 0.85	$4.20^{+4.12}_{-2.05}$	22.08 ± 7.62
alcaline-granite	10	3.96 ± 0.19	4.16 ± 1.33	$19.85^{+5.18}_{-4.16}$
eclogite	9	0.20 ± 0.13	0.26 ± 0.11	0.58 ± 0.74
granite	8	3.21 ± 1.14	3.11 ± 1.71	17.50 ± 9.08
orthogneiss	5	2.72 ± 0.40	3.26 ± 0.93	11.55 ± 4.02
tonalite	5	1.90 ± 1.02	1.95 ± 0.86	10.32 ± 3.71
sienogranite	4	4.45 ± 0.99	3.75 ± 2.18	22.32 ± 7.55
quartzodiorite	2	1.08 ± 0.34	0.57 ± 0.10	1.75 ± 0.27
mica-schist	2	2.27 ± 0.34	2.62 ± 0.11	13.06 ± 2.11
porphyry	1 ^a	3.90 ± 0.11	2.38 ± 0.09	12.60 ± 0.45
leuco-monzogranite	1	3.41 ± 0.10	2.65 ± 0.10	20.96 ± 0.64
meta-arenaria	1	3.58 ± 0.07	5.38 ± 0.21	13.96 ± 0.80
sienite	1	5.12 ± 0.08	1.34 ± 0.14	9.41 ± 0.73

a – the uncertainty correspond to the statistical uncertainty of the measurement.

II.2.2.3 Comparison of results and characterization of rocks from Sardinia Batholith for their radionuclide content

The results obtained by both investigation methods are compared by studying the frequency distribution functions and percent-probability plots respectively for the abundances of K (%) (**Fig. II.2.5**), U ($\mu\text{g/g}$) (**Fig. II.2.6**) and Th ($\mu\text{g/g}$) (**Fig. II.2.7**). This qualitative analysis shows a satisfactory agreement between both investigation methods. Indeed, the concentrations obtained for in-situ and laboratory measurements are 3.9 ± 0.8 (%) and 3.2 ± 1.3 (%) for K; $4.8^{+2.6}_{-1.7}$ ($\mu\text{g/g}$) and 3.4 ± 1.8 ($\mu\text{g/g}$) for U; and $17.0^{+9.4}_{-6.1}$ ($\mu\text{g/g}$) and 15.7 ± 8.1 ($\mu\text{g/g}$) respectively. It is observed a good agreement within 1σ (standard deviation) between in-situ and laboratory measurements.

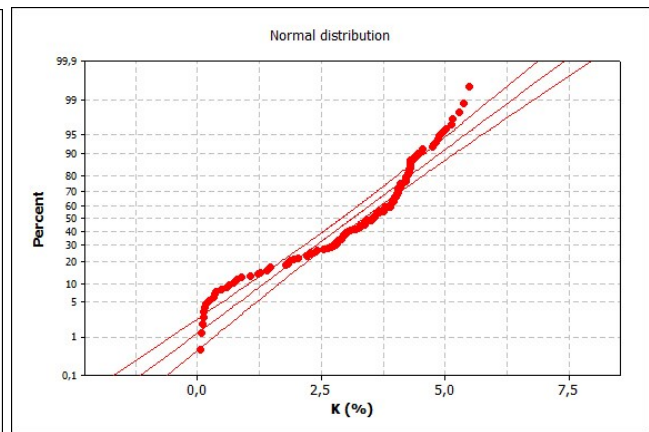
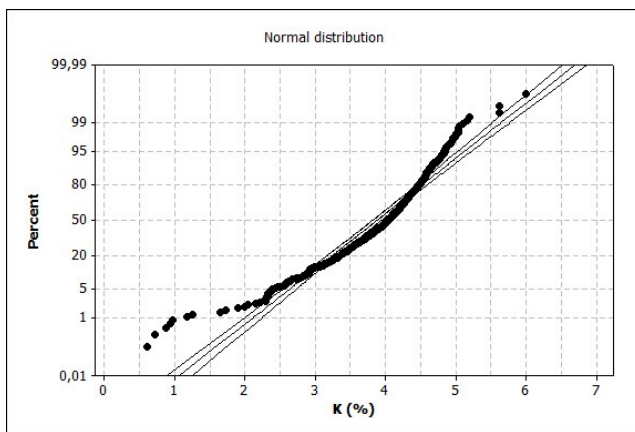
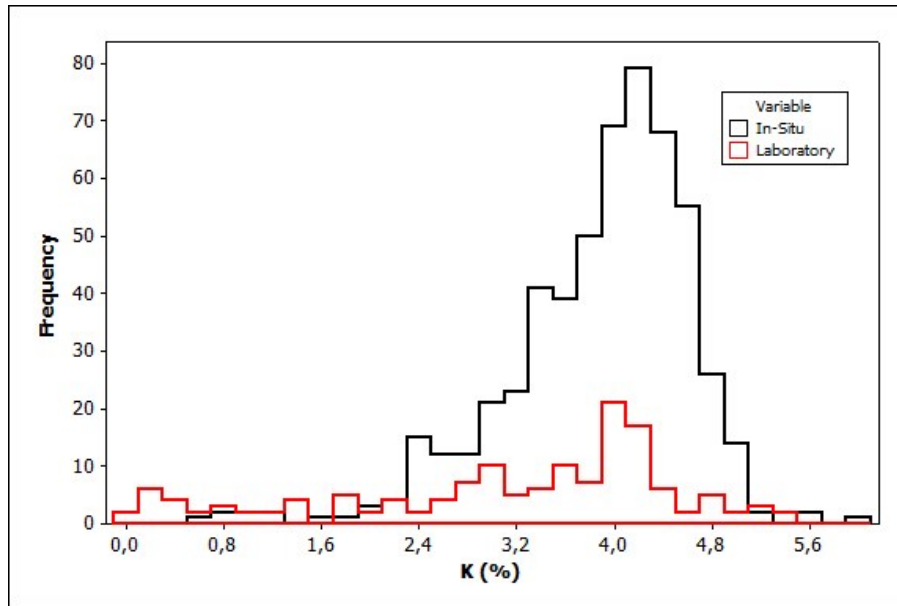
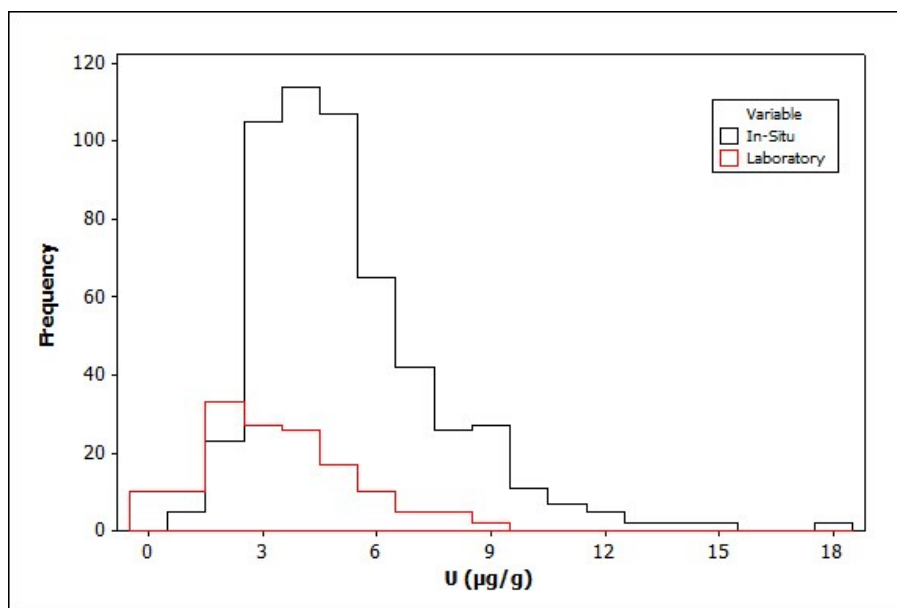


Figure II.2.5: frequency distributions and percent-probability plots for K (%) measured both in-situ (black dots) and in the laboratory (red dots).



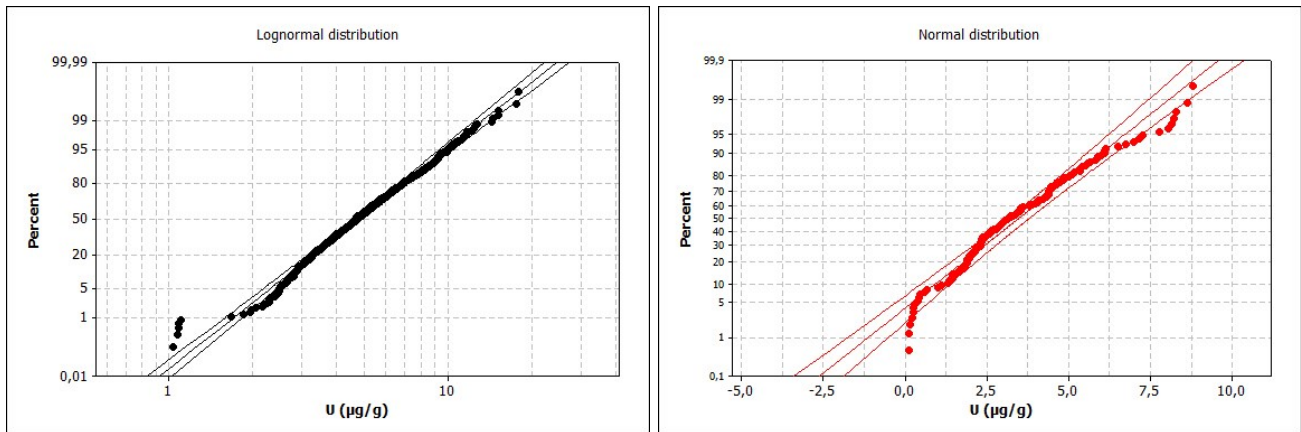


Figure II.2.6: frequency distributions and percent-probability plots for U ($\mu\text{g/g}$) measured both in-situ (black dots) and in the laboratory (red dots).

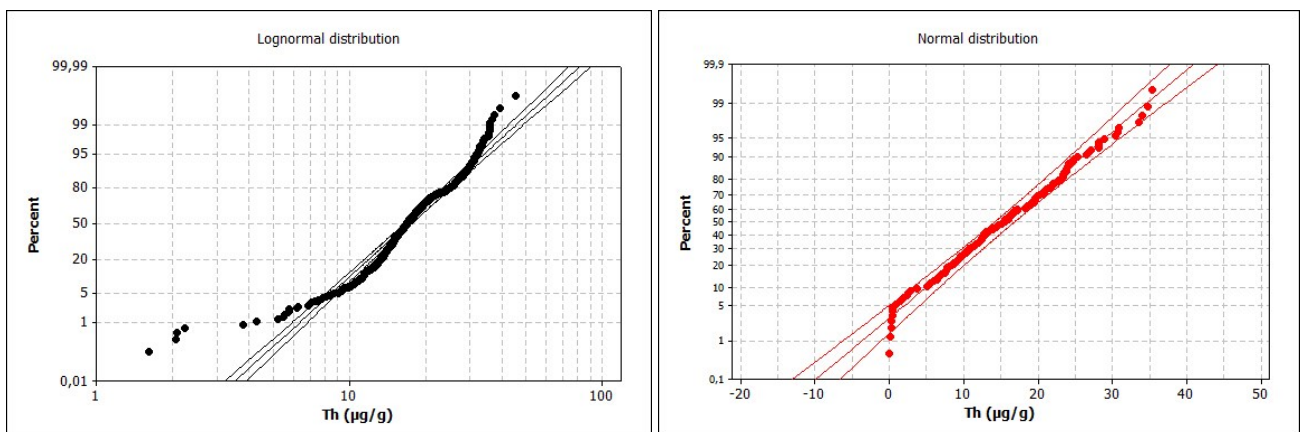
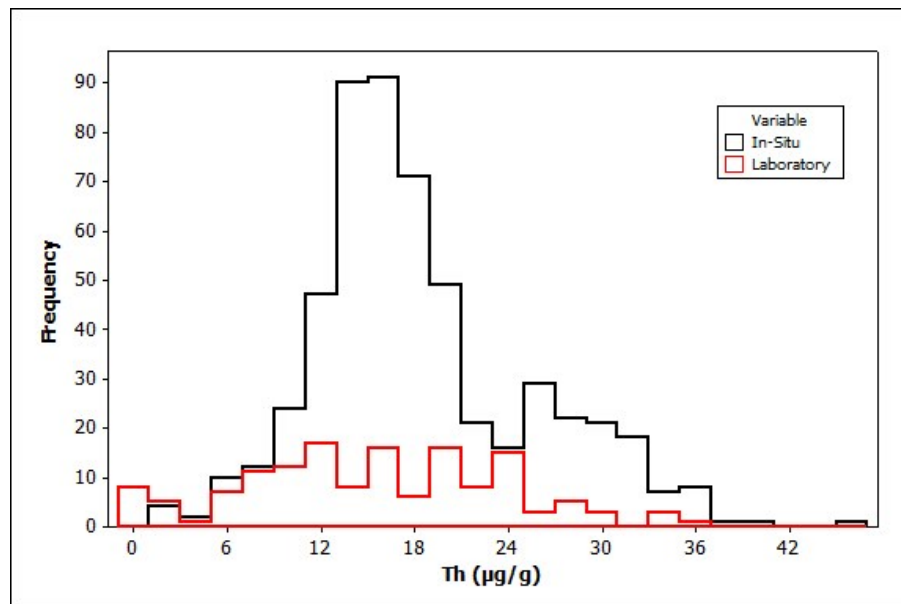


Figure II.2.7: frequency distributions and percent-probability plots for Th ($\mu\text{g/g}$) measured both in-situ (black dots) and in the laboratory (red dots).

For rock types, characterized by both methods with a statistics of $N > 2$ samples, are shown the variability in **Fig. II.2.8**, **Fig. II.2.10** and **Fig. II.2.11**. In general laboratory measurements show in average higher variability with relative uncertainties: in laboratory 30%, 45%, 45% and in situ 15%, 40%, 30%, respectively for ^{40}K , ^{238}U and ^{232}Th .

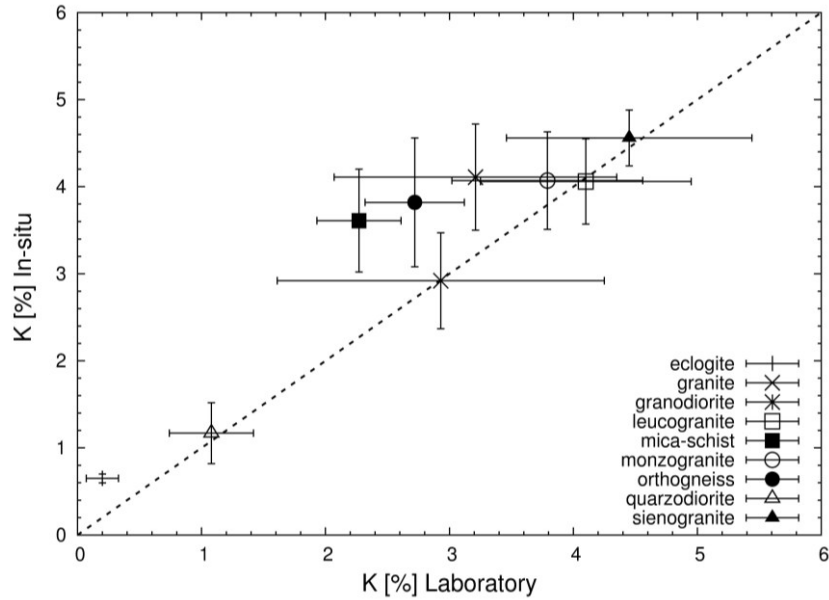


Figure II.2.8: comparison between laboratory and in-situ measurements for potassium.

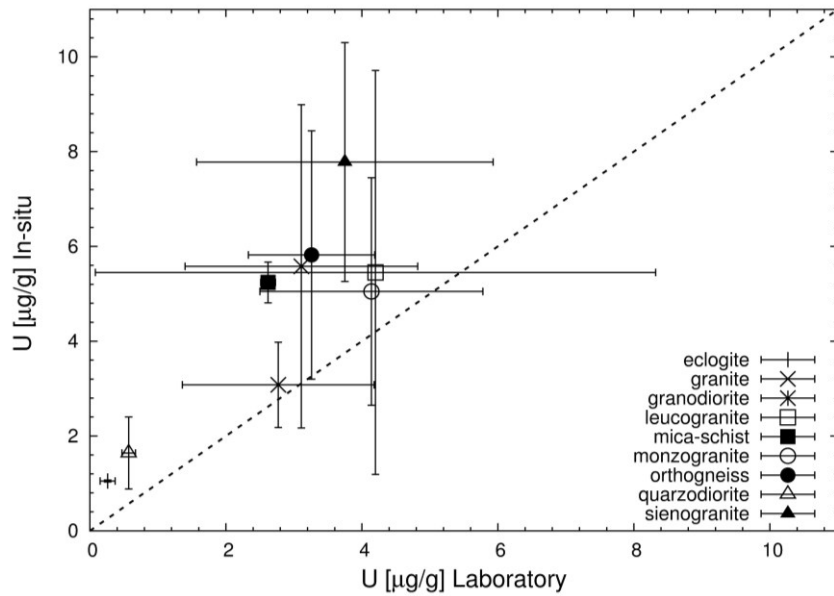


Figure II.2.9: comparison between laboratory and in-situ measurements for uranium.

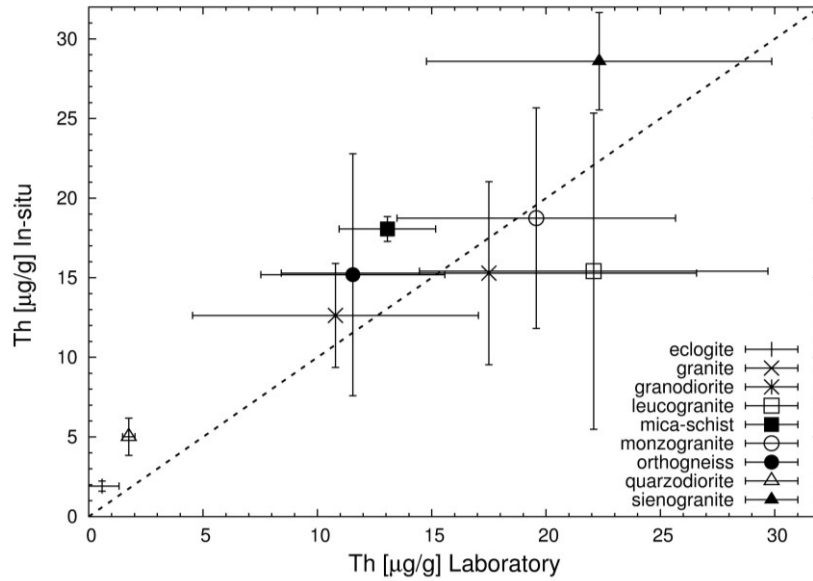


Figure II.2.9: comparison between laboratory and in-situ measurements for thorium.

The results show excellent agreement for potassium and thorium, while for uranium it shows an overestimation for in-situ measurements. This result is expected since the principal contributor to the standard spectrum of uranium is the decay of ^{214}Bi , a daughter of ^{222}Rn , which is present in the ground and in the air. Although the instrument cannot discriminate between the two contributions from the ground and the air, the systematic uncertainty in the ^{238}U measurement for the ground is of order 15 % (A. Cacioli, M. Baldoncini et al. 2012). Therefore, for further statistical analysis we consider both measurements without distinguishing between in-situ and laboratory methods.

In Table II.2.3 are summarized the concentrations ($\pm 1\sigma$ standard deviation) of ^{40}K , ^{238}U and ^{232}Th in different rock types investigated in Sardinia Batholith. The abundances of ^{40}K vary from $0.22^{+0.27}_{-0.12}$ % (eclogites) to 4.52 ± 0.51 % (sienogranites), showing mean values higher than 4 % for monzogranites, leucogranites, leuco-monzogranites, porphyry, monzo-sienogranites and sienites. The abundances of U range from $0.31^{+0.34}_{-0.16}$ $\mu\text{g/g}$ (eclogite) to 7.37 ± 2.74 $\mu\text{g/g}$ (leucomonzogranite) and 8.65 ± 3.63 $\mu\text{g/g}$ (monzo-sienogranite), showing mean values higher than 4 % for monzogranites, migmatites, granites, leucogranites, orthogneiss, sienogranites, alkaline-granites, porphyry and monzo-granodiorites. The abundances of Th range from $1.22^{+6.79}_{-1.04}$ (eclogite) to 29.26 ± 2.98 (monzo-sienogranite), showing mean values higher than 15 % for monzogranites, granites, leucogranites, leuco-monzogranites, sienogranites, alkaline-granites and porphyry.

Table II.2.3: characterization of investigating rock types for the abundances of K (%), U ($\mu\text{g/g}$) and Th ($\mu\text{g/g}$) and ratios of Th/U, K/Th and K/U within 1σ standard deviation.

rock-type	No.	K (%)	U ($\mu\text{g/g}$)	Th ($\mu\text{g/g}$)	Th/U	K/Th ($\times 10^4$)	K/U ($\times 10^4$)
monzogranite	446	4.02 ± 0.60	$4.85^{+2.40}_{-1.62}$	$18.70^{+7.11}_{-5.17}$	$3.85^{+2.63}_{-1.56}$	$0.21^{+0.09}_{-0.06}$	$0.82^{+0.44}_{-0.29}$
granodiorite	87	2.92 ± 0.87	$2.97^{+1.10}_{-0.81}$	12.41 ± 4.16	$4.07^{+2.29}_{-1.63}$	$0.23^{+0.15}_{-0.09}$	$0.96^{+0.50}_{-0.36}$
migmatite	25	3.42 ± 0.60	$4.55^{+1.40}_{-1.07}$	13.10 ± 4.76	$2.81^{+1.48}_{-1.14}$	$0.26^{+0.16}_{-0.08}$	$0.74^{+0.28}_{-0.21}$
granite	21	3.77 ± 0.94	$4.18^{+4.08}_{-2.07}$	16.13 ± 7.07	$3.62^{+4.51}_{-2.16}$	$0.23^{+0.19}_{-0.09}$	$0.88^{+0.94}_{-0.46}$
leucogranite	16	4.09 ± 0.74	$4.24^{+4.17}_{-2.11}$	19.99 ± 8.67	$4.43^{+5.45}_{-2.63}$	$0.20^{+0.16}_{-0.07}$	$0.95^{+0.98}_{-0.48}$
leuco-monzogranite	16	4.43 ± 0.50	7.37 ± 2.74	23.09 ± 8.31	$3.12^{+2.28}_{-1.31}$	$0.19^{+0.11}_{-0.05}$	$0.60^{+0.35}_{-0.17}$
orthogneiss	13	$3.31^{+0.93}_{-0.73}$	$4.40^{+2.42}_{-1.56}$	$12.78^{+5.96}_{-4.02}$	$2.91^{+2.26}_{-1.28}$	$0.26^{+0.15}_{-0.09}$	$0.75^{+0.49}_{-0.29}$
amphibolite	12	1.56 ± 0.70	2.11 ± 0.71	$8.01^{+2.90}_{-2.14}$	$3.89^{+2.57}_{-1.39}$	$0.19^{+0.12}_{-0.09}$	$0.74^{+0.54}_{-0.36}$
eclogite	11	$0.22^{+0.27}_{-0.12}$	$0.31^{+0.34}_{-0.16}$	$0.37^{+1.78}_{-0.31}$	$1.22^{+6.79}_{-1.04}$	$0.57^{+3.32}_{-0.49}$	$0.69^{+1.41}_{-0.46}$
sienogranite	11	4.52 ± 0.51	$5.58^{+4.27}_{-2.40}$	26.31 ± 5.46	$4.64^{+3.80}_{-2.14}$	$0.17^{+0.05}_{-0.03}$	$0.81^{+0.63}_{-0.36}$
alkaline-granite	10	3.96 ± 0.19	4.16 ± 1.33	$19.85^{+5.19}_{-4.16}$	$4.86^{+2.71}_{-1.52}$	$0.20^{+0.05}_{-0.04}$	$0.95^{+0.45}_{-0.24}$
porphyry	7	4.45 ± 0.46	4.92 ± 1.84	18.88 ± 6.08	$3.82^{+2.71}_{-1.51}$	$0.23^{+0.12}_{-0.06}$	$0.90^{+0.54}_{-0.26}$
meta-arenaria	6	3.35 ± 0.30	4.10 ± 1.14	14.34 ± 3.91	$3.50^{+1.74}_{-1.16}$	$0.23^{+0.09}_{-0.05}$	$0.82^{+0.33}_{-0.19}$
monzo-granodiorite	6	3.54 ± 0.67	4.65 ± 1.76	14.03 ± 1.96	$3.01^{+1.89}_{-0.90}$	$0.25^{+0.06}_{-0.06}$	$0.76^{+0.49}_{-0.24}$
quartzodiorite	6	1.14 ± 0.35	1.28 ± 0.81	3.93 ± 1.92	$2.73^{+3.81}_{-1.72}$	$0.28^{+0.27}_{-0.12}$	$0.81^{+1.01}_{-0.39}$
tonalite	6	1.94 ± 0.92	1.93 ± 0.77	10.15 ± 3.35	$5.21^{+3.99}_{-2.13}$	$0.19^{+0.14}_{-0.09}$	$0.99^{+0.87}_{-0.51}$
mica-schist	5	3.07 ± 0.89	4.19 ± 1.48	16.06 ± 3.17	$3.83^{+2.26}_{-1.21}$	$0.19^{+0.08}_{-0.06}$	$0.73^{+0.48}_{-0.27}$
monzo-sienogranite	5	4.40 ± 0.26	8.65 ± 3.63	29.26 ± 2.98	$3.36^{+2.36}_{-1.04}$	$0.15^{+0.02}_{-0.02}$	$0.50^{+0.35}_{-0.15}$
sienite	2	4.38 ± 0.74	2.82 ± 1.48	14.64 ± 5.23	-	-	-
marble	1 ^a	0.97 ± 0.02	1.08 ± 0.04	5.67 ± 0.21	-	-	-

a – the uncertainty correspond to the statistical uncertainty of the measurement.

As discussed in **Section II.1.2**, in particular the distribution of uranium over European Variscan orogen showed that the highest concentrations ($> 4 \mu\text{g/g}$ up to $53 \mu\text{g/g}$): this is confirmed by the results in the N-E Sardinia Batholith when the majority of granitic rocks show concentrations of $U > 4 \mu\text{g/g}$ in average. However, the abundances of uranium in granite rock in Bohemia massif, Central massif and Iberian massif show higher mean values while the data are comparable within the variability. While for Th and ^{40}K the data results comparable within the variability. In particular a comparison for the main emplaced batholiths of European Variscan orogeny is summarized in **Table II.2.4**. This study showed that the concentrations of K, U and Th in European Variscan Batholiths are comparable within the uncertainty and generally higher than those typically ($2.32 \text{ }^{40}\text{K}$, $2.7 \mu\text{g/g}$ U and $10.5 \mu\text{g/g}$ Th) for the upper continental crust (**R. L. Rudnick and S. Gao 2003**).

Th/U ratio throughout the various rock types of the batholith, range from $1.22^{+6.79}_{-1.04}$ (eclogite) to $5.21^{+3.99}_{-2.13}$ (tonalite), with values close to the average for the upper continental crust of 3.89. This is observed

also for the ratio K/U which is close to the average for the upper continental crust of $0.85 \cdot 10^4$ and ranging from $0.50^{+0.35}_{-0.15} \cdot 10^4$ (monzo-sienogranite) and $0.60^{+0.35}_{-0.17} \cdot 10^4$ (eclogite) to $0.99^{+0.87}_{-0.51} \cdot 10^4$ (tonalite).

Table II.2.4: comparison of abundances of ^{40}K , U and Th in different rock types for the main batholith emplacements of European Variscan orogeny.

Rock type	Radionuclide	Main European Variscan Batholiths						
		Central Massif (1)	Iberian Massif (2)	Bohemian Massif (3)	Armorican Massif (4)	Pyrenees Massif (5)	Corsica-Sardinia Massif	
							Ref. (6)	This study
amphibolite	^{40}K (%)	-	-	0.14 ± 0.01	-	-	0.14 ± 0.12	1.56 ± 0.70
	^{238}U ($\mu\text{g/g}$)	0.3	-	-	-	-	-	2.11 ± 0.71
	^{232}Th ($\mu\text{g/g}$)	-	-	-	-	-	-	$8.01^{+2.90}_{-2.14}$
eclogite	^{40}K (%)	-	-	0.20 ± 0.05	-	-	0.18 ± 0.14	$0.22^{+0.27}_{-0.12}$
	^{238}U ($\mu\text{g/g}$)	-	-	-	-	-	-	$0.31^{+0.34}_{-0.16}$
	^{232}Th ($\mu\text{g/g}$)	-	-	-	-	-	-	$0.37^{+1.78}_{-0.31}$
granodiorite	^{40}K (%)	3.64 ± 0.32	2.86 ± 0.85	3.73	2.98 ± 0.40	3.10 ± 0.32	2.66 ± 0.43	2.92 ± 0.87
	^{238}U ($\mu\text{g/g}$)	4.49 ± 0.35	4.32 ± 1.82	3.80	4.22 ± 0.68	9.48 ± 1.61	1.96 ± 0.54	$2.97^{+1.10}_{-0.81}$
	^{232}Th ($\mu\text{g/g}$)	2.67 ± 0.25	10.97 ± 0.07	32.60	10.09 ± 1.09	12.25 ± 4.16	15.38 ± 5.63	12.41 ± 4.16
tonalite	^{40}K (%)	-	2.68 ± 0.35	1.87 ± 0.49	-	1.40 ± 1.13	1.41 ± 0.30	1.90 ± 1.02
	^{238}U ($\mu\text{g/g}$)	4	5.58 ± 1.05	1.18 ± 0.32	-	-	1.02 ± 0.29	1.95 ± 0.86
	^{232}Th ($\mu\text{g/g}$)	-	18.67 ± 1.71	3.97 ± 4.57	-	-	5.78 ± 1.14	10.32 ± 3.71
migmatite	^{40}K (%)	-	3.55 ± 0.39	4.43 ± 0.26	2.58 ± 0.95	-	2.17 ± 0.41	3.42 ± 0.60
	^{238}U ($\mu\text{g/g}$)	3.04 ± 0.83	4.72 ± 0.81	2.66 ± 1.20	3.23 ± 1.74	-	2.06 ± 1.00	$4.55^{+1.40}_{-1.07}$
	^{232}Th ($\mu\text{g/g}$)	-	18.46 ± 6.20	11.62 ± 5.90	11.20 ± 6.87	-	10.31 ± 5.72	13.10 ± 4.76
orthogneiss	^{40}K (%)	-	1.79 ± 0.16	4.11 ± 0.38	3.18 ± 1.22	3.82 ± 0.25	-	2.72 ± 0.40
	^{238}U ($\mu\text{g/g}$)	3.29 ± 0.37	2.22 ± 0.26	2.23 ± 0.64	5.60 ± 3.51	4.53 ± 0.95	-	3.26 ± 0.93
	^{232}Th ($\mu\text{g/g}$)	-	7.29 ± 1.75	15.45 ± 4.61	10.10 ± 9.83	10.50 ± 0.75	-	11.55 ± 4.02
quarzodiorite	^{40}K (%)	-	-	-	-	-	1.04 ± 0.30	1.08 ± 0.34
	^{238}U ($\mu\text{g/g}$)	-	-	-	-	1.6	0.96 ± 0.10	0.57 ± 0.10
	^{232}Th ($\mu\text{g/g}$)	-	-	-	-	6.40 ± 1.33	2.18 ± 2.06	1.75 ± 0.27
granite	^{40}K (%)	3.90 ± 0.16	4.31 ± 0.44	3.62 ± 0.12	3.47 ± 0.03	3.81 ± 0.02	3.88 ± 0.16	3.77 ± 0.94
	^{238}U ($\mu\text{g/g}$)	9.30 ± 1.05	9.00 ± 4.62	10.36 ± 5.42	8.42 ± 4.44	4.93 ± 0.70	8.32 ± 4.29	$4.18^{+4.08}_{-2.07}$
	^{232}Th ($\mu\text{g/g}$)	16.92 ± 4.33	17.65 ± 7.19	22.84 ± 6.56	17.23 ± 9.04	14.33 ± 0.40	22.67 ± 3.80	16.13 ± 7.07
leucogranite	^{40}K (%)	3.77 ± 0.31	3.87 ± 0.44	3.39 ± 0.23	3.70 ± 0.91	4.06	3.77 ± 0.35	4.09 ± 0.74
	^{238}U ($\mu\text{g/g}$)	6.16 ± 1.48	9.00 ± 4.62	3.45 ± 0.15	-	10.30	17.6 ± 1.65	$4.24^{+4.17}_{-2.11}$
	^{232}Th ($\mu\text{g/g}$)	17.04 ± 0.73	17.65 ± 7.19	18.35 ± 0.35	7.73 ± 3.80	51.00	13.31 ± 3.26	19.99 ± 8.67
monzogranite	^{40}K (%)	3.79 ± 0.09	4.60 ± 0.02		1.24	3.70 ± 0.29	4.26 ± 1.01	4.02 ± 0.60
	^{238}U ($\mu\text{g/g}$)	9.54 ± 1.14	4.18 ± 1.85		-	5.14 ± 1.41	7.50 ± 4.80	$4.85^{+2.40}_{-1.62}$
	^{232}Th ($\mu\text{g/g}$)	36.22 ± 17.37	17.11 ± 2.05	-	5.05	39.42 ± 1.69	17.23 ± 1.10	$18.7^{+7.11}_{-5.17}$
sienite	^{40}K (%)	-	-	2.52 ± 2.25	-	-	2.28 ± 0.15	5.12 ± 0.08
	^{238}U ($\mu\text{g/g}$)	-	-	34.14 ± 21.74	-	-	7.23 ± 1.55	1.34 ± 0.14
	^{232}Th ($\mu\text{g/g}$)	-	-	44.86 ± 9.86	-	-	20.03 ± 6.35	9.41 ± 0.73

(1) (M. Pagel 1982; F. Lucazeau, G. Vasseur et al. 1984; H. Downes and Duthou 1988; Cuney 1992; D. Arniaud, C. Dupuy et al. 1995; B. J. Williamson, A. Shaw et al. 1996; R. Alther, A. Holl et al. 2000; J.-M. Stussi, A. Cheilletz et al. 2002; J. Kim and M. Cho 2003; F. Solgadi, J.-F. Moyen et al. 2007; G. Ielsch, M. E. Cushing et al. 2010),

(2) (J. A. Ramirez and S. Grundvig 2000; A. Castro, L. G. Corretge et al. 2003; A. Bandrès, L. Eguiluz et al. 2004; F.-J. L-Moro and M. L-Plaza 2004; C. Casquet, C. Galindo et al. 2005; T. Donaire, E. Pascual et al. 2005; R. Arenas, J. R. M. Catalán et al. 2007; C- Riuz, C. F-Leyva et al. 2008; I. M. H. R. Antunes, A. M. R. Neiva et al. 2008; A. M.R. Neiva, I.S. Williams et al. 2009; C. Villaseca, F. Bellido et al. 2009; H. C. B. Martins, H. Sant'Ovaia et al. 2009; M. E. P. Gomes, L. M. O. Martins et al. 2013),

- (3) (P. J. O'Brien 1989; K. Breiter, M. Sokolová et al. 1991; E. Jelink and A. dudek 1993; H. Klápová, J. Konopásek et al. 1998; H-J. Förster, G. Tischendorf et al. 1999; L. Hecht, K. Thuro et al. 1999; L. G. Medaris, B. L. Beard et al. 2005; V. Záček and P. Sulovsky 2005; P. Kováriková, W. Siebel et al. 2007; P. Hasalová, V. Janoušek et al. 2008; K. Breiter, L. Ackerman et al. 2013),
- (4) (D. F. Strong 1981; J. L. Vigneresse, M. Cuney et al. 1989; M. Caroff, N. Coin et al. 2011),
- (5) (S. Fourcade and C. J. Allegre 1981; M. P. Roberts, Pin. et al. 2000; Y. Denèle, Pasquette. et al. 2011),
- (6) (G. Poli, C. Ghezze et al. 1989; P. Rossi and A. Cocherie 1991; S. Tommasini and G. Poli 1992; S. Tommasini, G. Poli et al. 1995; M. Verdoya, W. Pasquale et al. 1998; S. Tommasini, G. Poli et al. 1999; A. Dini, G. Di Vincenzo et al. 2005; M. R. Renna, R. Tribuzio et al. 2007; G. Cruciani, M. Franceschelli et al. 2008; P. Barbey, D. Gasquet et al. 2008; A. Puccini, G. Xhixha et al. 2013)

In **Figure II.2.10**, **Figure II.2.11** and **Figure II.2.12** are shown the boxplot representation of the distribution of abundances of ^{40}K , U and Th in each rock type investigated, sorted according the mean value (continued line median value). In the box-plot representation, the box contains 50% of the observations while the whiskers are extended in order to enclose the other 45% of values. The values found to exceed the median ± 1.5 Inter Quartile Range, are classified as outliers. From the boxplot representation, it can be observed that the distribution of K and Th are generally symmetric (i.e. more close to normal distribution), while for U they generally show positive outliers (i.e. more close to lognormal distribution). From the boxplot representations, it can be observed that the abundances of K, U and Th show a slight increasing tendency from passing from mafic to intermediate to felsic rocks. Indeed, granoids can be classified according to their mineralogical content (described in **Figure II.2.2**) in mafic (abundant in dark-colored minerals: olivine, pyroxene, and plagioclase), intermediate (roughly equal amounts of dark- and light-colored minerals) and felsic (rich in light-colored minerals: quartz, alkali feldspar, and some plagioclase feldspar and poor in dark-colored minerals biotite and amphibole) rocks. Felsic igneous rocks contain high silica content, greater than $\sim 69\%$ SiO_2 (e.g. granite, monzogranite, sienogranite, leucogranite, leuco-monzogranite). Intermediate igneous rocks contain between 52-69% SiO_2 (e.g. tonalite, quartzodiorite, granodiorite). On the other hand, mafic igneous rocks (e.g. amphibolite, eclogite) contain low silica 45-52% and typically high iron-magnesium content.

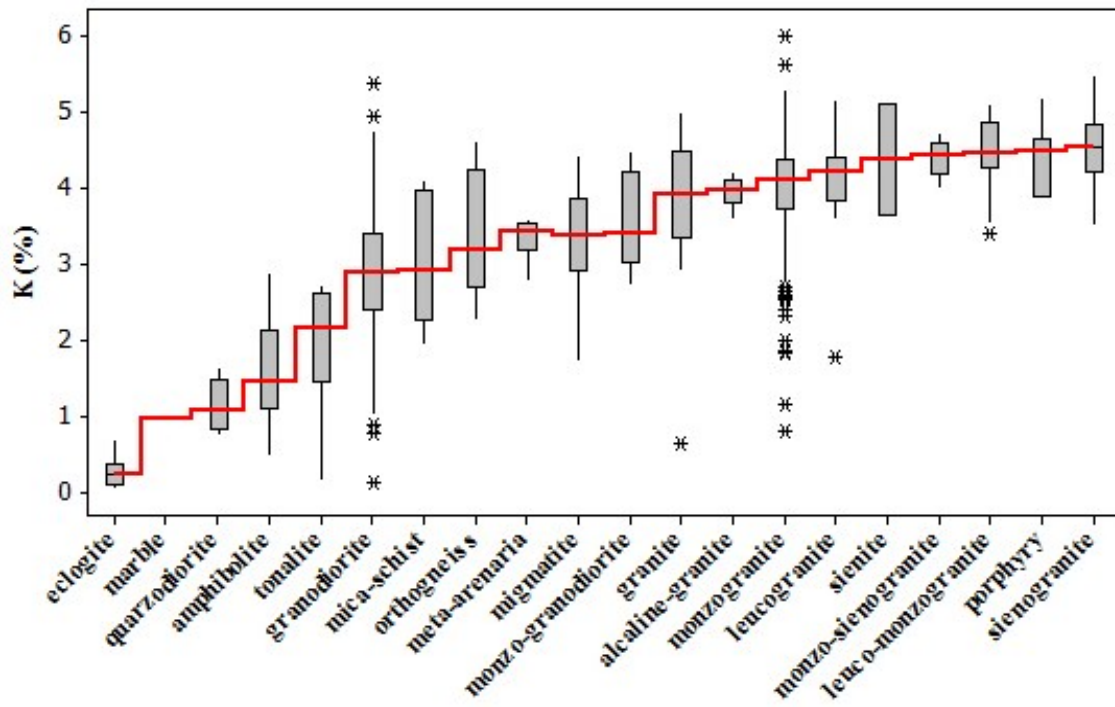


Figure II.2.10: boxplot representation of abundances of potassium (red line joins the median values).

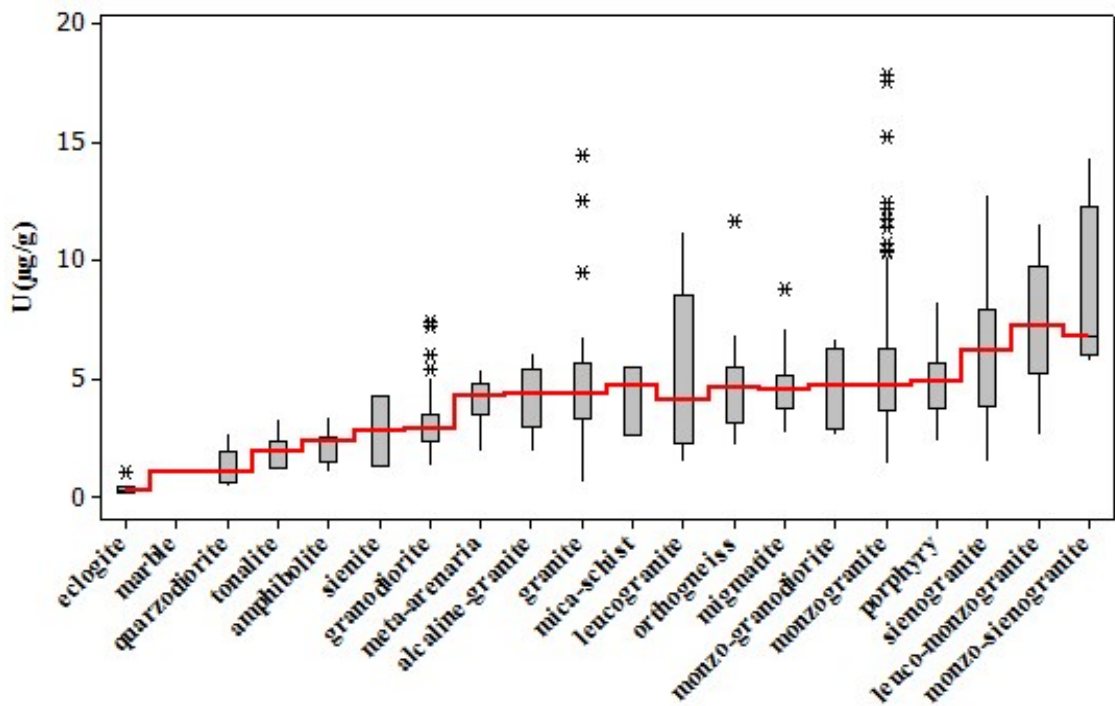


Figure II.2.11: boxplot representation of abundances of uranium (red line joins the median values).

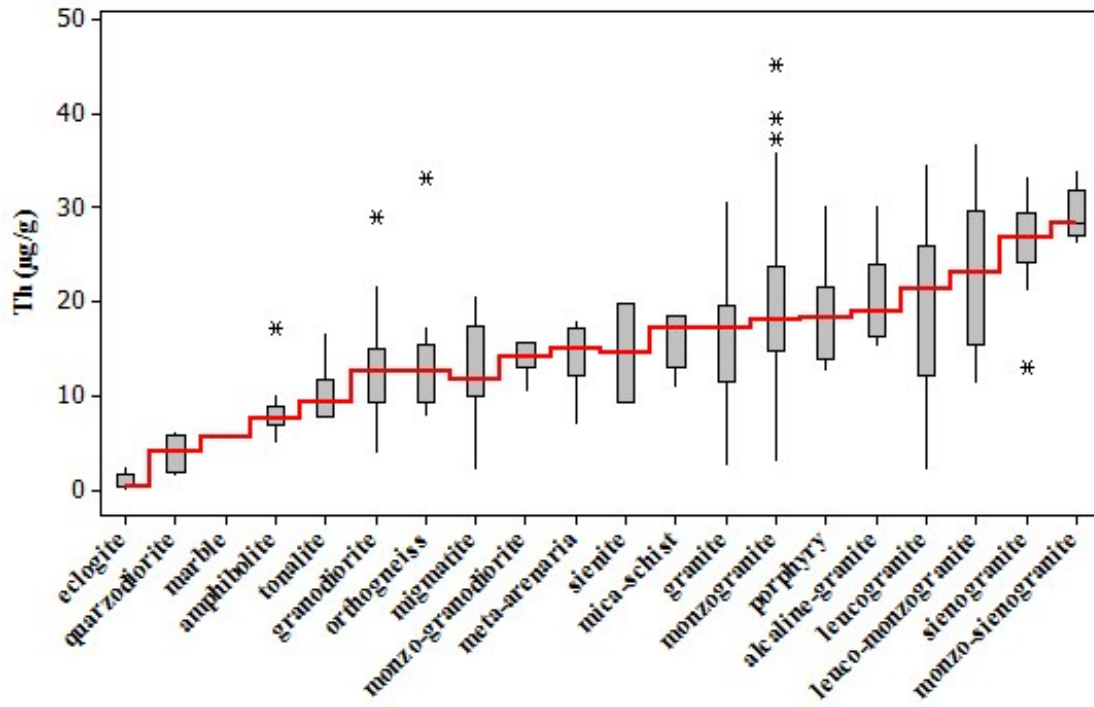


Figure II.2.12: boxplot representation of abundances of thorium (red line joins the median values).

Therefore, a more detailed study performed based on bibliographic data (Appendix A) on elemental composition (SiO₂ content) of the most representative rocks of the Corsica-Sardinia Batholiths and measured abundances of K, U and Th. In Figure II.2.14, Figure II.2.15 and Figure II.2.16 show a slight correlation between SiO₂ content and the K, U, Th abundances.

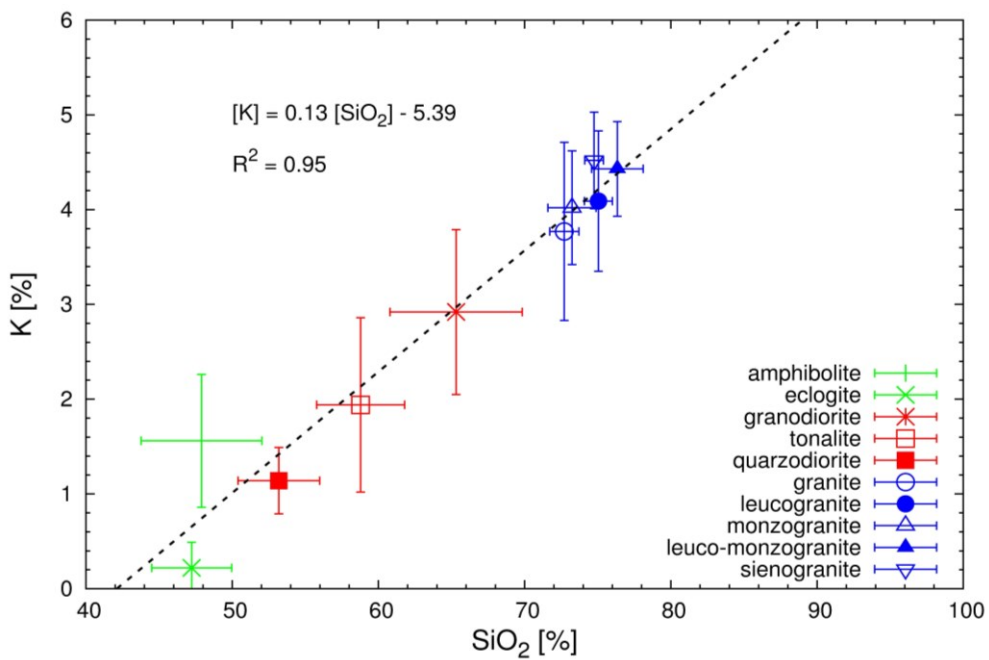


Figure II.2.14: correlation between SiO₂ and K content in Sardinia Batholith.

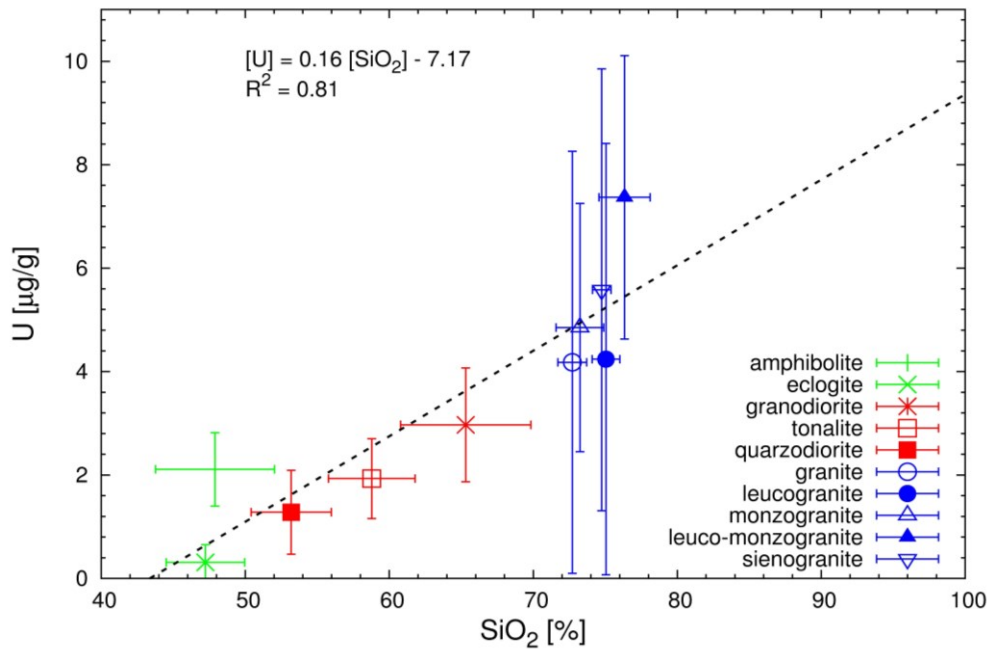


Figure II.2.15: correlation between SiO₂ and U content in Sardinia Batholith.

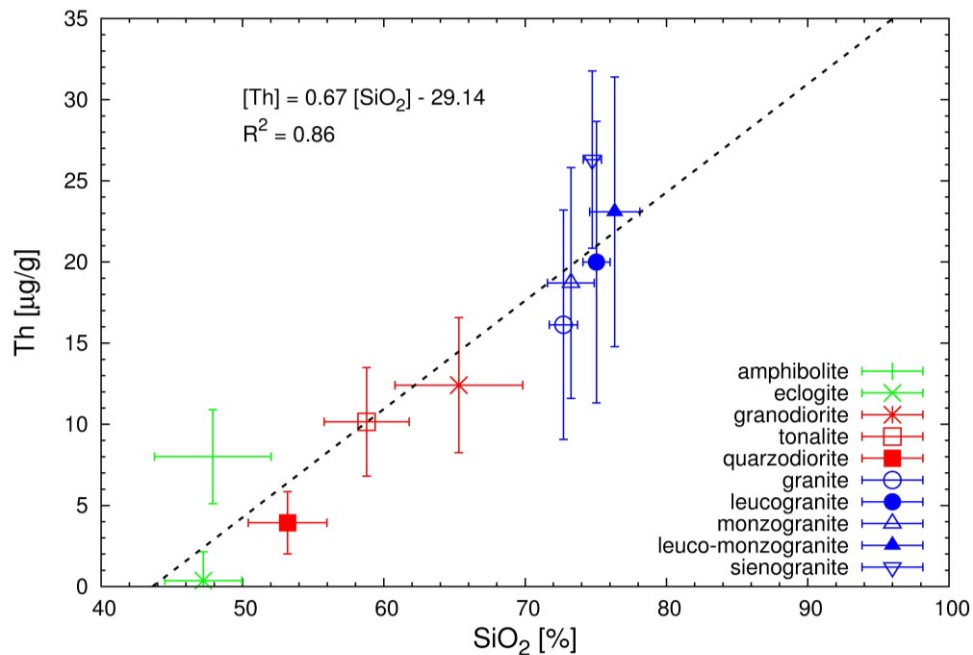


Figure II.2.16: correlation between SiO₂ and Th content in Sardinia Batholith.

In particular, in some recent studies (**Huang Y, Chubakov V et al. 2013**) and (**R. L. Rudnick and D. M. Fountain 1995**) there are developed studies attempting to understand the composition of earth crust by correlating the SiO₂ content with seismic velocity and the earth's crustal density. In particular, in (**Huang Y, Chubakov V et al. 2013**) the correlation between seismic velocities and SiO₂ (**Figure II.2.13**), are used to

provide constraints on the crustal composition. Therefore, the abundances of U, Th and K were derived for the average continental crust $1.31^{+0.29}_{-0.25}$ $\mu\text{g/g}$ U, $5.61^{+1.56}_{-0.89}$ $\mu\text{g/g}$ Th, and $1.52^{+0.29}_{-0.22}$ wt % K and ratios of Th/U = $4.3^{+1.6}_{-1.0}$, K/U = $11.621^{+3.512}_{-2.516}$ and the data were used to calculate the radiogenic heat production of $6.8^{+1.4}_{-1.1}$ TW.

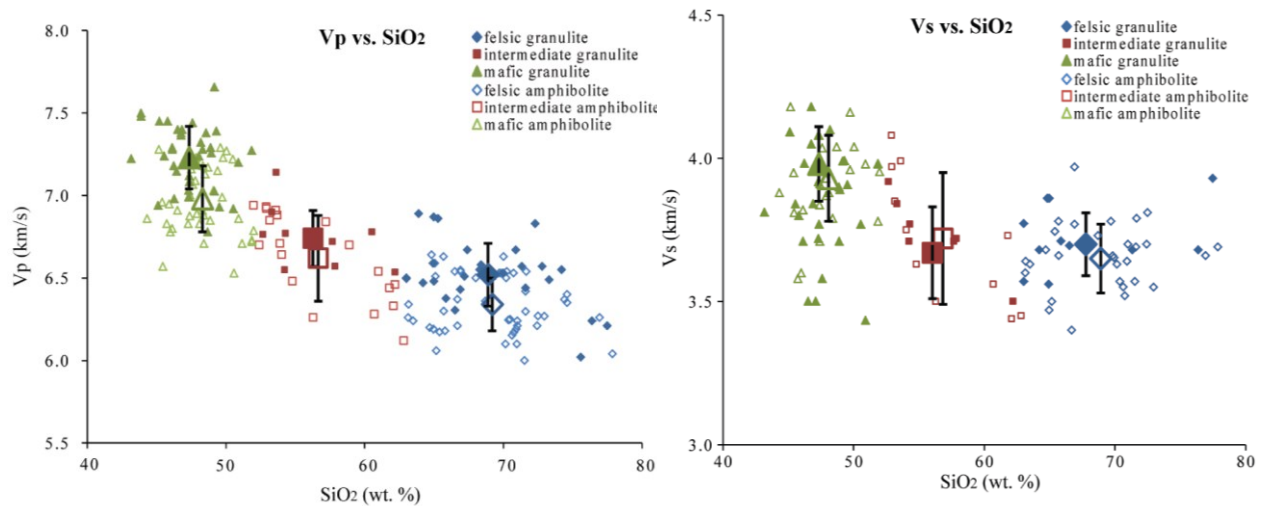


Figure II-2.13: felsic rocks are represented by blue diamonds, intermediate rocks by red squares, and mafic rocks by green triangles. Large symbols represent the means of Vp and Vs for felsic, intermediate and mafic rocks, and error bars represent the 1-sigma uncertainties. Vp and Vs generally decrease with increasing SiO₂ contents for both amphibolite and granulite facies rocks. (Figure from (Huang Y, Chubakov V et al. 2013).)

II.2.3 The distribution of abundances of ⁴⁰K, U and Th and ternary map

Geological reclassification and mapping

The mean values of abundances of each rock type (Table II.2.3) are used to characterize the cartographic units of the geologic map and to reclassify them by using ESRI ArcGIS® 9.3. In order to avoid arbitrary classes and any distribution of input data, we chose percentiles which are simply based on order statistics (C. Raimann 2005a). The activity concentration maps were constructed choosing five percentiles almost evenly spread across the range of values (Figure II.2.20, Figure II.2.21 and Figure II.2.22). The variability within a certain geological group is accurately estimated and it can be used as a prescription for how to read the legend of the map. In any case, the 1σ uncertainty of ⁴⁰K, ²³⁸U and ²³²Th content is included in the adjacent ranges of percentile respectively for 80%, 50% and 50% of geological formations (Figure II.2.20, Figure II.2.21 and Figure II.2.22). Only 25% of cartographic units of uranium, and 10% for thorium, shows a variation that exceeds the range of two adjacent percentiles, confirming a satisfactory degree of robustness on the choice of percentile ranges.

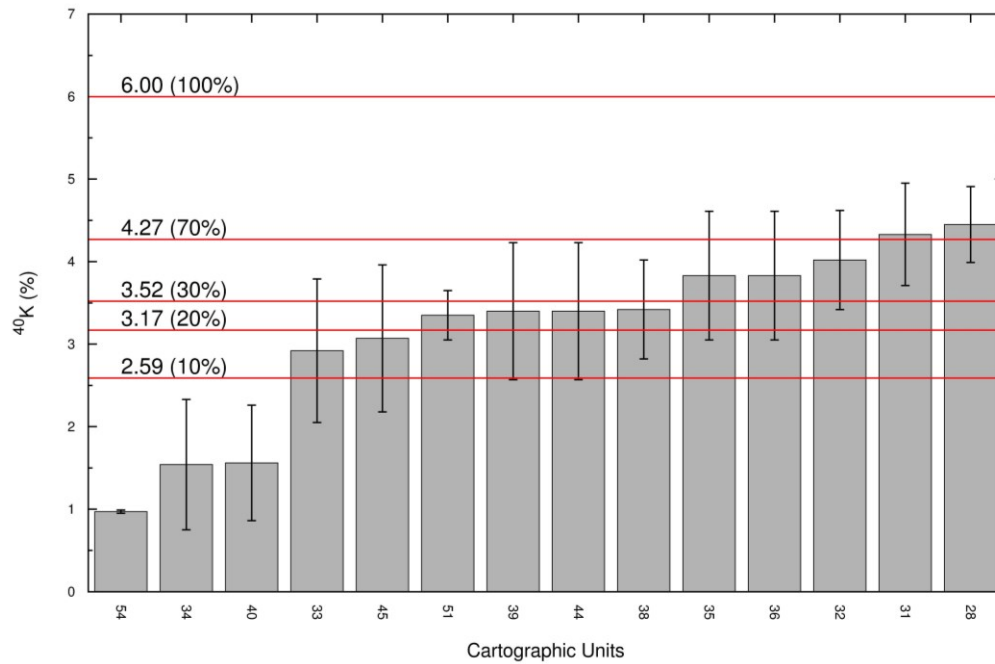


Figure II.2.20: the mean abundance concentration of ^{40}K (in %) for 12 cartographic units together with 1σ standard deviation. Horizontal lines represent the class limits and in brackets percentiles chosen in order to construct the map.

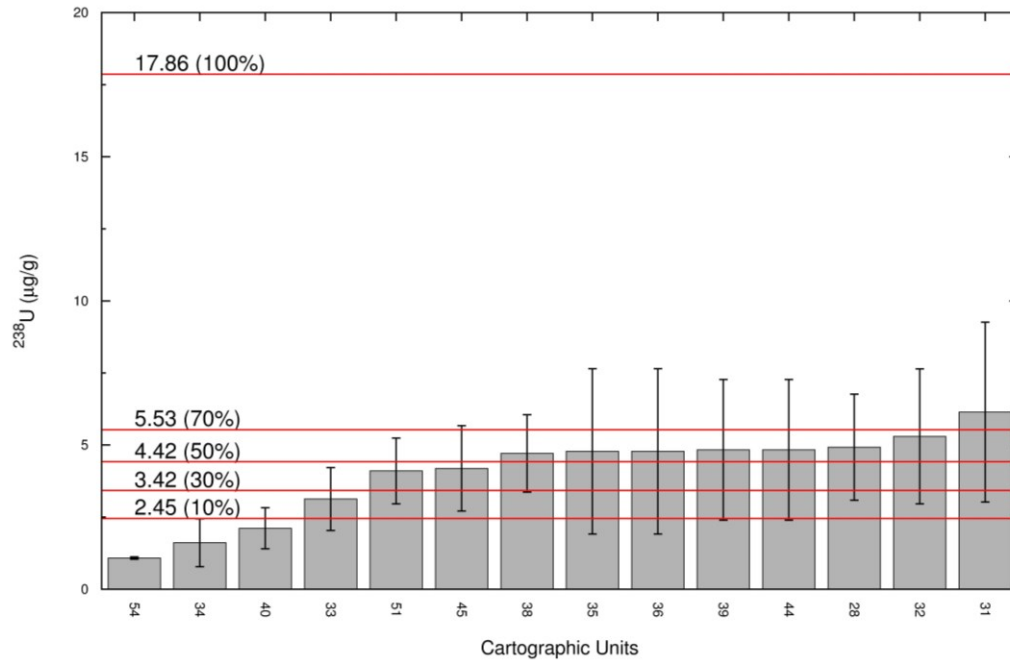


Figure II.2.21: the mean abundance concentration of ^{238}U (in µg/g) for 12 cartographic units together with 1σ standard deviation. Horizontal lines represent the class limits and in brackets percentiles chosen in order to construct the map.

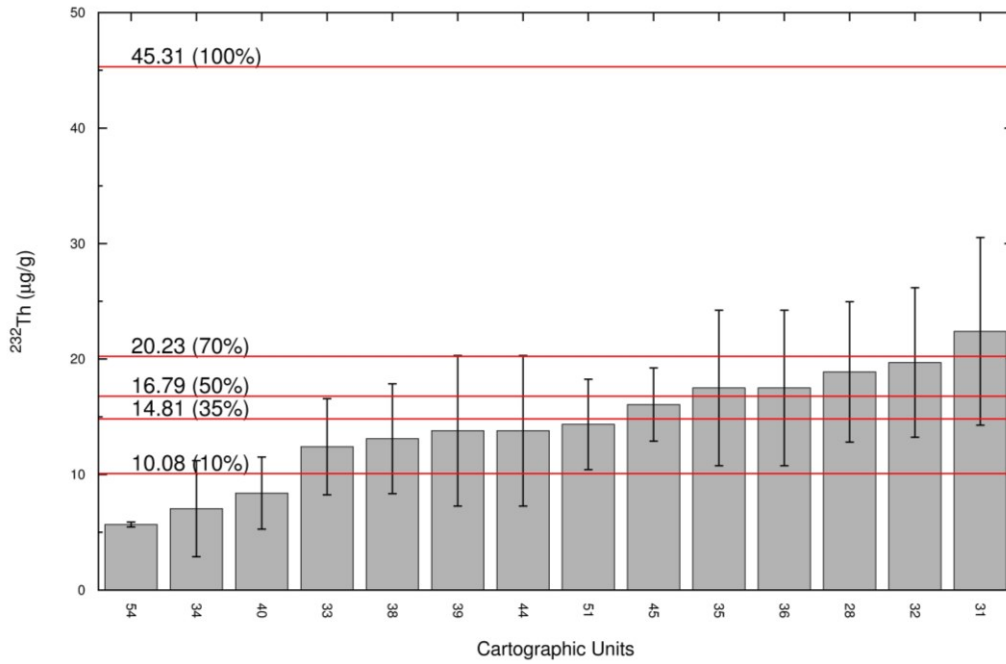


Figure II.2.21: the mean abundance concentration of ²³²Th (in µg/g) for 12 cartographic units together with 1σ standard deviation. Horizontal lines represent the class limits and in brackets percentiles chosen in order to construct the map.

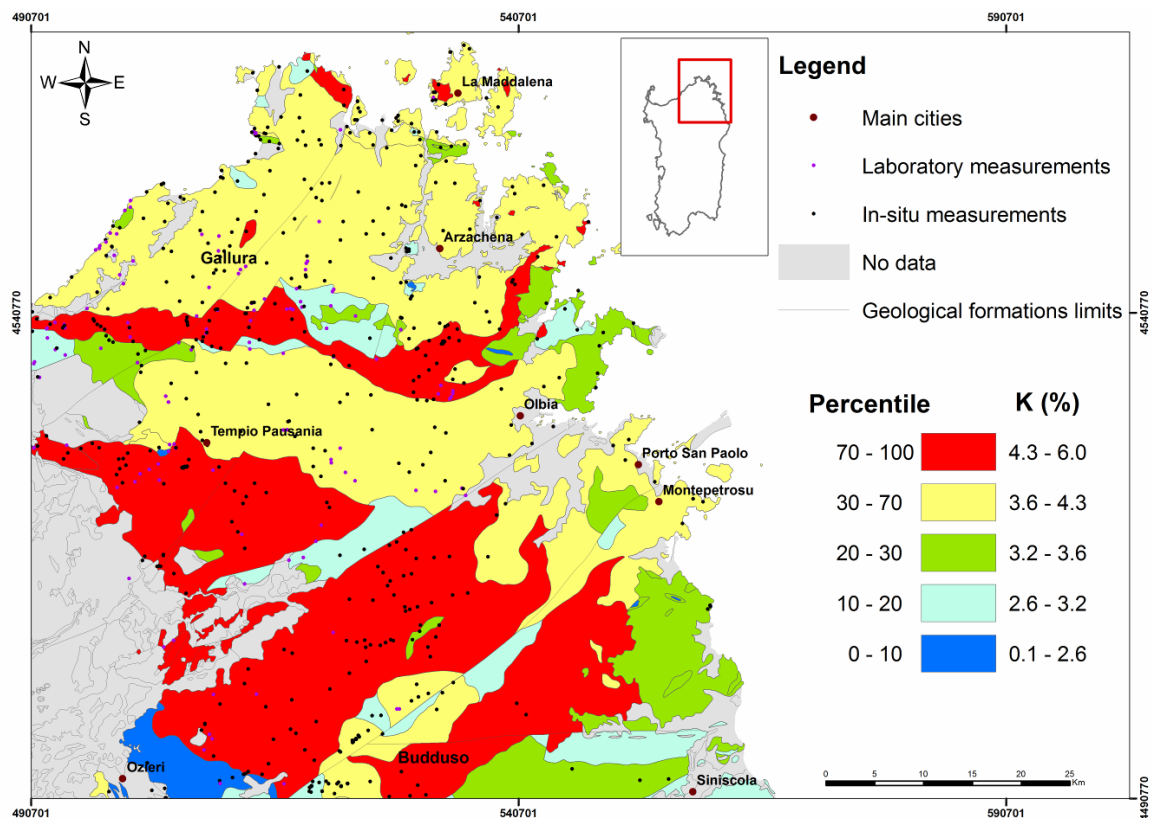


Figure II.2.22: map of concentration ⁴⁰K (%) in the N-E Sardinia Batholith obtained by reclassification of 12 cartographic units.

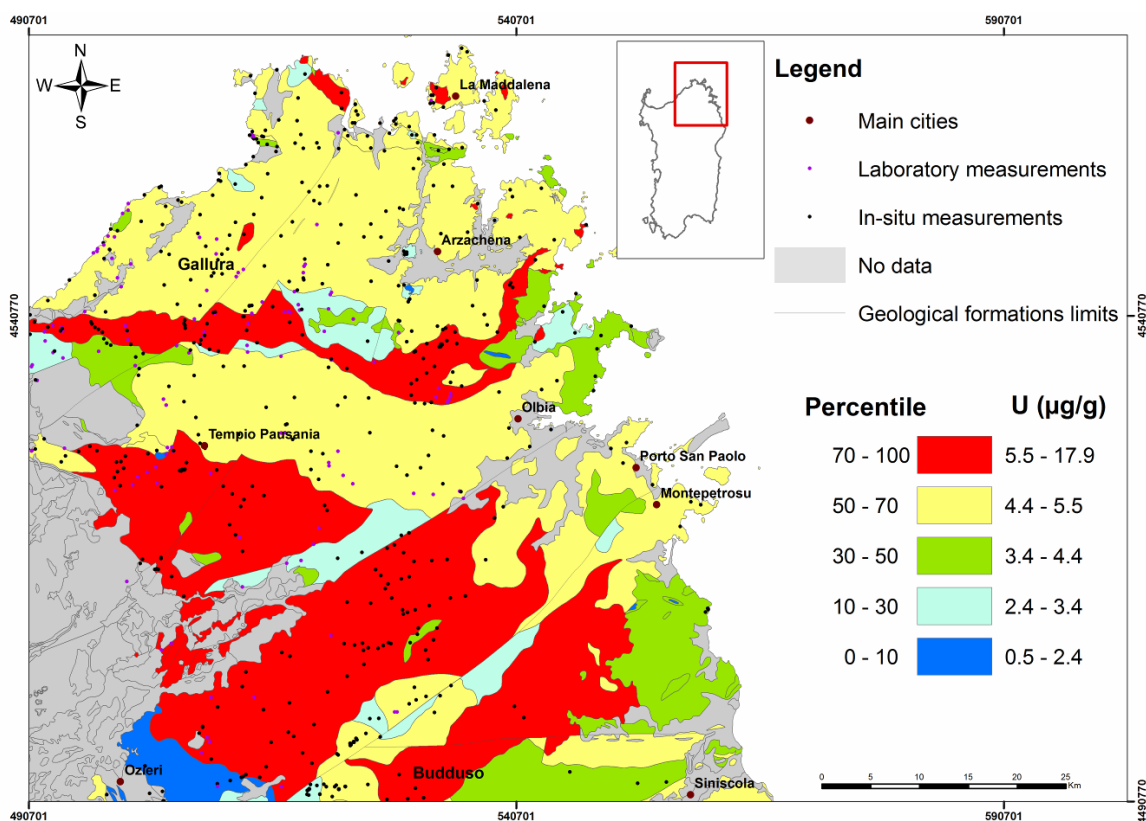


Figure II.2.23: map of concentration ^{238}U ($\mu\text{g/g}$) in the N-E Sardinia Batholith obtained by reclassification of 12 cartographic units.

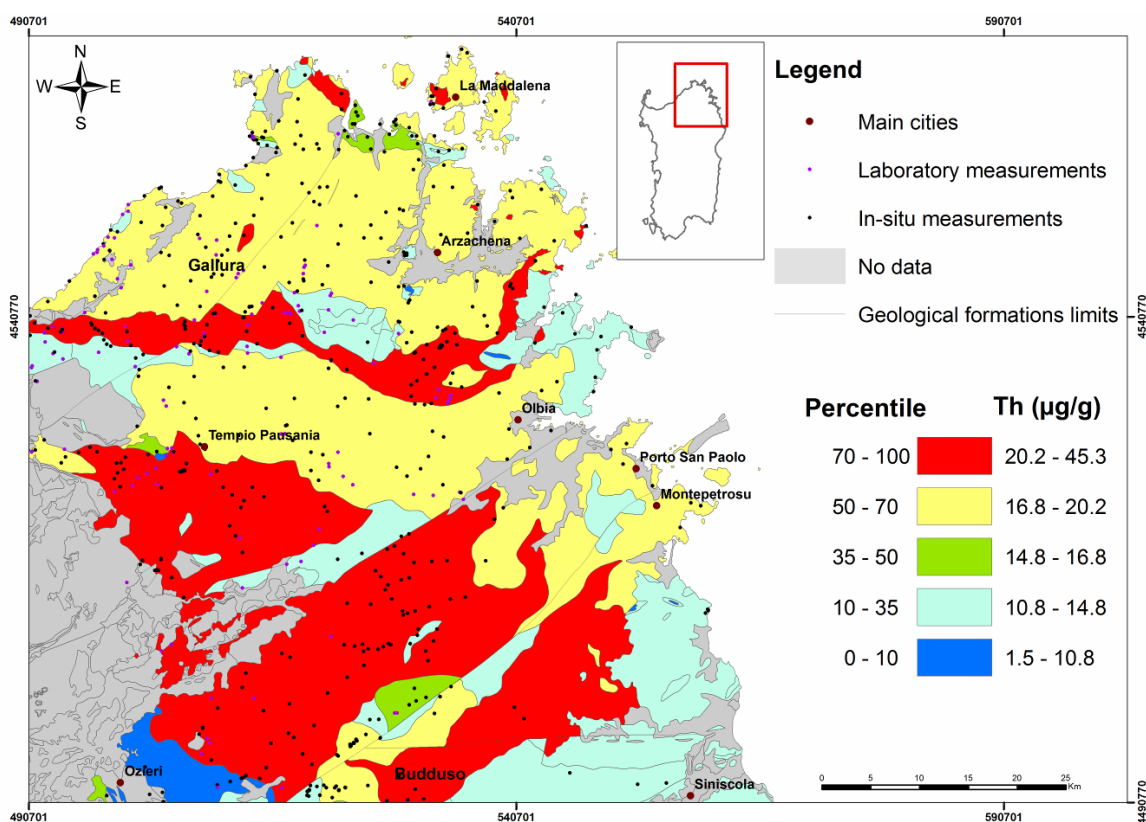


Figure II.2.24: map of concentration ^{232}Th ($\mu\text{g/g}$) in the N-E Sardinia Batholith obtained by reclassification of 12 cartographic units.

From the reclassified maps we can easily distinguish from the mean values of abundances of ^{40}K , U and Th that amphibolites, tonalites and quartzodiorites are characterized by the lowest abundances while leucogranites are characterized by the highest abundances in accordance with the results reported in **Table II.2.3**. The classes of radioactivity include rocks having similar radioactivity content and give a good first representation of the radioactivity distribution also in the cases when the sampling methodology doesn't satisfy the necessary criteria for using geostatistical interpolation. Again we see a clear correlation between radioelements, observed also from the homogeneity of ratios Th/U, K/U and K/Th (**Table II.2.3**). It is important to emphasize that even some particular cartographic units are grouped in a distinct radioactivity class the variation of radioactivity can be extended to the neighbor class. Therefore the distinction between monzogranites and leucogranites, which are the more extended cartographic units, must be considered smoothed because this variation. In particular the higher radioactivity content in leucogranites can be explained due to a non small presence of peraluminous leucogranites, which are rich with alkali content and therefore rich in potassium. We can also observe the leucogranites are richer in uranium and thorium content.

Geostatistical data analysis and mapping

In order to better estimate the variability within each cartographic unit, a geostatistical approach was used for the spatial distribution of the radiometric data through ESRI ArcGIS® 9.3. In Geostatistics each measured value, $z(x_n)$, at location x_n (x is the location coordinates vector and $n = 1, 2, \dots, m$ are the sampling points) is interpreted as a particular realization, or outcome, of a random variable $Z(x_n)$, where the set of dependent random variables $\{Z(x_n), n = 1, 2, \dots, m\}$ constitutes a random function $Z(x)$. For a detailed presentation of the theory of random functions, interested readers should refer to the works of (**P. Goovaerts 1997**), (**J-P. Chiles and P. Delfiner 1999**), (**R. Webster and M. A. Oliver 2007**), (**H. Wackernagel 2003**) among others. In **table II.2.5** are shown the descriptive statistical parameters of our radiometric data.

Table II.2.5: descriptive statistical parameters of radiometric data.

Variable	^{40}K (%)	^{238}U ($\mu\text{g/g}$)	^{232}Th ($\mu\text{g/g}$)
Counts ^a	701	701	701
Minimum	0.1	0.5	1.5
Maximum	6.0	17.9	45.3
Mean	3.8	4.9	18.0
Std. Dev.	0.9	2.4	7.1
Median	4.0	4.4	16.8
Variance	0.8	5.8	50.3
Kurtosis	2.1	3.5	0.2
Skewness	-1.2	1.5	0.6

^a for the spatial distribution analysis 11 eclogite samples were not considered.

An important tool in geostatistics is the experimental variogram, which is a quantitative measure of spatial correlation of the regionalized variable $z(x_n)$. The experimental variogram $\gamma(h)$ is a function of the lag h , a vector in distance and direction, of data pair values $[z(x_n), z(x_n+h)]$; it refers to the expected value of the squared differences; a way of calculating this is reported in **Eq. (II.2.1)**:

$$\gamma(h) = \frac{1}{2N(h)} \sum_{n=1}^{N(h)} [z(x_n) - z(x_n + h)]^2 \quad (\text{II.2.1})$$

where $N(h)$ is the number of data pairs for the specified lag vector h .

A theoretical function, known as the variogram model, is fitted to the experimental variogram to allow one to estimate the variogram analytically for any distance h . The aim is to build a model that describes the major spatial features of the attribute under study. In the former models the variance has a maximum (known as the sill variance) at a finite lag distance (range) over which pairs of values are spatially correlated. The best fitting function can be chosen by cross-validation, which checks the compatibility between the data and the model. It takes each data point in turn, removing it temporarily from the data set and using its neighboring information to predict the value of the variable at its location. The estimate is compared with the measured value by calculating the experimental error, i.e. the difference between estimation and measurement, which can also be standardized by estimating the standard deviation. The goodness of fit was evaluated by the mean error and the mean squared deviation ratio. The Mean of Standardized Errors (MSE) proves the un-biasedness of the estimate if its value is close to zero:

$$MSE = \frac{1}{m} \sum_{n=1}^m [z^*(x_n) - z(x_n)] \quad (\text{II.2.2})$$

where n is the number of observation points, $z^*(x_n)$ is the predicted value at location x_n , and $z(x_n)$ is the observed value at location x_n . The Mean Squared Variance Ratio (MSVR) is the ratio between the squared errors and the kriging variance $\sigma^2(x_n)$:

$$MSVR = \frac{1}{m} \sum_{n=1}^m \frac{[z^*(x_n) - z(x_n)]^2}{\sigma^2(x_n)} \quad (\text{II.2.3})$$

If the model for the variogram is accurate, the mean squared error should equal the kriging variance and the MSVR value should be unity. After selecting an appropriate variogram model (**Table II.2.6**), the parameters can be used with the data to predict radioactivity at unsampled locations using a kriging algorithm (**Figure II.2.25**, **Figure II.2.26** and **Figure II.2.27**). The classes were chosen as described above by taking the same percentiles (**Figure II.2.20**, **Figure II.2.21** and **Figure II.2.22**).

Table II.2.6: parameters of the model fitted on omnidirectional variograms calculated with 8 lags of 4000 m for ^{40}K , 10 lags of 2500 m for ^{238}U and 8 lags of 3000 m for ^{232}Th ; range and variability (sills) of each structure of the model are shown. Cross-validation results of the fitted model; Mean of Standardized Errors (MSE) and Mean Squared Variation Ratio (MSVR) of errors for all variables.

Variable	Model description			Cross-validation	
	Type of structures of variability	Range (m)	Sill	MSE	MSVR
^{40}K (%)	Nugget effect	-	$0.3\ \mu\text{g/g}^2$	$0.8\ 10^{-2}$	0.97
	Spherical model	19122	$0.4\ \mu\text{g/g}^2$		
^{238}U ($\mu\text{g/g}$)	Nugget effect	-	$1.6\ \mu\text{g/g}^2$	$0.2\ 10^{-4}$	1.17
	Spherical model	10000	$4.5\ \mu\text{g/g}^2$		
^{232}Th ($\mu\text{g/g}$)	Nugget effect	-	$15.5\ \mu\text{g/g}^2$	$0.6\ 10^{-2}$	1.02
	Spherical model	10531	$31.4\ \mu\text{g/g}^2$		

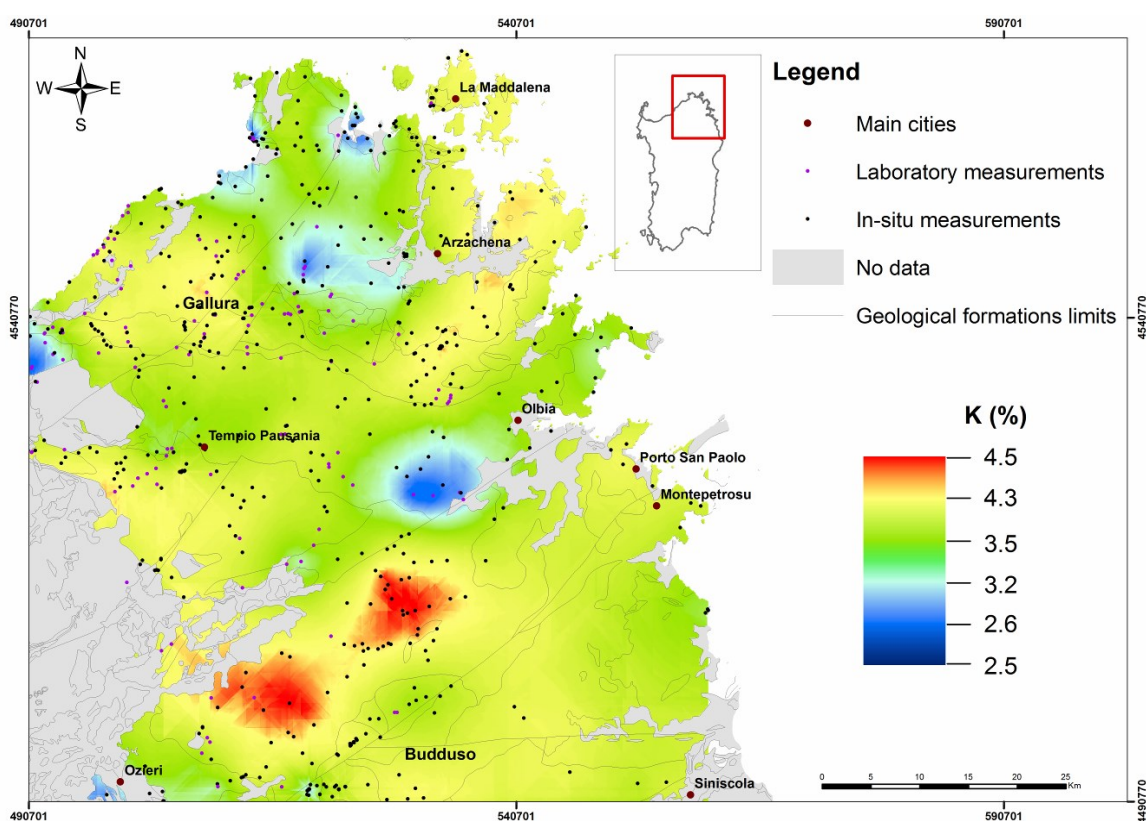


Figure II.2.25: map of concentration of ^{40}K (%) in the N-E Sardinia Batholith.

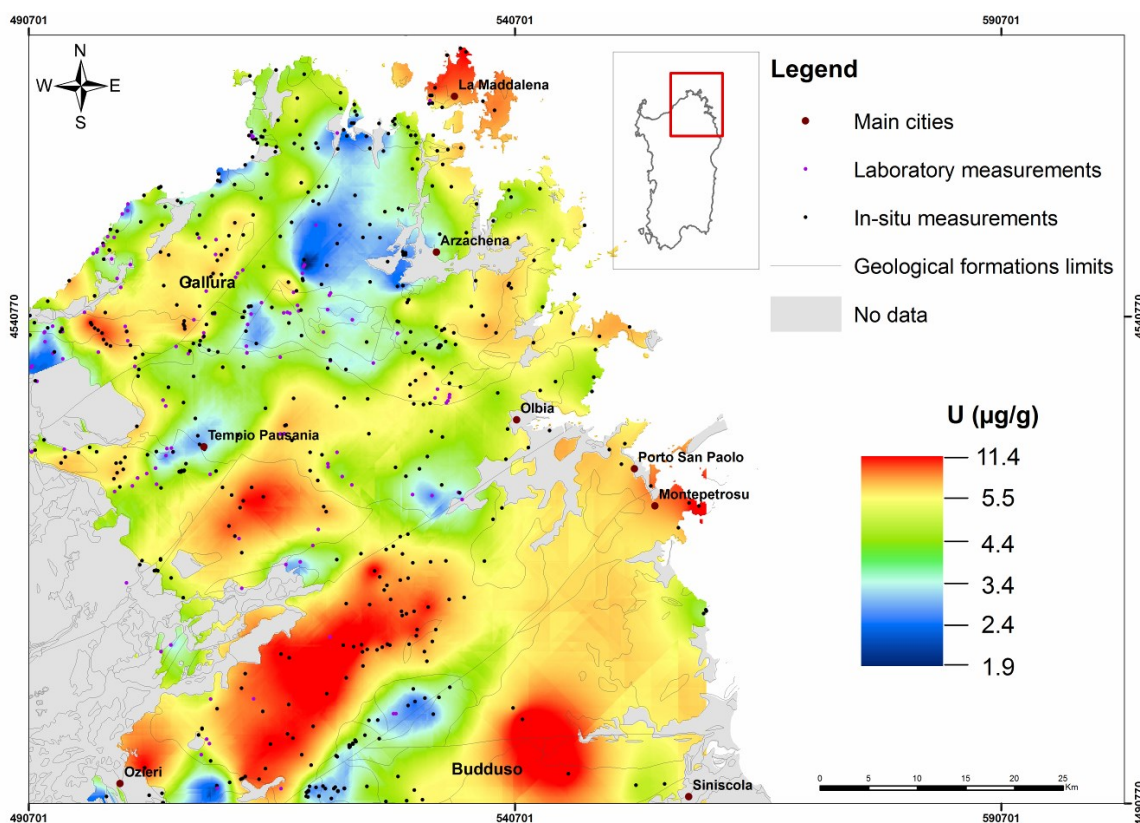


Figure II.2.26: map of concentration of ^{238}U ($\mu\text{g/g}$) in N-E Sardinia Batholith.

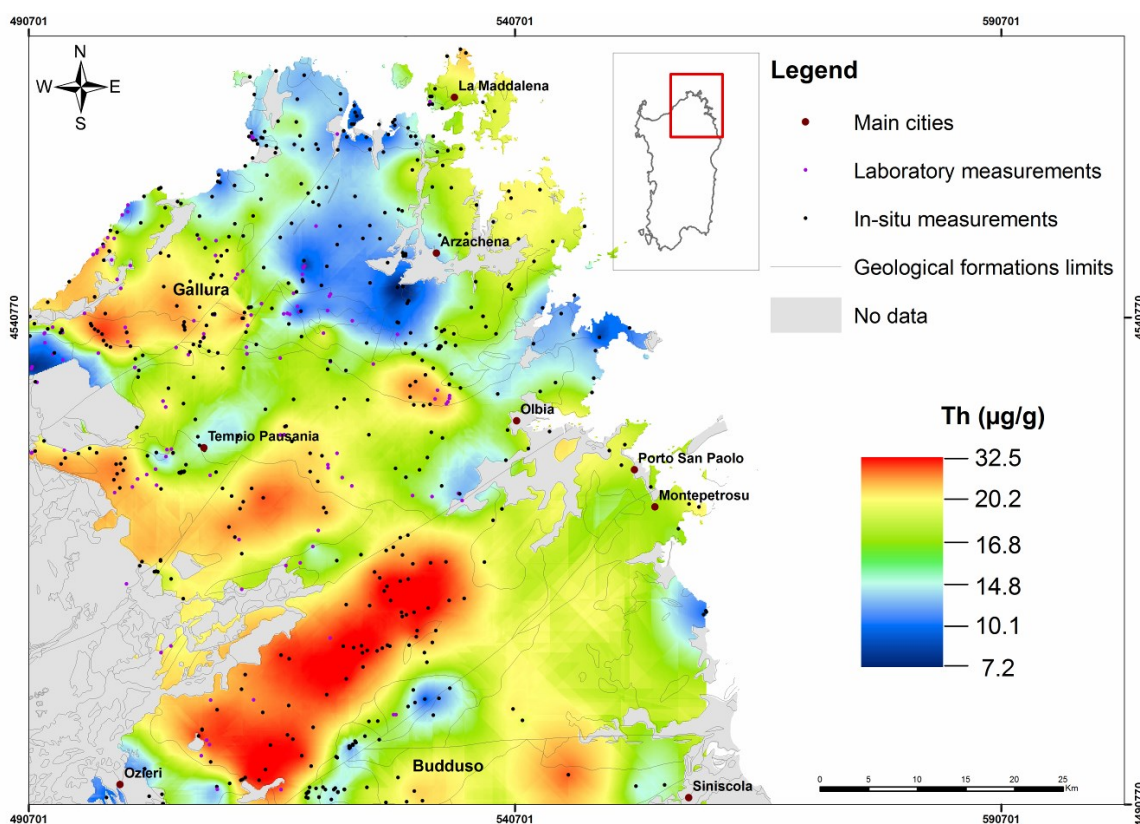


Figure II.2.27: map of concentration of ^{232}Th ($\mu\text{g/g}$) in N-E Sardinia Batholith.

We see a good agreement between the K, U and Th maps realized through the geological reclassification and through geostatistical interpolation, evidencing the homogeneity of the radioactivity content for different rock types (**Table II.2.3**). As it is expected, leucogranites show the highest activity concentration, showing a good agreement with the geological map (for Buddusò and Tempio Batholith), where we can easily identify the geological limits of leucogranites which seem to be quite homogeneous in radioactivity concentration. While leucogranites of Arzachena and Gallura Batholith, still show the presence of high values but with greater dis-homogeneity. The leucogranites of Buddusò Batholith evidences an anomaly of high K content, probably evidencing the presence of geological structure not evidenced in the geological map, probably alkali rich leucogranites.

On the other hand monzogranites show a high variability both in Tempio and Gallura Batholiths. However, it seems to be a slight correlation between the activity concentration and the intense presence of acid and basic dykes in this area. The lower concentration of radioactivity is found East corresponding to the presence of basic dykes and the highest concentration are found west corresponding with the presence of acid dykes. These results, gives an overview of the geological structure of N-E Sardinia Batholith showing a good correspondence between the radioactivity distribution and geology and revealing new insights on the geological structure which can help for future geochemical and geological studies.

Ternary map

The ternary radioelement map gives a color composite image generated by modulating the red (potassium), green (thorium) and blue phosphors (uranium) in proportion to the radioelement concentration values of the K, Th, U grids (**Fig. II.2.25**, **Fig. II.2.26** and **Fig. I.2.27** respectively). The sum-normalization can be used to compute relative concentrations of K, Th and U (self-normalized concentrations) prior to imaging as follows:

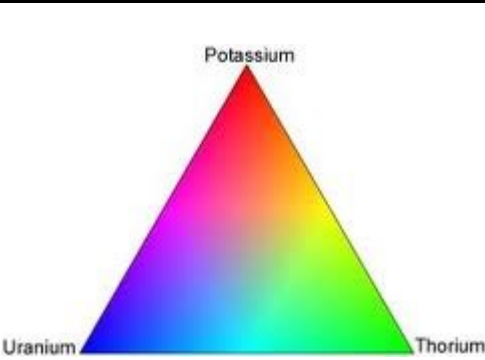
$$K_{norm} = \frac{K}{K + U + Th}$$

$$U_{norm} = \frac{U}{K + U + Th} \tag{II.2.4}$$

$$Th_{norm} = \frac{Th}{K + U + Th}$$

In this way the color legend can be read indicatively like summarized in **Table II.2.7**:

Table II.2.7: ternary legend characterization.

Ternary legend			K_{norm}	U_{norm}	Th_{norm}
	red		high	low	low
	blue		low	high	low
	green		low	low	high
	cyan		low	high	high
	magenta		high	high	low
	yellow		high	low	high
	black		low	low	low
	white		high	high	high

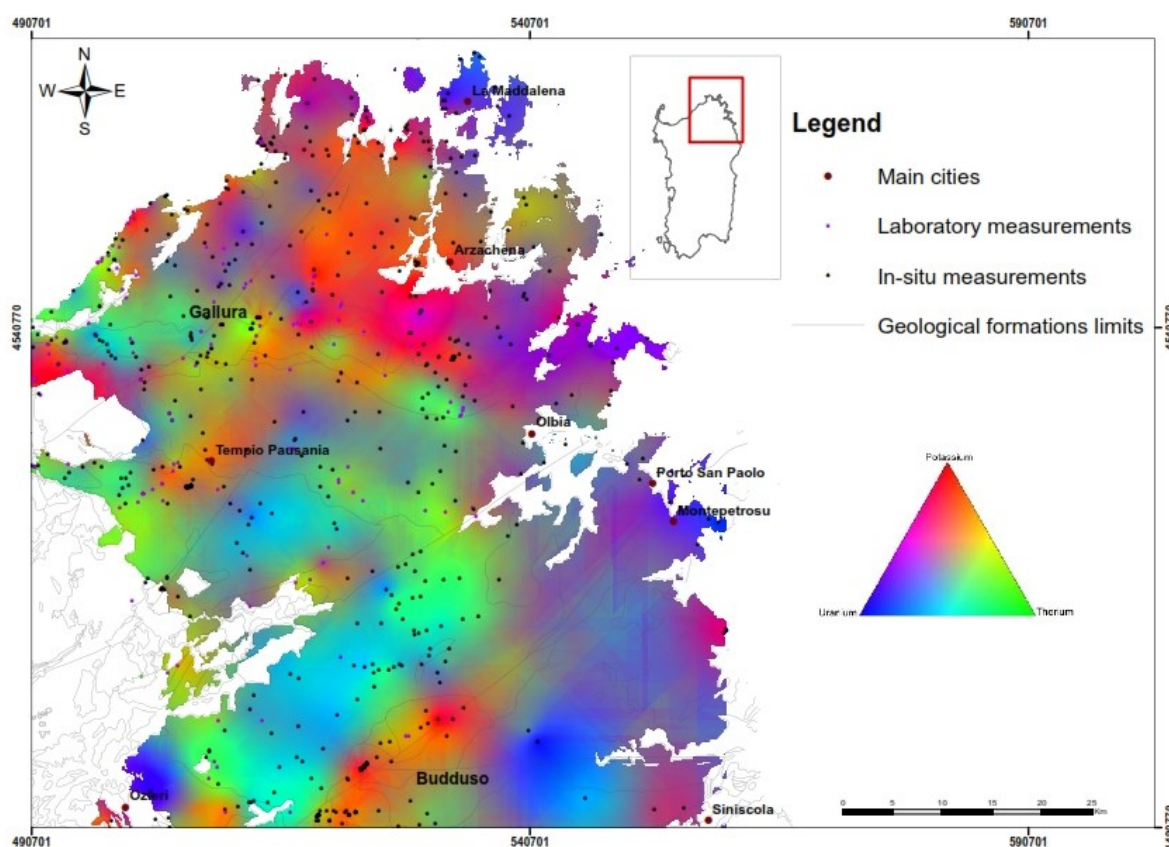


Figure II.2.28: radiometric ternary map (Red: K; Green: Th; Blue: U) of the N-E Sardinia Batholith.

In particular, low K values associate with leucogranites from Budduso batholith (particularly rich in uranium and thorium) confirming with the radiometric maps (Fig. II.2.25, Fig. II.2.26 and Fig. II.2.27). It is also possible to distinguish areas of low Th values (magenta) extended in east Sardinia. The variability of color tones in north Sardinia reflects the felsic and basic dyke intrusions and hydrothermal alterations with low thorium and particularly rich potassium. In particular, while the areas around La Madalena and Olzeri confirm the high U (blue) values (Fig. II.2.26).

II.2.4 Preliminary study of radiogenic heat generation from upper crust

The thermal structure of the continental crust is, undoubtedly, the main parameter that controls all geological processes occurring inside the crust as metamorphism, magmatism and deformation. The radiogenic heat, mainly due to the decay (chains) of ^{238}U (^{235}U), ^{232}Th and ^{40}K is an important contribution to the thermal budget, since these elements are concentrated in large quantities in the crust (especially in the upper and middle crust) and therefore contribute significantly to the (C. Jaupart and J-C. Marescha 2003).

The heat production rate is calculated by subtracting from the Q value the energy of anti-neutrinos averaged over the whole spectrum. In the case of ^{238}U and ^{232}Th chains the average anti-neutrino energy is about 8% and 6% of the total available energy: an error of 10% in the calculation of the energy is sufficient to determine the elemental heat production to better the 1% (G. Fiorentini, M. Lissia et al. 2007). For this reason in the literature individual determinations of beta spectra have not been used to determine neutrino energy loss. Instead, the approximate relationship that, on average, neutrinos carry 2/3 of the decay energy of beta decay has been applied (R. W. Van Schmus 1995). Table II.2.8 presents the specific heat production rate values for uranium, thorium and potassium calculated in various studies. In general the calculated coefficients of specific heat production rates agree within similar studies approximating the anti-neutrino energy: the coefficients from (L. Rybach 1988) are the most used in literature. More precise calculations on specific heat production rates (G. Fiorentini, M. Lissia et al. 2007), (S. T. Dye 2011), (S. Enomoto, E. Ohtani et al. 2007) gives heat roduction values differ at the approximately 4% level. For our study we will consider the coefficients calculated in (G. Fiorentini, M. Lissia et al. 2007): the radiogenic heat generation can be calculated as,

$$A (\mu\text{W} / \text{m}^3) = \rho(9.85C_U + 2.64C_{Th} + 3.33C_K) \times 10^{-5} \quad (\text{II.2.5})$$

where C_U , C_{Th} in $\mu\text{g/g}$ and C_K in % are the abundances of U, Th and ^{40}K , and ρ is the density in kg/m^3 giving the radiogenic heat generation A is given in $\mu\text{W/m}^3$.

Table II.2.8: specific heat production rate values for uranium, thorium and potassium.

References	HPR _U (W/kg) 10 ⁻⁵	HPR _{Th} (W/kg) 10 ⁻⁵	HPR _{40K} (W/kg) 10 ⁻⁹
(E. C. Bullard and F. R. S 1942)	-	2.65	1.61
(F. Birch 1954)	9.7	2.7	3.6
(H. C. Urey 1955)	9.73	2.6	3.53
(V. M. Hamza and A. E. Beck 1972)	9.77	2.63	3.4
(L. Rybach 1988)	9.52	2.56	3.48
(G. R. Beardsmore and J. P. Cull 2001)	9.67	2.63	3.5

(R. W. Van Schmus 1995)	9.81	2.64	3.45
(S. Enomoto 2005)	-	2.628	3.38
(G. Fiorentini, M. Lissia et al. 2007)	9.85	2.64	3.33
(S. T. Dye 2011)	9.85	2.63	3.33

In **table II.2.9** are shown the average radionuclides concentration and radiogenic radiogenic heat generation for various rock types. The radiogenic heat production rate for various types of rock range from $0.20^{+0.22}_{-0.09} \mu\text{W}/\text{m}^3$ (eclogite) to $4.87 \pm 1.00 \mu\text{W}/\text{m}^3$ (monzo-sienogranite). These results are comparable with other studies in Corsica-Sardinia batholith (**M. Verdoya, V. Pasquale et al. 1998**) were are reported radiogenic heat production rate vary from $0.2 \mu\text{W}/\text{m}^3$ (basalts) to $4.2 \mu\text{W}/\text{m}^3$ (calc-alkaline granites). Furthermore, studies from Iberian Massif, Bohemian Batholith show also comparable values ranging from granitic rocks ($2.5\text{-}3.5 \mu\text{W}/\text{m}^3$). While, as discussed in **Section II.1.2** typically high radiogenic heat production usually between $4\text{-}10 \mu\text{W}/\text{m}^3$ are reported in the Variscan Erzgebirge (Germany) granites (**A. Forster and H. J. Forster 2000**). In (**O. Lexa, K. Schulmann et al. 2011**) the exhumation of c. 340 Ma felsic granulites in the Bohemian Massif is modeled by attributing to the lower crust a high radioactive heat production of $4 \mu\text{W}/\text{m}^3$, typical of Ordovician felsic igneous rocks in the Fichtelgebirge (Saxothuringian domain), which are believed to have been relaminated at the bottom of thickened continental crust during the early Viséan continental underthrusting.

In a first approximation, we calculated the surface heat flow rate generated from the upper crust due to the presence of the isotope of ^{40}K , U and Th assuming a constant upper crust thickness:

$$H_{rad} (mW / m^2) = A \times h \quad \text{(II.2.6)}$$

The best approximation for the upper crustal thickness for N-E Sardinia can be derived from (**I. R. Finetti 2005**). The M2A/I is the only transcrustal seismic reflection section that crosses uninterrupted the entire Corso-Sardinia block from the Balearic sea to the Tyrrhenian basin (**Figure II.2.29**). The interpreted seismogeological section here present can considered of satisfactory reliability with regard to its fundamental crust stratigraphic and macro-tectonic setting. The Corso-Sardinia block present three distinct tectono-crustal zones: (1) an internal one, thinned and affected by transcrustal listric faults (Rf-1 to 6), connected with the opening of the Balearic back-arc basin (SP 3200-4600), giving with a good approximation a upper crust thickness of about 5 km; (2) a thicker crustal zone corresponding to the central Corso-Sardinia block area (roughly SP 4600-7200); (3) a Terrhenian margin zone, prominently stretched and delaminated (SP 7200-10450). This thinned continental zone terminates on the Selli line (some 13 km southeast of SP 10450) where the Tyrrhenian Sea floored by oceanic crust opens.

Table II.2.9: characterization of investigating rock types for the abundances of K (%), U ($\mu\text{g/g}$) and Th ($\mu\text{g/g}$) within 1σ standard deviation and the heat production rate A in $\mu\text{W/m}^3$.

rock-type	No.	K (%)	U ($\mu\text{g/g}$)	Th ($\mu\text{g/g}$)	ρ (kg/m^3)	a ($\mu\text{W/kg}$) ($\times 10^{-4}$)	A ($\mu\text{W/m}^3$)
monzogranite	446	4.02 \pm 0.60	4.85 $^{+2.40}_{-1.62}$	18.70 $^{+7.11}_{-5.17}$	2750	11.0 $^{+3.0}_{-2.3}$	3.12 $^{+0.83}_{-0.63}$
granodiorite	87	2.92 \pm 0.87	2.97 $^{+1.10}_{-0.81}$	12.41 \pm 4.16	2750	9.1 $^{+2.6}_{-2.0}$	2.51 $^{+0.71}_{-0.55}$
migmatite	25	3.42 \pm 0.60	4.55 $^{+1.40}_{-1.07}$	13.10 \pm 4.76	2750	9.1 $^{+1.8}_{-1.7}$	2.52 $^{+0.51}_{-0.46}$
granite	21	3.77 \pm 0.94	4.18 $^{+4.08}_{-2.07}$	16.13 \pm 7.07	2750	9.9 $^{+4.3}_{-2.9}$	2.73 $^{+1.16}_{-0.81}$
leucogranite	16	4.09 \pm 0.74	4.24 $^{+4.17}_{-2.11}$	19.99 \pm 8.67	2750	11.0 $^{+4.5}_{-3.3}$	3.07 $^{+1.24}_{-0.91}$
leuco-monzogranite	16	4.43 \pm 0.50	7.37 \pm 2.74	23.09 \pm 8.31	2750	15.0 \pm 3.5	4.08 $^{+0.97}_{-0.95}$
orthogneiss	13	3.31 $^{+0.93}_{-0.73}$	4.40 $^{+2.42}_{-1.56}$	12.78 $^{+5.96}_{-4.02}$	2750	9.1 $^{+2.9}_{-2.1}$	2.51 $^{+0.77}_{-0.56}$
amphibolite	12	1.56 \pm 0.70	2.11 \pm 0.71	8.01 $^{+2.90}_{-2.14}$	3300	4.7 $^{+1.1}_{-1.0}$	1.57 $^{+0.34}_{-0.32}$
eclogite	11	0.22 $^{+0.27}_{-0.12}$	0.31 $^{+0.34}_{-0.16}$	0.37 $^{+1.78}_{-0.31}$	3300	0.6 $^{+0.7}_{-0.3}$	0.20 $^{+0.22}_{-0.09}$
sienogranite	11	4.52 \pm 0.51	5.58 $^{+4.27}_{-2.40}$	26.31 \pm 5.46	2750	14.0 $^{+4.3}_{-2.9}$	3.87 $^{+1.20}_{-0.78}$
alkaline-granite	10	3.96 \pm 0.19	4.16 \pm 1.33	19.85 $^{+5.19}_{-4.16}$	2750	11.0 $^{+1.9}_{-1.7}$	2.95 $^{+0.52}_{-0.48}$
porphyry	7	4.45 \pm 0.46	4.92 \pm 1.84	18.88 \pm 6.08	2750	11.0 \pm 2.4	3.11 \pm 0.67
meta-arenaria	6	3.35 \pm 0.30	4.10 \pm 1.14	14.34 \pm 3.91	2400	8.9 \pm 1.5	2.14 \pm 0.37
monzo-granodiorite	6	3.54 \pm 0.67	4.65 \pm 1.76	14.03 \pm 1.96	2750	9.5 \pm 1.8	2.60 \pm 0.50
quartzodiorite	6	1.14 \pm 0.35	1.28 \pm 0.81	3.93 \pm 1.92	2750	2.7 \pm 1.0	0.73 \pm 0.26
tonalite	6	1.94 \pm 0.92	1.93 \pm 0.77	10.15 \pm 3.35	2750	5.2 \pm 1.2	1.44 \pm 0.33
mica-schist	5	3.07 \pm 0.89	4.19 \pm 1.48	16.06 \pm 3.17	2400	9.4 \pm 1.7	2.25 \pm 0.41
monzo-sienogranite	5	4.40 \pm 0.26	8.65 \pm 3.63	29.26 \pm 2.98	2750	18.0 $^{+3.6}_{-3.7}$	4.87 \pm 1.00
sienite	2	4.38 \pm 0.74	2.82 \pm 1.48	14.64 \pm 5.23	2750	-	-
marble	1 ^a	0.97 \pm 0.02	1.08 \pm 0.04	5.67 \pm 0.21	2400	-	-

a – the uncertainty correspond to the statistical uncertainty of the measurement.

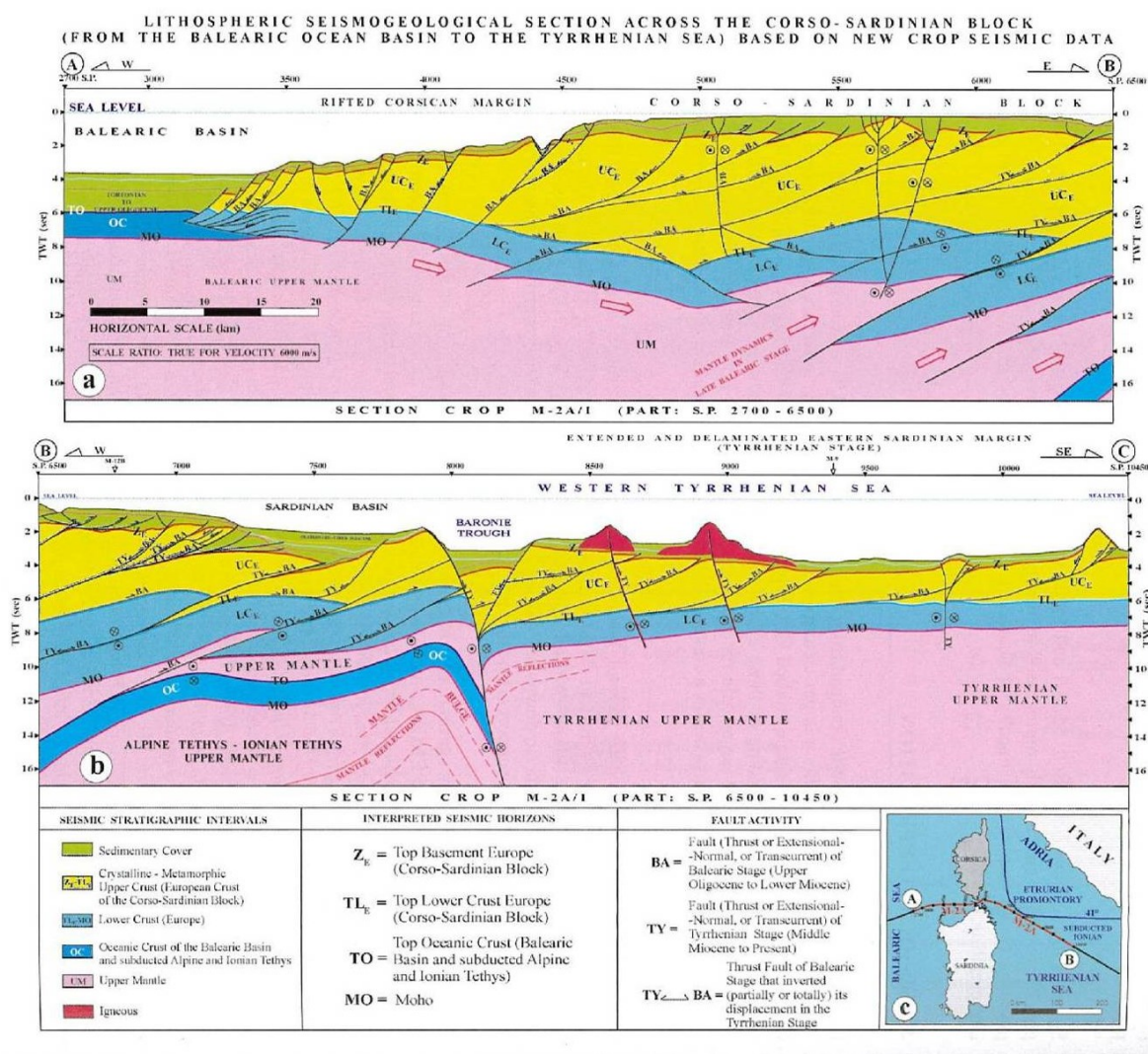


Figure II.2.29: lithospheric seismogeological section across the Corso-Sardinia block figure from (I. R. Finetti 2005).

The surface heat flow map of N-E Sardinia is realized through the geological reclassification and geostatistical distribution as described above. In **Figure II.2.30** is shown the choice of the classes of the map based on the percentiles.

The surface heat flow rate was realized both through the geological reclassification (**Fig. II.2.31**). By applying the **Eq. II.2.6** to the geostatistical outputs **Fig. II.2.25**, **Fig. II.2.26** and **Fig. II.2.27** was calculated the distribution of surface heat flow rate generated by the upper crust (**Fig. II.2.32**).

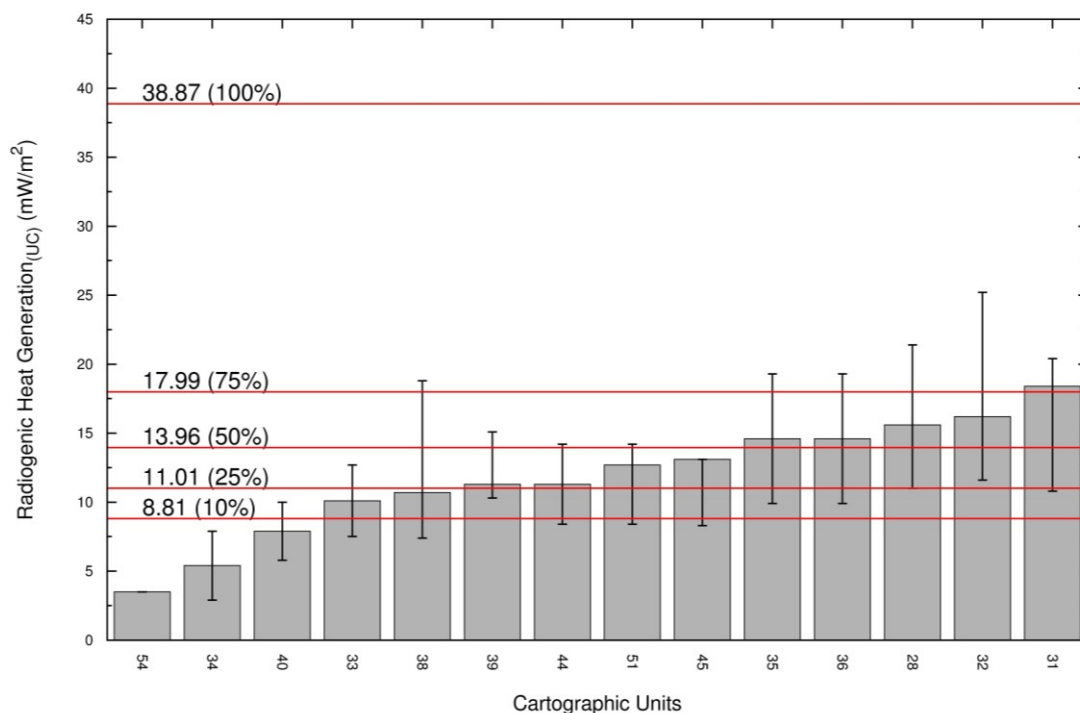


Figure II.2.30: the mean surface heat flow H (in mW/m^2) for 12 cartographic units together with 1σ standard deviation. Horizontal lines represent the class limits and in brackets percentiles chosen in order to construct the map.

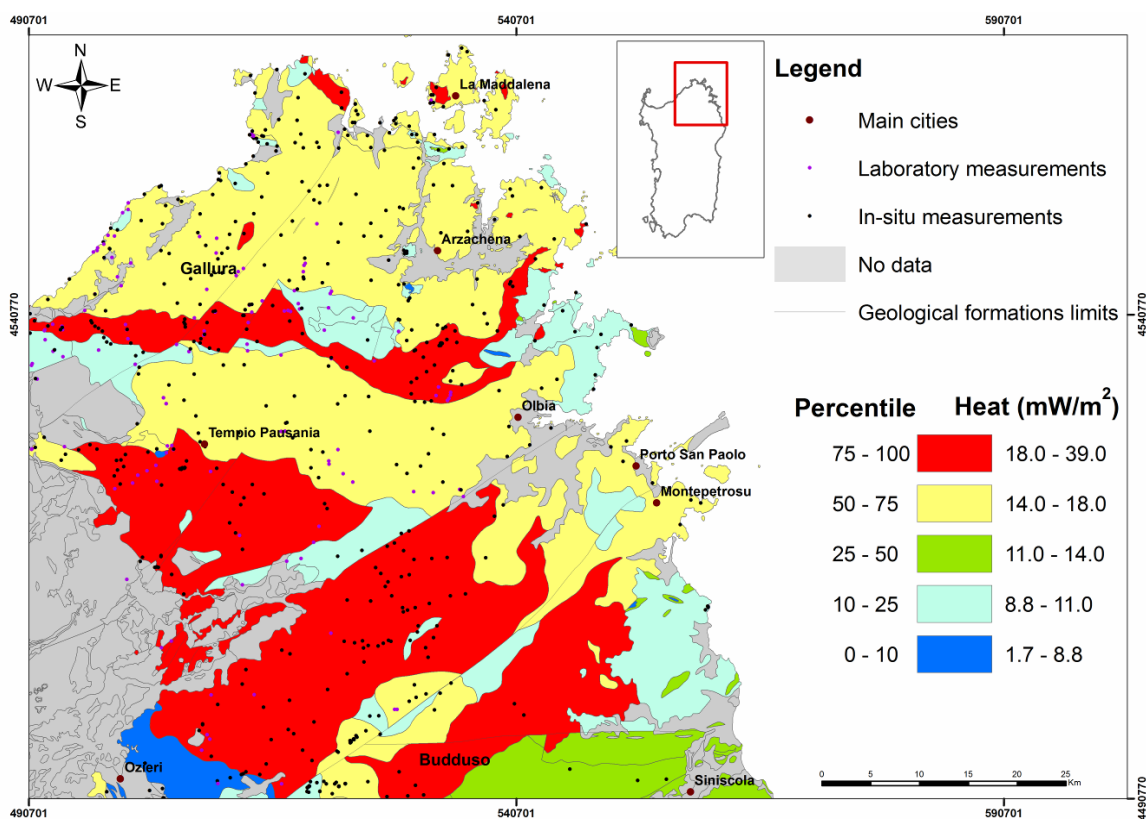


Figure II.2.31: map of surface heat production rate H (in mW/m^2) in the N-E Sardinia Batholith obtained by reclassification of 12 cartographic units.

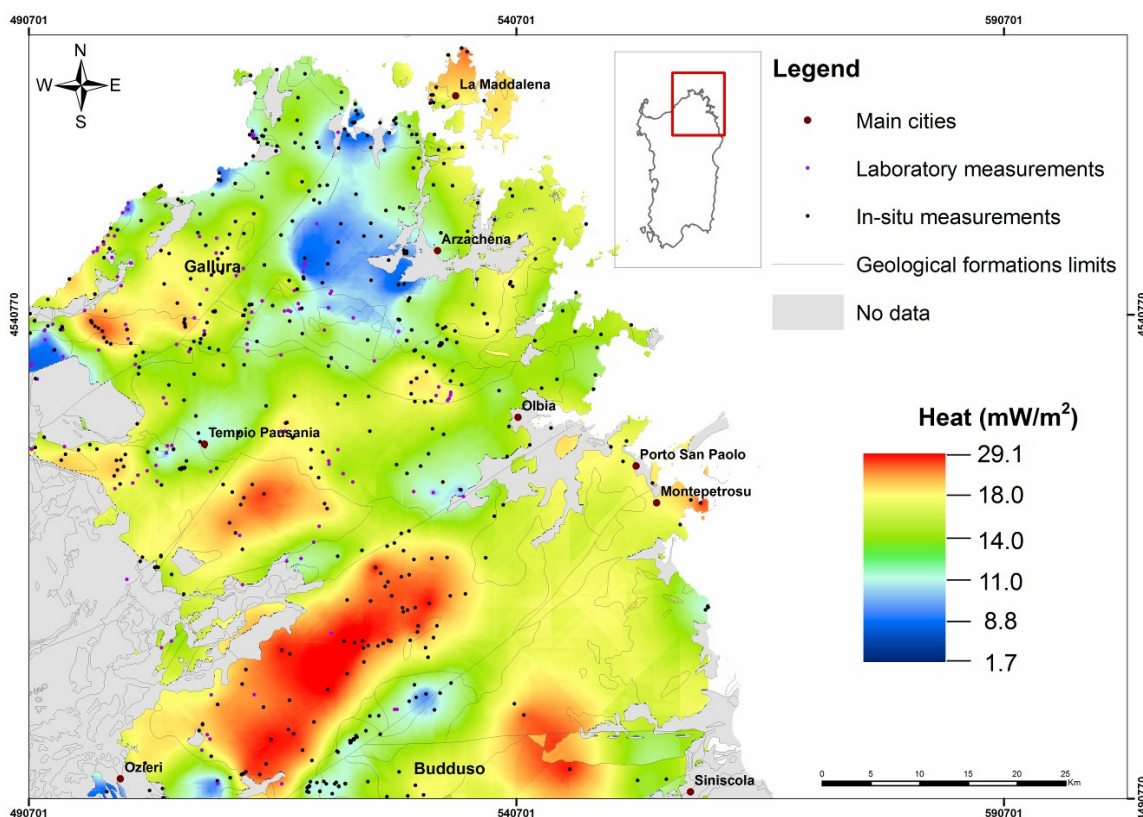


Figure II.2.32: map of surface heat production rate H (in mW/m^2) in some type rocks in N-E Sardinia Batholith.

The surface heat production rate varies between $5.4 \pm 2.5 \text{ mW/m}^2$ (quarzodiorite) to $18.4 \pm 6.8 \text{ mW/m}^2$ (leucogranite) with an average of $14.9 \pm 5.6 \text{ mW/m}^2$. Similar studies in this are performed in Corsica indicate that the heat conducted through the crust from the underlying mantle is on average is 33 mW/m^2 (**M. Verdoya, V. Pasquale et al. 1998**). Considering that the upper crust is richer with radionuclides respect to middle and lower crust even its thickness is much lower it can be reasonably expected that the its contribution to the radiogenic heat to be higher.

Chapter II.3

Discussions and conclusions

The N-E Sardinia (4165 km²), part of the Hercynian basement, was investigated with at least one sample per approximately 6 km² in average. This area was investigated with 545 in-situ measurement using a portable gamma-ray spectrometer NaI(Tl) and by collecting 167 rock samples and measuring them in the laboratory using high-resolution gamma-ray spectrometer (HPGe). Both methods show a satisfactory agreement between: indeed, the concentrations obtained for in-situ and laboratory measurements are 3.9 ± 0.8 (%) and 3.2 ± 1.3 (%) for K; $4.8^{+2.6}_{-1.7}$ (μg/g) and 3.4 ± 1.8 (μg/g) for U; and $17.0^{+9.4}_{-6.1}$ (μg/g) and 15.7 ± 8.1 (μg/g) respectively. Up to 18 rock types were characterized for the radioactivity content of K (%), U (μg/g) and Th (μg/g) with at least 5 measurements. The statistical data analysis confirmed that K (%) and Th (μg/g) show generally Gaussian distribution while U (μg/g) show log-normal distribution. In **Table II.2.3** are summarized the concentrations ($\pm 1\sigma$ standard deviation) of ⁴⁰K, ²³⁸U and ²³²Th in different rock types investigated in the N-E Sardinia Batholith. The abundances of ⁴⁰K vary from $0.22^{+0.27}_{-0.12}$ % (eclogites) to 4.52 ± 0.51 % (sienogranites); for U varies from $0.31^{+0.34}_{-0.16}$ μg/g (eclogite) to 7.37 ± 2.74 μg/g (leucomonzogranite) and 8.65 ± 3.63 μg/g (monzo-sienogranite); and for Th varies from $1.22^{+6.79}_{-1.04}$ (eclogite) to 29.26 ± 2.98 (monzo-sienogranite).

The concentration of K (%), U (μg/g) and Th (μg/g) showed an increasing tendency from passing from mafic to intermediate to felsic rocks. A study of correlation between the SiO₂ content (**Appendix A**) and the abundances confirmed a slight correlation between them: indeed felsic igneous rocks contain high silica content, greater than ~69% SiO₂ (e.g. granite, monzogranite, sienogranite, leucogranite, leuco-monzogranite) show the highest concentration of radioelements and great variability, while intermediate igneous rocks contain between 52-69% SiO₂ (e.g. tonalite, quartzodiorite, granodiorite) and mafic igneous rocks (e.g. amphibolite, eclogite) contain low silica 45-52% and typically high iron-magnesium content show lower concentrations of radioelements. This study is of particular interest for understanding the composition of the earth's crust and estimating the contribution of radiogenic heat to the Earth's thermal budget (Huang Y, Chubakov V et al. 2013) and (**R. L. Rudnick and D. M. Fountain 1995**).

This study showed that the concentrations of ⁴⁰K, U and Th in European Variscan Batholiths are comparable within the uncertainty and in average higher than typical concentrations (2.32 ⁴⁰K, 2.7 μg/g U and 10.5 μg/g Th) for the upper continental crust (**R. L. Rudnick and S. Gao 2003**). These results were further compared (**Table II.2.4**) with bibliographic studies for the emplaced batholiths of European Variscan orogeny: in general the activity concentration in different rock types showed a good agreement within the standard uncertainty with the data obtained from this study. In particular the distribution of uranium over European Variscan orogen showed that the highest concentrations (> 4 μg/g up to 53 μg/g): this is confirmed by the results in the N-E Sardinia Batholith when the majority of granitic rocks show concentrations of U > 4 μg/g in average. However, the abundances of uranium in granite rock in Bohemia massif, Central massif and

Iberian massif show higher mean values while the data are comparable within the variability. While for Th and ^{40}K the data results comparable within the variability.

The mean ratios of Th/U, K/U and K/Th for different rock types show a slight variation and comparable with bibliographic studies for the upper continental crust. In particular, Th/U ratio throughout the various rock types of the batholith, range from $1.22^{+6.79}_{-1.04}$ (eclogite) to $5.21^{+3.99}_{-2.13}$ (tonalite), with values close to the average for the upper continental crust of 3.89. This is observed also for the ratio K/U which is close to the average for the upper continental crust of $0.85 \cdot 10^4$ and ranging from $0.50^{+0.35}_{-0.15} \cdot 10^4$ (monzonogranite) and $0.60^{+0.35}_{-0.17} \cdot 10^4$ (eclogite) to $0.99^{+0.87}_{-0.51} \cdot 10^4$ (tonalite) also for the ratio K/Th which is close to the average for the upper continental crust of $0.85 \cdot 10^4$ and ranging from $0.50^{+0.35}_{-0.15} \cdot 10^4$ (monzonogranite) and $0.60^{+0.35}_{-0.17} \cdot 10^4$ (eclogite) to $0.99^{+0.87}_{-0.51} \cdot 10^4$ (tonalite).

The spatial distribution of the activity concentrations of K (%), U ($\mu\text{g/g}$) and Th ($\mu\text{g/g}$) were first studied through the classification of 12 cartographic units of the geological map based on the mean values of abundances by using ESRI ArcGIS® 9.3. Based on measured data, were identified five classes of radioactivity by choosing an appropriate range of percentiles (C. Raimann 2005a). The variability within a certain geological group indicates that, the 1σ uncertainty of ^{40}K , ^{238}U and ^{232}Th abundances is included in the adjacent ranges of percentile respectively for 80%, 50% and 50% of geological formations. The maps of K (%), U ($\mu\text{g/g}$) and Th ($\mu\text{g/g}$) (Fig. II.2.22, Fig. II.2.23 and Fig. II.2.24) gives a satisfactory representation of the radioactivity distribution, where can easily distinguish from the mean values of abundances of ^{40}K , U and Th that amphibolites, tonalities and quartzodiorites are characterized by the lowest abundances while leucogranites are characterized by the highest abundances in accordance with the results reported in Table II.2.3. It is important to emphasize that even some particular cartographic units are grouped in a distinct radioactivity class the variation of radioactivity can be extended to the neighbor class. Therefore the distinction between monzogranites and leucogranites, which are the more extended cartographic units, must be considered smoothed because this variation.

In order to emphasize the spatial variability of the measures as second approach we performed a geostatistical data analysis by using Kriging interpolation through ESRI ArcGIS® 9.3 (Figure II.2.25, Figure II.2.26 and Figure II.2.27), considering the same classes of percentiles as above. The abundances of K (%), U ($\mu\text{g/g}$) and Th ($\mu\text{g/g}$) were considered Gaussian distribution (Table II.2.5) and the interpolation model was cross-validated with a good approximation, with MSE close to zero and MSVR close to unity (Table II.2.6). We can evidence a good agreement between the K (%), U ($\mu\text{g/g}$) and Th ($\mu\text{g/g}$) maps realized through the geological reclassification and through geostatistical interpolation, evidencing the homogeneity of the radioactivity content for different rock types (Table II.2.3). In particular, leucogranites show the highest activity concentration, showing a good agreement with the geological map (for Buddusò and Tempio Batholith), where we can easily identify the geological limits of leucogranites which seem to be quite homogeneous in radioactivity concentration. This map shows a high K content, probably evidencing the

presence of geological structure not evidenced in the geological map, e.g. alkali rich leucogranites. While leucogranites of Arzachena and Gallura Batholith, still show the presence of high values but with great dishomogeneity. The leucogranites of Buddusò Batholith evidences an anomaly of high K content, probably evidencing the presence of geological structure not evidenced in the geological map, probably alkali rich leucogranites. Monzogranites show a high variability both in Tempio and Gallura Batholiths, however, it seems to be a slight correlation between the activity concentration and the intense presence of acid and basic dykes in this area. The lower concentration of radioactivity is found East corresponding to the presence of basic dykes and the highest concentration are found west corresponding with the presence of acid dykes. These results, gives an overview of the geological structure of N-E Sardinia Batholith showing a good correspondence between the radioactivity distribution and geology and revealing new insights on the geological structure which can help for future geochemical and geological studies.

The radiogenic heat production rate for various types of rock in the N-E Sardinia Batholith varies from $0.20^{+0.22}_{-0.09} \mu\text{W}/\text{m}^3$ (eclogite) to $4.87 \pm 1.00 \mu\text{W}/\text{m}^3$ (monzo-sienogranite). These results are comparable with other studies in Corsica-Sardinia batholith (**M. Verdoya, V. Pasquale et al. 1998**) were are reported radiogenic heat production rate vary from $0.2 \mu\text{W}/\text{m}^3$ (basalts) to $4.2 \mu\text{W}/\text{m}^3$ (calc-alkaline granites). Furthermore, studies from Iberian Massif, Bohemian Batholith show also comparable values ranging from granitic rocks ($2.5\text{-}3.5 \mu\text{W}/\text{m}^3$). While, typically high radiogenic heat production usually between $4\text{-}10 \mu\text{W}/\text{m}^3$ are reported in the Variscan Erzgebirge (Germany) granites (**A. Forster and H. J. Forster 2000**). In (**O. Lexa, K. Schulmann et al. 2011**) the exhumation of c. 340 Ma felsic granulites in the Bohemian Massif is modeled by attributing to the lower crust a high radioactive heat production of $4 \mu\text{W}/\text{m}^3$, typical of Ordovician felsic igneous rocks in the Fichtelgebirge (Saxothuringian domain), which are believed to have been relaminated at the bottom of thickened continental crust during the early Viséan continental underthrusting.

In a first approximation, we calculated the surface heat flow rate generated from the upper crust due to the presence of the isotope of ^{40}K , U and Th assuming a constant upper crust thickness. The best approximation for the upper crustal thickness for N-E Sardinia was derived from (**I. R. Finetti 2005**). The surface heat production rate varies between $5.4 \pm 2.5 \text{mW}/\text{m}^2$ (quarzodiorite) to $18.4 \pm 6.8 \text{mW}/\text{m}^2$ (leucogranite) with an average of $14.9 \pm 5.6 \text{mW}/\text{m}^2$. Similar studies in this are performed in Corsica indicate that the heat conducted through the crust from the underlying mantle is on average is $33 \text{mW}/\text{m}^2$ (**M. Verdoya, V. Pasquale et al. 1998**). Considering that the upper crust is richer with radionuclides respect to middle and lower crust even its thickness is much lower it can be reasonably expected that the its contribution to the radiogenic heat to be higher.

PART III

A new portable instrument for detailed in-situ gamma-ray survey



Table of content:

Chapter III.1: Introduction and objectives

III.1.1 State of art: in-situ γ -ray spectrometry

III.1.2 Objectives of the study

Chapter III.2: Cava-Rad system: a collimated instrument for in-situ gamma-ray measurements

III.2.1 Cava-Rad system: set-up design

III.2.2 Cava-Rad system: sensitivity calibration

III.2.3 Experimental validation of the sensitivity calibration method

Chapter III.3: Discussions and conclusions

Chapter III.1

Introduction and objectives

III.1.1 State of art: in-situ γ -ray spectrometry

In situ γ -ray spectrometry with sodium iodide scintillators is a well developed and consolidated method for radioactive survey (C. Nuccetelli 2008); (P. Chiozzi, P. De. Felice et al. 2000); (A. N. Tyler 2008) with a wide area of applications from mineral exploration to environmental radiation monitoring, providing quantitative information especially about abundances of principal natural radioisotopes, ^{40}K , ^{238}U and ^{232}Th (IAEA 1990). The experiences of nuclear power plant accidents and atmospheric nuclear weapon tests taught us that the fallout of man-made radioisotopes (^{137}Cs , ^{134}Cs and ^{131}I) can affect wide portions of the planet. While in-situ gamma ray spectrometry have been shown to provide rapid and spatially representative estimates of environmental radioactivity however, one of the principal complication of this technique has been the influence of changes in the vertical distribution of the source (e.g. ^{137}Cs) on the observed photon fluence resulting in a significant reduction in the accuracy of the in situ activity measurement. In particular three methods are the most used; the multiple peak method (W. Sowa, E. Martini et al. 1989); (M. Korun, A. Likar et al. 1994); (K. M. Miller, P. Shebell et al. 1994); (K. Rybacek, and et al. 1992), the peak to valley method (P. Zombori, A. Andrasi et al. 1992) and the lead plate method (M. Korun, A. Likar et al. 1994), for deriving the depth distribution. The latter method uses a circular lead plate positioned between the detector and the ground to shield out gamma rays from small angles. The contribution to the flux from large angles varies with the depth parameter and thus the ratio of the peak counts obtained with the lead plate in place to that obtained without the lead plate will give an indication of the activity–depth distribution. The lead plate method shows the lowest uncertainty for all distributions and, thus, appeared to offer the best method (J. MacDonald, C. J. Gibson et al. 1997).

However, in many situations in-situ measurements show not only depth variation but also the spatial variability (e.g. **Figure III.1.1**) which not necessary follows a distribution law but depends more on the geological processes. Such situations are common during geological surveys and exhibit particular interest since given clues on geochemical processes. Moreover, the radioactivity assessment for screening proposes of the quarried dimension stones are of particular interest for the radiological impact. This exhibits a particular interest in N-E Sardinia, indeed approximately 400 quarries are exploited for granite dimension stones which are used worldwide in construction. In many situation dimension stones of different lithological origin, with high variability of radioactivity concentration (**Table I.1.1**), are stacked and therefore influence the accuracy of activity concentration assessment (e.g. **Figure III.1.2**). In general these studies are realized by collecting samples and by laboratory measurements, therefore a new method for accurately asses the radioactivity concentration in-situ is necessary.



Figure III.1.1: outcrop of pyroclastic volcanic deposits at Mt. Vulsini South Tuscany Region, Italy.



Figure III.1.2: quarry site in the N-E Sardinia Region, Italy.

Some attempts are done for collimating portable detector to quantify radionuclides in materials other than depth distribution of radioelements described above, is performed by using lead collimators limiting to the detection of unattenuated γ -rays from a selected range of polar angles (**R.R. Benke and K. J. Kearfott 2002**) (**L. Lovborg, H. Wollenberg et al. 1971**). The disadvantages are that collimation adds weight to the in situ system and increases the counting time by reducing the detector's field of view. Therefore, taking advantage of the existing state-of-art the core objective of this study is the realization of a portable collimated gamma-ray spectrometer by optimizing weights and counting time.

Other than folding the portable detector with lead, the lead plate method can be improved in order to increase the capability to filter the background in high-spatial variability in-situ measurements. As described above the lead plate principle two spectra are acquired in-situ: the first without the lead plate (PbOut spectra) and the second with the lead plate (PbIn spectra). By subtracting from PbOut spectra the PbIn spectra the difference spectra gives the unattenuated γ -rays from a selected range of polar angles, by filtering the surrounding background and simulating the collimation effect. The use of filtering “rolling” average background spectra is first introduced in (**A.J. Cresswell and D.C.W. Sanderson 2009**) in order to improve the signal to background ratio for location of point sources in mobile gamma-ray spectrometry measurements. However, in our approach attention must be done since both background and target sample spectra are of quite similar strength. Therefore, the choice of dimensions of the lead plate will determine the accuracy of the measurement, since it determines the quality of the difference spectra. The advantages of the indirect collimation permits both to reduce the weights necessary to fold the detector inside and optimizing the counting time through the use of relatively high volume of NaI(Tl) without giving up the portability of the instrument.

III.1.2 Objectives of the study

The objectives of this study are:

1. The design and realization of a portable collimated gamma-ray spectrometer, called Cava-Rad system, capable to perform in-situ measurements on a restricted area. For the realization of the new instrument will take advantage on existing state-of-art by improving the design and analysis methods.

2. The calibration of the Cava-Rad system through use of natural calibration sites by Full Spectrum Analysis method with Non-Negative Least Squares constrain (described in **Section I.2.3.3**). For this reason a set of calibration sites particularly rich in one of the radionuclides will be investigated and characterized for ^{40}K , ^{238}U , ^{232}Th and ^{137}Cs by collecting samples and measuring in the laboratory with the MCA-Rad system.

3. The assessment of the accuracy of the calibration method: for this reason some specific geological sites showing small scale (order of one meter) spatial variability will be used to validate the results obtained from Cava-rad system. In particular, for each measurement performed in-situ with Cava-Rad system will be collected one sample and further measured in the laboratory for ^{40}K , ^{238}U , ^{232}Th and ^{137}Cs ; and the results will be compared in order to validate the accuracy of the Cava-rad system.

Chapter III.2

Cava-Rad system: a collimated instrument for in-situ gamma-ray measurements

III.2.1 Cava-Rad system: set-up design

The core of the Cava-Rad system (**Table III.2.1**) is composed of a sodium iodide scintillator detector NaI(Tl) of cubic shape and volume of approximately 0.4 L with energetic resolution of 7.3 % at 662 keV (^{137}Cs), 5.2 % at 1172 and 1332 keV (^{60}Co). The NaI(Tl) detector is mounted on self-constructed PVC rugged rack mount case (**Fig. III.2.1**) and accurately fixed in order to prevent possible damages on the field. The detector is coupled with a photomultiplier (PMT) base with integrated bias supply, preamplifier and digital multichannel analyzer (MCA) called digiBASE (ORTEC[®]). The digiBASE is powered through a universal serial bus (USB) communication connector by a notebook which is also used for data storage. The Cava-rad system uses the lead plate method in order to shield background radiation and perform measurements on a restricted area. The lead shield of dimensions 9 cm x 9 cm x 3cm is used to partially shield an area of approximately 100 cm²: about 20% of the total counts is screened from the shielding configuration. The lead used as a shielding material adds some extra background due to the presence of ^{210}Pb , having a half-life of 22.3 years and emitting a characteristic gamma energy of 46.5 keV and a bremsstrahlung continuum from beta decay of its daughter ^{210}Bi extending from low energy up to 1162 keV. Furthermore when strikes the lead surface, characteristic lead X-rays may escape and hit the detector. The lead plate gives rise also to backscattered events within a broad range of energy between 200 keV and 300 keV. The contribution of these effects on the quality of the spectra will be discussed later. A typical measurement is realized by performing two measurements; the first one with the lead plate out of the detector-target, called PbOut spectra and the second one with the lead plate between the detector-target, called PbIn spectra. The movement of the lead shield upon a conveyor belt is driven through an electric motor powered by a 9 V alkaline battery: which is automatically governed by a home made electronic set-up through a self development program based on Java Environment, called “goCava-Rad”.

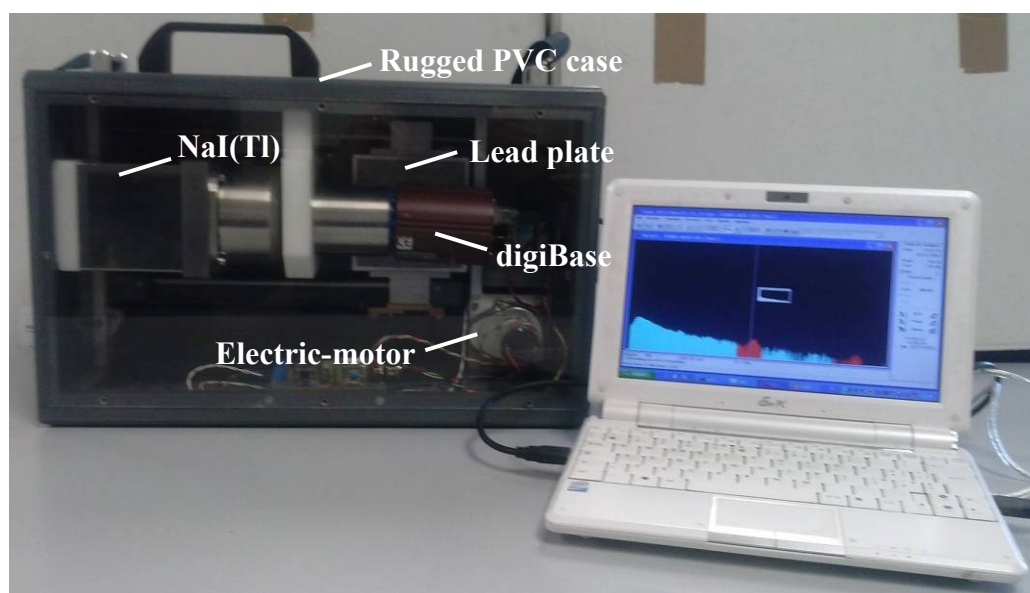
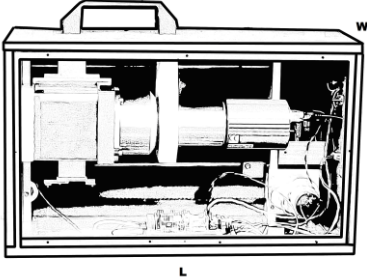


Figure III.2.1: Cava-Rad system.

Table III.2.1: summarized technical data sheet for the Cava-Rad system

	Main constituents	Main features
Cava-Rad		<p>Power consumption < 3W</p> <p>Physical parameters Dimensions (L 43.0 cm x H 27.0 cm x W 13.5 cm) Weight 8.0 kg</p> <p>Environmental parameters Temperature -10 to +50 °C Humidity 85%</p>
	NaI(Tl) detector	<p>Energy resolution 7.3 % at 662 keV (^{137}Cs) 5.2 % at 1172 and 1332 keV (^{60}Co)</p> <p>Physical parameters Dimensions (L 7.62 cm x H 7.62 cm x W 7.62 cm) Weight 2.0 kg</p>
	Lead plate	<p>Physical parameters Dimensions (L 9.0 cm x H 9.0 cm x W 3.0 cm) Weight 3.0 kg</p>

In particular, the acquisition software, “goCava-Rad” (Fig. III.2.2), is a batch of the sequence of commands which:

- check the position of the lead plate and lunch Maestro ORTEC[®] software for gamma-ray spectrum acquisition and save the first spectra. First it is made attention to supply manually the correct operation High Voltage to the NaI(Tl) detector. The duration of the acquisition Live Time is a parameter programmable through “goCava-Rad;
- move the lead plate in the next position, lunching the second spectrum acquisition for the same acquisition Live Time and save the second spectra.



Figure III.2.2: GUI of goCava-Rad program.

The sensitivity calibration of the Cava-Rad system is performed using the same approach as in **Section I.2.3.3** with the FSA-NNLS method, which is discussed below.

III.2.2 Cava-Rad system: sensitivity calibration

The Cava-Rad system scintillation detector was calibrated based on the selection of calibration sites characterized by a prevalent concentration of one of the natural radionuclides (as described in **Section I.2.3.3**) and using the Full Spectrum Analysis with Non-Negative Least Square method. At each site we perform two measurements, coded as PbOut and PbIn (described in **Section III.2.1**). We chose two different approaches to calibrate the Cava-Rad system:

- *Method I:* for each site we subtract the energy calibrated spectra, PbOut – PbIn and use the difference spectra as input for the FSA-NNLS algorithm in order to obtain the sensitivity spectra of the differences (see **Figure III.2.3**);

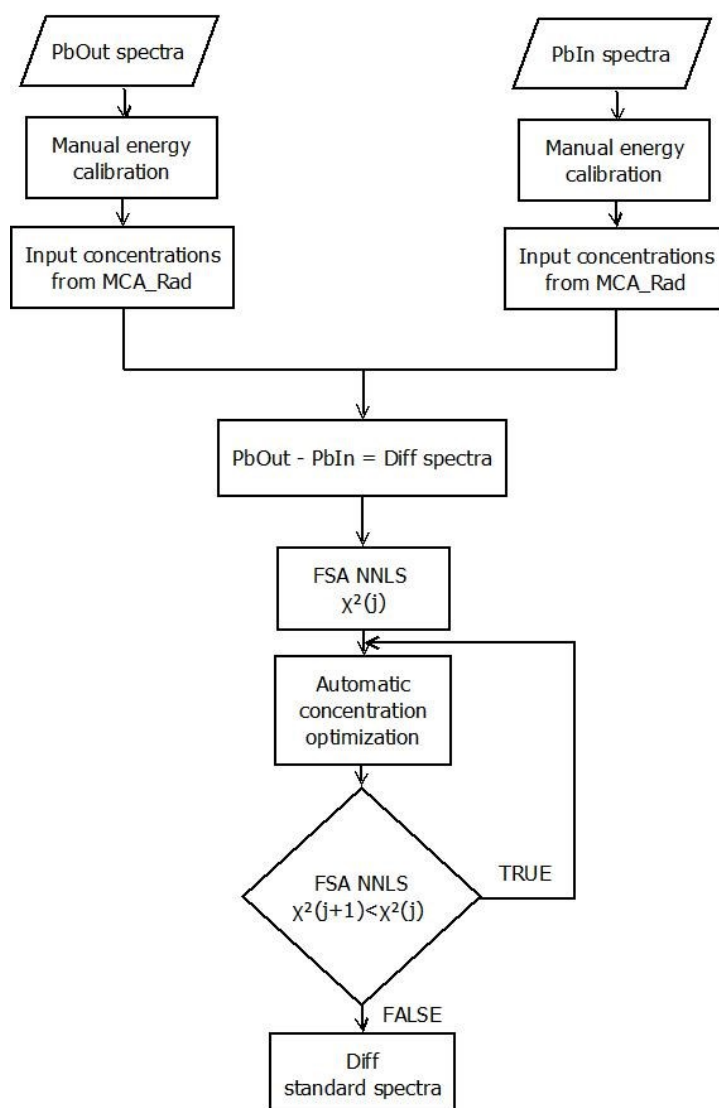


Figure III.2.3: schematic diagram representing the main operations for *Method I*.

- *Method II:* we use the energy calibrated PbOut spectra as input for FSA-NNLS algorithm in order to obtain the PbOut sensitivity spectra. We repeat the same procedure for PbIn spectra and obtain the PbIn sensitivity spectra. Finally, we subtract the PbIn sensitivity spectra from PbOut sensitivity spectra in order to obtain the difference of the sensitivity spectra (see **Figure III.2.4**).

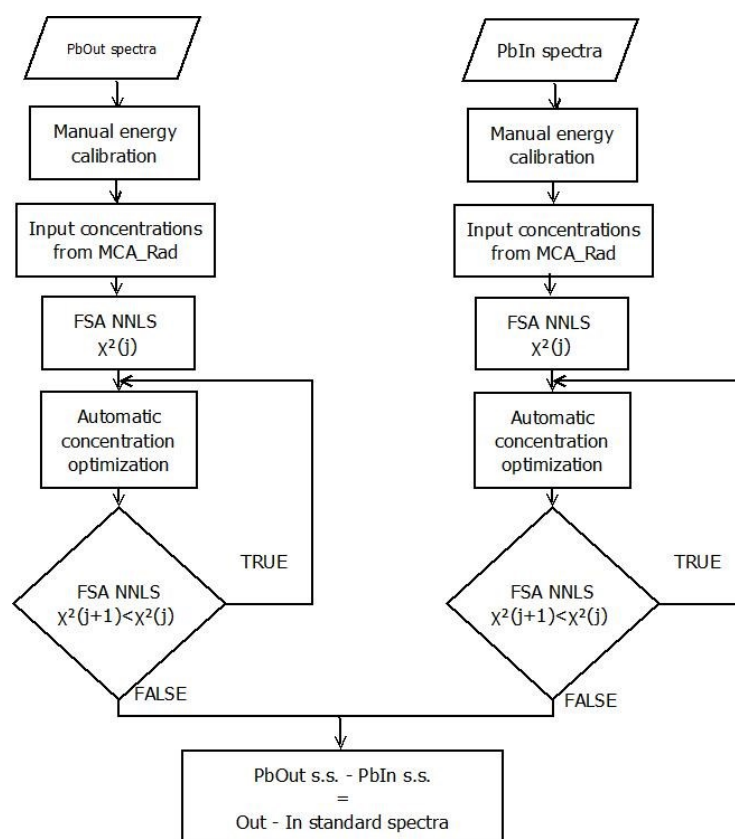


Figure III.2.4: schematic diagram representing the main operations for *Method II*.

Therefore, we selected nine calibration sites, which were further characterized for their radioactivity content by collecting at least two rock/soil samples (one from the target source under the position when was fixed Cava-Rad and a bulk sample around that position within 1 m of radius) and further analyzing them in the laboratory using the MCA-Rad system. Samples were homogenized up to 1 cm grain size, dried at 60°C temperature, and then filled in measurement containers and left undisturbed for at least 3 weeks in order to establish radioactive equilibrium in ^{226}Ra decay chain segment prior to be measured. The activity concentrations are summarized in **Table III.2.2**.

Table III.2.2: activity concentrations ($\pm 1 \sigma$ statistical uncertainty) of the distribution of radioelements and the average concentrations (\pm max. semidispersion) for the calibration sites. The experimental uncertainty laboratory measurements (MCA-Rad system) was estimated to be less than 5%.

Place/ID	Site type	Coordinates	Sample location	K (%)	U ($\mu\text{g/g}$)	Th ($\mu\text{g/g}$)	Cs (Bq/kg)
Galzignano/K2	Potassium	45°17'06.96''N 11°45'41.18''E	under	6.04 \pm 0.09	4.91 \pm 0.17	27.86 \pm 1.10	10.19 \pm 1.06
			around	6.27 \pm 0.09	4.70 \pm 0.31	21.81 \pm 0.92	4.93 \pm 0.94
			average	6.16 \pm 0.12	4.81 \pm 0.11	24.84 \pm 3.03	7.56 \pm 2.63
Recoaro/K4	Potassium	45°42'24.85''N 11°13'29.99''E	under	2.80 \pm 0.06	2.52 \pm 0.31	13.39 \pm 0.76	6.46 \pm 0.78
			around	3.85 \pm 0.07	3.90 \pm 0.18	18.35 \pm 0.87	4.60 \pm 0.84
			average	3.33 \pm 0.53	3.21 \pm 0.69	15.87 \pm 2.48	5.53 \pm 0.93
Piovene Rocchette/U1	Uranium	45°46'25.84''N 11°24'41.74''E	under	0.04 \pm 0.04	7.44 \pm 0.19	1.01 \pm 1.01	2.00 \pm 0.60
			around	0.07 \pm 0.01	6.68 \pm 0.19	1.08 \pm 1.08	5.72 \pm 0.65
			average	0.06 \pm 0.02	7.06 \pm 0.38	1.05 \pm 0.04	3.86 \pm 1.86
Arsiero/U3	Uranium	45°48'26.81''N 11°19'34.81''E	under	0.05 \pm 0.01	7.53 \pm 0.22	1.04 \pm 1.04	1.45 \pm 1.45
			around	0.06 \pm 0.01	7.63 \pm 0.19	1.57 \pm 0.40	1.39 \pm 1.39
			average	0.06 \pm 0.01	7.58 \pm 0.05	1.31 \pm 0.27	1.42 \pm 0.03
Castelvecchio/Th1	Thorium	45°37'29.41''N 11°16'22.90''E	under	2.09 \pm 0.06	0.94 \pm 0.09	4.23 \pm 0.56	1.61 \pm 1.61
			around	0.68 \pm 0.03	1.70 \pm 0.33	4.33 \pm 0.50	1.31 \pm 1.31
			average	1.39 \pm 0.71	1.32 \pm 0.38	4.28 \pm 0.05	1.46 \pm 0.15
Mt. Novegno/Cs1	Cesium	45°46'21.50''N 11°18'57.40''E	under	0.50 \pm 0.05	1.24 \pm 0.22	3.91 \pm 3.91	1495.67 \pm 12.51
			around	0.45 \pm 0.05	2.05 \pm 0.22	3.23 \pm 3.23	1022.03 \pm 9.68
			average	0.48 \pm 0.03	1.65 \pm 0.41	3.57 \pm 0.34	1258.85 \pm 236.82
Galzignano/H1	Mix	45°19'04.79''N 11°43'51.26''E	under	4.18 \pm 0.08	12.27 \pm 0.27	55.93 \pm 1.50	2.82 \pm 2.82
			around	4.01 \pm 0.07	13.95 \pm 0.28	64.56 \pm 1.51	2.79 \pm 2.79
			average	4.10 \pm 0.09	13.11 \pm 0.84	60.25 \pm 4.32	2.81 \pm 0.01
Galzignano/H2	Mix	45°21'17.34''N 11°43'20.99''E	under	4.10 \pm 0.08	8.04 \pm 0.44	36.81 \pm 1.28	2.55 \pm 2.55
			around	4.41 \pm 0.08	9.95 \pm 0.45	40.10 \pm 1.27	2.53 \pm 2.53
			average	4.26 \pm 0.16	9.00 \pm 0.96	38.46 \pm 1.65	2.54 \pm 0.01
Lido Spina/B1	Background	44°39'30.54''N 12°15'06.10''E	n/a	n/a	n/a	n/a	n/a

The variability of the distribution of ^{40}K , ^{238}U , ^{232}Th and ^{137}Cs in calibration sites were found to be respectively, < 30% (except the Castelvecchio/Th1 site which is 50%), < 30%, < 20% and ~20% (for the Mt. Novegno/Cs1 site). This variability is satisfactory for the calibration process.

At each calibration site the Cava-Rad system in place on target and two measurements of 15 minutes each are performed, coded as PbOut and PbIn, which indicate the position of the lead plate away and under the NaI(Tl) detector (**Figure III.2.2**). The background site, i.e. free of radioactivity, was chosen in the sea (Lido di Spina), by performing 1 hour measurement on an inflatable boat about 0.5 km offshore (approximately 3 m depth): this water column is enough to shield more than 99% of the seabed radioactivity satisfying our requests. The main sources of events for the background are cosmic radiation (see **Section I.1.3**) and atmospheric radon (^{222}Rn) and the lead shield activity.

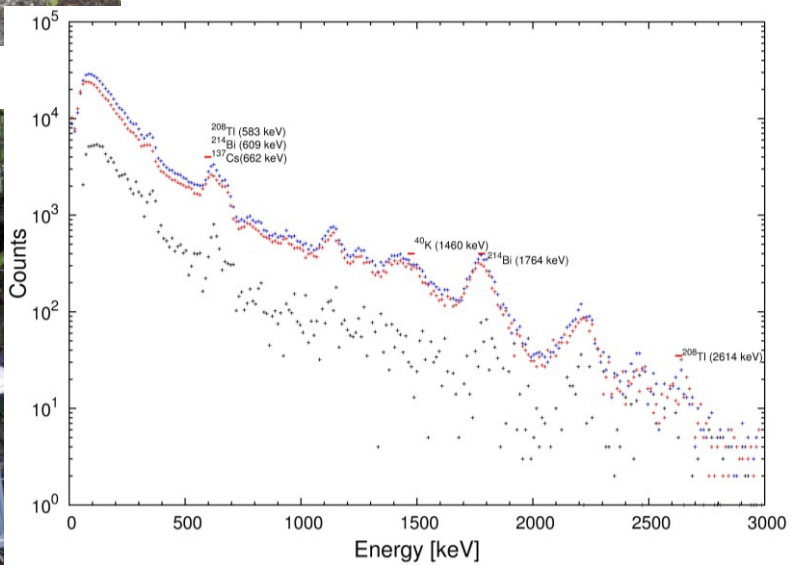
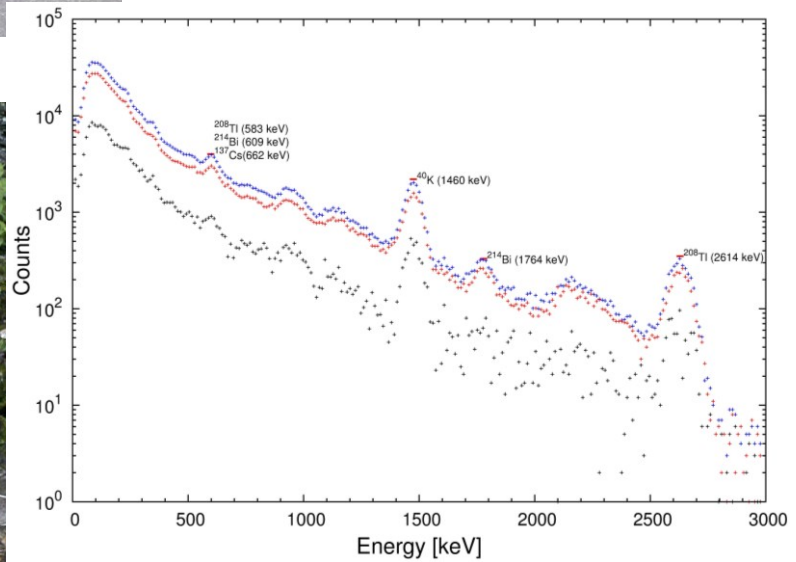
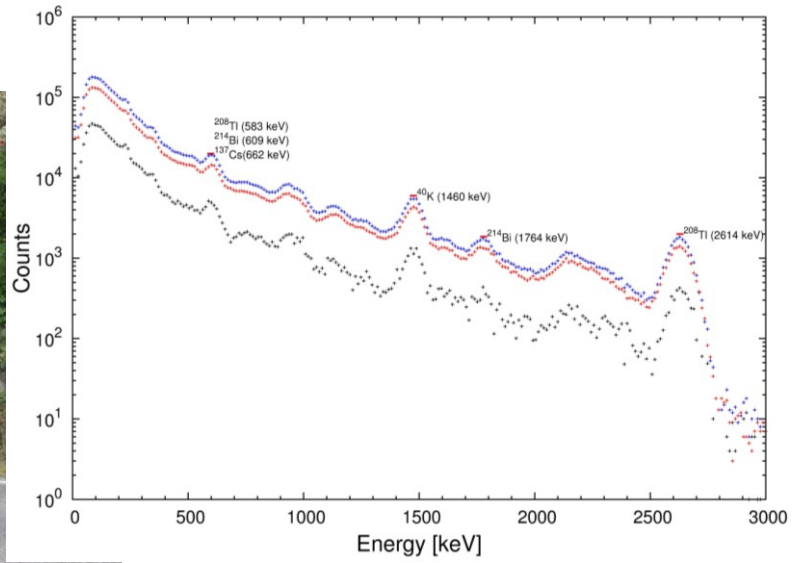


Figure III.2.5: e.g. of measurement in calibration site (left) and measured (energy calibrated) spectra (right).

When dealing with spectrum subtraction, as described in the *Method I* (**Figure III.2.3**) and *Method II* (**Figure II.2.4**), the energy calibration and gain shift adjustment processes are very important in order not to introduce any bias in the sensitivity spectra. Therefore, each measured spectra is first energetically calibrated and then the spectrum events are redistributed, or “rebinned”, by using a pseudo-random number generator, in a new spectrum with linear calibration having zero offset and a fixed keV/channel parameter. In order to ensure enough statistics, especially after spectra subtraction differently from the procedure explained in **Section I.2.3.3** the energetically calibrated spectra are rebinned with 12 keV/channel, i.e. 256 channels. Since we are interested only in the energy range from 300 keV to 2900 keV (**A. Caciolli, M. Baldoncini et al. 2012**) the influence of lead plate on the spectrum quality is negligible.

By using the FSA-NNLS method we obtain the calibration spectra as described in the *Method I* (**Fig. III.2.6**) and *Method II* (**Fig. III.2.7**). The process of minimization of χ^2 , from 7.2 to 2.1, for sensitivity spectra of Method I, is performed by trimming the input concentrations measured by MCA-Rad system within 95% confidence level. While for Method II, the process of minimization of χ^2 , from 25.0 to 2.1 for PbOut spectra and from 23.9 to 1.8 for PbIn spectra, are performed by trimming the input concentrations measured by MCA-Rad system within 95% confidence level.

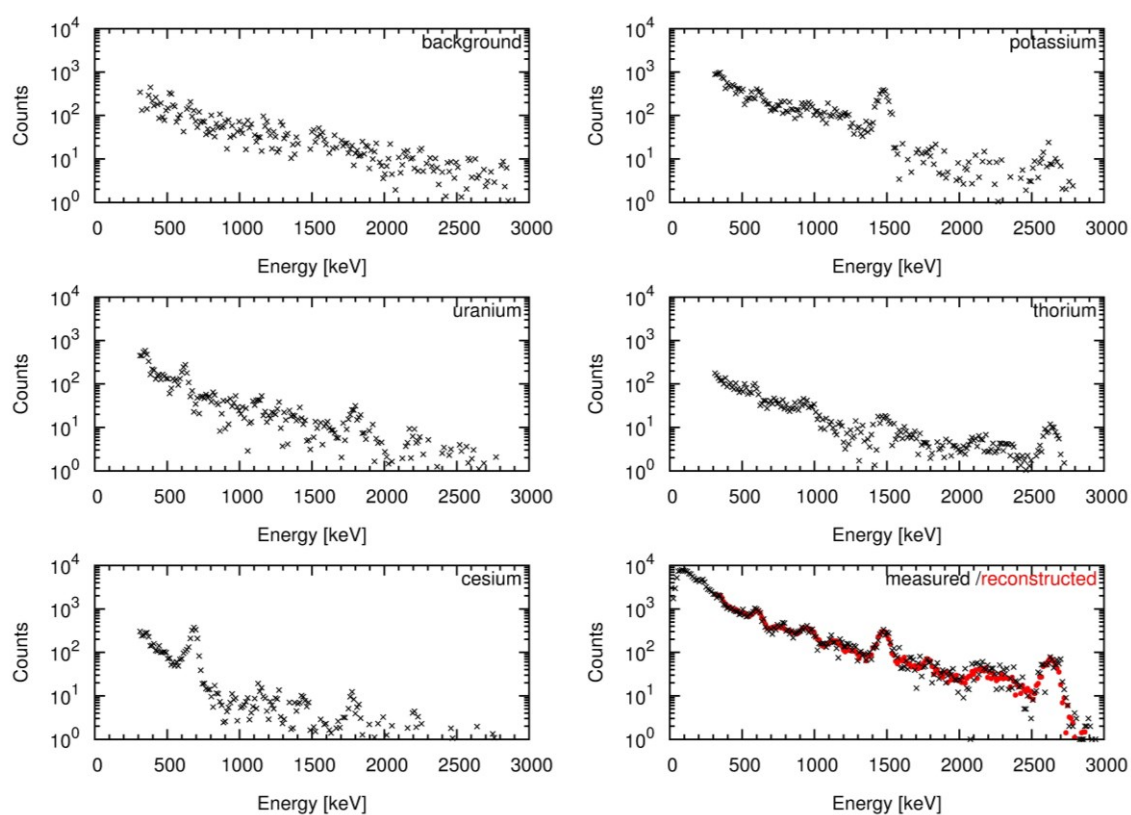


Figure III.2.6: sensitivity spectra of background, ^{40}K , U, Th and ^{137}Cs obtained following the Method I. Example of quality of the fitting process (bottom-right) showing and e.g. of measured spectra and reconstructed with the sensitivity spectra.

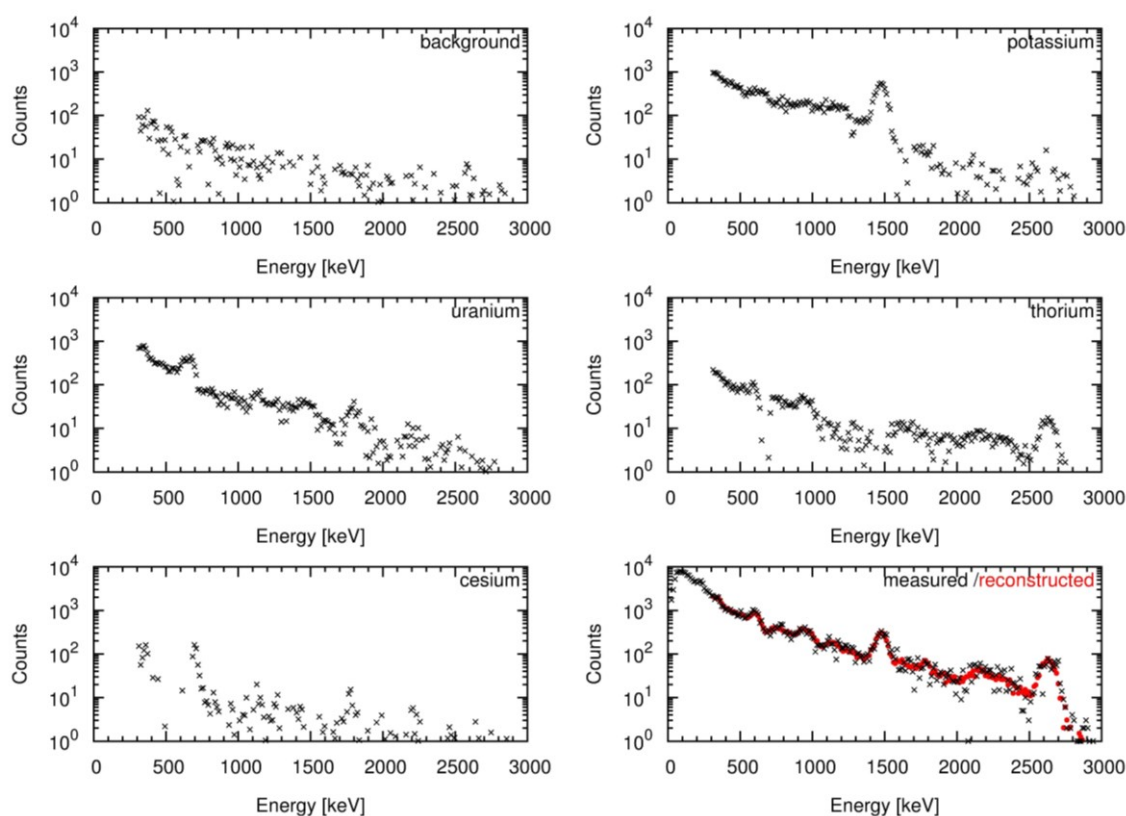


Figure III.2.7: sensitivity spectra of background, ^{40}K , U, Th and ^{137}Cs obtained following the Method II. Example of quality of the fitting process (bottom-right) showing and e.g. of measured spectra and reconstructed with the sensitivity spectra.

III.2.3 Experimental validation of the sensitivity calibration method

The sensitivity calibration method was validated by comparing the results obtained with Cava-Rad, both Method I and Method II, with results obtained by measuring samples in the laboratory with the MCA-rad system. For each in-situ measurement with Cava-Rad (5 minute acquisition time for each measurement) one rock sample is collected and prepared for laboratory measurement with the MCA-Rad system. The testing sites divided by their location are:

- Mt. Vulsini (South Tuscany region) is a volcanic area part of the Tuscan Magmatic Province where outcrops pyroclastic rocks (ignimbrites). The stratigraphy of such outcrops shows the volcanic deposits layers, where the chemical composition can widely vary according the volcano's lifetime activity. Up to 20 in-situ measurement were performed in 7 different sites and 20 rock samples were collected and further measured in the laboratory (**Figure II.2.8**).

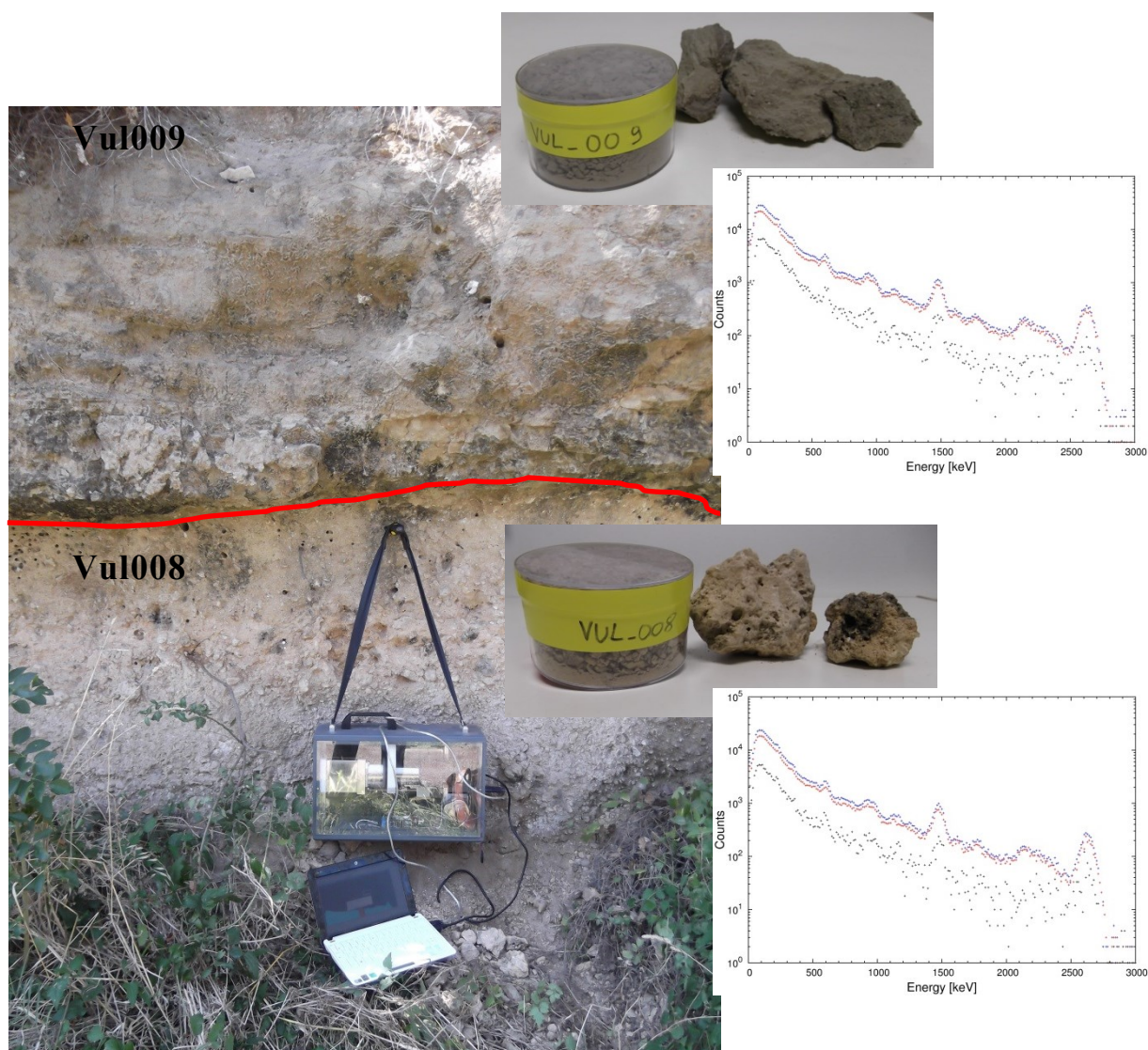


Figure III.2.8: e.g. of in-situ measurement in Mt. Vulsini (Tuscany Region).

- Euganean hills (Veneto Region) have a volcanic origin too where outcrops acid effusive rocks (like trachyte, rhyolites). Up to 8 in-situ measurements were performed in 7 different sites and 8 rock samples were collected and further measured in the laboratory (**Figure III.2.9**).



Figure III.2.9: e.g. of in-situ measurement in Euganean hills (Veneto Region).

In **Table III.2.3** have summarized the results obtained by laboratory measurement with MCA-Rad system on 28 rock samples collected in each target location where was performed an in-situ measurement with Cava-Rad system (**Fig. III.2.8** and **Fig. III.2.9**).

Table III.2.3: concentrations of K, U, Th and ^{137}Cs obtained from measurement in laboratory of samples collected at each testing site.

Site ID	Measurement/ Sample ID	Site description	Coordinates	K (%)	U ($\mu\text{g/g}$)	Th ($\mu\text{g/g}$)	^{137}Cs (Bq/kg)
A	Vul001	Grey ignimbrite with black and white pumices	42°44'23.26''N	7.41 ± 0.12	16.05 ± 0.36	68.97 ± 1.92	8.92 ± 1.68
	Vul002	Reddish ignimbrite with black pumices and litici	11°46'28.46''E	4.85 ± 0.10	6.77 ± 0.22	56.23 ± 1.61	89.80 ± 2.44
B	Vul003	Gray ignimbrite with heterometric pumices	42°43'41.35''N 11°44'46.71''E	1.61 ± 0.06	3.95 ± 0.17	35.35 ± 1.23	< 2.25
	Vul004	Yello/gray ignimbrite with heterometric pumices		3.43 ± 0.08	8.65 ± 0.25	48.51 ± 1.55	< 2.72
	Vul005	Gray ignimbrite with heterometric pumices		2.59 ± 0.07	7.84 ± 0.28	40.89 ± 1.46	< 2.85
	Vul006	Yello/gray ignimbrite with heterometric pumices		2.91 ± 0.07	7.54 ± 0.23	36.00 ± 1.34	< 2.50

	Vul007	Reddish ignimbrite and litici		2.46 ± 0.07	8.20 ± 0.25	36.68 ± 1.39	< 2.65
C	Vul008	Gray ignimbrite with light-gray pumices	42°41'15.00''N	5.03 ± 0.11	12.09 ± 0.34	71.01 ± 2.08	< 3.68
	Vul009	Multilayers light-gray ignimbrite	11°41'56.57''E	4.39 ± 0.09	12.46 ± 0.31	51.93 ± 1.63	< 3.05
D	Vul010	Reddish ignimbrite with black pumices and litici	42°35'54.08''N	6.26 ± 0.11	6.79 ± 0.24	48.62 ± 1.52	17.24 ± 1.45
	Vul011	Dark gray ignimbrite with black pumices	11°38'45.90''E	7.08 ± 0.12	11.50 ± 0.31	50.28 ± 1.68	22.66 ± 1.77
E	Vul012	Pinkish ignimbrite with black and light-gray pumices	42°35'52.47''N 11°38'48.37''E	5.32 ± 0.10	6.26 ± 0.21	43.07 ± 1.47	< 3.05
	Vul013	Multilayersblight-grey ignimbrite		5.87 ± 0.11	8.13 ± 0.25	40.63 ± 1.42	< 2.88
	Vul014	Brown/gray ignimbrite		6.37 ± 0.11	13.75 ± 0.23	59.22 ± 1.81	< 3.40
F	Vul015	Black ignimbrite with white pumices	42°35'53.66''N 11°38'52.66''E	3.90 ± 0.09	34.26 ± 0.69	45.93 ± 1.59	< 3.25
	Vul016	Gray ignimbrite		6.38 ± 0.12	20.20 ± 0.43	87.52 ± 2.28	< 4.15
	Vul017	Light gray ignimbrite with big litici and gray pumices		5.42 ± 0.10	9.77 ± 0.27	51.30 ± 1.56	< 2.87
	Vul018	Fine-grained brown / gray ignimbrite		3.90 ± 0.09	17.78 ± 0.37	71.15 ± 1.87	< 3.44
G	Vul019	Gray ignimbrite with black pumices	42°41'03.88''N	7.65 ± 0.12	13.61 ± 0.32	61.10 ± 1.78	< 3.64
	Vul020	Yellow ignimbrite with light-gray pumices	11°42'34.19''E	6.12 ± 0.11	15.73 ± 0.36	73.53 ± 1.95	< 3.53
H	Eug001	Trachyte	42°14'33.55''N 11°45'09.60''E	5.20 ± 0.09	7.90 ± 0.24	36.01 ± 1.26	5.49 ± 1.13
I	Eug002	Basalt	45°19'19.06''N	3.21 ± 0.07	26.51 ± 0.49	54.46 ± 1.54	< 3.03
	Eug003	Rhyolite	11°44'06.75''E	3.81 ± 0.08	9.32 ± 0.25	58.57 ± 1.56	3.27 ± 1.23
J	Eug004	Latite	45°18'38.11''N 11°47'02.15''E	3.05 ± 0.07	3.71 ± 0.15	12.27 ± 0.79	5.81 ± 0.84
K	Eug005	Latite	45°19'13.83''N 11°46'00.07''E	4.91 ± 0.08	6.39 ± 0.20	26.88 ± 1.08	< 2.29
L	Eug006	Rhyolite	45°19'13.37''N 11°45'59.46''E	2.39 ± 0.06	19.41 ± 0.42	61.53 ± 1.57	< 2.80
M	Eug007	Rhyolite	45°19'13.96''N 11°40'07.90''E	4.25 ± 0.08	5.44 ± 0.18	32.07 ± 1.16	< 2.31
N	Eug008	Trachyte	45°17'34.71''N 11°37'10.42''E	4.35 ± 0.08	2.83 ± 0.13	14.82 ± 0.8	< 1.91

The in-situ measurements were analyzed using FSA-NNLS method taking the sensitivity spectra obtained both through Method I and Method II. In **Fig. III.2.10**, **Fig. III.2.11** and **Fig. III.2.12** are shown the comparison of the results obtained by the laboratory measurements (**Table III.2.3**). In-situ measurements with Cava-Rad system suffer higher statistical uncertainty respect to laboratory measurements: such result has been expectable since only approximately 20% of measured spectra is considered in the analysis process. The typical relative statistical uncertainties are less than 30% for ^{40}K and ^{238}U , and less than 15% for ^{232}Th compared with laboratory measurements were relative statistical uncertainties are less than 5% for all radionuclides. We can observe that the results obtained using sensitivity spectra of Method II systematically underestimate respect the results obtained in the laboratory, why the results obtained using sensitivity spectra of Method I are comparable within 95% confidence level with laboratory measurements. The sensitivity spectra obtained through the Method II are obtained subtracting from the sensitivity spectra of PbOut the sensitivity spectra of PbIn which use the whole spectrum statistics and therefore fit the difference spectra with concentrations underestimated respect to those obtained through Method I. Therefore, we will use the sensitivity spectra obtained through Method I for analyzing in-situ measurements with Cava-Rad system.

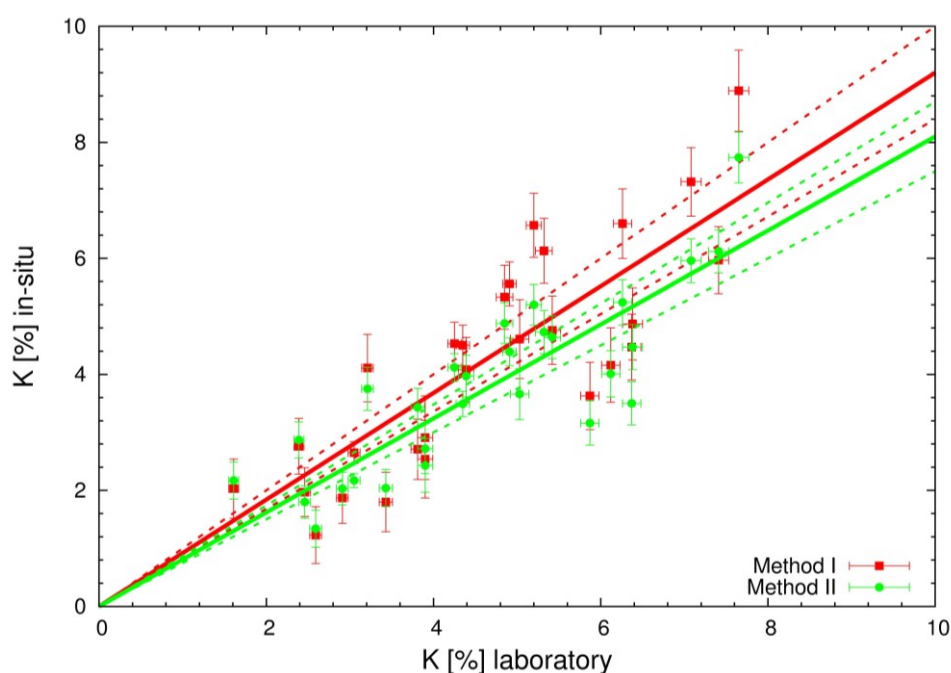


Figure III.2.10: correlation of the results obtained in-situ with Cava-Rad system analyzed with Method I ($K_{\text{situ}} = 0.92 \pm 0.08 K_{\text{lab}}$) and Method II ($K_{\text{situ}} = 0.81 \pm 0.06 K_{\text{lab}}$) sensitivity spectra compared with laboratory measurements with the MCA-Rad system.

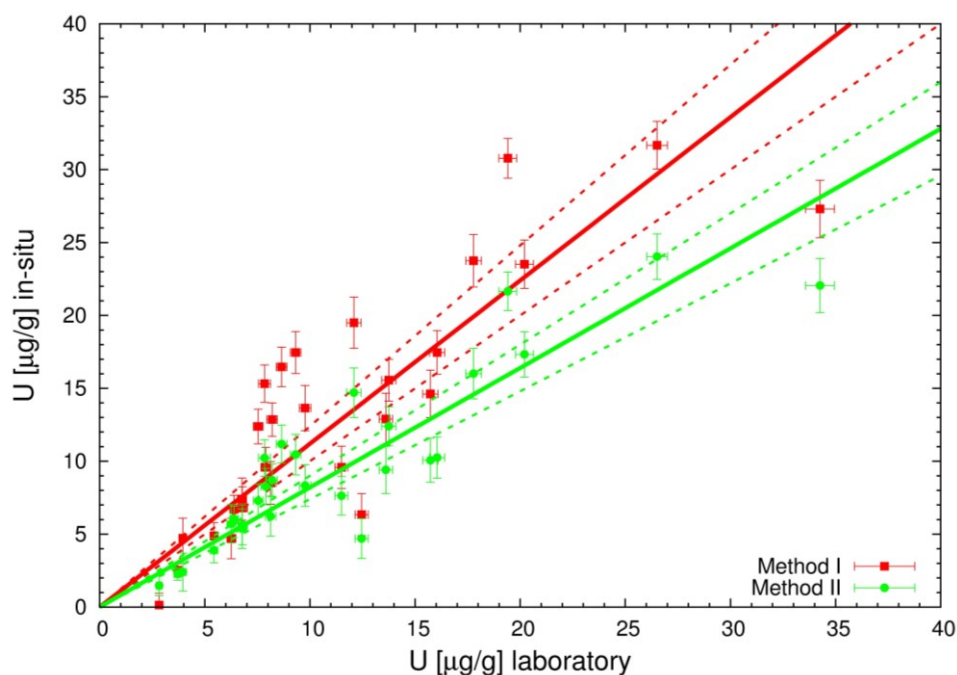


Figure III.2.11: correlation of the results obtained in-situ with Cava-Rad system analyzed with Method I ($U_{\text{situ}} = 1.12 \pm 0.12 U_{\text{lab}}$) and Method II ($U_{\text{situ}} = 0.82 \pm 0.08 U_{\text{lab}}$) sensitivity spectra compared with laboratory measurements with the MCA-Rad system.

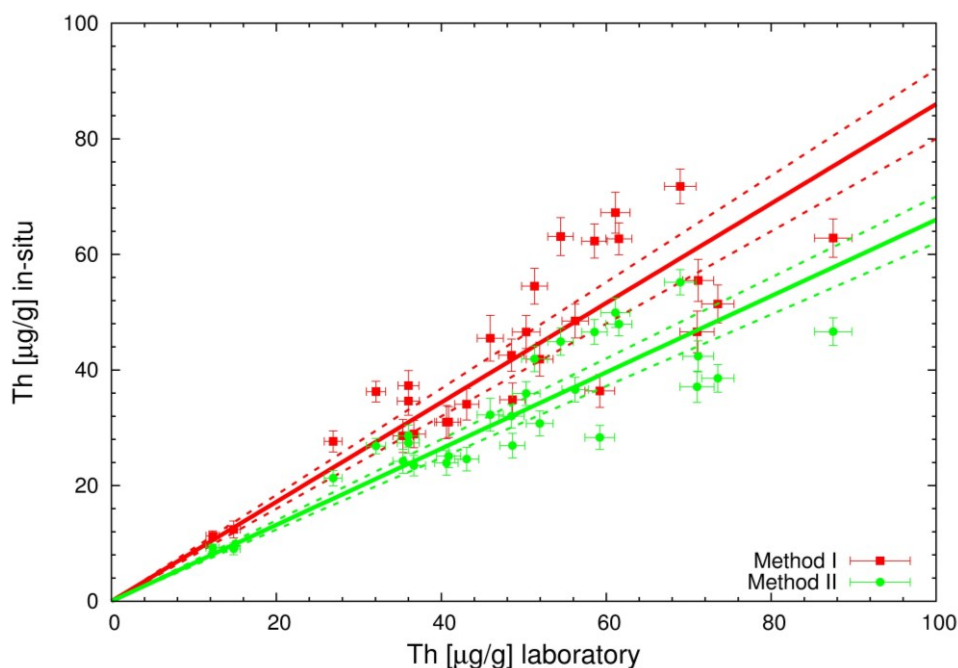


Figure III.2.12: correlation of the results obtained in-situ with Cava-Rad system analyzed with Method I ($Th_{\text{situ}} = 0.86 \pm 0.06 Th_{\text{lab}}$) and Method II ($Th_{\text{situ}} = 0.66 \pm 0.04 Th_{\text{lab}}$) sensitivity spectra compared with laboratory measurements with the MCA-Rad system.

In order to evaluate the capability of the Cava-Rad system to realize in-situ measurements of restricted area the results obtained with Method I were compared with the results obtained by analyzing only PbOut spectra respect to laboratory measurements. The second method is similar to the measurements described in Section I.2.3 and therefore measure the surrounding average environmental radioactivity. In Fig. III.2.13, Fig.III.2.14 and Fig. III.2.15 have shown the correlation obtained with laboratory measurements. We can observe that the statistical uncertainties obtained from the analysis of PbOut spectra are comparable with those obtained in the laboratory, differently from Method I. However, as it may be expected due to the site geometry the results obtained from the analysis of PbOut spectra are away from bisector within 95% confidence level for ^{40}K and ^{238}U , while for ^{232}Th is comparable within the uncertainty differently for results obtained with Method I which seems to underestimate ^{232}Th concentrations. To conclude, the Cava-Rad system give satisfactory results in the determination of ^{40}K and ^{238}U with some reserves for ^{232}Th . However, considering that the statistical uncertainty goes from less than 30% for ^{40}K and ^{238}U , and less than 15% for ^{232}Th this results seems weaker. Therefore, we believe that by considering other calibration sites and by performing longer calibration measurements, in order to achieve more statistics, these results will improve considerably.

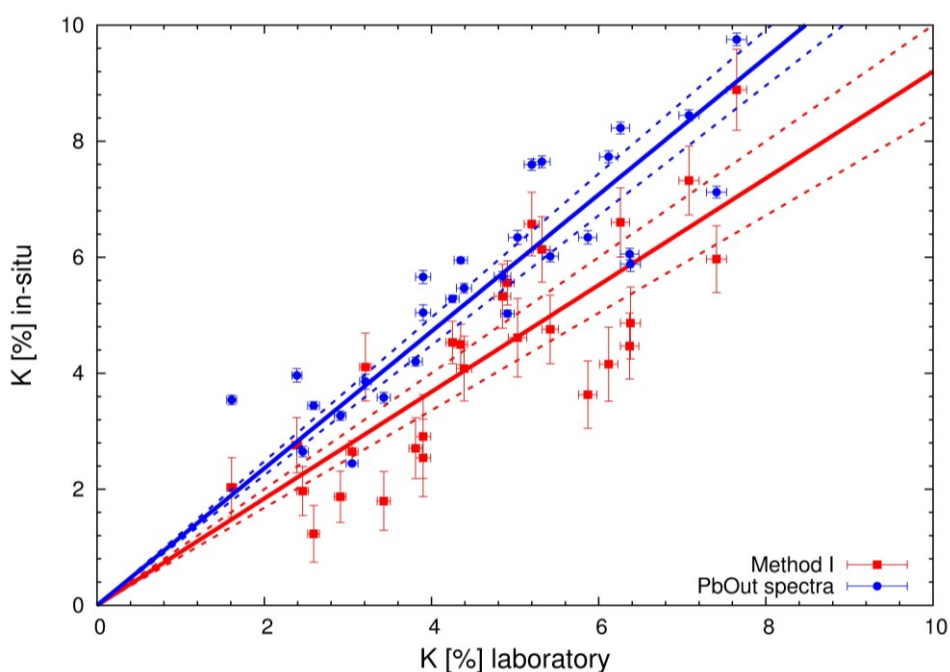


Figure III.2.10: correlation of the results obtained in-situ with Cava-Rad system analyzed with Method I ($K_{\text{situ}} = 0.92 \pm 0.08 K_{\text{lab}}$) and PbOut spectra ($K_{\text{situ}} = 1.18 \pm 0.06 K_{\text{lab}}$) sensitivity spectra compared with laboratory measurements with the MCA-Rad system.

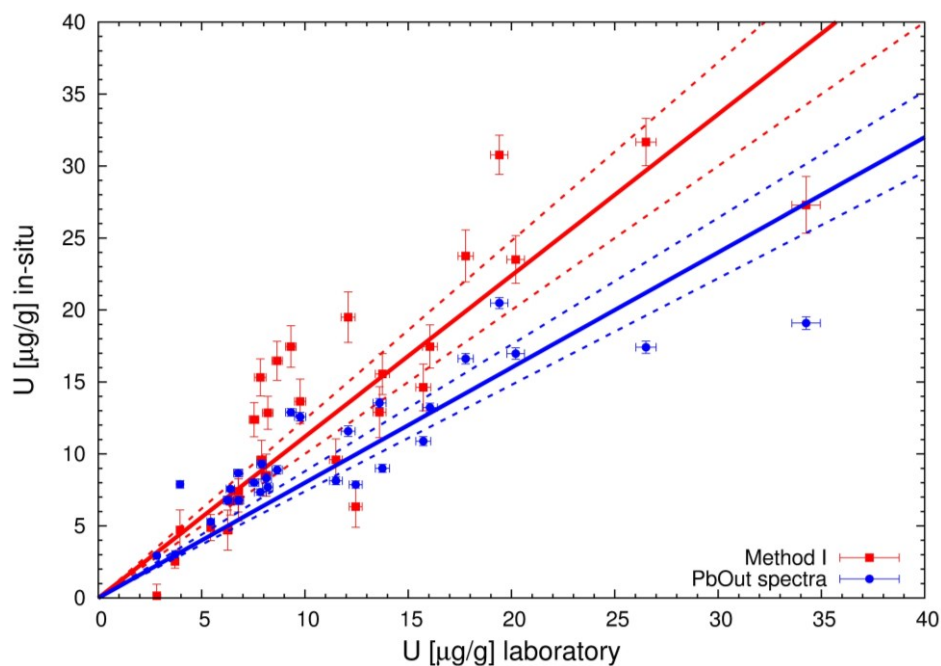


Figure III.2.14: correlation of the results obtained in-situ with Cava-Rad system analyzed with Method I ($U_{\text{situ}} = 1.12 \pm 0.12 U_{\text{lab}}$) and PbOut spectra ($U_{\text{situ}} = 0.80 \pm 0.08 U_{\text{lab}}$) sensitivity spectra compared with laboratory measurements with the MCA-Rad system.

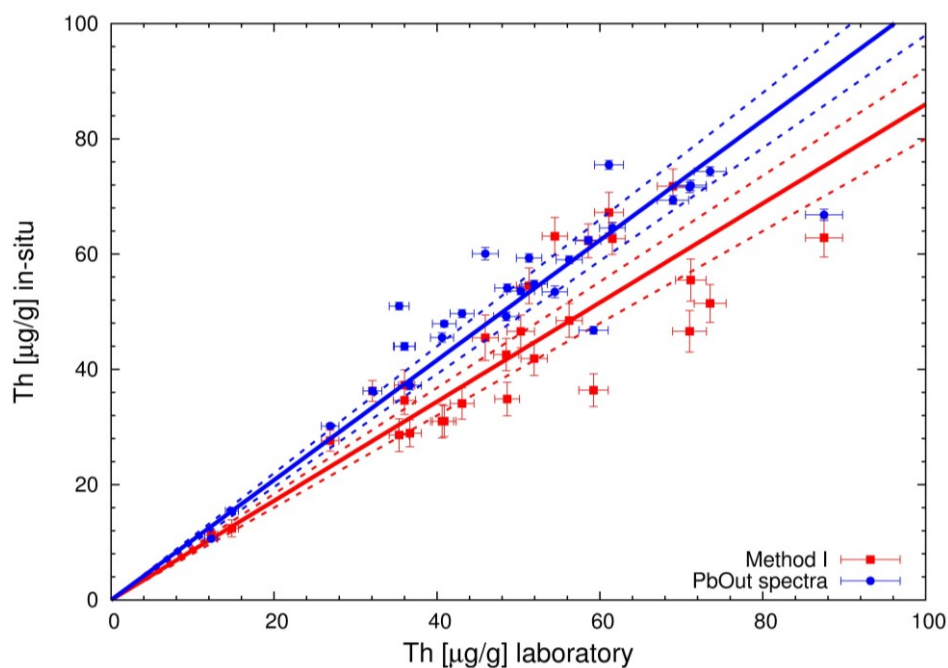


Figure III.2.15: correlation of the results obtained in-situ with Cava-Rad system analyzed with Method I ($Th_{\text{situ}} = 0.86 \pm 0.06 Th_{\text{lab}}$) and PbOut spectra ($Th_{\text{situ}} = 1.04 \pm 0.06 Th_{\text{lab}}$) sensitivity spectra compared with laboratory measurements with the MCA-Rad system.

Chapter III.3

Discussions and conclusions

In-situ gamma-ray spectrometry with scintillation NaI(Tl) detectors is widely used for assessing natural radionuclides (^{40}K , ^{238}U and ^{232}Th) under homogeneous spatial variability. Effort is made to improve the accuracy of in-situ measurements for determining the depth variability of radionuclides, especially artificial radionuclides like ^{137}Cs , by different methods. However, no effort is made on improving the accuracy of in-situ measurements in performing surveys on a restricted area, other than realizing collimated detectors by folding them with lead material. The disadvantages of such approach are that the lead used adds weight risking the portability of the instrument, and the counting time increases both because of the reduction of the field of view and size of the detector. Therefore, we designed and realized a portable collimated gamma-ray detector, called Cava-Rad system, with the objective of optimizing the weights in order to ensure the portability of the instrument and to reduce the counting time.

The basic principle of work of the Cava-Rad system was based on the lead plate method, introduced by (M. Korun, A. Likar et al. 1994). This method uses a circular lead plate positioned between the detector and the ground to shield out gamma rays from small angles in order to give an indication of the activity-depth distribution from the ratio of the peak counts obtained with the lead plate in place to that obtained without the lead plate. We improved such method in order to “filter” the background by subtracting the two measured spectra: the obtained difference spectra gives the unattenuated gamma-rays from a restricted area. The dimension of the lead plate is of fundamental importance since determine the quality of the difference spectra and therefore the accuracy of the measurement. In order to achieve reliable results in a shorter time we adopted the Full Spectrum Analysis method with Non-Negative Least Squares constrain for the calibration and spectrum analysis process. Therefore, a set of nine calibration sites was identified and characterized for ^{40}K , ^{238}U , ^{232}Th and ^{137}Cs by collecting samples and measuring them in the laboratory with the MCA-Rad system. Two different approaches were used to calibrate the Cava-rad system: the first methods use the difference spectra as input in order to obtain the sensitivity spectra, while the second method use the two sets of PbOut spectra and PbIn spectra to obtain the sensitivity spectra and then subtract them to obtain the Cava-rad sensitivity spectra. Finally, Cava-Rad system results to be a portable collimated gamma-ray spectrometer with a total weight of approximately 8 kg which can be used to realize in-situ measurements for counting times from 10 min to 30 min depending on the concentration of radionuclides.

Indeed, the Cava-Rad system was found to be a quick and practical instrument when applied on geological sites of particular spatial variability. In order to assess the accuracy of the results obtained from Cava-Rad system in 28 sites, located in Southern Tuscany Region and Veneto Region, we collected samples of rocks which were further measured in laboratory and the results were compared. The comparison between Cava-Rad results and laboratory results showed that the second approach of sensitivity calibration gives

underestimated concentrations of ^{40}K , ^{238}U and ^{232}Th . While, the first method gives results comparable with the laboratory measurements within 95% confidence level for ^{40}K and ^{238}U , and slightly underestimate the concentrations of ^{232}Th . This result is acceptable since ^{232}Th daughters have higher gamma-ray energies and therefore the spectra quality for a fixed counting time is slightly worse than other radionuclides. Therefore, this study poses as future prospectives the inclusion of other calibration sites and the increase of counting time in order to better validate the accuracy of the Cava-Rad system. Furthermore, in order to observe the capability of the Cava-Rad system to distinguish between close spatial variabilities the results were compared with those obtained from analyzing PbOut spectra (without collimation) respect to laboratory measurements. We observe that uncollimated spectra give overestimated results for ^{40}K and underestimated results for ^{238}U compared with laboratory measurements, while as it is expected for ^{232}Th show comparable results. As a consequence, the Cava-Rad system showed to give reliable results and to have a good spatial sensitivity on distinguishing close geological spatial variabilities.

References

- A. Bandrès, L. Eguiluz, et al. (2004). "The northern Ossa-Morena Cadomian batholith (Iberian Massif): magmatic arc origin and early evolution." Int J Earth Sci (Geol Rundsch) **93**: 860-885.
- A. Bralia, C. Ghezzi, et al. (1981). "Aspetti genetici del Batolite Sardo-Corso." Rend. Soc. It. Min. Petr. **38**: 701-764.
- A. Caciolli, M. Baldoncini, et al. (2012). "A new fsa approach for in situ gamma-ray spectroscopy." Science of The Total Environment **414**: 639-645.
- A. Castro, L. G. Corretge, et al. (2003). "The Appinite-Migmatite Complex of Sanabria, Nw Iberian Massif, Spain." Jornal of Petrology **44**(7): 1309-1344.
- A. Cesana and M. Terrani (1989). "An empirical method for peak-to-total ratio computation of a gamma-ray detector." Nuclear Instruments and Methods in Physics Research A **281**: 172-175.
- A. Cocherie (1978). "Geochemie des terres rares dans les granodiorites." Univ. Rennes.
- A. Cocherie (1985). "Interaction manteau-croûte: son rôle dans la genèse d'associations plutoniques calcoalcalines, contraintes geochemiques (éléments en traces et isotopes du strontium et de l'oxygène)." Doc. B.R.G.M **99**: 246.
- A. D. Moro, P. D. Simplicio, et al. (1975). "Radiometric data and intrusive sequence in the Sardinian Batholith." N. Jb. Miner. Abh **126**: 28-44.
- A. Di. Pisa, M. Attiglio, et al. (1992). "Pre-Hercynian magmatic activity in the Nappe Zone (internal and external) of Sardinia: evidence of two Within Plate basaltic cycles." Contribution to the Geology of Italy with special regard to the Paleozoic basement.
- A. Dini, G. Di Vincenzo, et al. (2005). "Monte Ollastèdu, a new gold discovery in the Variscan basement of Sardinia (Italy): first isotopic (^{40}Ar – ^{39}Ar , Pb) and fluid inclusion data." Mineralium Deposita **40**: 337-346.
- A. Forster and H. J. Forster (2000). "Crustal composition and mantle heat flow: Implication from surface heat flow and radiogenic heat production in the Variscan Erzgebirg (Germany)." Journal of Geophysical Research **105**: 27.917-927.938.
- A. Gèbelin, F. Roger, et al. (2009). "Syntectonic crustal melting and high-grade metamorphism in a transpressional regime, Variscan Massif Central, France." Tectonophysics **477**: 229-243.
- A. Gerdes, G. Worner, et al. (2000). "Post-collisional granite generation and HT–LP metamorphism by radiogenic heating: the Variscan South Bohemian Batholith." Journal of the Geological Society **157**: 577-587.

- A. J. Cresswell, D. C. W. Sanderson, et al. (2006). "137Cs measurement uncertainties and detection limits for airborne gamma spectrometry (AGS) data analysed using a spectral windows method." Appl Radiat Isot **64**: 247-253.
- A. M.R. Neiva, I.S. Williams, et al. (2009). "Geochemical and isotopic constraints on the petrogenesis of Early Ordovician granodiorite and Variscan two-mica granites from the Gouveia area, central Portugal." Lithos: 17.
- A. N. Tyler (2008). "In situ and airborne gamma-ray spectrometry." Radioactivity in the Environment **11**: 407-448.
- A. Puccini, G. Xhixha, et al. (2013). "Radiological characterization of granitoid outcrops and dimension stones of the Variscan Corsica-Sardinia Batholith." Environ Earth Sci.
- A.J. Cresswell and D.C.W. Sanderson (2009). "The use of difference spectra with a filtered rolling average background in mobile gamma spectrometry measurements." Nuclear Instruments and Methods in Physics Research A **607**: 685–694.
- B. De. Vivo, M. Boni, et al. (1997). "Baseline geochemical mapping of Sardinia (Italy)." Journal of Geochemical Exploration **60**(14): 77-90.
- B. J. Orsini (1980). "Le batholite Corso-Sarde: anatomie d'un batholite hercynien."
- B. J. Williamson, A. Shaw, et al. (1996). "Geochemical constraints on the genesis of Hercynian two-mica leucogranites from the Massif Central, France." Chemical Geology **127**: 25-42.
- B. R. S. Minty (1992). "Airborne gamma-ray spectrometric background estimation using full spectrum analysis." Geophysics **57**: 279.
- B. Tourlière, J. Perrin, et al. (2003). Use of airborne gamma-ray spectrometry for kaolin exploration.
- BIPM-5, M. (2004). "Table of Radionuclides." Bureau International des Poids et Mesure **2**(ISBN 92-822-2207-1).
- C- Riuz, C. F-Leyva, et al. (2008). "Geochemistry, geochronology and mineralisation potential of the granites in the Central Iberian Zone: The Jalama batholith." Science Direct **68**: 413-429.
- C. Boutsidis and P. Drineas (2009). "Random projections for the nonnegative least-squares problem." Linear Algebra Appl **431**: 760.
- C. Casquet, C. Galindo, et al. (2005). "The Aguablanca Cu–Ni ore deposit Extremadura, Spain , a case of synorogenic orthomagmatic mineralization: age and isotope
Abstract composition of magmas (Sr, Nd)and or (S)." Ore Geology Reviews **18**: 237-250.

- C. Ghezzi and J. B. Orsini (1982). "Lineamenti strutturali e composizionali del batolite ercinica Sardo-Corso in Sardinia." Guide Geologiche Regionali **165-182**.
- C. Jaupart and J-C. Marescha (2003). "Constraints on Crustal Heat Production from Heat Flow Data." Elsevier **3**.
- C. L. Lawson and R. J. Hanson (1995). Solving Least Square Problems, SIAM.
- C. Nuccetelli (2008). "In situ gamma spectroscopy in environmental research and monitoring." Applied Radiation and Isotopes **66**: 1615-1618.
- C. Raimann (2005a). "Geochemical mapping: technique or art?" Geochemistry: Exploration, Environment, Analysis **5**: 359-370.
- C. Vaccaro, P. Atzori, et al. (1991). "Geochronology and Sr isotope geochemistry of late-hercynian dykes from Sardinia." Schweiz. mineral. petrogr. **71**: 221-230.
- C. Villaseca, F. Bellido, et al. (2009). "Multiple crustal sources for post-tectonic I-type granites in the Hercynian Iberian Belt." Miner Petrol **96**: 197-211.
- Cuney, M. (1992). "The Beauvoir Topaz-Lepidolite Albite Granite (Massif Central, France): The Disseminated Magmatic Sn-Li-Ta-Nb-Be Mineralization." Economic Geology **87**: 1766-1794.
- D'Amico, C. (1960). "La massa dioritico-quarzifera di Bitti-Onani (Sardegna)." Acta Geol. Alpina **9**: 129-180.
- D. Arniaud, C. Dupuy, et al. (1995). "Geochemistry of Auriat Granite (Massif Central, France)." Chemical Geology **45**: 263-277.
- D. C. W. Sanderson, M. S. Baxter, et al. (1989). "COGER." Lancaster Conference.
- D. F. Strong (1981). "The leucogranites of southern Brittany: origin by faulting, Frictional heating, Fluid flux and Fraction melting
" Mineralogist **19**: 163-176.
- D. J. Crossley and A. B. Reid (1982). "Inversion of gamma ray data for element abundances." Geophysics **47**: 117.
- D. Langmuir and J. S. Herman (1980). "The mobility of thorium in natural waters at low temperatures." Geochim. Cosmochim. Acta **44**: 1753-1766.
- D. R. Bartlett (2004). "Radiation protection aspects of the cosmic radiation exposure of aircraft crew." Radiation Protection Dosimetry **4**: 349-355.

- E. C. Bullard and F. R. S (1942). "Radioactive heat generation in rocks " Royal Astron. Soc. Monthly Notices, Geophys. Suppl., **5**(2): 41-47.
- E. Jelink and A. dudek (1993). "Geochemistry of subsurface Precambrian plutonic rocks from the Brunovistulian complex in the Bohemian massif, Czechoslovakia " Elsevier **62**: 103-125.
- E. Tomarchio and S. Rizzo (2011). "Coincidence-summing correction equations in gamma-ray spectrometry with p-type HPGe detectors." Radiation Physics and Chemistry **80**: 318-323.
- F-J. L-Moro and M. L-Plaza (2004). "Monzonitic series from the Variscan Tormes Dome (Central Iberian Zone): petrogenetic evolution from monzogabbro to granite magmas." Lithos **72**.
- F. A. Secchi, P. Brotzu, et al. (1991). "The Arburese igneous complex (SW Sardinia, Italy) an example of dominant igneous fractionation leading to peraluminous cordierite-bearing leucogranites as residual melts " (Chemical Geology **92**: 213-249.
- F. Bea, P. Montero, et al. (1999). "Mafic Precursors, Peraluminous Granitoids, and Late Lamprophyres in the Avila Batholith: A Model for the Generation of Variscan Batholiths in Iberia."
- F. Birch (1954). "The present state of Geothermal investigations." Geophysics **19**(4): 645-659.
- F. Castorina and R. Petrini (1989). "Radiometric geochronology: some constraints to the isochron method by an iterative least-square approach." Geochemical Journal **23**: 100-1001.
- F. Finger, M. P. Roberts, et al. (1997). "Variscan granitoids of central Europe: their typology, potential sources and tectonothermal relations " Mineralogy and Petrology **61**: 67-96.
- F. Giacomini, R. M. Bomparola, et al. (2005). "Petrology and geochronology of metabasites with eclogite facies relics from NE Sardinia: constraints for the Palaeozoic evolution of Southern Europe." Lithos **82**: 221-248.
- F. Giacomini, R. M. Bomparola, et al. (2006). "The geodynamic evolution of the Southern European Variscides: constraints from the U/Pb geochronology and geochemistry of the lower Palaeozoic magmatic-sedimentary sequences of Sardinia (Italy)." Contrib Mineral Petrol **152**: 19-42.
- F. Lucazeau, G. Vasseur, et al. (1984). "Interpretation of heat flow data in the French Massif Central." Tectonophysics **103**: 99-119.
- F. Solgadi, J-F. Moyen, et al. (2007). "The role of Crustal Anatexis and Mantle-Derived Magmas in the Genesis of synorogenic Hercynian Granites of the Livradois area, French Massif Central." The Canadian Mineralogist **45**: 581-606.
- F.G. Knoll (1999). " Radiation Detection and Measurements." Third Edition, John Wiley & Sons.

- G. C. Negretti (1966). "Ricerche petrografiche sul complesso granitoide del settore di Busachi (Sardegna centrale)." Boll. Serv. Geol.d'It **87**: 145-247.
- G. Cruciani, M. Franceschelli, et al. (2001). "Migmatites, eclogitic, and granulitic rocks in NE Sardinia." Rendiconti Seminario Facoltà Scienze Università Cagliari Supplemento **71**.
- G. Cruciani, M. Franceschelli, et al. (2008). "Amphibole-bearing migmatites from the Variscan Belt of NE Sardinia, Italy: Partial melting of mid-Ordovician igneous sources." Lithos **105**: 208-224.
- G. Di. Vincenzo, R. Carosi, et al. (2004). "The Relationship between Tectono-metamorphic Evolution and Argon Isotope Records in White Mica: Constraints from in situ ^{40}Ar – ^{39}Ar Laser Analysis of the Variscan Basement of Sardinia." Journal of Petrology **45**(5): 1013-1043.
- G. Fiorentini, M. Lissia, et al. (2007). "Geo-neutrinos and earth's interior." Physics Reports **453**(5-6): 117-172.
- G. Ielsch, D. Thièblemont, et al. (2001). "Radon (^{222}Rn) level variations on a regional scale: influence of the basement trace element (U, Th) geochemistry on radon exhalation rates." Environmental Radioactivity **53**: 75-90.
- G. Ielsch, M. E. Cushing, et al. (2010). "Mapping of the geogenic radon potential in France to improve radon risk management: methodology and first application to region Bourgogne." Journal of Environmental Radioactivity **101**: 813-820.
- G. Menard and P. Molnar (1988). "Collapse of Hercynian Tibetan plateau into a Paleozoic European basin and range province." Nature **334**: 235-237.
- G. Musumeci (1992). "Ductile wrench tectonics and exhumation of Hercynian metamorphic basement in Sardinia: Monte Grighini Complex." Geodinamica Acta **5**: 119-133.
- G. Oggiano and A. D. Pisa (2001). "Introduction to the Sardinia geologic evolution." Rendiconti Seminario Facoltà Scienze Università Cagliari Supplemento **71**.
- G. Oggiano and Di. Pisa (1988). "I graniti peralliminiferi sin-tettonic nell'area di Aggius-Trinita D'Agultu e loro rapporti con le metamorfiti di alto grado della bassa Gallura." Bollettino della Società Geologica Italiana **107**(03-04).
- G. Poli, C. Ghezzi, et al. (1989). "Geochemistry of granitic rocks from the Hercynian Sardinia-Corsica batholith: Implication for magma genesis." Lithos **23**: 247-266.
- G. Poli and S. Tommasini (1999). "Geochemical modeling of acid–basic magma interaction in the Sardinia–Corsica Batholith: the case study of Sarrabus, southeastern Sardinia, Italy." Lithos **46**: 553-571.

- G. R. Beardsmore and J. P. Cull (2001). *Crustal Heat Flow: a guide to measurement and modelling*, 2001.
- G. R. Gilmore (2008). *Practical Gamma-ray Spectrometry*, John Wiley & Sons, Ltd.
- G. Reitz (1993). "Radiation Environment in the Stratosphere." *Health Physics* 48(5).
- G. Xhixha, G. P. Bezzon, et al. (2013). "The worldwide NORM production and a fully automated gamma-ray spectrometer for their characterization." *Journal of Radioanalytical and Nuclear Chemistry* 295: 445-457.
- H-J. Förster, G. Tischendorf, et al. (1999). *Jornal of Petrology* 40(11): 1613-1645.
- H. C. B. Martins, H. Sant'Ovaia, et al. (2009). "Genesis and emplacement of felsic Variscan plutons within a deep crustal lineation, the Penacova-Régua-Verín fault: An integrated geophysics and geochemical study (NW Iberian Peninsula)." *Lithos* 111: 142-155.
- H. C. Urey (1955). "The cosmic abundances of potassium, uranium, and thorium and the heat balances of the Earth, The moon, and mars." *Chemistry* 41.
- H. D. Smith, C. A. Robbins, et al. (1983). "A multi-function compensated spectral natural gamma ray logging system." *Soc Petrol Eng SPE* 12050.
- H. Downes and J.-L. Duthou (1988). "Isotopic and Trace-Element arguments for the lower-crustal origin of Hercynian granitoids and Pre-Hercynian Orthogneisses, Masiif Central (France)." *Chemical Geology* 68(291-308).
- H. Klápvová, J. Konopásek, et al. (1998). "Eclogites from the Czech part of the Erzgebirge: multi-stage metamorphic and structural evolution." *Journal of the Geological Society*, 155: 567-583.
- H. N. Cutshall, L. I. Larsen, et al. (1983). "Direct analysis of Pb-210 in sediment samples: self-absorption corrections." *Nuclear Instruments and Methods* 206: 309-312.
- H. Wackernagel (2003). "Multivariate Geostatistics: an introduction with Applications." *Springer-Verlag: Berlin*.
- Huang Y, Chubakov V, et al. (2013). "A reference Earth model for the heat-producing elements and associated geoneutrino flux." *Geochemistry, Geophysics, Geosystems* 14(6): 2003-2029.
- I. Barnet, P. Pacherová, et al. (2008). "Radon i geological Environment - Czech Experience " *Geological Survey*.
- I. M. H. R. Antunes, A. M. R. Neiva, et al. (2008). "The leucogranites of southern Brittany: origin by faulting, Frictional heating, Fluid flux and Fraction melting" *Lithos* 103: 445-465.

I. R. Finetti, Ed. (2005). Crop Project: deep Scismic Exploration of the central Mediterranean and Italy, Library of congress Cataloging in publication Data.

IAEA (1990). "Use of gamma ray data to define the natural radiation environment." IAEA-TECDOC566.

IAEA (2003). "Guidelines for radioelement mapping using gamma ray spectrometry data." IAEA-TECDOC1363.

J-M. Stussi, A. Cheilletz, et al. (2002). "The hidden monzogranite of Soultz-sous-Forêts (Rhine Graben, France)." Mineralogy, petrology and genesis 45-64.

J-P. Chiles and P. Delfiner (1999). "Geostatistics: modeling spatial uncertainty, Probability and Statistics Series, John Wiley and Sons, New York." Chichester.

J. A. Desbarats and G. P. Killeen (1990). "A least-squares inversion approach to stripping in gamma-ray spectral logging." Nucl Geophys 4(3): 343-410.

J. A. Plant, S. Reeder, et al. (2003). "The distribution of uranium over Europe: geological and environmental significance." Applied Earth Science 112.

J. A. Ramirez and S. Grundvig (2000). "Causes of geochemical diversity in peraluminous granitic plutons: the Jalama pluton, Central-Iberian Zone (Spain and Portugal)" Lithos 50: 171-190.

J. D. Appleton and J. C. H. Miles (2010). "A statistical evaluation of the geogenic controls on indoor radon concentrations and radon risk." Journal of Environmental Radioactivity 101: 799-803.

J. H. Schoen (2011). "Physical Properties of Rocks." Elsevier 2011.

J. Kemski, R. Klingel, et al. (2009). "From radon hazard to risk prediction-based on geological maps, soil gas and indoor measurements in Germany." Environ Geol 56: 1269-1279.

J. Kim and M. Cho (2003). "Low-pressure metamorphism and leucogranite magmatism, northeastern Yeongnam Massif, Korea: implication for Paleoproterozoic crustal evolution." Science Direct 122: 235-251.

J. L. Vigneresse and M. Cuney (1991). "Are Granites Representative of Heat Flow Provinces."

J. L. Vigneresse, M. Cuney, et al. (1989). "Selective heat-production element enrichment in a crust segment of the mid-European Variscan chain."

J. Lameyre and P. Bowden (1982). "Plutonic rock type series: Discrimination of various granitoid series and related rocks." Journal of Volcanology and Geothermal Research 14: 169-186.

- J. MacDonald, C. J. Gibson, et al. (1997). "A theoretical comparison of methods of quantification of radioactive contamination in soil using in situ gamma spectrometry." J. Radiol. Prot. **17**.
- K. Breiter, L. Ackerman, et al. (2013). "Behavior of trace elements in quartz from plutons of different geochemical signature: A case study from the Bohemian Massif, Czech Republic." Lithos **175-176**: 54-67.
- K. Breiter, M. Sokolová, et al. (1991). "Geochemical specialization of the tin-bearing granitoid massifs of NW Bohemia" Mineral. Deposita **26**: 298-306.
- K. M. Miller, P. Shebell, et al. (1994). "In situ gamma-ray spectrometry for the measurement of uranium in surface coils" Health Physics **67**: 140.
- K. Rybacek, P. J. and, et al. (1992). "In-situ determination of deposited radionuclide activities: improved method using derived depth distributions from measured photon spectra" Health Physics **62**: 519-528.
- L. Carmignani, G. Oggiano, et al. (2012). "Carta Geologica della Sardegna. Scala 1:250.00."
- L. Carmignani, G. Oggiano, et al. (2001). Memorie Carta Geologica D'Italia. Geologia della Sardegna a scala 1:200.000.
- L. Carmignani, P. Conti, et al. (2001). "Note Illustrative della Carta Geologica d'Italia alla scala 1:50.000, ." Servizio Geologico d'Italia. Casa Editrice: Istituto Poligrafico e Zecca dello Stato, Roma, Italia.
- L. Cortesogno, G. Cassinis, et al. (1998). "The Variscan post-collisional volcanism in LateCarboniferous–Permian sequences of Ligurian Alps, Southern Alps and Sardinia Italy : a synthesis." Lithos **45**: 305-328.
- L. Fedele, J. A. Plant, et al. (2008). "The rare earth element distribution over Europe: geogenic and anthropogenic sources." Geochemistry, Exploration, Environment, Analysis **8**: 3-18.
- L. G. Medaris, B. L. Beard, et al. (2005). "Garnet pyroxenite and eclogite in the Bohemian Massif: geochemical evidence for Variscan recycling of subducted lithosphere." Geol Rundsch **84**: 489-505.
- L. Grasty, L. K. Kosanke, et al. (1979a). "Fields of view of airborne gamma-ray detectors." Geophysics **44**: 1447-1411.
- L. Hecht, K. Thuro, et al. (1999). "Mineralogical and geochemical characteristics of hydrothermal alteration and episyenitization in the Königshain granites, northern Bohemian Massif, Germany." Earth Sciences **88**: 236-252.
- L. Lovborg, H. Wollenberg, et al. (1971). "Field Determination of Uranium and Thorium by Gamma-Ray Spectrometry, Exemplified by Measurements in the Ilimaussaq Alkaline Intrusion, South Greenland." Economic Geology **66**: 368-384.

- L. Moens, J. De Donder, et al. (1981). "Calculation of the absolute peak efficiency of gamma-ray detectors for different counting geometries." Nuclear Instruments and Methods **187**: 451-472.
- L. Rybach (1988). Determination of heat production rate. Handbook of terrestrial Heat-Flow Density Determination. R. Haenel, L. Rybach and L. Stegena: 125-142.
- M. Baldoncini (2010). Applicazione del metodo Non Negative Least Square alla Full Spectrum Analysis nel processo di calibrazione di uno spettrometro di raggi gamma portatile. Department Physics. Ferrara, University of Ferrara
- M. Caroff, N. Coin, et al. (2011). "The mafic–silicic layered intrusions of Saint-Jean-du-Doigt (France) and North-Guernsey (Channel Islands), Armorican Massif: Gabbro–diorite layering and mafic cumulate–pegmatoid association." Lithos: 675-692.
- M. Corsini and Y. Rolland (2009). "Late evolution of the southern European Variscan belt: Exhumation of the lower crust in a context of oblique convergence." Comptes Rendus Geoscience **341**(2-3): 214-223.
- M. Cuney (1987). "Geologic Environment, Mineralogy and fluid Inclusion of the Bois Noirs-Limouzat Uranium Vein, Forez, France." **73**: 1567-1610.
- M. E. P. Gomes, L. M. O. Martins, et al. (2013). "Natural radiation and geochemical data for rocks and soils, in the North International Douro Cliffs (NE Portugal)." Journal of Geochemical Exploration **130**: 60-64.
- M. Fernández, I. Marzàn, et al. (1998). "Heat flow, heat production, and lithospheric thermal regime in the Iberian Peninsula." Tectonophysics **291**: 29-53.
- M. Korun, A. Likar, et al. (1994). "In-situ measurement of Cs distribution in the soil " Nuclear Instruments and Methods in Physics Research **93**: 485-491.
- M. Maino, G. Dallagiovanna, et al. (2012). "U–Pb zircon geochronological and petrographic constraints on late to postcollisional Variscan magmatism and metamorphism in the Ligurian Alps, Italy." GEOLOGICAL JOURNAL **47**: 632-652.
- M. Maucec, P. H. G. M. Hendriks, et al. (2009). "Determination of correction factors for borehole natural gamma-ray measurements by Monte Carlo simulations." Nucl Instrum Methods A **609**: 1094-1011.
- M. P. Roberts, C. Pin., et al. (2000). "Petrogenesis of Mafic to Felsic Plutonic Rock Associations: the Calc-alkaline Quèrigut Complex, French Pyrenees." JOURNAL OF PETROLOGY **41**(6): 809-844.
- M. Pagel (1982). "The mineralogy and geochemistry of uranium, thorium, and rare-earth elements in two radioactive granites of the Vosges, France " Mineral petrologi **46**(339).

- M. R. Renna, R. Tribuzio, et al. (2006). "Interaction between basic and acid magmas during the latest stages of the post-collisional Variscan evolution: Clues from the gabbro–granite association of Ota (Corsica–Sardinia batholith)." Lithos **90**: 92-110.
- M. R. Renna, R. Tribuzio, et al. (2007). "Origin and timing of the post-Variscan gabbro–granite complex of Porto (Western Corsica)." Contrib Mineral Petrol **154**: 493-517.
- M. Verdoya, P. Chiozzi, et al. (2009). "Natural gamma ray spectrometry as a tool for radiation dose and radon hazard modelling." Appl Radiat Isot **67**: 964-965.
- M. Verdoya, V. Pasquale, et al. (1998). "Radiogenic heat production in the Variscan crust: new determinations and distribution models in Corsica (northwestern Mediterranean)." Elsevier **291**: 63-75.
- M. Verdoya, W. Pasquale, et al. (1998). "Radiogenic heat production in the Variscan crust: new determinations and distribution models in Corsica (northwestern Mediterranean)" Tectonophysics **291**(1-4): 63-75.
- O. Lexa, K. Schulmann, et al. (2011). "Heat sources and trigger mechanisms of exhumation of HP granulites in Variscan orogenic root." Metamorphic geology **29**: 79-102.
- P. Barbey, D. Gasquet, et al. (2008). "Igneous banding, schlieren and mafic enclaves in calc-alkaline granites: The Budduso pluton (Sardinia)" Lithos **104**(1-4): 147-163.
- P. Brotzu, L. Morbidelli, et al. (1978). "Caratteri petrografici e chimici delle sieniti del Sarrabus meridionale." Period. Min **47**: 83-98.
- P. Chiozzi, P. De. Felice, et al. (2000). "Laboratory application of NaI(Tl) gamma-ray spectrometry to studies of natural radioactivity in geophysics." Applied Radiation and Isotopes **53**: 127.
- P. Conti, L. Carmignani, et al. (1999). "From thickening to extension in the Variscan belt — kinematic evidence from Sardinia (Italy)." Terra Nova **11**(2-3): 93-99.
- P. De. Felice, A. Fazio, et al. (2006). "Close-geometry efficiency calibration of p-type HPGe detectors with a Cs-134 point source." Applied Radiation and Isotopes **64**: 1303-1306.
- P. De. Felice, P. Angelini, et al. (2000). "Fast procedures for coincidence-summing correction in g-ray spectrometry." Applied Radiation and Isotopes **52**: 745-752.
- P. Désesquelles, T. M. H. Ha, et al. (2009). "NNLC: non-negative least chi-square minimization and application to HPGe detectors." J Phys G: Nucl Part Phys **36**.

P. Di Simplicio, G. Ferrara, et al. (1974b). "Notes on the Paleozoic magmatism and metamorphism of Sardinia." Mem. Soc. Geol. It **13**: 161-164.

P. Dryàk and P. Kovàr (2009). "Table for true summation effect in gamma-ray spectrometry." Journal of Radioanalytical and Nuclear Chemistry **279**: 385-394.

P. Goovaerts (1997). "Geostatistics for natural resources evaluation, Applied geostatistics series.,." Geology Statistical methods, , Applied geostatistics series., Oxford University Press, New York ; Oxford.

P. H. G. M. Hendriks, J. Limburg, et al. (2001). "Full-spectrum analysis of natural γ -ray spectra. ." J Environ Radioact **53**: 365.

P. Hasalová, V. Janoušek, et al. (2008). "From orthogneiss to migmatite: Geochemical assessment of the melt infiltration model in the Gföhl Unit (Moldanubian Zone, Bohemian Massif)." Lithos **102**: 508-537.

P. J. Bolivar, M. Garcia-Leon, et al. (1997). "On Self-attenuation Corrections in Gamma-ray Spectrometry." Appl. Radiat(48): 1125-1126.

P. J. O'Brien (1989). "The petrology of retrogrades eclogites of the Oberpfalz Forest, northeastern Bavaria, West Germany " Tectonophysics **157**: 195-212.

P. Kovàriková, W. Siebel, et al. (2007). "Petrology, geochemistry and zircon age for redwitzite at Abertamy, NW Bohemian Massif (Czech Republic): tracing the mantle component in Late Variscan intrusions." Science Direct **67**: 151-174.

P. Macera, S. Conticelli, et al. (1989). "Geochemistry and Rb–Sr age of syntectonic peraluminous granites of Western Gallura, Northern Sardinia: constraints on their genesis." Periodico di mineralogia **58**(01-03): 25-43.

P. Matte (2001). "The Variscan collage and orogeny (480–290 Ma) and the tectonic definition of the Armorica microplate: a review." Terra Nova **13**(2): 122-128.

P. Rossi and A. Cocherie (1991). "Genesis of a Variscan batholith: Field, petrological and mineralogical evidence from the Corsica-Sardinia batholith." Tectonophysics **195**(2-4): 319-346.

P. Rossi, G. Oggiano, et al. (2009). "A restored section of the “southern Variscan realm” across the Corsica–Sardinia microcontinent." Comptes Rendus Geoscience **341**(2-3): 224-238.

P. Zombori, A. Andradi, et al. (1992). A New Method for the Determination of Radionuclide Distribution in the Soil by In-Situ Gamma-Ray Spectrometry Central Research Institute for Physics, Hungarian Academy of Sciences.

- R. Alther, A. Holl, et al. (2000). "High-potassium, calc-alkaline I-type plutonism in the European Variscides: northern Vosges (France) and northern Schwarzwald (Germany)." Lithos **50**: 51-73.
- R. Arenas, J. R. M. Catalàn, et al. (2007). "The Vila de Cruces Ophiolite: A Remnant of the Early Rheic Ocean in the Variscan Suture of Galicia (Northwest Iberian Massif)." The Journal of Geology **115**: 129-148.
- R. Carosi, C. Frassi, et al. (2005). "Post collisional transpressive tectonics in northern Sardinia (Italy)." The Virtual Explorer **19**.
- R. Carosi, C. Frassi, et al. (2006). "The Varsican basement of northern sardinia (Italy): Field guide to the excursion in the Baronie region." Atti Soc. tosc. Sci. nat., Mem.: 111.
- R. Carosi and G. Oggiano (2002). "Transpressional deformation in northwestern Sardinia (Italy): insights on the tectonic evolution of the Variscan Belt." Comptes Rendus Geoscience **334**(4).
- R. Carosi and R. Palmeri (2002). "Orogen-parallel tectonic transport in the Variscan belt of northeastern Sardinia (Italy): implications for the exhumation of medium-pressure metamorphic rocks." Geological Magazine **139**(05): 495-511.
- R. L. Rudnick and D. M. Fountain (1995). "Nature and Composition of the Continental Crust: A Lower crustal Perspective." Reviews of Geophysics **3**: 267-309.
- R. L. Rudnick and S. Gao (2003). "Composition of the Continental Crust." Treatise on geochemistry
- R. Tartese, G. Ruffet, et al. (2011). " Simultaneous resetting of the muscovite K-Ar and monazite U-Pb geochronometers: a story of fluids." Terra Nova **23**: 390-398.
- R. W. Van Schmus (1995). "Natural Radioactivity in Crust and Mantle. In T. J. Ahrens (ed.) Global Earth Physics – a Handbook of Physical Constants." AGU Reference Shelf 1, American geophysical Union, Washington D. C.: 283-291.
- R. Webster and M. A. Oliver (2007). "Geostatistics for Environmental Scientist." Chichester: Wiley.
- R.R. Benke and K. J. Kearfott (2002). "Demonstration of a collimated in situ method for determining depth distributions using gamma-ray spectrometry." Nuclear Instruments and Methods in Physics Research A **482**: 814–831.
- S. Enomoto (2005). Neutrino Geophysics and Observation of Geo-Neutrinos at KamLAND. Tohoku University.
- S. Enomoto, E. Ohtani, et al. (2007). "Neutrino geophysics with KamLAND and future prospects " Elsevier: Earth and Planetary Science Letters **258**: 147-159.

- S. Fourcade and C. J. Allegre (1981). "Trace Elements Behavior in Granite Genesis: A Case Study. The Calc-Alkaline Plutonic Association from the Queriguit Complex (Pyrénées, France) " Contrib Mineral Petrol **76**: 177-195.
- S. T. Dye (2011). "Geo-neutrinos as indicators of the origin and thermal history of the Earth " Thermal Geophysics, Elsevier, Amsterdam.
- S. Tommasini and G. Poli (1992). "Petrology of the late-Carboniferous Punta Falcone gabbroic complex, northern Sardinia, Italy " Contrib Mineral Petrol **110**: 16-32.
- S. Tommasini, G. Poli, et al. (1995). "The Role of Sediment Subduction and Crustal Growth in Hercynian Plutonism: Isotopic and Trace Element Evidence from the Sardinia—Corsica Batholith." Journal of Petrology **36**(5): 1305-1332.
- S. Tommasini, G. Poli, et al. (1999). "Trace element inferences on the evolution and genesis of the Monte Pulchiana Leucogranites, northern Sardinia, Italy." Periodico di Mineralogia **68**(1): 53-67.
- T. Donaire, E. Pascual, et al. (2005). "Microgranular enclaves as evidence of rapid cooling in granitoid rocks: the case of the Los Pedroches granodiorite, Iberian Massif, Spain." Contrib Mineral Petro **149**: 247-265.
- UNSCEAR (2008). Sources and Effects of Ionizing Radiation. United Nations Scientific Committee on the Effects of Atomic Radiation. **I**: 654.
- V. M. Hamza and A. E. Beck (1972). "terrestrial Heat Flow, the Neutrino Problem, and a Possible Energy Source in the Core." Nature Publishing group **240**.
- V. Záček and P. Sulovsky (2005). "The dyke swarm of fractionated tourmaline-bearing leucogranite and its link to the Vydra Pluton (Moldanubian batholith), Sumava Mts., Czech Republic." Journal of the Czech Geological Society **50**: 3-4.
- V. Ziegler and J. Dardel (1984). "Uranium deposits in Europe " Direction de l' Approvisionnement en Matieres Nucleaires, Commissariat a l'Energie Atomique, Paris, France.
- W. Sowa, E. Martini, et al. (1989). "Uncertainties of in-situ gamma spectrometry for environmental monitoring Radiat." Prot. Dosim. **27**: 93-101.
- Y. Denèle, J.-L. Pasquette., et al. (2011). "Permian granites in the Pyrenees: the Aya pluton (Basque Country)." Terra Nova **24**: 105-113.

Appendix A

The average SiO₂ content in rocks of Sardinia

Table A.1: The average ($\pm 1 \sigma$ standard deviation) SiO₂ (in % wt.) content in the rocks of Sardinia obtained from bibliographic studies.

Rock type		SiO ₂ $\pm \sigma$ (wt. %)
amphibolite	Mafic (45-52 %) ⁽¹⁾	47.9 \pm 4.1
eclogite		47.2 \pm 2.7
granodiorite	Intermediate (52-63%) ⁽²⁾	65.3 \pm 4.5
tonalite		58.8 \pm 3.0
quartzodiorite		53.2 \pm 2.8
granite	Felsic (> 63%) ⁽³⁾	72.7 \pm 1.0
leucogranite		75.1 \pm 1.0
monzogranite		73.2 \pm 1.6
leuco-monzogranito		76.3 \pm 1.8
sienogranito		74.7 \pm 0.6

(1) (G. Cruciani, M. Franceschelli et al. 2001); (F. Giacomini, R. M. Bomparola et al. 2005);

(2) (A. Puccini, G. Xhixha et al. 2013); (P. Barbey, D. Gasquet et al. 2008); (S. Tommasini and G. Poli 1992); (G. Cruciani, M. Franceschelli et al. 2008); (F. A. Secchi, P. Brotzu et al. 1991); (M. R. Renna, R. Tribuzio et al. 2006) (F. Giacomini, R. M. Bomparola et al. 2006); (G. Poli and S. Tommasini 1999);

(3) (G. Poli, C. Ghezzi et al. 1989); (F. A. Secchi, P. Brotzu et al. 1991); (A. Puccini, G. Xhixha et al. 2013); (P. Barbey, D. Gasquet et al. 2008); (S. Tommasini and G. Poli 1992); (P. Rossi and A. Cocherie 1991).

Appendix B

List of publications

Appendix B1

E. Guastaldi, M. Baldoncini, G.P. Bezzon, C. Broggin, G.P. Buso, A. Caciolli, L. Carmignani, I. Callegari, T. Colonna, K. Dule, G. Fiorentini, **M. Kaçeli Xhixha**, F. Mantovani, G. Massa, R. Menegazzo, L. Mou, C. Rossi Alvarez, V. Strati, G. Xhixha, A. Zanon. *A multivariate spatial interpolation of airborne γ -ray data using the geological constraints. Remote Sensing of Environment (2013)*. Doi: <http://dx.doi.org/10.1016/j.rse.2013.05.027> (*Impact Factor 5.1*)

Appendix B2

I. Callegari, G.P. Bezzon, C. Broggin, G.P. Buso, A. Caciolli, L. Carmignani, T. Colonna, G. Fiorentini, E. Guastaldi, **M. Kaçeli Xhixha**, F. Mantovani, G. Massa, R. Menegazzo, L. Mou, A. Pirro, C. Rossi Alvarez, V. Strati, G. Xhixha, A. Zanon. *Total natural radioactivity map of Tuscany (Italy). Journal of Maps (2013)*. Doi: <http://dx.doi.org/10.1080/17445647.2013.802999> (*Impact Factor 0.7*)

Appendix B3

A. Puccini, G. Xhixha, S. Cuccuru, G. Oggiano, **M. Kaçeli Xhixha**, F. Mantovani, C. Rossi Alvarez, L. Casini. *Radiological characterization of granitoid outcrops and dimension stones of the Variscan Corsica-Sardinia Batholith. Environmental Earth Sciences (2013)*. Doi: <http://dx.doi.org/10.1007/s12665-013-2442-8> (*Impact Factor 1.4*)

Appendix B4

G. Xhixha, A. Ahmeti, G.P. Bezzon, M. Bitri, C. Broggin, G.P. Buso, A. Caciolli, I. Callegari, F. Cfaraku, T. Colonna, G. Fiorentini, E. Guastaldi, F. Mantovani, G. Massa, R. Menegazzo, L. Mou, D. Prifti, C. Rossi Alvarez, Dh. Sadiraj Kuqi, M. Shyti, L. Tushe, **M. Xhixha Kaçeli**, A. Zyfi. *First Characterization Of Natural Radioactivity In Building Materials Manufactured In Albania. Radiation Protection Dosimetry (2013) 155(2):217–223*. Doi: <http://dx.doi.org/10.1093/rpd/ncs334> (*Impact Factor 0.9*)

Appendix B5

G. Xhixha, G.P. Bezzon, C. Broggin, G.P. Buso, A. Caciolli, I. Callegari, S. De Bianchi, G. Fiorentini, E. Guastaldi, F. Mantovani, G. Massa, R. Menegazzo, L. Mou, A. Pasquini, C. Rossi Alvarez, M. Shyti, **M. Kaçeli Xhixha**. *The worldwide NORM production and a fully automated gamma-ray spectrometer for their characterization. Journal of Radioanalytical and Nuclear Chemistry (2013) 295:445–457*. Doi: <http://dx.doi.org/10.1007/s10967-012-1791-1> (*Impact Factor 1.5*)



Contents lists available at SciVerse ScienceDirect

Remote Sensing of Environment

journal homepage: www.elsevier.com/locate/rse

A multivariate spatial interpolation of airborne γ -ray data using the geological constraints



Enrico Guastaldi ^{a,*}, Marica Baldoncini ^c, Giampietro Bezzon ^d, Carlo Broggin ^b, Giampaolo Buso ^d, Antonio Cacioli ^b, Luigi Carmignani ^a, Ivan Callegari ^a, Tommaso Colonna ^a, Kujtim Dule ^h, Giovanni Fiorentini ^{c,d,e}, Merita Kaçeli Xhixha ^g, Fabio Mantovani ^{c,e}, Giovanni Massa ^a, Roberto Menegazzo ^b, Liliana Mou ^d, Carlos Rossi Alvarez ^b, Virginia Strati ^c, Gerti Xhixha ^{c,d,f}, Alessandro Zanon ^d

^a CGT Center for GeoTechnologies, University of Siena, Via Vetri Vecchi, 34, 52027 San Giovanni Valdarno, Arezzo, Italy

^b Istituto Nazionale di Fisica Nucleare (INFN), Padova Section, Via Marzolo 8, 35131 Padova, Italy

^c Department of Physics and Earth Sciences, University of Ferrara, Via Saragat, 1, 44100 Ferrara, Italy

^d Istituto Nazionale di Fisica Nucleare (INFN), Legnaro National Laboratory, Via dell'Università, 2, 35020 Legnaro, Padova, Italy

^e Istituto Nazionale di Fisica Nucleare (INFN), Ferrara, Via Saragat, 1, 44100 Ferrara, Italy

^f Faculty of Forestry Science, Agricultural University of Tirana, Kodër Kamëz, 1029 Tirana, Albania

^g University of Sassari, Botanical, Ecological and Geological Sciences Department, Piazza Università 21, 07100 Sassari, Italy

^h Faculty of Natural Sciences, University of Tirana, Bulevardi "Zogu I", Tirana, Albania

ARTICLE INFO

Article history:

Received 4 February 2013

Received in revised form 24 May 2013

Accepted 26 May 2013

Available online xxxx

Keywords:

Multivariate analysis

Airborne γ -ray spectrometry

Collocated cokriging interpolator

Elba Island

Natural radioactivity

Geological constraint

ABSTRACT

In this paper we present maps of K, eU, and eTh abundances of Elba Island (Italy) obtained with a multivariate spatial interpolation of airborne γ -ray data using the constraints of the geologic map. The radiometric measurements were performed by a module of four NaI(Tl) crystals of 16 L mounted on an autogyro. We applied the collocated cokriging (CCoK) as a multivariate estimation method for interpolating the primary under-sampled airborne γ -ray data considering the well-sampled geological information as ancillary variables. A random number has been assigned to each of 73 geological formations identified in the geological map at scale 1:10,000. The non-dependency of the estimated results from the random numbering process has been tested for three distinct models. The experimental cross-semivariograms constructed for radioelement-geology couples show well-defined co-variability structures for both direct and crossed variograms. The high statistical correlations among K, eU, and eTh measurements are confirmed also by the same maximum distance of spatial autocorrelation. Combining the smoothing effects of probabilistic interpolator and the abrupt discontinuities of the geological map, the results show a distinct correlation between the geological formation and radioactivity content. The contour of Mt. Capanne pluton can be distinguished by high K, eU and eTh abundances, while different degrees of radioactivity content identify the tectonic units. A clear anomaly of high K content in the Mt. Calamita promontory confirms the presence of felsic dykes and hydrothermal veins not reported in our geological map. Although we assign a unique number to each geological formation, the method shows that the internal variability of the radiometric data is not biased by the multivariate interpolation.

© 2013 Elsevier Inc. All rights reserved.

1. Introduction

Airborne γ -ray spectrometry (AGRS) is a fruitful method for mapping natural radioactivity, both in geoscience studies and for purposes of emergency response. One of the principal advantages of AGRS is that it is highly appropriate for large scale geological and environmental surveys (Bierwirth & Brodie, 2008; Minty, 2011; Rybach et al., 2001; Sanderson et al., 2004). Typically, the AGRS system is composed of four 4 L NaI(Tl) detectors mounted on an aircraft. For fixed conditions of flight a challenge is to increase the amount of geological information, developing dedicated algorithms for data analysis

and spatial interpolation. The full spectrum analysis (FSA) with the non-negative least squares (NNLS) constraint (Cacioli et al., 2012) and noise-adjusted singular value decomposition (NASVD) analysis (Minty & McFadden, 1998) introduces notable results oriented to improve the quality of the radiometric data. On the other hand, the multivariate interpolation has the great potential to combine γ -ray data with the preexisting information contained in geological maps for capturing the geological local variability.

Elba Island (Italy) is a suitable site for testing a multivariate interpolation applied to AGRS data because of its high lithological variability, excellent exposure of outcropping rocks and detailed geological map. In multivariate statistical analysis, different pieces of information about the particular characteristics of a variable of interest may be better predicted by combining them with other interrelated ancillary information

* Corresponding author. Tel.: +39 0559119423; fax: +39 0559119439.

E-mail addresses: guastaldi@unisi.it, enrico.guastaldi@gmail.com (E. Guastaldi).

into a single optimized prediction model. This approach improves the results of the spatial interpolation of environmental variables. However, sometimes primary and ancillary variables are sampled by different supports, measured on different scales, and organized in different sampling schemes, which makes spatial prediction more difficult.

In this study the collocated cokriging (CCoK) was used in a non-conventional way for dealing with the primary (AGRS data) and secondary (geological data) variables when the variable of interest has been sampled at a few locations and the secondary variable has been extensively sampled. Using this approach, we provide the map of natural radioactivity of Elba Island.

2. Instruments and methods

2.1. Geological setting

Elba is the biggest island of the Tuscan Archipelago and is located in the northern part of the Tyrrhenian Sea, between Italy and Corsica Island (France). It is one of the westernmost outcrop of the Northern Apennines mountain chain (Fig. 1).

The geological distinctive features of this island are linked to its complex stack of tectonic units and the well-known Fe-rich ores, as well as the well-exposed interactions between Neogene magmatic intrusions and tectonics (Bortolotti et al., 2001; Dini et al., 2002; Musumeci & Vaselli, 2012; Trevisan, 1950). The structure of Elba Island consists of thrust sheets stacked during the late Oligocene to middle Miocene northern Apennines deformation. Thrust sheets are cross-cut by late Miocene extensional faults (Bortolotti et al., 2001; Keller & Coward, 1996; Smith et al., 2011).

The tectonics of Elba Island is composed of a structural pile of five main units called by Trevisan (1950) as “Complexes” and hereafter called “Complexes of Trevisan” (TC): the lowermost three belong to the Tuscan Domain, whereas the uppermost two are related to the Ligurian Domain. Bortolotti et al. (2001) performed 1:10,000 mapping of central-eastern Elba and proposed a new stratigraphic and tectonic model in which the five TC were reinterpreted and renamed. TCs are shortly described below.

The Porto Azzurro Unit (TC I) (Mt. Calamita Unit Auct.) consists of Paleozoic micaschists, phyllites, and quartzites with local amphibolitic horizons, as well as Triassic-Hettangian metasiliciclastics and meta-carbonates. Recently Musumeci et al. (2011) point out Early Carboniferous age for the Calamita Schist by means of U–Pb and ^{40}Ar – ^{39}Ar radioisotopic data. In particular, in the Porto Azzurro area and the eastern side of Mt. Calamita, the micaschists are typically crosscut by the aplitic and microgranitic dykes that swarm from La Serra–Porto Azzurro monzogranitic pluton (5.1–6.2 Ma, Dini et al., 2010 and references therein). Magnetic activities have produced thermometamorphic imprints in the host rocks (Garfagnoli et al., 2005; Musumeci & Vaselli, 2012).

The Ortano Unit (lower part of TC II) includes metavolcanics, metasandstone, white quartzites and minor phyllites. The Acquadolce Unit (upper part of TC II) is composed of locally dolomitic massive marbles, grading upwards to calcschists (Pandeli et al., 2001). This lithology is capped by a thick siliciclastic succession. Ortano and Acquadolce units experienced late Miocene contact metamorphism under low to medium metamorphic grade conditions (Duranti et al., 1992; Musumeci & Vaselli, 2012).

The Monticiano–Roccastrada Unit (lower part of TC III) includes basal fossiliferous graphitic metasediments of the Late Carboniferous–Early

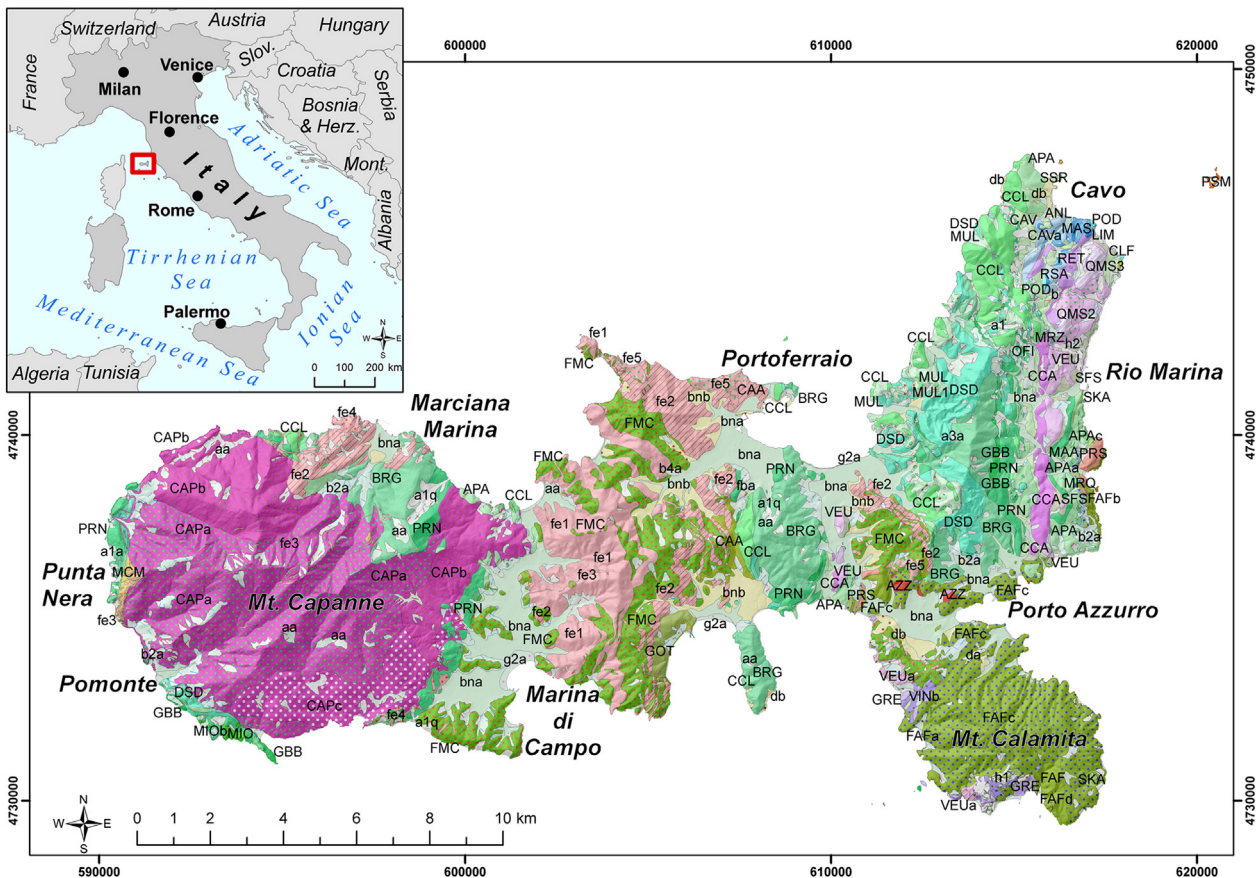


Fig. 1. Geological map of Elba Island (taken from the Geological Map of Tuscany region realized at scale 1:10,000, see CGT, 2011): the western sector is mainly characterized by intrusive igneous rocks (magenta), the central and eastern sectors are characterized by a wide lithological variation (green, purple, and pink), while the southeastern outcrop is constituted almost exclusively of metamorphic rocks (Mt. Calamita). For the legend of the geologic map, see <http://www.geologiatoscana.unisi.it>. The coordinate system is UTM WGS84 Zone 32 North. (For interpretation of the references to color in this figure legend, the reader is referred to the web version of this article.)

Permian, unconformably overlain by the detrital Verrucano succession (Middle-Late Triassic) (Bortolotti et al., 2001). The Tuscan Nappe Unit (central part of TC III) is represented by calcareous-dolomitic breccias and overlying carbonatic outcrops northwards. Most of the Grassera Unit (upper part of TC III) is composed of varicolored slates and siltstones with rare metalimestone or meta-chert intercalations; basal calcschists also occur.

The Ophiolitic Unit (TC IV) is composed of several minor thrust sheets or tectonic sub-units, which are characterized by serpentinites, ophicalcites, Mg-gabbros, and Jurassic-Lower Cretaceous sedimentary cover (Bortolotti et al., 2001).

The Paleogene Flysch Unit (lower part of TC V) mainly consists of shales, marls with limestone, sandstone, and ophiolitic breccia intercalations including fossils of the Paleocene-Eocene age. The Lower-Upper Cretaceous Flysch Unit (upper part of TC V) consists of basal shales and varicolored shales. These lithologies vertically pass to turbiditic siliciclastic sandstones and conglomerates, which in turn alternate with marlstones and marly limestones. Both Flysch Units were intruded by aplitic and porphyritic dykes and laccoliths approximately 7–8 Ma ago (Dini et al., 2002).

The geological structure of the island allows a nearly complete representation of lithologies present in the Northern Apennines mountain chain (Fig. 1). This feature makes Elba Island a complex system in terms of both geological formations and lithologies. Therefore, it is a formidable research site for applying a multivariate interpolation of radiometric data in relationship to lithological properties.

2.2. Experimental setup, survey, and data

The AGRS system is a modular instrument composed of four NaI(Tl) detectors (10 × 10 × 40 cm each) with a total volume of 16 L mounted on an autogyro (Fig. 2). The system is further equipped with a 1 L “upward-looking” NaI(Tl) detector, partially shielded from the ground radiation and used to account for atmospheric radon. Other auxiliary instruments, including the GPS antenna and pressure and temperature sensors, are used to record the position of the AGRS system and to measure the height above the ground using the Laplace formula (IAEA, 1991).

As a survey strategy, we planned to be as perpendicular as possible to the main N–S strike of the geological structures of the area (Fig. 1). The flight lines were designed in a spiral structure, constrained by the morphology of the terrain (elevations 0–1010 m a.m.s.l.), starting from the shore and following the heights of the mountains in the counterclock direction (Figs. 6, 7, 8). The unique region not properly covered by the airborne γ -ray survey is the top of Capanne Mt., because of the cloudy weather conditions. Averaging the flight altitudes recorded every 2 s we have 140 ± 50 m (standard deviation). The survey parameters were designed for a cruise speed of approximately 100 km/h, with space lines at most 500 m from one another. For our flight conditions, the detection system is able to measure the signal (97%) coming from a spot area of approximately 600 m radius, even if 90% comes from the half of this radius. In this study, the effect of attenuation of the signal from the biomass (Carroll & Carroll, 1989; Schetselaar et al., 2000) was neglected since Elba Island is covered by a large extension of rock outcrops and scattered vegetation of Mediterranean scrub.

The signal is acquired in list mode (event by event) using an integrated electronic module with four independent signal-processing channels and then analyzed offline in 10 s intervals. This time interval is chosen such as to optimize the loss in spatial resolution and to reduce the statistical uncertainty to less than 10%. The γ -spectra are calibrated and analyzed using the full spectrum analysis with non-negative least squares (FSA-NNLS) approach as described in Cacioli et al. (2012). According to the FSA method the spectrum acquired during the offline analysis is fitted as a linear combination of the fundamental spectra derived for each radioelement and for

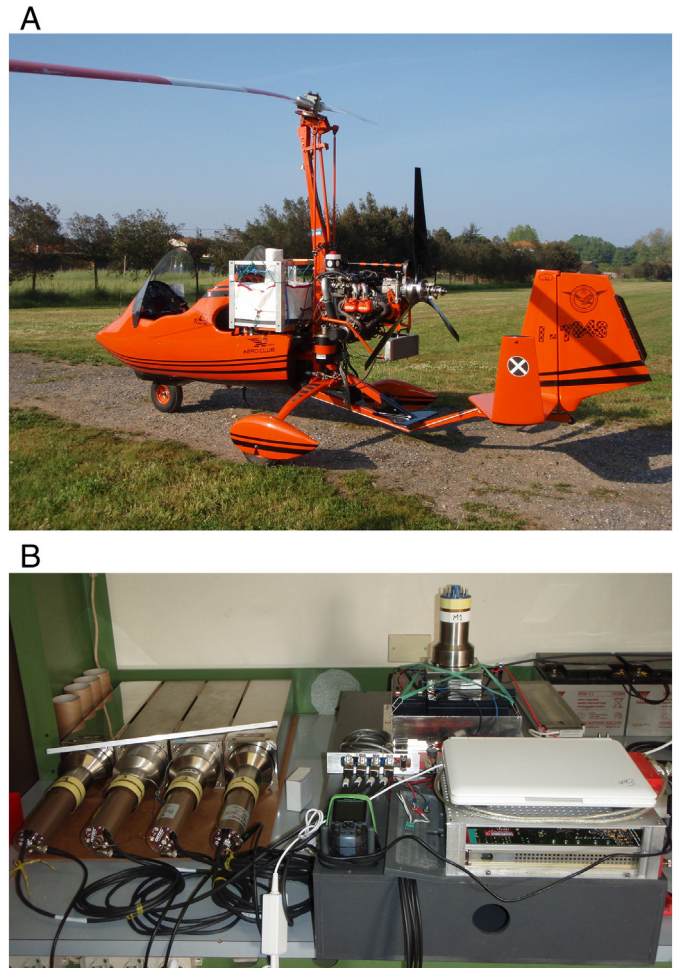


Fig. 2. The airborne γ -ray setup (B) mounted on the autogyro (A). The main detector system is inserted in the box under the “upward-looking” detector, which is placed behind the laptop.

background from the calibration process. The abundances are determined applying the non-negative least squares to minimize the χ^2 : the NNLS algorithm reduces the presence of non-physical results, which can lead to systematic errors (Cacioli et al., 2012).

Several corrections are applied to the signal measured at different flight altitudes to determine the concentrations of K, eU (equivalent uranium) and eTh (equivalent thorium) at the ground: a) aircraft and cosmic background correction; b) topology correction; c) flying altitude and height correction and d) atmospheric radon correction. The dead time correction was found to be negligible due to relatively low count rates measured during the flight. The background correction is taken into account during the calibration process where the fundamental spectra of the background due to the aircraft and cosmic radiation are estimated. The numeric regional topographic map at 1:10,000 scale of the ground surface has been accounted for the digital elevation model, which has a 10 m spatial resolution. The effects of the steep Elba Island's topography (ranging between 0 m to 1010 m a.m.s.l.) are corrected following the method described in Schwarz et al. (1992). Finally, to compute the concentration at the ground surface, the signal is further corrected by an empirical factor obtained by measuring the signal at several altitudes over a flat surface well characterized by ground measurements. The altitude and topography corrections introduce a total systematic uncertainty on the order of 10% in the final results.

Further corrections are required for eU concentration because the signal coming from ground uranium is increased by the radon gas in the air. It is evaluated by using the method of the “upward-looking”

detector, following the procedure described in IAEA (1991). The atmospheric radon concentration is estimated by analyzing the spectrum acquired with the “upward-looking” detector, which is calibrated by flying over the Tyrrhenian Sea at the beginning and the end of the survey. The radon concentration has been calculated for each time interval and was almost stable during the entire flight ($0.2 \pm 0.1 \mu\text{g/g}$). Since the ground abundance of eU varies from $0.2 \mu\text{g/g}$ up to $28.0 \mu\text{g/g}$ over all of Elba Island, the uncertainty concerning the atmospheric radon subtraction for each single measurement varies from 2% up to 100%: indicatively in average the relative uncertainty was 23%.

The relative uncertainties for K, eU, and eTh abundances¹ in the final results are summarized in Table 1. The systematic relative uncertainties are estimated by combining the contributions from the altitude and topography corrections and the calibration process. We emphasize that the data used as input in the CCoK interpolation are taken into account without experimental uncertainties and that their positions are related to the center of the spot area.

2.3. Geostatistical data analysis

Geostatistics involves spatial datasets, predicting distributions that characterize the coregionalization between the variables. The CCoK is a special case of cokriging wherein a secondary variable is available at all prediction locations and is used to estimate a primary under-sampled variable, restricting the secondary variable search to a local neighborhood. Frequently, the primary and ancillary (secondary) variables are sampled by different supports, measured on different scales, and organized in different sampling schemes, making the spatial prediction more complex. The integration of data that may differ in terms of type, reliability, and scale has been studied in several works. In Babak and Deutsch (2009), for instance, this approach is adopted using dense 3D seismic data and test data for an improved characterization of reservoir heterogeneity.

This approach is also used for mapping soil organic matter (Pei et al., 2010), rainfall, or temperature over a territory (Goovaerts, 1999; Hudson & Wackernagel, 1994); ground based radiometry data (Atkinson et al., 1992); estimating environmental variables, such as pollutants or water tables (Desbarats et al., 2002; Guastaldi & Del Frate, 2012; Hoeksema et al., 1989); and mapping geogenic radon gas in soil (Buttafuoco et al., 2010). To date, this method has not been applied to airborne γ -ray measurements integrated with geological data. A multivariate technique for interpolating airborne γ -ray data on the basis of the geological map information is desirable.

We used the collocated cokriging as a multivariate estimation method for the interpolation of primary under-sampled airborne γ -ray data using a constraint based on the secondary well-sampled geological information. This section briefly describes the theoretical background of CCoK interpolation and its application to airborne γ -ray data using geological constraints.

2.3.1. Collocated cokriging: theoretical background

Geostatistical interpolation algorithms construct probability distributions that characterize the present uncertainty by the coregionalization among variables (Wackernagel, 2003). The CCoK is an interpolation method widely used when applying a linear coregionalization model (LCM) to a primary under-sampled variable $Z_1(x)$ and a secondary widely sampled variable $Z_2(x)$ continuously known at all grid nodes (Goovaerts, 1997).

Xu et al. (1992) advanced a definition in which the neighborhood of the auxiliary variable $Z_2(x)$ is arbitrarily reduced to the target

¹ The activity concentrations of $1 \mu\text{g/g}$ U (Th) corresponds to 12.35 (4.06) Bq/kg and 1% K corresponds to 313 Bq/kg.

Table 1

Experimental relative uncertainties for the measured abundances of K, eU, and eTh.

Radionuclide	Statistical	Systematic
K	7%	14%
eU	8%	~30% ^a
eTh	8%	15%

^a Includes the uncertainty related to atmospheric radon correction.

estimation location x_0 only. They formulated CCoK as a simple cokriging linked to the covariance structure (Chiles & Delfiner, 1999):

$$\rho_{12}(h) = \rho_{12}(0)\rho_{11}(h) \quad (1)$$

where $\rho_{11}(h)$ is the correlogram of the primary variable $Z_1(h)$ and $\rho_{12}(h)$ is the cross-correlogram, which quantifies the spatial correlation between the primary (Z_1) and the secondary (Z_2) data at a distance h .

Assuming $Z_1(x)$ to be known, the value of the primary variable Z_1 at target location x_0 is independent of the value of the secondary variable Z_2 if Z_1 and Z_2 have a mean of zero and a variance of one. In this case, which is called a “Markov-type” model, the cross covariance functions are proportional to the covariance structure of the primary variable (Almeida & Journel, 1994; Xu et al., 1992). A strictly CCoK estimator $Z_{1\text{ccok}}^{**}$ at target location x_0 depends on both the linear regression of the primary variable Z_1 and the simple kriging variance σ_{SK}^2 , for $\rho = \rho_{12}(0)$ as follows (Chiles & Delfiner, 1999):

$$Z_{1\text{ccok}}^{**}(x_0) = \frac{(1-\rho^2)Z_1^*(x_0) + \sigma_{SK}^2\rho Z_2(x_0)}{(1-\rho^2) + \rho^2\sigma_{SK}^2} \quad (2)$$

where Z_1^* is the kriging estimation of Z_1 at the target location x_0 and the accuracy of the CCoK estimation is given by

$$\sigma_{\text{CCoK}}^2 = \sigma_{SK}^2 \frac{(1-\rho^2)}{(1-\rho^2) + \rho^2\sigma_{SK}^2} \quad (3)$$

2.3.2. Interpolating airborne γ -ray data on geological constraints

In our study, we used the CCoK as a multivariate estimation method for the interpolation of airborne γ -ray data using the geological map information. The primary variable $Z_1(x)$ refers to the discrete distribution of the natural abundances of K, eU, or eTh (equivalent thorium) measured via airborne γ -ray spectrometry, whereas the secondary variable $Z_2(x)$ refers to the continuous distribution of the geological formations (i.e., the geological map). In this work, these two sets of information are independent of one another. The data gained through airborne γ -ray spectrometry define a radiometric spatial dataset integrating the sample point positions with the natural abundances of K (%), eU ($\mu\text{g/g}$), and eTh ($\mu\text{g/g}$), together with their respective uncertainties.

The geological map at a 1:10,000 scale (CGT, 2011), obtained from a geological field survey, covers the entire area in detail. Moreover,

Table 2

Descriptive statistical parameters of airborne γ -ray data.

Parameter	K (%)	eU ($\mu\text{g/g}$)	eTh ($\mu\text{g/g}$)
Count	806	805	807
Minimum	0.2	0.2	0.03
Maximum	4.8	28.0	34.0
Mean	1.9	6.4	11.1
Std. Dev.	0.9	4.4	5.9
Variance	0.8	19.7	35.2
Variation coeff.	0.5	0.7	0.5
Skewness	0.2	1.3	0.5

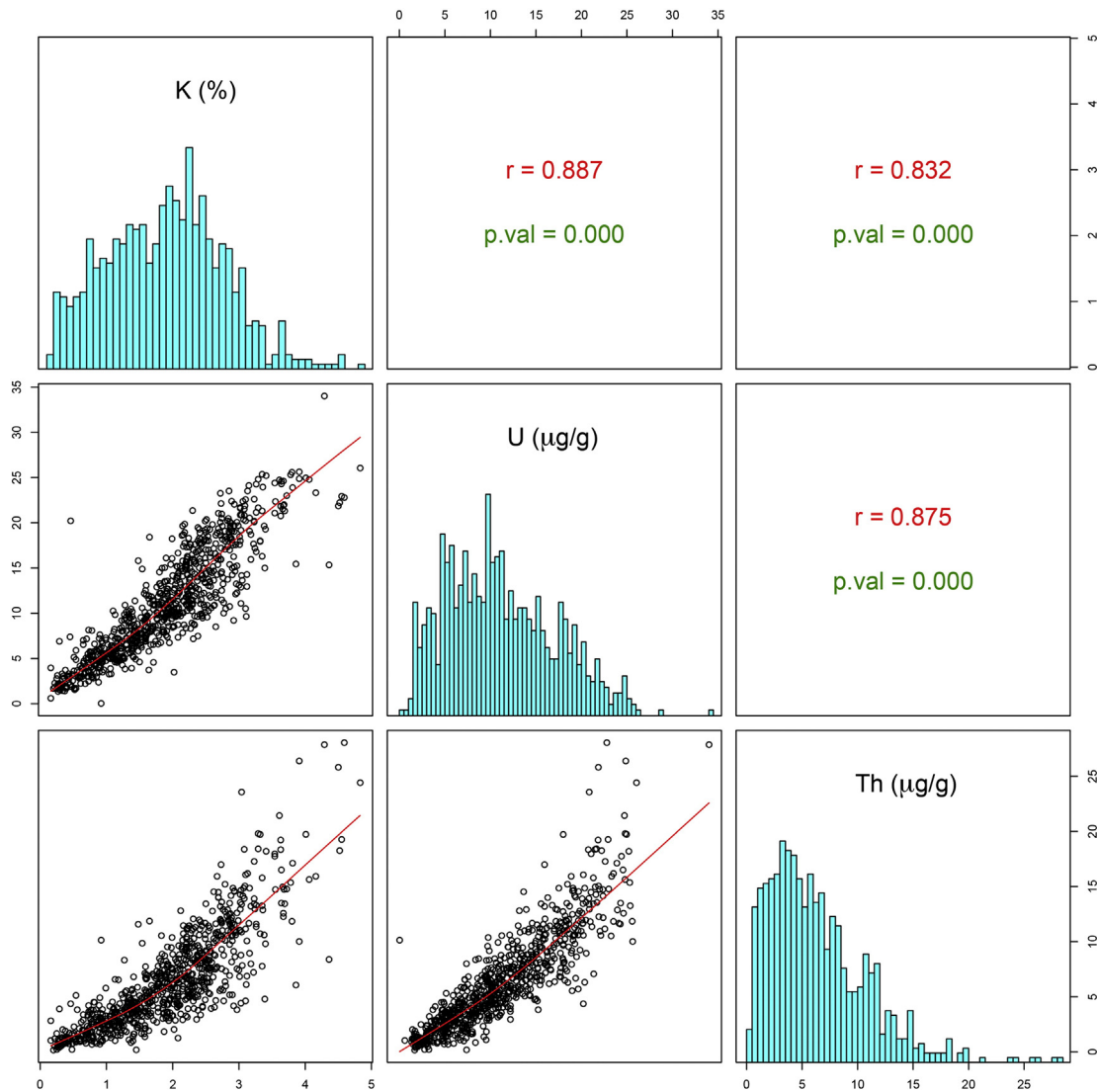
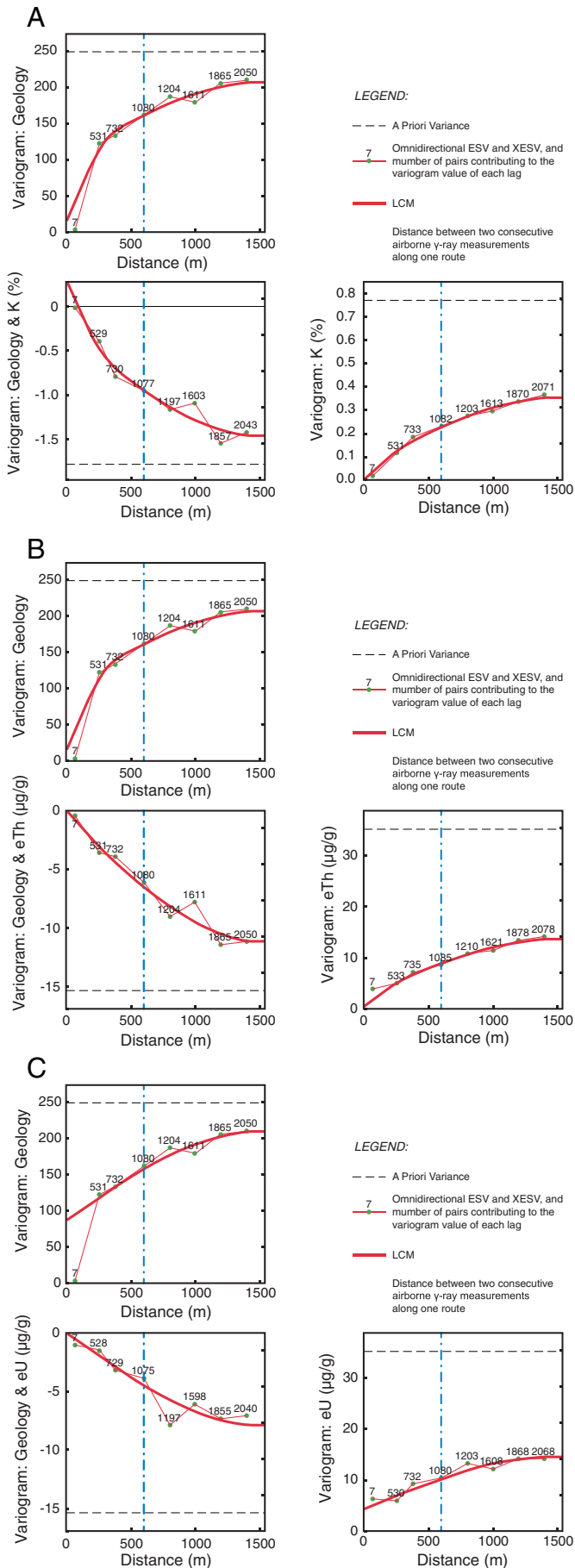


Fig. 3. Correlation matrix of abundance variables: the lower panel shows the bi-variate scatter plots for each pair of variables and the robust locally weighted regression (Cleveland, 1979), red line; cells on the matrix diagonal show the univariate distributions of abundances; the upper panel shows both Pearson's linear correlation coefficient value for each bivariate distribution and the statistical significance testing scores (p-value) for each correlation test. (For interpretation of the references to color in this figure legend, the reader is referred to the web version of this article.)

Table 3

Parameters of linear coregionalization models fitted on omnidirectional variograms calculated with 8 lags of 200 m: groups of primary (radionuclides) and secondary variables; number and types of systems of functions fitted on experimental variograms; range distances for each system of function; matrices of each structure of variability of linear coregionalization model (LCM) fitted for different groups (model values for EVs in each matrix diagonal cells, model values for XESVs in lower left panel of each matrix; variability values of the parametric geology, in the right column, are unitless); cross-validation results of the fitted LCM (only the primary variables scores are listed; MSE: mean of standardized errors; VSE: variance of standardized errors) for all groups of variables.

Group of variables	Number and type of structures of variability		Range (m)	LCM matrices		Cross-validation	
						MSE	VES
K & geology	1	Nugget effect model	–	0.01% ²	–	–0.0016	0.68
	2	Spherical model	400	0.3% ²	15		
	3	Spherical model	1500	–0.6% ²	87		
eU & geology	1	Nugget effect model	–	0.1% ²	–	–0.00016	0.73
	2	Spherical model	1500	–5.7 µg/g ²	120		
	3	Spherical model	1500	–1.2% ²	105		
eTh & geology	1	Nugget effect model	–	2.5 µg/g ²	–	–0.0008	0.65
	2	Spherical model	400	0.1 µg/g ²	87		
	3	Spherical model	1500	–0.4 µg/g ²	–		
				–0.1 µg/g ²	15		
				2.1 µg/g ²	–		
				–0.4 µg/g ²	87		
				11.2 µg/g ²	–		
				–10.6 µg/g ²	105		



the geological map lists 73 different geological formations, defining in this way a categorical variable. For such a large number of variables, the approach based on categorical variables (Bierkens & Burrough, 1993; Goovaerts, 1997; Hengl et al., 2007; Journel, 1986; Pardo-Iguzquiza & Dowd, 2005; Rossi et al., 1994) requires a long time for processing and interpretation. Therefore, we had to consider the geological qualitative (categorical) map as a quasi-quantitative constraining variable. In order to study the frequency of sampling we sorted in alphabetical ascending order the geological formation names and assigned to each one a progressive number. We rearranged the frequencies for obtaining normal distributions of the secondary variable (geology). As we show in the following section, this procedure does not affect the final interpolation results. Thus, we spatially conjoined the airborne γ -ray measures to the geological map. This migration of geological data from the continuous grid (the geological map) to the sample points (the airborne γ -ray measuring locations) is performed to yield a multi-variate point dataset to be interpolated by CCoK. As shown in Table 2, K (%) and eTh ($\mu\text{g/g}$) abundances have a quasi-Gaussian distributions, whereas eU ($\mu\text{g/g}$) abundance distribution tends to be positively skewed. The linear correlation is high between pairs of abundance variables (Fig. 3). Based on the previous assumptions, the linear correlation coefficient between radioactivity measures and values arbitrary assigned to geological formations is meaningless.

The CCoK interpolation models, both for the direct spatial correlation and the cross-correlation of these regionalized variables, were obtained by calculating experimental semi-variograms (ESV) and experimental cross-semivariograms (X-ESV), and interpreting the models by taking into account factors conditioning the spatial distribution of these regionalized variables. The distributions of radioelements of our dataset show a positive skewness of 0.2, 0.5 and 1.3 for K, eTh and eU respectively (Table 2). In the case of skewness values less than 1, several authors (Rivoirard, 2001; Webster & Oliver, 2001) suggest to not perform any normal transformation of the data. Considering that the measurement of eU is contaminated by radon, which increases the experimental uncertainty, we considered redundant any refinement of data processing. In addition, supported by well-structured ESVs and X-ESVs for the raw datasets, we didn't perform any normal transformation for K, eU and eTh.

The directional X-ESVs show erratic behavior. Therefore, we modeled the experimental co-variability as isotropic, and an omnidirectional LCM has been fitted using a trial-and-error procedure. As shown in Table 3, the Gaussian distribution has the mean of standardized errors equal to zero and the variance of standardized errors equal to unity, which allows us to use a cross-validation method. We double-checked the quality of the model (Clark & Harper, 2000; Goovaerts, 1997; Isaaks & Srivastava, 1989) by comparing the errors made in estimating airborne γ -ray measures at sample locations with the theoretical standard Gaussian distribution.

Each group of variables shows the same spatial variability of the geology in the coregionalization matrices because the same parametric variable is still used for all models in the estimation of abundance distribution maps of radioactive elements (Table 3). The result shows a well-structured spherical variability for all groups of variables (Fig. 4).

3. Results and discussion

On the 3rd of June, 2010, the autogyro flew over Elba Island (224 km²): during approximately two hours of flight, the ARGS system collected 807 radiometric data with an average spot area of approximately 0.25 km² (source of 90% of the signal). The average altitude of the flight was 140 ± 50 m.

Fig. 4. Omidirectional Linear Coregionalization Model fitted for the experimental semi-variograms (ESV, on diagonal cells of the matrix) and cross-semivariograms (XESV lower left corner cell) for all groups of radionuclides and parametric geology: (A) Geology and K; (B) Geology and eTh; (C) Geology and eU. (For interpretation of the references to color in this figure, the reader is referred to the web version of this article.)

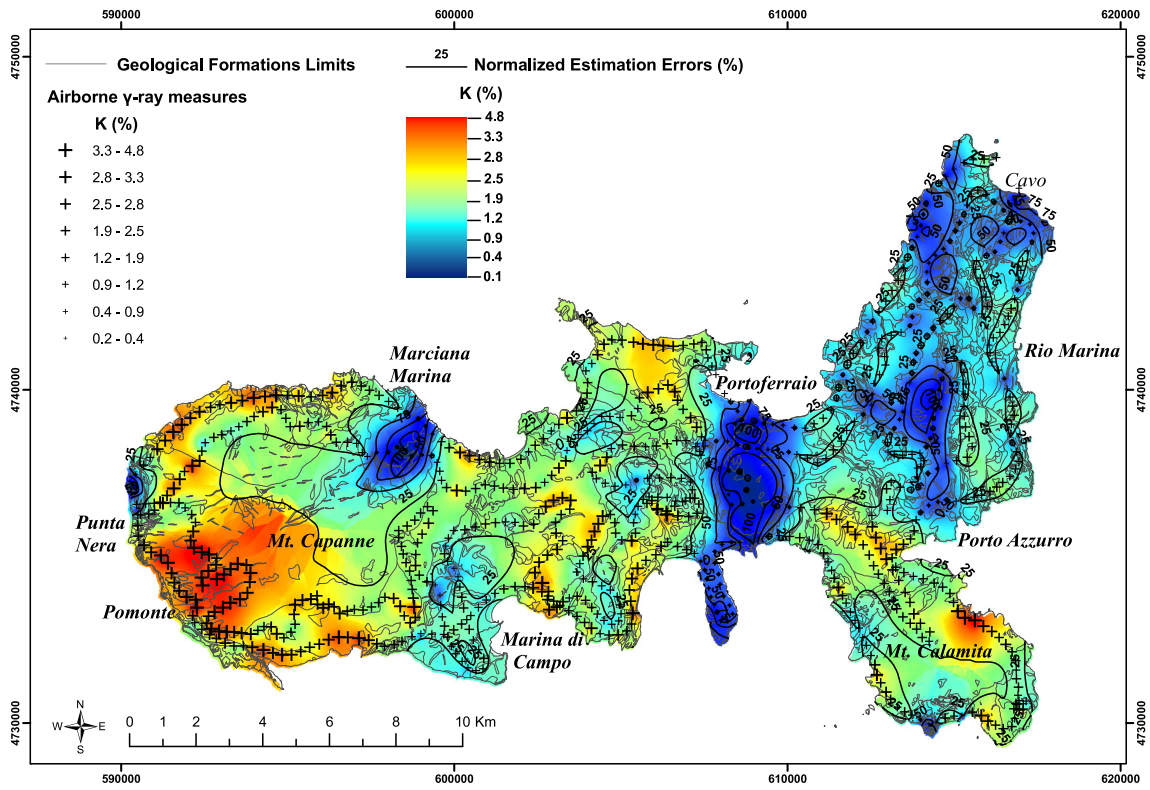


Fig. 5. Estimation map of K (%) abundance and normalized estimation errors.

Performing the post-processing described in Section 2.2, we associated homogenous K, eU, and eTh abundances to each spot area. Considering that 96% of the total 2574 geological polygons covering the

surface of Elba Island have an area less than 0.25 km², we observe that many of the airborne γ -ray measurements refer to the contributions coming from several geological formations with different lithological

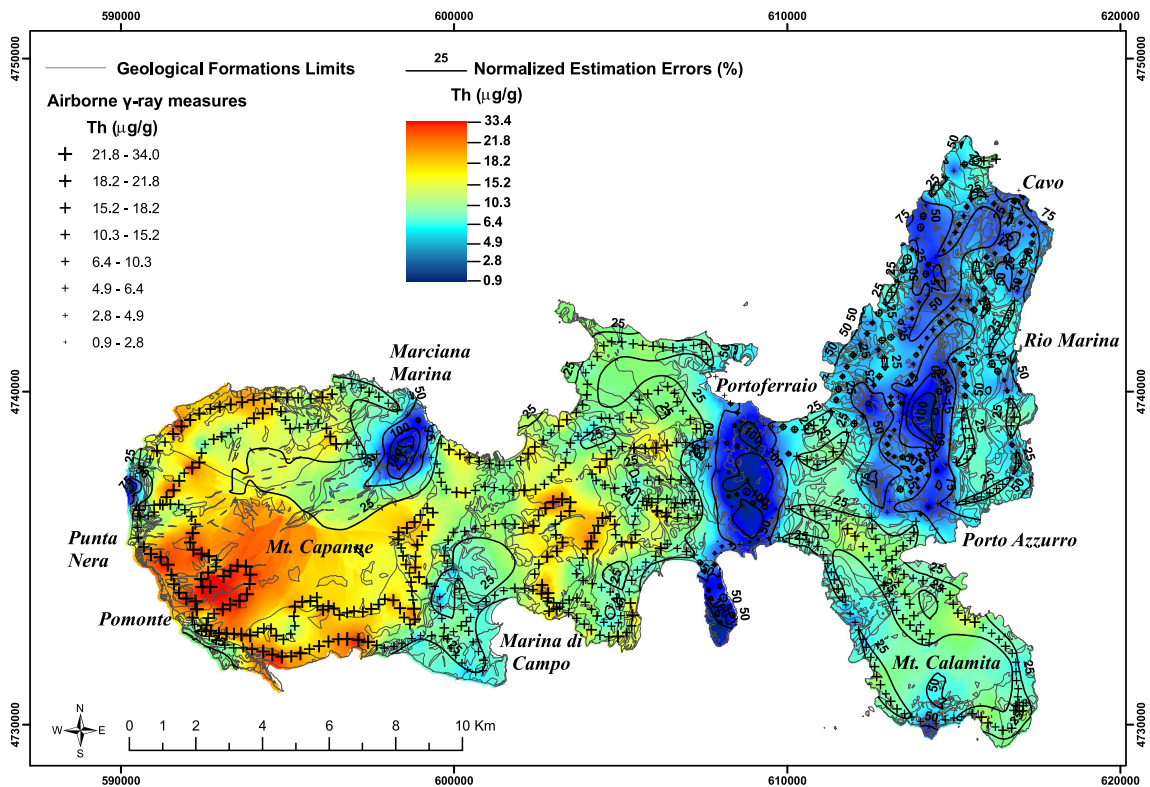


Fig. 6. Estimation map of eTh ($\mu\text{g/g}$) abundance and normalized estimation errors.

compositions. However, these polygons cover only 25% of the surface of Elba Island. The high density of radioactivity data and the highly refined geological map allowed to construct a well tested LCM: the cross-validation results are shown in Table 3. Based on this consistent framework, the multivariate analysis produced data characterized by a good assessment of spatial co-variability. According to the flight plan, the autogyro crossed its own route resulting in a very low variability in the first lags of the omnidirectional co-regionalization model (e.g. ESV of K in Fig. 4(a)). The ESV models referred to AGRS measurements show regular structures with low variability at small distances and generally higher variability at the spherical parts. Indeed, the nugget effect of K abundance contributes almost 2% of the total amount of spatial variability, providing evidence of autocorrelation. The same features are found for the eTh and eU abundances, whose variances at small distances contribute 3% and 30% of the total spatial variation, respectively.

Moreover, we notice a low spatial variability below 600 m (indicating the spot area radius, indicated by the blue dashed line in Fig. 4), which corresponds to data obtained by partially overlapping spot areas. The maximum distance of spatial autocorrelation for K, eU, and eTh is 1500 m (Table 3), this also due to their high statistical correlation (Fig. 3). These features reconstructed the spatial resolution of the AGRS survey, confirming the consistency of the model and the AGRS data.

The variability of the parametric geology variogram at small distances shows a weak variability discontinuity at lag $h = 0$, i.e., a nugget effect. This contributes almost 50% of the total spatial variability together with the first range of autocorrelation found at 400 m. This is due to either the random values assigned to the categories of the geological map, where a significant difference can be found between the sample values of two adjacent geological formations or in the 600 m spot area radius (Fig. 4).

The X-ESVs constructed for radioelement-geology couples generally show well-defined co-variability structures. Indeed, both the spherical components of the model are well structured and the contribution of

the random part of the variability is always minimized (Fig. 4). Therefore, we conclude that these choices ensure the consistency of the results achieved by the CCoK multivariate interpolator.

The estimated maps of the K, eTh, and eU abundances are shown in Figs. 6, 7, and 8. These maps are calculated with a high spatial resolution (pixel size $10\text{ m} \times 10\text{ m}$) in accordance with the choice of the geological map at scale 1:10,000. We also report the accuracy of the estimations in terms of the variance, normalized in respect to the estimated values of the abundances (normalized standard deviation, NSD). The percentage uncertainties of the abundances are higher when the absolute measures are smaller, with average NSDs of 27%, 28%, and 29% for K, eU, and eTh, respectively.

In the geostatistical approach described above, we faced the problem of correlating a quantitative variable (radioactivity content) to a typical categorical extensive variable (geological map). As a first solution, the standard Gaussian distribution of the secondary variable (Geo1) was chosen in a range of values from -10^2 to 10^2 . In order to test possible bias introduced by the choice of the interval of values, we constructed two different distributions in the range of values from 1 to 10^2 (Geo2) and from 1 to 10^5 (Geo3). The main results of these tests are summarized in Table 4 and Fig. 8; for the sake of simplicity, we only compare here the estimated maps of K abundance. However, the entire procedure for every radioelement combined with the geological parametrical map has been performed. The normalized differences between pairs of maps realized for different casual geological arrays through CCoK interpolations (Table 4 and Fig. 9) confirm that the random assignment does not introduce any systematic bias. Moreover, the normalized fluctuations of K abundances estimated by three different models are contained in a range of less than 5%. The quality of the models is not weakened by the assignment of random values to geological categories.

The main features of the resulting radiometric maps of abundances for the natural radioelements overlay the prominent geological formations of Elba Island. Indeed, the relevant geological structures defined

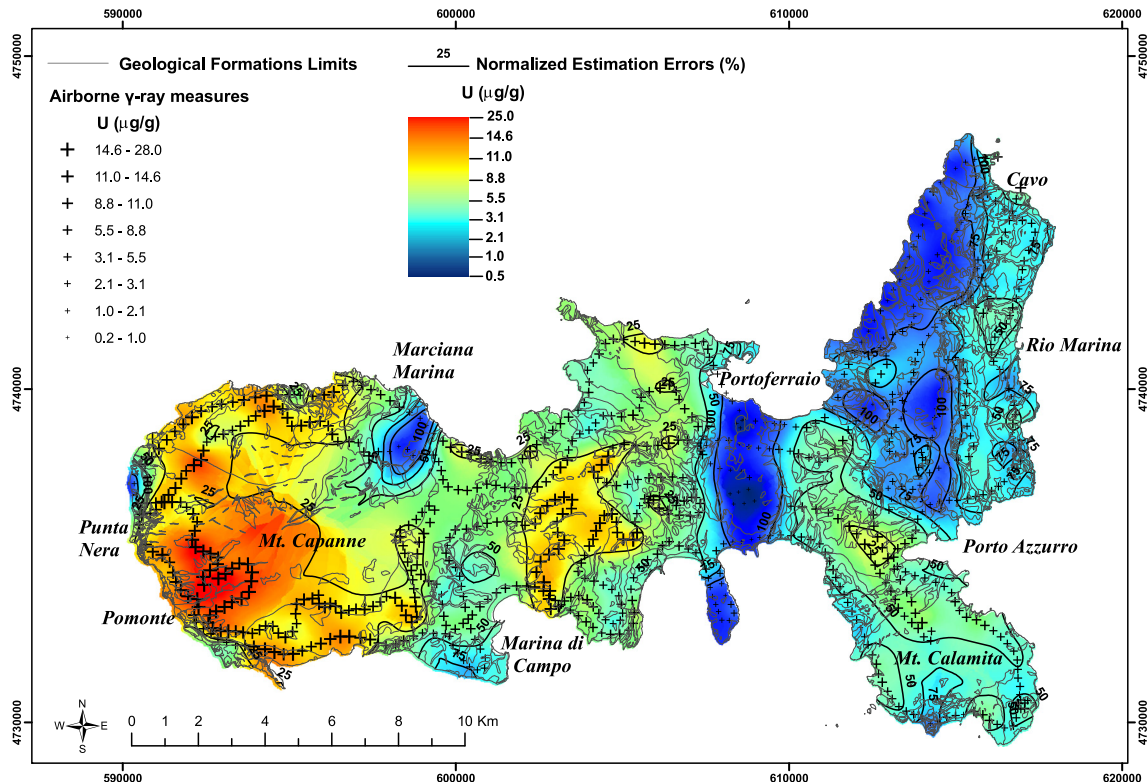


Fig. 7. Estimation map of eU ($\mu\text{g/g}$) abundance and normalized estimation errors.

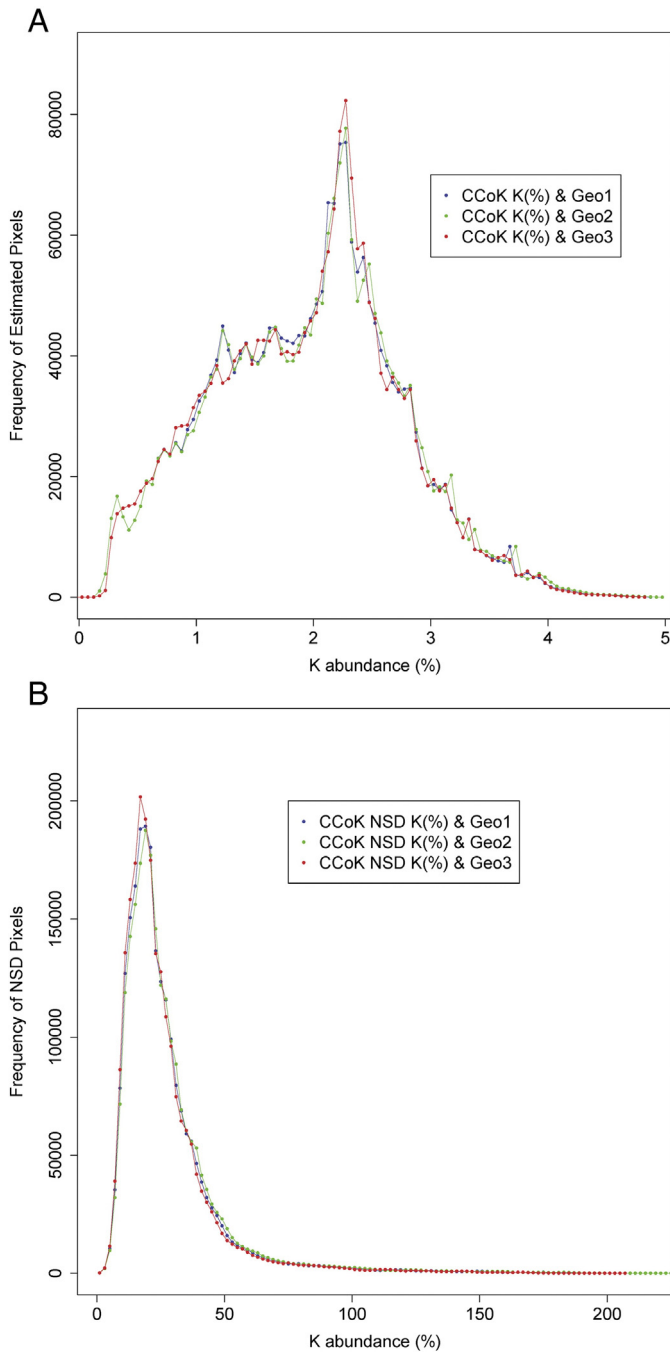


Fig. 8. A) Frequency distributions of kriged maps of K abundances estimated by CCoK through three different reclassifications of the geological map of Elba Island. B) Frequency distributions of the normalized standard deviation maps (the accuracy of CCoK estimations).

by the TCs, described in Section 2.1, can easily be identified by comparing similar abundances of natural radioelements.

The radiometric maps of K, eTh, and eU abundances (Figs. 6, 7, and 8) show high values in the western sector of the island, corresponding to the intrusive granitic complex on Mt. Capanne (indicated as the “CAPa” and “CAPb” geological formations in Fig. 1). In 19 rock samples of Mt. Capanne pluton reported in Farina et al. (2010) the abundances of K, Th, and U are $3.6 \pm 0.2\%$, $20.8 \pm 1.6 \mu\text{g/g}$ and $8.2 \pm 5.1 \mu\text{g/g}$ respectively. The values match with those estimated in Figs. 5, 6 and 7. Although the distributions of radioelements do not distinguish among the three intrusive facies, which are mainly characterized by the widespread occurrence of euhedral K-feldspar

Table 4

Descriptive statistics of the CCoK estimation maps of K abundances (unit of measurement: mg/g) using three different parametric classifications of the geological map (Geo1, Geo2, and Geo3), the respective estimation errors maps (NSD), and their algebraic map differences (unit of measurement: %).

Type	Geological map	Min.	Max.	Mean	Std. Dev.
CCoK estim.	Geo1	0.15	48.80	19.37	0.79
	Geo2	0.15	48.80	19.37	0.79
	Geo3	0.16	48.24	19.36	0.79
NSD	Geo1	0.79	187.62	27.24	19.58
	Geo2	0.79	217.74	27.24	19.69
	Geo3	6.00	255.00	27.22	19.89
Differ. CCoK	(Geo1-Geo2)/Geo1	-0.33	0.56	-0.001	0.001
	(Geo1-Geo3)/Geo1	-1.84	1.60	-0.004	0.076
	(Geo2-Geo3)/Geo2	-1.72	1.49	-0.007	0.082
Differ. NSD	(Geo1-Geo2)/Geo1	-44.11	91.87	-1.01	-0.88
	(Geo1-Geo3)/Geo1	-85.19	90.55	-0.09	1.21
	(Geo2-Geo3)/Geo2	-34.67	49.03	0.10	0.81

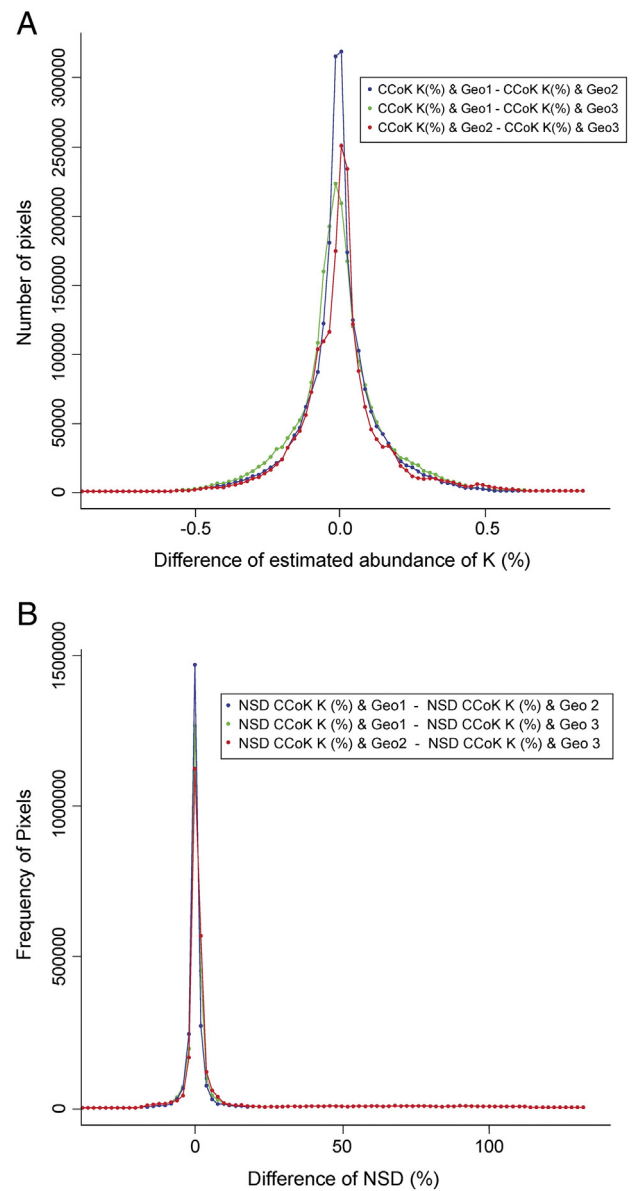


Fig. 9. A) Frequency distributions of the differences between pairs of kriged maps of K abundances estimated by CCoK through three different reclassifications of geological maps of Elba Island. B) Frequency distributions of the differences between pairs of normalized standard deviation maps.

megacrysts, the area with high content of K, Th and U obtained by multivariate analysis follows the contour map of Mt. Capanne pluton reported in Fig. 9a in Farina et al. (2010). However, the highest contents of K, Th and U are localized in the southwestern part of pluton with the maximum concentration in correspondence of the Pomonte valley, SW–NE oriented that is one of the most prominent morphological lineament of western Elba (Figs. 5, 6, and 7). This is an important tectonic lineament crossing all the Mt. Capanne, abruptly separating two different morphological assets: the north-western part shows rough slopes and deep valleys, while the south-eastern one is characterized by gently landscape. The hypothesis of an enrichment of radioelements related to this tectonic lineament should be investigated by further airborne and ground surveys.

As shown in Figs. 5, 6, and 7 the geological formations belonging to TC II and TC III have low natural radioelement abundances. The main outcrops are located in the northeastern sector of Elba Island, between Porto Azzurro and Cavo and in the southern part of Portoferraio, where we find peridotites and pillow lavas (indicated as “PRN” and “BRG”, Fig. 1). Finally, low abundance values are found in the area of Punta Nera Cape at the western edge of the Elba Island, where lithologies belonging to the Ophiolitic Unit crop out (TC IV).

We emphasize that, although we assign a unique number to each geological formation the internal variability of the radiometric data is not biased by the multivariate interpolation. The main evidence of this feature can be observed inside the polygon including Mt. Calamita, which is identified by a unique geological formation “FAFc” (Fig. 1). We note a clear anomaly of high K abundance in the northeastern sector of the Mt. Calamita promontory, close to Porto Azzurro (Fig. 5). This anomaly can be geologically explained considering two related factors. The intense tectonization and following fracturation of this sector allowed a significant circulation of magmatic fluids related to the emplacement of monzogranite pluton of La Serra–Porto Azzurro. Moreover, the presence of felsic dykes, metasomatic masses and hydrothermal veins are recently confirmed by Dini et al. (2008) and Mazzarini et al. (2011). Although our geological map doesn't report these lithological details, the quality of radiometric survey is such as to identify the location of the felsic dyke swarm. These dykes 30–50 cm thick represent the dominant lithology at the mesoscopic scale and their high frequency in FAFc geological formation contributes to increase the gamma-ray signal. These details are not compromised by the multivariate analysis. The spatial extension of high K content validates the geological sketch reported in Fig. 1 by Dini et al. (2008).

4. Conclusions

In this study we realized the first detailed maps of K, eU, and eTh abundances of Elba Island showing the potential of the multivariate interpolation based on combination of AGRS data and preexisting information contained in the geological map (at scale 1:10,000). We summarize here the main results reached in this study.

- The multivariate analysis technique of collocated cokriging (CCoK) was applied in a non-conventional way, using the well-sampled geology as a quasi-quantitative variable and constraining parameter. This approach gives a well-structured LCMs which show a good spatial co-variation in the omnidirectional coregionalization ESV model. The ESV models show low spatial variability below 600 m, which also corresponds to the radiometric data obtained by partially overlapped spot areas as well as the autocorrelation distance of 1500 m for the three radionuclides. The ESV model of the geology shows a weak variability discontinuity in the first lag, corresponding to the random assignment of quasi-quantitative values of adjacent geological formations, but also a strong spatial relationship up to the first range of autocorrelation. The procedure of the cross-validation of the model yields a mean close to zero for the

standardized errors (MSE) and a variance of standardized errors (VSE) close to unity for all groups of variables.

- The CCoK based on the geological constraint was performed by randomly assigning a number to each category of the 73 geological formations. Three different geological quasi-quantitative variable datasets were used, and satisfactory results were achieved by assuring the non-dependency of the model. The normalized fluctuations of three different models are contained in a range of less than 5%.
- Combining the smoothing effects of the probabilistic interpolator (CCoK), and the abrupt discontinuities of the geological map, we observe a distinct correlation between the geological formation and radioactivity content as well as high K, eU and eTh abundances in the intrusive granitic complex on Mt. Capanne and low abundances in the geological formations belonging to TC II, TC III and TC IV.
- Although we assign a unique number to each geological formation, the internal variability of the radiometric data is not biased by the multivariate interpolation. The main evidence of this feature can be observed in the northeastern sector of the geological polygon including Mt. Calamita. A clear anomaly of high K content has confirmed the presence of felsic dykes and hydrothermal veins not reported in our geological map, but recently studied (Dini et al., 2008) as a proxy of the high temperature system currently active in the deep portion of Larderello–Travale geothermal field.

Acknowledgments

The authors are indebted to E. Bellotti, G. Di Carlo, P. Altair, S. De Bianchi, P. Conti and R. Vannucci for useful discussions and to the anonymous referees for their invaluable suggestions. This work has been sponsored by the INFN, Cassa di Credito Cooperativo Padova e Rovigo, and funded by the Tuscany Region.

References

- Almeida, A., & Journel, A. (1994). Joint simulation of multiple variables with a Markov-type coregionalization model. *Mathematical Geology*, 26(5), 565–588.
- Atkinson, P. M., Webster, R., & Curran, P. J. (1992). Cokriging with ground-based radiometry. *Remote Sensing of Environment*, 41(1), 45–60.
- Babak, O., & Deutsch, C. V. (2009). Improved spatial modeling by merging multiple secondary data for intrinsic collocated cokriging. *Journal of Petroleum Science and Engineering*, 69(1–2), 93–99.
- Bierkens, M. F. P., & Burrough, P. (1993). The indicator approach to categorical soil data: Theory. *Journal of Soil Science*, 44, 361–368.
- Bierwirth, P. N., & Brodie, R. S. (2008). Gamma-ray remote sensing of Aeolian salt sources in the Murray–Darling Basin, Australia. *Remote Sensing of Environment*, 112(2), 550–559.
- Bortolotti, V., Fazzuoli, M., Pandeli, E., Principi, G., Babbini, A., & Corti, S. (2001). Geology of central and eastern Elba Island, Italy. *Ofioliti*, 26(2a), 97–150.
- Buttafuoco, G., Tallarico, A., Falcone, G., & Guagliardi, I. (2010). A geostatistical approach for mapping and uncertainty assessment of geogenic radon gas in soil in an area of southern Italy. *Environmental Earth Sciences*, 61(3), 491–505.
- Caciolli, A., Baldoncini, M., Bezzon, G. P., Broggin, C., Buso, G. P., Callegari, I., Colonna, T., Fiorentini, G., Guastaldi, E., Mantovani, F., Massa, G., Menegazzo, R., Mou, L., Rossi Alvarez, C., Shyti, M., Zanon, A., & Xhixha, G. (2012). A new FSA approach for in situ γ ray spectroscopy. *Science of The Total Environment*, 414, 639–645. <http://dx.doi.org/10.1016/j.scitotenv.2011.10.071> (ISSN 0048-9697).
- Carroll, S. S., & Carroll, T. R. (1989). Effect of forest biomass on airborne snow water equivalent estimates obtained by measuring terrestrial gamma radiation. *Remote Sensing of Environment*, 27(3), 313–319.
- CGT (2011). Accordo di programma quadro ricerca e trasferimento tecnologico per il sistema produttivo - c.1. geologia e radioattività naturale - sottoprogetto a: Geologia (regional framework program for research and technological transfer to industry, c.1. geology and natural radioactivity, sub-project a: Geology). Technical report, CGT Center for GeoTechnologies, University of Siena; Tuscany Region: Italian Ministry of Education, University and Research. For the official legend for the geological formations, see <http://www.geologiatoscana.unisi.it>.
- Chiles, J. -P., & Delfiner, P. (1999). *Geostatistics: Modeling spatial uncertainty*. Probability and statistics series. New York; Chichester: John Wiley and Sons.
- Clark, I., & Harper, W. V. (2000). *Practical Geostatistics 2000*, vol. 1, Columbus, Ohio, U.S.A.: Ecosse North America Llc.
- Cleveland, W. S. (1979). Robust locally weighted regression and smoothing scatterplots. *Journal of the American Statistical Association*, 74, 829–836.
- Desbarats, A. J., Logan, C. E., Hinton, M. J., & Sharpe, D. R. (2002). On the kriging of water table elevations using collateral information from a digital elevation model. *Journal of Hydrology*, 255(1–4), 25–38.

- Dini, A., Innocenti, F., Rocchi, S., Tonarini, S., & Westerman, D. (2002). The magmatic evolution of the late miocene laccolith–pluton–dyke granitic complex of Elba Island, Italy. *Geological Magazine*, 139(3), 257–279.
- Dini, A., Mazzarini, F., Musumeci, G., & Rocchi, S. (2008). Multiple hydro-fracturing by boron-rich fluids in the Late Miocene contact aureole of eastern Elba Island (Tuscany, Italy). *Terra Nova*, 20, 318–326.
- Dini, A., Rocchi, S., Westerman, D. S., & Farina, F. (2010). The late Miocene intrusive complex of Elba Island: Two centuries of studies from Savi to Innocenti. *Acta Vulcanologica*, 21, 169–190.
- Duranti, S., Palmeri, R., Pertusati, P. C., & Ricci, C. A. (1992). Geological evolution and metamorphic petrology of the basal sequences of Eastern Elba (Complex II). *Acta Vulcanologica*, 2, 213–229.
- Farina, F., Dini, A., Innocenti, F., Rocchi, S., & Westerman, D. S. (2010). Rapid incremental assembly of the Monte Capanne pluton (Elba Island, Tuscany) by downward stacking of magma sheets. *Geological Society of America Bulletin*, 122(9–10), 1463–1479.
- Garfagnoli, F., Menna, F., Pandeli, E., & Principi (2005). The Porto Azzurro Unit (Mt. Calamita promontory, south-eastern Elba Island, Tuscany): Stratigraphic, tectonic and metamorphic evolution. *Bollettino della Societa Geologica Italiana*, 3, 119–138.
- Goovaerts, P. (1997). *Geostatistics for natural resources evaluation*. Oxford, New York: Oxford University Press (ISBN-13 978-0-19-511538-3).
- Goovaerts, P. (1999). Using elevation to aid the geostatistical mapping of rainfall erosivity. *Catena*, 34, 227–242.
- Guastaldi, E., & Del Frate, A. A. (2012). Risk analysis for remediation of contaminated sites: The geostatistical approach. *Environmental Earth Sciences*, 65(3), 897–916.
- Hengl, T., Toomanian, N., Reuter, H. I., & Malakouti, M. J. (2007). Methods to interpolate soil categorical variables from profile observations: Lessons from Iran. *Geoderma*, 140(4), 417–427.
- Hoeksema, R., Clapp, R., Thomas, A., Hunley, A., Farrow, N., & Dearstone, K. (1989). Cokriging model for estimation of water table elevation. *Water Resources Research*, 25(3), 429–438.
- Hudson, G., & Wackernagel, H. (1994). Mapping temperature using kriging with external drift: Theory and an example from Scotland. *International Journal of Climatology*, 14, 77–91.
- IAEA (1991). *Airborne gamma-ray spectrometry surveying*. Technical Report Series, 323, Vienna: International Atomic Energy Agency.
- Isaaks, E. H., & Srivastava, R. M. (1989). *Applied geostatistics*. Oxford, New York: Oxford University Press.
- Journel, A. (1986). Constrained interpolation and qualitative information. *Mathematical Geology*, 18(3), 269–286.
- Keller, J. V. A., & Coward, M. P. (1996). The structure and evolution of the Northern Tyrrhenian Sea. *Geological Magazine*, 133, 1–16.
- Mazzarini, F., Musumeci, G., & Cruden, A. R. (2011). Vein development during folding in the upper brittle crust: The case of tourmaline-rich veins of eastern Elba Island, northern Tyrrhenian Sea, Italy. *Journal of Structural Geology*, 33(10), 1509–1522.
- Minty, B. R. S. (2011). Airborne geophysical mapping of the Australian continent. *Geophysics*, 76(A27).
- Minty, B., & McFadden, P. (1998). Improved NASVD smoothing of airborne gamma-ray spectra. *Exploration Geophysics*, 29(4), 516–523.
- Musumeci, G., Mazzarini, F., Tiepolo, M., & Di Vincenzo, G. (2011). U–Pb and ⁴⁰Ar–³⁹Ar geochronology of Palaeozoic units in the northern Apennines: Determining protolith age and alpine evolution using the Calamita Schist and Ortano Porphyroid. *Geological Journal*, 46, 288–310.
- Musumeci, G., & Vaselli, L. (2012). Neogene deformation and granite emplacement in the metamorphic units of northern Apennines (Italy): Insights from milonite marbles in the Porto Azzurro pluton contact aureole (Elba Island). *Geosphere*, 8(2), 470–490.
- Pandeli, E., Puxeddu, M., & Ruggieri, G. (2001). The metasiliclastic-carbonate sequence of the Acquadolce Unit (eastern Elba Island): New petrographic data and paleogeographic interpretation. *Ofioliti*, 26(2a), 207–218.
- Pardo-Iguzquiza, E., & Dowd, P. A. (2005). Multiple indicator cokriging with application to optimal sampling for environmental monitoring. *Computers and Geosciences*, 31(1), 1–13.
- Pei, T., Qin, C. -Z., Zhu, A. -X., Yang, L., Luo, M., Li, B., et al. (2010). Mapping soil organic matter using the topographic wetness index: A comparative study based on different flow-direction algorithms and kriging methods. *Ecological Indicators*, 10(3), 610–619.
- Rivoirard, J. (2001). Which Models for Collocated Cokriging? *Mathematical Geology*, 33(2), 117–131.
- Rossi, R. E., Dungan, J. L., & Beck, L. R. (1994). Kriging in the shadows: Geostatistical interpolation for remote sensing. *Remote Sensing of Environment*, 49(1), 32–40.
- Rybach, L., Bucher, B., & Schwarz, G. (2001). Airborne surveys of Swiss nuclear facility sites. *Journal of Environmental Radioactivity*, 53, 291–300.
- Sanderson, D. C. W., Cresswell, A. J., Hardeman, F., & Debauche, A. (2004). An airborne gamma-ray spectrometry survey of nuclear sites in Belgium. *Journal of Environmental Radioactivity*, 72(1–2), 213–224.
- Schetselaar, E. M., Chung, C. -J. F., & Kim, K. E. (2000). Integration of Landsat TM, gamma-ray, magnetic, and field data to discriminate lithological units in vegetated granite-gneiss terrain. *Remote Sensing of Environment*, 71(1), 89–105.
- Schwarz, G., Klingele, E., & Rybach, L. (1992). How to handle rugged topography in airborne gamma-ray spectrometry surveys. *First Break*, 10(1), 11–17.
- Smith, S. A. F., Holdsworth, R. E., & Colletini, C. (2011). Interactions between low-angle normal faults and plutonism in the upper crust: Insights from the Island of Elba, Italy. *Geological Society of America Bulletin*, 123, 329–346.
- Trevisan, L. (1950). L'Elba orientale e la sua tettonica di scivolamento per gravità. *Memorie degli Istituti di Geologia e Mineralogia dell'Università di Padova*, 16, 5–35.
- Wackernagel, H. (2003). *Multivariate geostatistics: An introduction with applications* (3rd ed.) Berlin, Germany: Springer-Verlag.
- Webster, R., & Oliver, M. (2001). *Geostatistics for natural environmental scientists*. Chichester: John Wiley & Sons 0-471-96553-7.
- Xu, W., Tran, T., Srivastava, R., & Journel, A. (1992). Integrating seismic data in reservoir modeling: The collocated cokriging alternative. *SPE annual technical conference and exhibition*. Washington, D.C.: Society of Petroleum Engineers Inc (page).

SCIENCE

Total natural radioactivity, Tuscany, Italy

Ivan Callegari^{a*}, Gian Pietro Bezzon^b, Carlo Brogгинi^c, Gian Paolo Buso^b, Antonio Caciolli^c, Luigi Carmignani^a, Tommaso Colonna^a, Giovanni Fiorentini^{b,d,e}, Enrico Guastaldi^a, Merita Kaçeli Xhixha^f, Fabio Mantovani^{d,e}, Giovanni Massa^a, Roberto Menegazzo^c, Liliana Mou^b, Altair Pirro^a, Carlos Rossi Alvarez^c, Virginia Strati^{b,d}, Gerti Xhixha^{d,e,g} and Alessandro Zanon^b

^aUniversity of Siena, Center for GeoTechnologies, Via Vetri Vecchi, 34 - 52027 San Giovanni Valdarno, Arezzo, Italy; ^bIstituto Nazionale di Fisica Nucleare (INFN), Legnaro National Laboratory, Via dell'Università, 2 - 35020 Legnaro, Padova, Italy; ^cIstituto Nazionale di Fisica Nucleare (INFN), Padova Section, Via Marzolo 8 - 35131 Padova, Italy; ^dPhysics and Earth Science Department, University of Ferrara, Via Saragat, 1 - 44100 Ferrara, Italy; ^eIstituto Nazionale di Fisica Nucleare (INFN), Ferrara Section, Via Saragat, 1 - 44100 Ferrara, Italy; ^fBotanical, Ecological and Geological Sciences Department, University of Sassari, Piazza Università 21- 07100 Sassari, Italy; ^gFaculty of Forestry Science, Agricultural University of Tirana, Kodër Kamëz - 1029 Tirana, Albania

(Received 30 October 2012; Resubmitted 18 March 2013; Accepted 3 May 2013)

In this paper, we report an extensive survey of the natural radioactive content of rocks of the Tuscany Region (Italy): this permitted the first total natural radioactivity map of the region. The sampling was planned using the geological map of Tuscany at scale 1:250,000, which contains 45 distinct geological groups recognized by tectonic and stratigraphic features. Each geological group was characterized for the total activity by measuring the activity concentrations of ⁴⁰K, ²³⁸U and ²³²Th in 865 samples using a high-purity germanium (HPGe) gamma-ray spectrometer. The average areal distribution of samples is approximately one sample per 25 km². The radiometric map was constructed through the reclassification of each geological formation based on the median value of the total activity. Seven classes of total activity are identified by choosing percentiles almost evenly spread across the range of values. This map represents the starting point for future studies on natural background radiation, geochemical processes and epidemiological investigations.

Keywords: total natural radioactivity map; HPGe gamma-ray spectrometer; geological map reclassification; percentile; Tuscany region

1. Introduction

The environment and health are closely related to healthcare policies due to the effects of natural radiation. In this framework, Article 36 of the [EURATOM Treaty \(1957\)](#) requires the competent authority of each Member State to regularly provide levels of environmental radioactivity. With the ratification of [Council Directive 96/29/EURATOM \(D. Lgs 26 may 2000, nr. 241\)](#), Italy is obligated to measure levels of environmental radioactivity. In particular, some Member States

*Corresponding author. Email: callegari@unisi.it



like: Greece (Anagnostakis, Hiniš, Simopoulos, & Angelopoulos, 1996), Switzerland (Rybach, Bachler, Bucher, & Schwarz, 2002), Slovenia (Andjelov & Brajnik, 1996), Czech Republic (Mikšová & Barnet, 2002) and Slovak Republic (Source: Štátný Geologický Ústav Dionýza Štúra) have already produced natural radioactivity maps of their territories. Moreover, other countries like the USA, Canada (Grasty 1975; Grasty & LaMarre 2004), Australia (Minty 2011) and China (Zhuo, Chen, Li, & Liu, 2008) also possess such maps.

In this framework, this study aims to survey of the natural radioactivity content of rocks of Tuscany Region (Italy). The construction of the natural radioactivity map was based on the geological map of Tuscany at 1:250,000 scale (Carmignani, Conti, Cornamusini, & Pirro, 2012 submitted for publication). By reclassification of the 45 geological formations identified in the geological map we constructed the first map of the total activity of bedrock in Tuscany Region (Italy).

2. Geological setting

The Northern Apennine orogen is a classical fold-and-thrust belt (Barchi et al., 1998; Boccaletti, Elter, & Guazzone, 1971) consisting of a stack of several detached nappes (Figure 1). A Cretaceous-Tertiary convergence linked with the Alpine Orogenesis led to the eastward thrusting of the inner units (Ligurian and Sub-Ligurian units) onto the outer nappes (Tuscan and Umbria–Marchean units) and caused a final Eocene–Oligocene continental collision (Carmignani et al., 2001). The successive collapse of the orogen, linked with the Tyrrhenian rifting has been related to the development of a post-nappe Miocene to Pleistocene basin complex (Martini & Sagri, 1993).

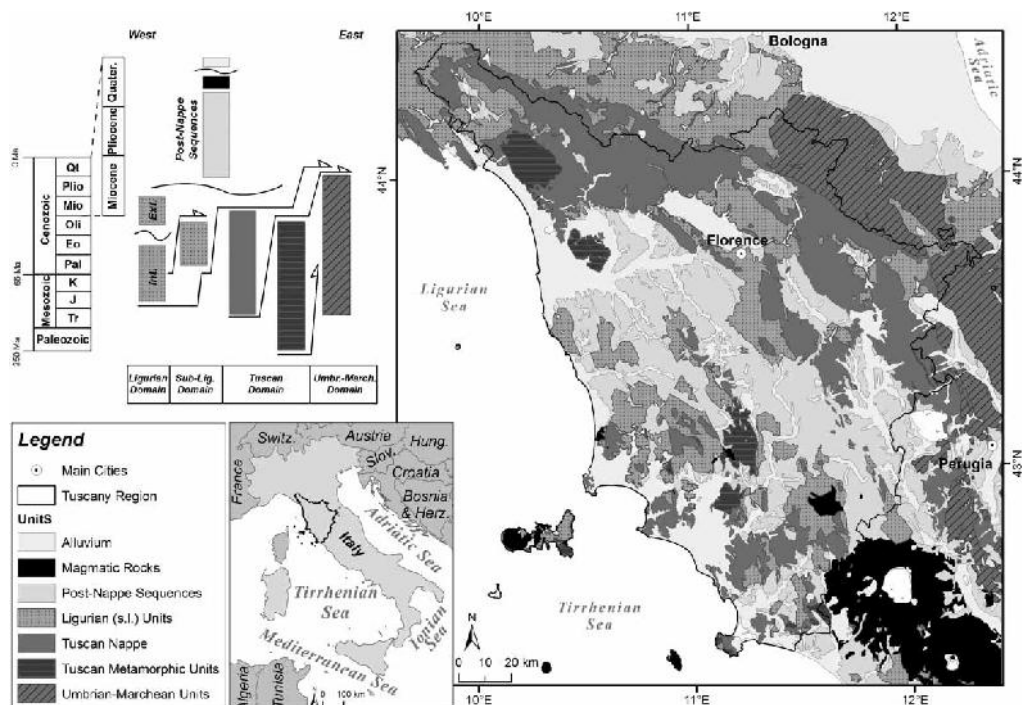


Figure 1. Simplified tectonic sketch of Tuscany Region (modified after Cornamusini, Ielpi, Bonciani, Callegari, & Conti, 2012).

In the Northern Apennines orogenic wedge we recognize tectonic units originating from the African continent and relics of the Tethys oceanic crust. Successions derived from the oceanic crust outcrops in the entire region: the oceanic realm, named the ‘Ligurian domain’ in the Italian geologic literature, is part of the Alpine Tethys. It is furthermore separated in:

- Internal Ligurian Domain, which is characterized by the presence of Jurassic ophiolites and the Late Jurassic-Cretaceous sedimentary cover (cherts, Calpionella limestone and Palombini shales) associated with a Cretaceous-Paleocene siliciclastic turbidite sequence (Lavagna slates, Gottero sandstones and Bocco/Colli Tavarone shaly complex).
- External Ligurian Domain, which is characterized by the presence of Cretaceous-Paleocene calcareous-dominant flysch sequences (Helminthoid flysch) associated with complexes or pre-flysch formations called ‘basal complexes’. The pre-Cretaceous substrate is represented in part by ophiolites and in part by continental crust. Therefore, it is a domain that joined the oceanic area with the Apulia continental margin.

In Figure 1 the Internal and External Ligurian Domains are represented for simplicity with the same color.

Moving toward the African continent the ‘Subligurian Domain’ is distinguished. This is an intensely deformed Paleogene sequence (Canetolo Unit), whose original extent and substratum are unknown. This sequence was probably deposited in a transitional area between the oceanic and Apulia continental crust.

The Tuscan Domain represents the western margin of the Apulia continental crust that outcrops in the Italian peninsula, with the following distinctions:

- The Internal Tuscan Domain (Tuscan Nappe), with non-metamorphic (to low-grade metamorphic) formations of Late Triassic to Early Miocene age.
- The External Tuscan Domain (Tuscan Metamorphic Nappes), affected by greenschist facies metamorphism, with a Mesozoic-Tertiary succession that covers a Paleozoic basement with Hercynian deformation.

Moving toward the east, the Umbria–Marchean Domain is distinguished. This tectonic unit consists of carbonates belonging to the Jurassic–Paleogene multilayer and turbidites belonging to Neogene clastic wedge. This last only crops out in the eastern areas of Tuscany Region.

The sediments unconformably deposited after the main Tertiary tectonic phases are identified as sedimentary successions (post-nappe sequences), placed on the Tyrrhenian side of the Northern Apennines. These successions are separated by regional unconformities. From top to bottom they are: Pliocene to Quaternary continental and coastal deposits, Pliocene to Quaternary marine deposits, Messinian lacustrine, lagoonal evaporitic and pre-evaporitic deposit, Early Turolian lacustrine deposits and Epiligurian deposits. Finally, some lithostratigraphic units like magmatic intrusive and sub-volcanic rocks, effusive and pyroclastic rocks linked to Neogene magmatism and Quaternary cover have been grouped together.

3. Methods

3.1 Reference geological map and sampling strategy

The geological map of Tuscany at 1:250,000 scale (Carnignani et al., 2012 submitted for publication) was used as a guide for the survey of natural radioactivity. The legend of the geological map was organized in to 45 items formed by groups of formations belonging to the tectonic domains described in Section 2.

The entire Tuscany Region (Italy) (22,994 km²) was investigated for the characterization of natural radioactivity by collecting 865 rock samples. The sampling was guided by criteria closely related to the reference geological information. Except for alluvial deposits, the samples come from outcrops with fresh rocks, selected in order to characterize the composite lithologies of the geological groups. Sampling was performed in order to allow a coherent statistical coverage for all 45 geological groups. At least one sample was collected every 80 km² for each geological group with an overall average of one sample per 25 km².

3.2 Gamma-ray spectrometry measurements and results

The specific activities of ⁴⁰K, ²³⁸U and ²³²Th were measured in 865 representative rock samples by using a high-purity germanium (HPGe) gamma-ray spectrometer. Each rock sample was crushed, homogenized (less than 2 mm fine grain size) and constant weight dried at 110°C temperature. Then, each sample was sealed in a 180 cm³ cylindrical polycarbonate container. After sealing, each container was left undisturbed for at least four weeks before spectrum acquisition: this step provides enough time to establish secular equilibrium between ²²⁶Ra and ²²²Rn. The measurements were performed by using the MCA_Rad system (Xhixha et al., 2013). This is a fully automated high-resolution gamma-ray spectrometer, composed of two 60% relative efficiency coaxial HPGe p-type detectors, having an energy resolution of about 1.9 keV at 1332.5 keV (⁶⁰Co) and efficiency estimated with an overall uncertainty of 5%.

Adopting a log-normal distribution as a fundamental law of geochemistry, we enhance the presence of high values contained in the tails of the distributions of ⁴⁰K, ²³⁸U and ²³²Th (Ahrens, 1954). The total activity was calculated for each geological group, by using the

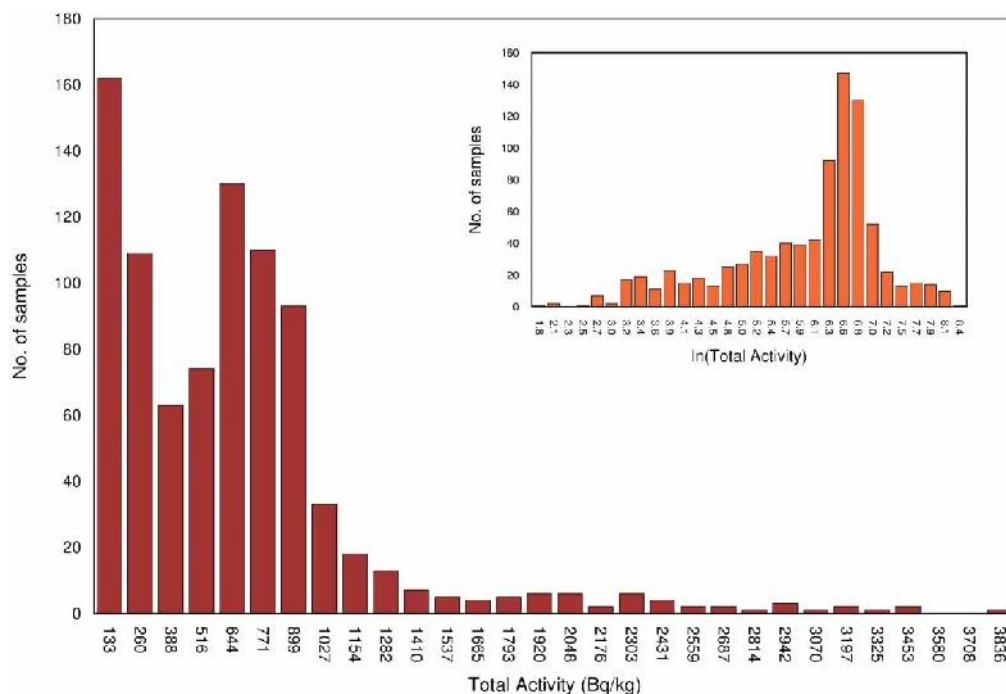


Figure 2. Histogram of total activity for 865 samples; that demonstrates logarithmic distribution with the inset showing a log transformation that conforms to a normal distribution.

Monte Carlo technique: in particular, by summing the generated pseudo-random matrices (with up to 10^5 records) following the individual probability functions (for potassium, uranium and thorium). Figure 2 shows the distribution of total activity for the records.

3.3 Mapping the radiometric data

The map of total activity was constructed based on the median values of the distributions of ^{40}K , ^{238}U and ^{232}Th for each geological group. A total of 28 records, which are found to be outliers (i.e. exceeding the median ± 1.5 Inter Quartile Range) using the graphical box-plot, were rejected from the analysis. Subsequently the median and 1σ uncertainty of the total activity were calculated for each geological group. The reclassification of the geological groups was performed based on their radiometric response by using a geographical information system (GIS). To avoid arbitrary classes and any distribution of records, we represent total activity choosing the percentiles which are simply based on order statistics (Reimann, 2005). In particular seven classes of total activity are identified, choosing the 10%, 30%, 50%, 70%, 85% and 100% percentiles, almost evenly spread across the range of values. In order to emphasize the ‘high’ values we added an extra class of total activity chosen at the 95% percentile.

4. Conclusions

This study is the first extended investigation of natural radioactivity in rocks, performed in the Tuscany Region (Italy). A total of 865 samples distributed over 45 geological groups were collected guided by the geological map of Tuscany at 1:250,000 scale. In particular, on average of at least one sample per 80 km^2 was collected, with an overall average of one sample per 25 km^2 . The total activity for each geological group was calculated by measuring the activity concentrations of ^{40}K , ^{238}U and ^{232}Th using a HPGe gamma-ray spectrometer. The results of this survey are represented by reclassifying the geological map of Tuscany for the median total activities.

The congruence between the total activity and the lithological characteristics of the geological groups is emphasized. In particular, the acid magmatic rocks of the Tuscan Magmatic Province in southern Tuscany, well-known for the highest content of natural radioactivity, are confirmed by these results. Furthermore, the carbonate rocks of Apuane Alps (External Tuscan Domain) as expected show the lowest total activity. These facts confirm the high degree of geological control on the radiometric response validating the method used for sampling and analysis.

Software

The geological map was digitalized using the ESRI ArcGIS 9.3 with final map production and layout completed using the Maplex extension for labeling management.

Acknowledgements

This work is partly supported by Direzione Generale Politiche Formative, Beni e Attività Culturali (Regione Toscana), partly by the Istituto Nazionale di Fisica Nucleare (INFN) and partly by Centro di GeoTecnologie (Università di Siena) and Fondazione Cassa di Risparmio di Padova e Rovigo. Authors would like to thank for their continuous support: Istituto Geografico Militare, Dipartimento di Scienze della Terra (University of Pisa), Litografia Artistica Cartografica and Litografia Artistica Cartografica. A special thanks goes to Antoniovanni M., Bellotti E., Blasi P., Di Carlo G., Fabbri A., Fabbri P., Fantozzi P. L., Mariani S., Morini D., Pagotto C., Shyti M. and Vannucci R. for helping us collect samples and develop the map.

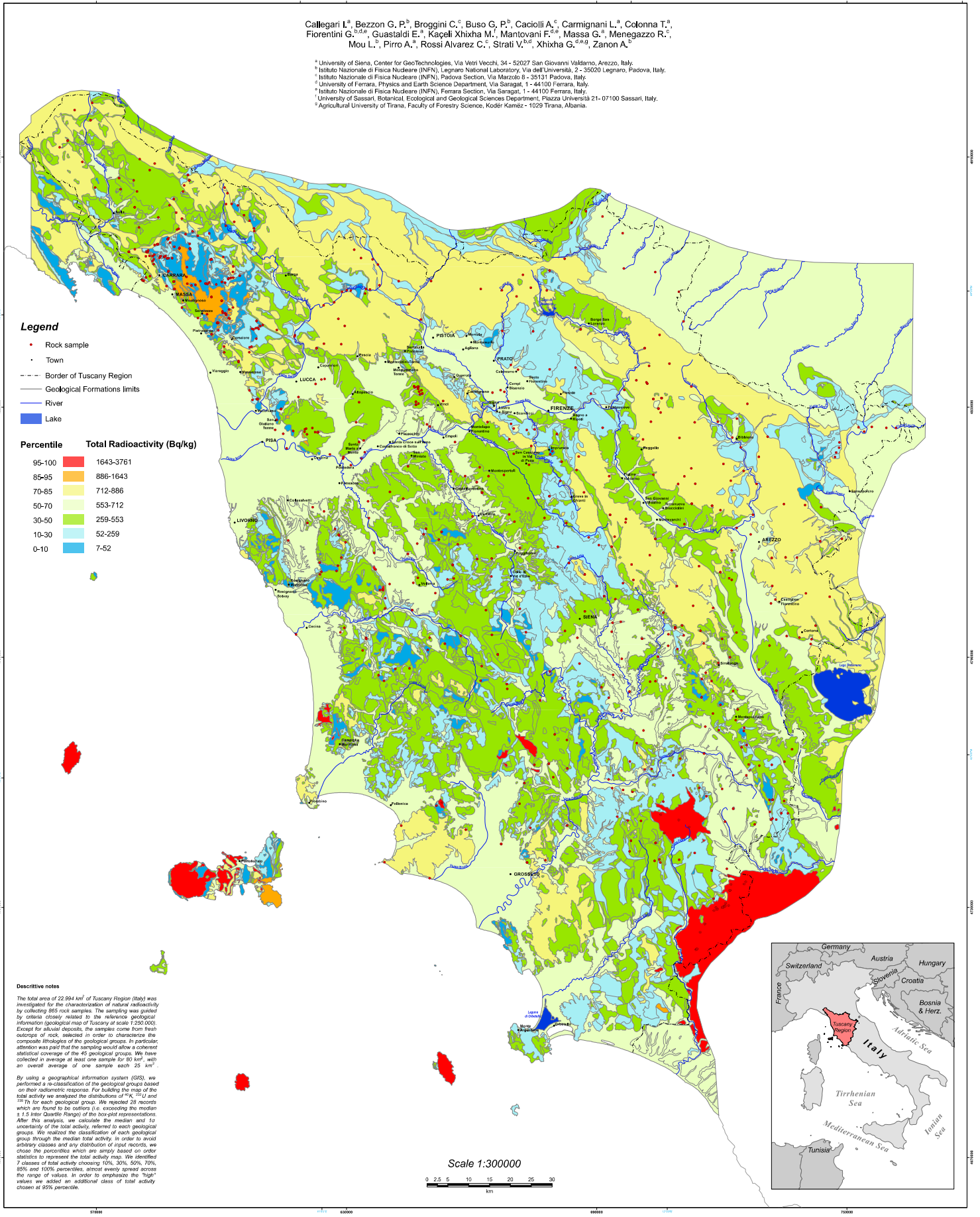
References

- Ahrens, L. H. (1954). The lognormal distributions of the elements. (A fundamental law of geochemistry and its subsidiary). *Geochimical Cosmochimical Acta*, 5, 49–73. doi: 10.1016/0016-7037(54)90040-X.
- Anagnostakis, M. J., Hinis, E. P., Simopoulos, S. E., & Angelopoulos, M. G. (1996). Natural radioactivity mapping of Greek surface soils. *Environment International*, 22(1), S3–S8. doi: 10.1016/S0160-4120(96)00085-2.
- Andjelov, M., & Brajnik, D. (1996). Map of natural radioactivity and radon emanation in Slovenia. *Environment International*, 22(1), S799–S804. doi: 10.1016/S0160-4120(96)00186-9.
- Barchi, M. R., De Feyter, A., Magnani, M. B., Minelli, G., Piali, G., & Sotera, B. G. (1998). The structural style of the Umbria-Marche fold and thrust belt. *Memorie della Società Geologica Italiana*, 52, 557–558. ISSN: 0375-9857.
- Boccaletti, M., Elter, P., & Guazzone, G. (1971). Plate tectonics model for the development of the Western Alps and Northern Apennines. *Nature*, 234, 108–111. doi: 10.1038/physci234108a0.
- Carmignani, L., Conti, P., Cornamusini, G., & Pirro, A. (2012). The geological map of Tuscany (Italy). Submitted for publication to Journal of Maps.
- Carmignani, L., Decandia, F. A., Disperati, L., Fantozzi, P. L., Kligfield, R., Lazzarotto, A., . . . Meccheri, M. (2001). Inner Northern Apennines. In G. B. Vai & I. P. Martini (Eds.), *Anatomy of an Orogen: The Apennines and adjacent Mediterranean basins* (pp. 197–214). Dordrecht (The Netherlands): Kluwer Acad. Publ.
- Cornamusini, G., Ielpi, A., Bonciani, F., Callegari, I., & Conti, P. (2012). Geological map of the Chianti Mts (Northern Apennines, Italy). *Journal of Maps*, 8(1), 22–32. doi: 10.1080/17445647.2012.668423.
- Council Directive 96/29/Euratom - ionizing radiation of 13 May 1996 laying down basic safety standards for the protection of the health of workers and the general public against the dangers arising from ionizing radiation.
- D.Lgs. 26 May 2000, nr. 241. Decreto Legislativo 26 maggio 2000, nr. 241 – Attuazione della direttiva 96/29/Euratom in materia di protezione sanitaria della popolazione e dei lavoratori contro i rischi derivanti dalle radiazioni ionizzanti – GU n.203 del 31/08/00.
- EURATOM Treaty. (1957). The Treaty establishing the European Atomic Energy Community (Euratom). Retrieved from LexNet website: <http://www.lexnet.dk/law/subjects/treaties.htm>
- Grasty, R. L. (1975). Uranium measurement by airborne gamma-ray spectrometry. *Geophysics*, 40, 503–519. doi: 10.1190/1.1440542.
- Grasty, R. L., & LaMarre, J. R. (2004). The annual effective dose from natural sources of ionising radiation in Canada. *Radiation Protection Dosimetry*, 108(3), 215–226. doi: 10.1093/rpd/nch022.
- Martini, I. P., & Sagri, M. (1993). Tectono-sedimentary characteristics of late miocene-quaternary extensional basins of the Northern Apennines, Italy. *Earth Sciences Reviews*, 34, 197–233. doi: 10.1016/0012-8252(93)90034-5.
- Mikšová, J., & Barnet, I. (2002). Geological support to the National Radon Programme (Czech Republic). *Bulletin of the Czech Geological Survey*, 77(1), 13–22. ISSN: 1210-3527.
- Minty, B.R. S. (2011). Airborne geophysical mapping of the Australian continent. *Geophysics*, 76(5), A27–A30. doi: 10.1190/geo2011-0056.1.
- Reimann, C. (2005). Geochemical mapping: Technique or art? *Geochemistry: Exploration, Environment, Analysis*, 5(4), 359–370. doi: 10.1144/1467-7873/03-051.
- Rybach, L., Bachler, D., Bucher, B., & Schwarz, G. (2002). Radiation doses of Swiss population from external sources. *Journal of Environmental Radioactivity*, 62, 277–286. doi: 10.1016/S0265-931X(01)00169-2.
- Štány Geologický Ústav Dionýza Štúra. Geophysical maps SR M 1: 500.000. Retrieved from Štány Geologický Ústav Dionýza Štúra website: http://www.geology.sk/?pg=geois.ms_gf-500_mpr_en
- Xhixha, G., Bezzon, G. P., Broggini, C., Buso, G. P., Caciolli, A., Callegari, I., . . . Xhixha Kaçeli, M. (2013). The worldwide NORM production and a fully automated gamma-ray spectrometer for their characterization. *Journal of Radioanalytical and Nuclear Chemistry*, 295, 445–457. doi: 10.1007/s10967-012-1791-1.
- Zhuo, W., Chen, B., Li, D., & Liu, H. (2008). Reconstruction of database on natural radionuclide contents in soil in China. *Journal of Nuclear Science and Technology*, 6, 180–184.

TOTAL NATURAL RADIOACTIVITY MAP OF TUSCANY (ITALY)

Callegari I.^a, Bezzon G. P.^b, Brogгинi C.^c, Buso G. P.^b, Caciolli A.^c, Carmignani L.^a, Colonna T.^d, Fiorentini G.^{b,d,e}, Guastaldi E.^a, Kaçeli Xhixha M.^f, Mantovani F.^g, Massa G.^h, Menegazzo R.ⁱ, Mou L.^j, Pirro A.^a, Rossi Alvarez C.^k, Strati V.^{l,m}, Xhixha G.^{d,e,g}, Zanon A.ⁿ

^a University of Siena, Center for GeoTechnologies, Via Vetrini Vecchi, 34 - 52027 San Giovanni Valdarno, Arezzo, Italy.
^b Istituto Nazionale di Fisica Nucleare (INFN), Legnaro National Laboratory, Via dell'Università, 2 - 35020 Legnaro, Padova, Italy.
^c Istituto Nazionale di Fisica Nucleare (INFN), Padova Section, Via Marzolo 8 - 35131 Padova, Italy.
^d University of Ferrara, Physics and Earth Science Department, Via Saragat, 1 - 44100 Ferrara, Italy.
^e Istituto Nazionale di Fisica Nucleare (INFN), Ferrara Section, Via Saragat, 1 - 44100 Ferrara, Italy.
^f University of Sassari, Botanical, Ecological and Geological Sciences Department, Piazza Università 21-07100 Sassari, Italy.
^g Agricultural University of Tirane, Faculty of Forestry Science, Koder Kamës - 1029 Tirane, Albania.



- Legend**
- Rock sample
 - Town
 - - - Border of Tuscany Region
 - Geological Formations limits
 - River
 - Lake

Percentile	Total Radioactivity (Bq/kg)
95-100	1643-3761
85-95	886-1643
70-85	712-886
50-70	553-712
30-50	259-553
10-30	52-259
0-10	7-52

Descriptive notes

The total area of 22 994 km² of Tuscany Region (Italy) was investigated for the characterization of natural radioactivity by collecting 265 rock samples. The sampling was guided by criteria closely related to the reference geological information (geological map of Tuscany at scale 1:250 000). Except for alluvial deposits, the samples come from fresh outcrops of rock, selected in order to characterize the composite lithologies of the geological groups. In particular, attention was paid that the sampling would allow a coherent statistical coverage of the 45 geological groups. We have collected in average at least one sample for 80 km², with an overall average of one sample each 25 km².

By using a geographical information system (GIS), we performed a re-classification of the geological groups based on their radiometric response. For building the map of the total activity we analyzed the distributions of ²³⁸U and ²³⁵Th for each geological group. We rejected 28 records which are found to be outliers (i.e. exceeding the median ± 1.5 Inter-Quartile Range) of the non-outlier concentrations. After this analysis, we calculate the median and 1 σ uncertainty of the total activity, referred to each geological groups. We realized the classification of each geological group through the median total activity. In order to avoid arbitrary classes and any distribution of input records, we chose the percentiles which are simply based on order statistics to represent the total activity map. We identified 7 classes of total activity choosing 10%, 30%, 50%, 70%, 85% and 100% percentiles, almost evenly spread across the range of values. In order to emphasize the "high" values we added an additional class of total activity chosen at 95% percentile.

Scale 1:300000

0 2.5 5 10 15 20 25 30 km



Radiological characterization of granitoid outcrops and dimension stones of the Variscan Corsica-Sardinia Batholith

Antonio Puccini · Gerti Xhixha · Stefano Cuccuru · Giacomo Oggiano · Merita Kaçeli Xhixha · Fabio Mantovani · Carlos Rossi Alvarez · Leonardo Casini

Received: 11 January 2013 / Accepted: 21 March 2013
© Springer-Verlag Berlin Heidelberg 2013

Abstract This study focuses on the radiological characterization of granitoid outcrops and dimension stones using in situ gamma-ray spectrometry. Extensive measurements were performed on 210 granitoid outcrops of the Corsica-Sardinia Batholith. The large statistical sample allowed us to improve the analysis by considering a log-normal distribution of radioelements and propagating the uncertainties using Monte Carlo method. The activity concentrations of ^{40}K , ^{226}Ra (^{238}U) and ^{232}Th in C-SB area were $1,177^{+408}_{-304}$, 60^{+36}_{-23} and 69^{+38}_{-25} Bq/kg (at 1σ uncertainty). The median abundance of K, U and Th on the Variscan C-SB was higher than the average values of the upper continental crust and was comparable with Variscan belt. This

corresponds to an outdoor absorbed dose rate of 124^{+33}_{-26} nGy/h at 1σ uncertainty which is 3σ higher than the population-weighted average absorbed dose rate (60 nGy/h). Seven commercial granites (*Rosa Beta*, *Ghiandone*, *Giallo San Giacomo*, *Rosa Cinzia*, *Grigio Malaga*, *Bianco Sardo* and *Grigio Perla*) were investigated to characterize their radiological hazard through 147 measurements taken in 73 extractive quarries. All of the commercial granites were categorized as A2 material based on their activity concentration indices, excluding (at the 3σ level) any restriction on their utilization as superficial materials. *Rosa Beta*, *Grigio Malaga*, *Grigio Perla* and *Bianco Sardo* can also be used as bulk materials as they can be included in the A1 category. In the case of *Ghiandone*, *Giallo San Giacomo* and *Rosa Cinzia*, we are confident of an A1 classification only at the 1σ level.

Electronic supplementary material The online version of this article (doi:10.1007/s12665-013-2442-8) contains supplementary material, which is available to authorized users.

A. Puccini · S. Cuccuru · G. Oggiano · M. K. Xhixha · L. Casini
Department of Science of Nature and Environmental Resources,
University of Sassari, Via Piandanna, 4, 07100 Sassari, Italy

G. Xhixha · F. Mantovani (✉)
Physics Department, University of Ferrara,
Via Saragat, 1, 44100 Ferrara, Italy
e-mail: Mantovani@fe.infn.it

G. Xhixha
Faculty of Forestry Science, Agricultural University of Tirana,
Kodër Kamëz, 1029 Tirana, Albania

G. Xhixha · F. Mantovani
Istituto Nazionale di Fisica Nucleare (INFN),
Ferrara Section, Via Saragat, 1, 44100 Ferrara, Italy

C. R. Alvarez
Istituto Nazionale di Fisica Nucleare (INFN),
Padova Section, Via Marzolo 8, 35131 Padua, Italy

Keywords In-situ gamma-ray spectrometry · Variscan Corsica-Sardinia Batholith · Granite · Dimension stones · Radiological hazard

Introduction

The gamma rays emitted from natural radioelements and, in particular, from ^{238}U and ^{232}Th decay chains and ^{40}K are important contributors to external radiation exposure. Approximately, 15 % of the world average radiation exposure comes from radioelements occurring naturally in the Earth's crust. The world average radioactivity content in the upper continental crust is 33 ± 7 , 43 ± 4 and 727 ± 60 Bq/kg for ^{238}U , ^{232}Th and ^{40}K , respectively (Rudnick and Gao 2003). Materials derived from rocks and soils widely used in the construction industry may be responsible for an excess in external radiation exposure and

may also contribute to the internal radiation (owing primarily to radon and its daughters).

An enrichment of radioactivity content and, in particular, of ^{238}U and ^{232}Th in metamorphic and granitic igneous rocks is often found in a few minerals such as apatite, sphene and zircon and other accessory phases (Whitfield et al. 1959; Rogers and Ragland 1961). Igneous plutonic rocks are characterized by relatively high concentrations of natural radionuclides varying over a wide range of up to 2,000 Bq/kg for ^{40}K (Anjos et al. 2005), 600 Bq/kg for ^{238}U (^{226}Ra) (Tzortzis et al. 2003; Salas et al. 2006) and 900 Bq/kg for ^{232}Th (Tzortzis et al. 2003).

Granite production in Europe is often linked to the occurrence of several Variscan batholiths throughout the continent, from Portugal and Spain in the west to Bohemia and Poland in the east. One of the largest batholiths is the Corsica-Sardinia Batholith (C-SB) (Rossi et al. 2009), exposed in the Sardinia-Corsica Microplate. In northern Sardinia, many varieties of granitoid rocks are frequently quarried and exported throughout the world. These rocks display substantial variation in their chemical–mineralogical composition and texture, making them appealing as dimension stones for flooring, columns, ashlar and other architectural structures.

The aims of this study are

1. the realization of an extensive in situ radiometric characterization of the C-SB area using a portable scintillation gamma-ray spectrometer and the evaluation of the outdoor external dose rate;
2. the radiological characterization of commercial granite dimension stones quarried in C-SB area by adopting the activity concentration index (ACI) (EC 2011) to evaluate the radiological implications of using these rocks as building materials in dwellings.

The geochemical features of commercial granite dimension stones were discussed based on inductively coupled plasma mass spectrometry (ICP-MS) measurements. The results were cross-checked with measurements performed using a high-purity germanium (HPGe) gamma-ray spectrometer and ICP-MS.

The late Variscan granites of the Corsica-Sardinia Batholith

A large part of Sardinia, $\sim 6,000\text{ km}^2$ in total area (Ghezzi and Orsini 1982), consists of C-SB granitic rocks (Fig. 1). The C-SB is closely related to the evolution of the south European Variscan belt (Paquette et al. 2003). The C-SB formed over a time interval of approximately 60 Ma, from 340 to 280 Ma (Paquette et al. 2003; Renna et al. 2006; Gaggero et al. 2007). The long period of emplacement

reflects important differences in terms of chemical composition, mineralogy and texture (Casini et al. 2012). The oldest intrusions ($\sim 340\text{ Ma}$; Paquette et al. 2003) exposed in NW Corsica are represented by the so-called “durbachites” of high Mg–K calc-alkaline association. The calc-alkaline association is widespread in Sardinia and Corsica and consists mostly of metaluminous to slightly peraluminous monzogranites, granodiorites and subordinate leucomonzogranites. The youngest magmatic bodies of calc-alkaline to transitional alkaline affinity consist of small mafic bodies, dated at approximately 285 Ma (Renna et al. 2006; Gaggero et al. 2007), that crop out in southern Corsica and Sardinia. The dominant rock types are gabbros, diorites and quartzdiorite with a tholeiitic signature. Finally, in Corsica, an alkaline association of early Permian age is also documented (Cocherie et al. 2005). The Sardinian sector of the C-SB arose from the coalescence of many calc-alkaline plutons dominated by monzogranites and subordinately by granodiorites; gabbroic rocks and tonalites are very scarce (Bralia et al. 1981; Casini et al. 2012).

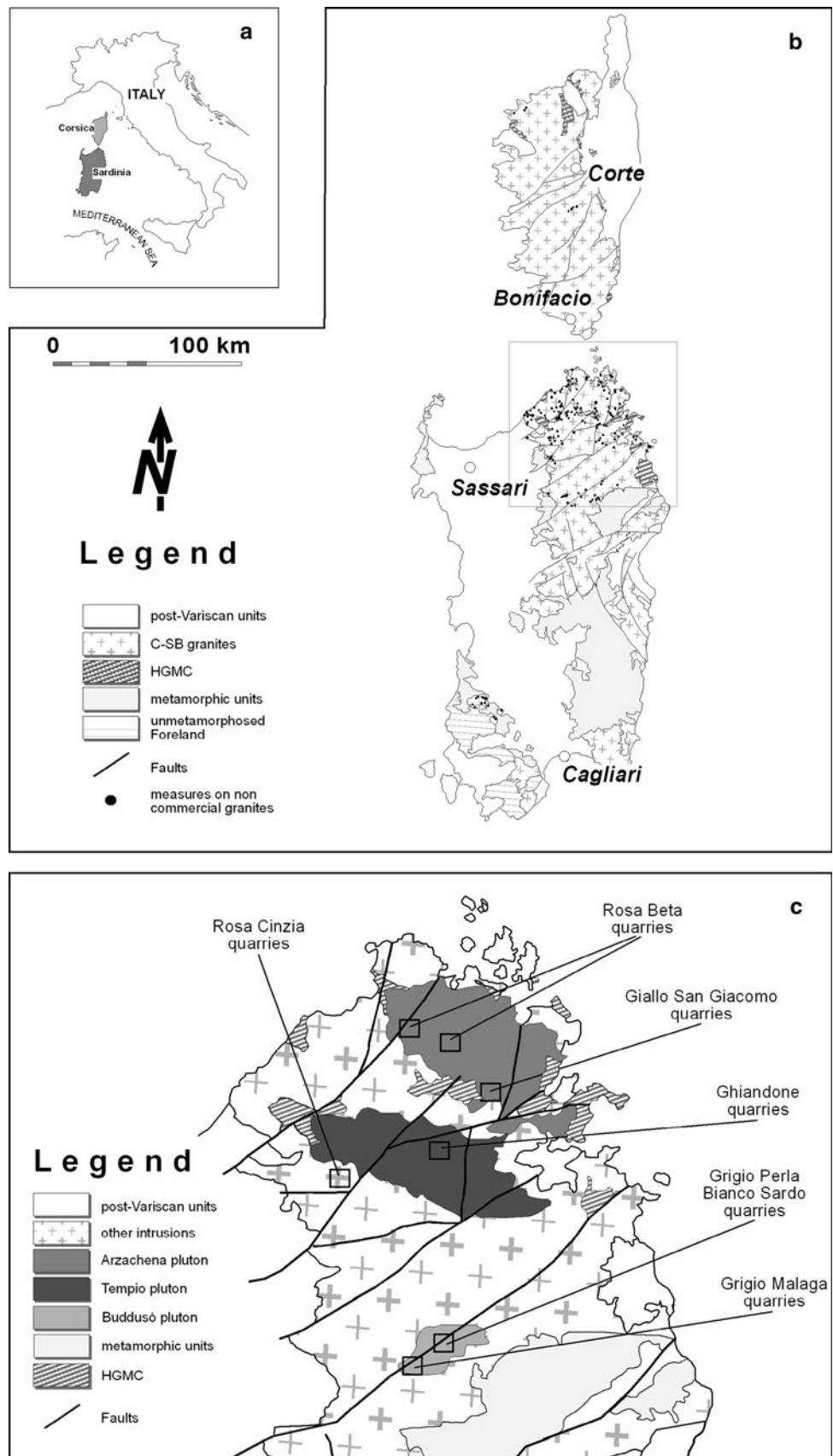
The dating of the calc-alkaline magmatism in Sardinia has recently been improved based on U/Pb zircon ages and Ar/Ar hornblende, muscovite and biotite ages; collectively, the data indicate a temporal window between 321 and 285 Ma (Oggiano et al. 2007; Gaggero et al. 2007). Most of the plutons emplaced between 311 and 300 Ma are mildly peraluminous monzogranites in their composition; between 300 and 285 Ma, the volume of granodiorite increased (Oggiano et al. 2005).

Three main plutons, distributed over an area of $\sim 1,000\text{ km}^2$, supply most of the granite production from Sardinia (Fig. 1c). They are, in order of importance

- the Arzachena pluton (Oggiano et al. 2005; Casini et al. 2012), which is the largest one. It shows a variety of lithofacies from almost equigranular to strongly porphyritic monzogranite (due to the occurrence of 2–3 cm-large K-feldspar phenocrysts) to equigranular granodiorites;
- the Tempio pluton (Cherchi 2005), which is comprised mostly coarse-grained biotite-rich monzogranites with huge (3–12 cm) K-feldspar xenocrysts and leucomonzogranites;
- the Buddusò pluton (Barbey et al. 2008), characterized by an abundance of granodiorites, monzogranites and leucomonzogranites.

The Tempio and Arzachena plutons exhibit a similar inverse zonation; the granodiorites are found in the core and progressively more differentiated terms such as monzogranites, and leucomonzogranites are found in the outer shells. The Buddusò pluton, on the other hand, displays a normal zonation, ranging from granodioritic facies in the external shell to monzogranitic and leucomonzogranitic facies in the core.

Fig. 1 **a** Position of the Corsica-Sardinia block in the Mediterranean Sea. **b** Geological sketch map of the C-SB. The 210 measurements used for its characterization are indicated by the *black circles*. **c** Position of seven extractive districts where 147 in situ measurements were performed. The Buddusò, Arzachena and Tempio plutons are also indicated. *HGMC* high grade metamorphic complex



The study of heat radiogenic elements in Sardinian sector of the C-SB is relevant for the comprehension of the origin of the extensive high-temperature and low pressure (HT-LP) province established in the Variscan belt during the Carboniferous-Permian transition. The causes of high thermal gradients which brought about anatexis melting is still debated (Cocherie et al. 1994; Faure et al. 2010). One of the hypotheses is based on a significant enrichment of heat radiogenic elements in the lower crust (Lexa et al. 2011): HT-metamorphism could be a consequence of melt-induced rheological adjustments of thick orogenic roots. The present radiological characterization of C-SB area might be included as a constraint of models which study the thermal budget of Variscan crust (Casini 2012).

Sardinian granite dimension stones and their geochemical characterization

Granites from the C-SB have been utilized extensively since ancient times (Poggi and Lazzarini 2005) and are still exploited from approximately 400 quarries in Northeast Sardinia (RAS 2007) and traded worldwide (Fig. 1c). The dimension stones are appreciated by the market as both structural (concrete, masonries, columns, etc.) and ornamental components (flooring, tiles, boards, etc.). The most famous granites¹ from C-SB are known commercially as *Rosa Beta*, *Ghiandone*, *Giallo San Giacomo*, *Rosa Cinzia*, *Grigio Malaga*, *Bianco Sardo* and *Grigio Perla*.

Rosa Beta (Fig. 2a) and *Giallo San Giacomo* (Fig. 2c) are the two commercial granites exploited from the Arzachena pluton (Fig. 1c). *Rosa Beta* is the most commercialized biotite-monzogranite among the Sardinian granites (RAS 2007). This pinkish rock has a medium grain size ranging from 0.5 to 2 cm and a strong porphyritic fabric owing to the presence of K-feldspar phenocrysts (2–3 cm). *Giallo San Giacomo* is a biotitic leucomonzogranite with an apparently isotropic and almost equigranular fabric; this granite is highly valued in the current market for its typically yellowish hue, arising from selective weathering and oxidation of Fe–Mg minerals (Cuccuru et al. 2012).

Ghiandone (Fig. 2b) is found in the Tempio pluton (Cherchi 2005) and was the most widely traded granite in the 1970s and 1980s (RAS 2007). It is a coarse-grained, strongly porphyritic biotite-monzogranite with large K-feldspar phenocrysts (up to 12 cm) dispersed within a finer-grained matrix (0.5–2 cm) composed of K-feldspar, quartz and plagioclase. *Rosa Cinzia* (Fig. 2d) is a pinkish, nearly equigranular biotite-monzogranite exploited in only three quarries located around the town of Tempio Pausania.

Its grain size ranges from 0.5 to ~1.5 cm, which is finer than that of *Rosa Beta*.

Grigio Malaga (Fig. 2e), *Grigio Perla* (Fig. 2f) and *Bianco Sardo* (Fig. 2g) are the three commercial granites exploited in the Buddusò pluton and represent the least, intermediate and most differentiated terms of the Buddusò intrusion, respectively (Barbey et al. 2008). *Grigio Malaga* is a tonalitic granodiorite with a grain size between 0.5 and 1.5 cm. This stone displays a well-foliated fabric that is revealed by the shape preferred orientation of its mafic enclaves and its amphibole-biotite-rich domains. *Grigio Perla* is a biotite-monzogranite with a grain size of approximately 1 cm and a gray, nearly equigranular fabric. *Bianco Sardo* is a leuco-monzogranite characterized by an equigranular fabric, relatively fine grain size (~1 cm) and overall whitish color owing to a scarcity of biotites.

The geochemical characterization is obtained from ICP-MS analysis of representative samples, which are ordered in Table 1 according to silica content. The SiO₂ content of samples ranges from 68.8 % in *Grigio Malaga* to 77.6 % in *Giallo San Giacomo*. The A/CNK ratio² generally increases with the silica content, varying from 0.96 in *Rosa Beta* up to 1.04 in *Giallo San Giacomo*. This indicates that all granites are metaluminous to slightly peraluminous, as commonly observed in most granites of the C-SB (Casini et al. 2012; Barbey et al. 2008).

The abundances of Ba and Sr show a negative correlation with the SiO₂ content. This behavior is even more apparent for other trace elements at the scale of a single pluton such as Buddusò pluton (*Grigio Malaga*, *Grigio Perla* and *Bianco Sardo*). The chondrite-normalized rare earth element (REE) contents are consistent in all samples (Fig. 3) showing almost flat heavy REE patterns and moderately enriched light REE, which indicates slight fractionation (Ce/Yb = 8 ÷ 10). All samples are characterized by a negative Eu anomaly, which increases from relatively basic (*Grigio Malaga*) to the more acidic materials (*Bianco Sardo*, *Giallo San Giacomo*) (Fig. 3). These observations suggest that all of the investigated granites derived from a common crustal source, as already proposed by Ferrè and Leake (2001).

The high radioactivity content in igneous rocks is generally attributed to the enrichment of U and Th. Uranium phases such as uraninite, beta- and alpha-uranophane and thorium phases such as thorianite have occasionally been identified only in pegmatites and similar highly evolved magmatic liquids (Gamboni and Gamboni 2006). Although these bodies may be common in the apical part of any intrusions (e.g., the Arzachena Pluton (Cuccuru et al. 2011)), their volume and consequently their contribution to

¹ The names of granite dimension stones are taken from UNI EN 12440 (2008).

² The ratio of aluminum/total alkali content is obtained by Al₂O₃/(CaO + Na₂O + K₂O).

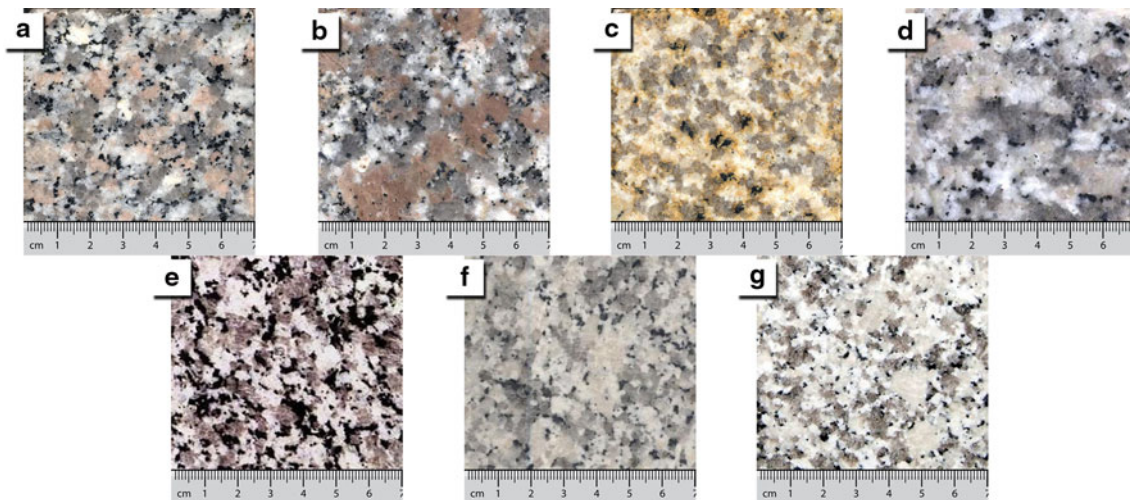


Fig. 2 Seven commercial granite tiles of **a** *Rosa Beta*, **b** *Ghiandone*, **c** *Giallo San Giacomo*, **d** *Rosa Cinzia*, **e** *Grigio Malaga*, **f** *Grigio Perla* and **g** *Bianco Sardo*

the bulk radioactivity are generally negligible. However, most granites contain a significant (1–2 wt%) quantity of U and Th bearing accessory mineral phases, such as zircon, allanite, apatite, monazite and xenotime (Gamboni and Gamboni 2006).

In our samples, the general increase of U and Th observed in the more evolved granites ($\text{SiO}_2 > 70$ wt%) correlates well with a decrease in the ZrO_2 component and increase of Y. This indicates that zircon is probably the main U and Th bearing mineral in the less evolved samples such as *Rosa Beta*, *Ghiandone* and *Grigio Malaga*, while Y-bearing phases such as allanite and xenotime become progressively more important during the evolution of magmas.

Materials and methods

In this study, a total of 357 in situ gamma-ray measurements were performed. Of these, 210 were measured on granitoid outcrops of the C-SB (Fig. 1b) and 147 were measured on 73 quarries of *Rosa Beta*, *Ghiandone*, *Giallo San Giacomo*, *Rosa Cinzia*, *Grigio Malaga*, *Bianco Sardo* and *Grigio Perla*, collecting for each lithotype 21 measurements (Table A.1).

A portable equipment mounted in a backpack and enfolded in shock-resistant materials to prevent damage in outdoor environments was used. The scintillation gamma-ray spectrometer inside the backpack consisted of an NaI(Tl) crystal with a cubic shape ($10.2 \times 10.2 \times 10.2$ cm³) and an energy resolution of 7.3 % at 662 keV (¹³⁷Cs) and 5.2 % at 1,172 and 1,332 keV (⁶⁰Co). The crystal was optically coupled to a photomultiplier tube with integrated electronics consisting of a bias supply,

preamplifier and digital multichannel analyzer (MCA). The system was managed using a notebook computer fitted with a GPS antenna (54 channels and 10 m accuracy).

The instrument was carefully calibrated following the method described in Caciolli et al. (2012). Using full spectrum analysis with the non-negative least squares (FSA-NNLS) constraint, each measured spectrum is reconstructed from a linear combination of standard spectra for ²³⁸U, ²³²Th, ⁴⁰K, ¹³⁷Cs and background. The systematic uncertainty of the method is estimated to be 5 % for ⁴⁰K and 7 % for ²³²Th. The primary contributor to the U standard spectrum is the decay of ²¹⁴Bi, a daughter of ²²²Rn, which is present in the ground and in the air. Although the instrument cannot discriminate between the two contributions from the ground and the air, the systematic uncertainty in the ²³⁸U measurement for the ground is of order 15 % (Caciolli et al. 2012). In the case of 5-min in situ measurements on C-SB outcrops, the statistical uncertainties were <1.5, 3 and 3 % for ⁴⁰K, ²³⁸U and ²³²Th, respectively (Table A.1).

The main advantages of using in situ measurements are (a) quick feedback, (b) a large sample size, (c) immediate repeatability of the measurement and (d) low management costs. In contrast to laboratory HPGc spectrometry and ICP-MS, in situ gamma-ray spectroscopy provides a direct measurement of the radioactivity content of a large portion of rock. In our study, 357 in situ measurements were performed with the detector on the ground. In this configuration, 90 % of the signal reaching the detector came from a volume of radius 35 cm and ~20 cm thick, corresponding to an effective rock mass of ~200 kg.

A number of relevant precautions were taken to ensure the reliability of our measurements. To minimize the interference due to morphology, relatively flat outcrops

Table 1 Whole-rock major (wt %) and trace ($\mu\text{g/g}$) element compositions of the 7 commercial granites. Conservatively, an accuracy of 10 % for ICP-MS results was assumed

Chemical composition	Commercial granites						
	Grigio Malaga Sa15 ^a	Rosa Beta	Grigio Perla	Ghiandone	Rosa Cinzia	Bianco Sardo Sa22c ^a	San Giacomo
Major elements (expressed in wt%)							
SiO ₂	68.75	71.11	72.43	73.02	74.31	75.09	77.59
Al ₂ O ₃	15.28	13.85	14.02	13.35	13.41	13.48	12.18
Fe ₂ O ₃	3.81	0.8	0.62	1.18	0.69	1.42	0.78
FeO	–	1.82	1.46	1.09	0.93	–	0.29
CaO	3.34	2.33	1.84	2.46	1.75	1.52	0.57
Na ₂ O	3	3.57	3.38	3.2	3.15	3.07	3.34
K ₂ O	3.72	3.91	4.37	3.22	4.62	4.81	4.74
MgO	0.92	0.71	0.44	0.75	0.29	0.24	0.05
TiO ₂	0.4	0.353	0.187	0.295	0.163	0.09	0.06
P ₂ O ₅	0.15	0.34	0.06	0.09	0.04	0.07	0.03
MnO	0.05	0.065	0.082	0.065	0.033	0.04	0.02
LOI	0.5	0.72	0.54	0.62	0.44	0.59	0.28
Total	99.92	99.78	99.59	99.46	99.93	100.42	99.95
Trace elements (expressed in $\mu\text{g/g}$)							
Be	–	3	2	2	2	–	1
Sc	–	7	6	5	3	–	2
V	43	33	14	36	13	6	<5
Cr	10	<20	<20	<20	<20	–	40
Co	5	3	2	3	1	1	<1
Ni	–	<20	<20	<20	<20	–	<20
Cu	–	< 10	< 10	20	< 10	–	<10
Zn	57	<30	50	50	<30	25	<30
Ga	19	16	17	16	15	15	18
Ge	–	1	2	2	2	–	1
As	–	<5	<5	<5	<5	–	<5
Rb	108	120	165	112	139	123	101
Sr	195	211	88	171	93	70	13
Y	17	23	38	15	16	11	29
Zr	177	251	115	113	107	25	269
Nb	9	13	13	10	9	6	6
Mo	–	<2	<2	<2	<2	–	4
Ag	–	1.1	<0.5	<0.5	<0.5	–	<0.5
In	–	<0.2	<0.2	<0.2	<0.2	–	<0.2
Sn	–	4	5	3	3	–	4
Sb	–	<0.5	<0.5	<0.5	<0.5	–	<0.5
Cs	4	3	3	2.7	2.9	2	1.1
Ba	1,197	888	465	470	507	285	189
La	49.9	38.6	26.6	24.9	26.9	17	32.6
Ce	95.2	74.8	54	48.3	54	37.5	73.5
Pr	10.56	8.13	6.5	5.46	6.28	4.51	7.82
Nd	36.8	28.8	24.7	20.1	23	15.9	27.7
Sm	6.06	5.6	5.5	3.5	4.1	3.09	5.3
Eu	1.23	1.08	0.57	0.69	0.67	0.49	0.21
Gd	3.88	4.6	5	2.7	3.1	2.28	4.7
Tb	0.6	0.7	0.9	0.4	0.5	0.31	0.7

Table 1 continued

Chemical composition	Commercial granites						
	Grigio Malaga Sa15 ^a	Rosa Beta	Grigio Perla	Ghiandone	Rosa Cinzia	Bianco Sardo Sa22c ^a	San Giacomo
Dy	3.12	4	5.8	2.5	2.7	1.74	3.7
Ho	0.59	0.8	1.2	0.5	0.5	0.34	0.7
Er	1.62	2.2	3.6	1.5	1.5	0.97	2.2
Tm	0.21	0.34	0.61	0.25	0.23	0.14	0.32
Yb	1.51	2.3	4.1	1.7	1.6	0.95	2.1
Lu	0.24	0.37	0.7	0.32	0.29	0.18	0.33
Hf	4	6.7	3.3	3	2.8	3	7.6
Ta	–	1.4	1.5	1	0.7	–	0.5
W	–	<1	<1	<1	<1	–	<1
Tl	–	0.5	1	0.6	0.8	–	0.5
Pb	–	21	26	18	21	–	27
Bi	–	< 0.4	< 0.4	< 0.4	< 0.4	–	<0.4
Th	15	12.9	17	14.4	15.6	11	15.1
U	2	5.2	3.1	4	3.6	2	2.6

^a Data taken from (Barbey et al. 2008)

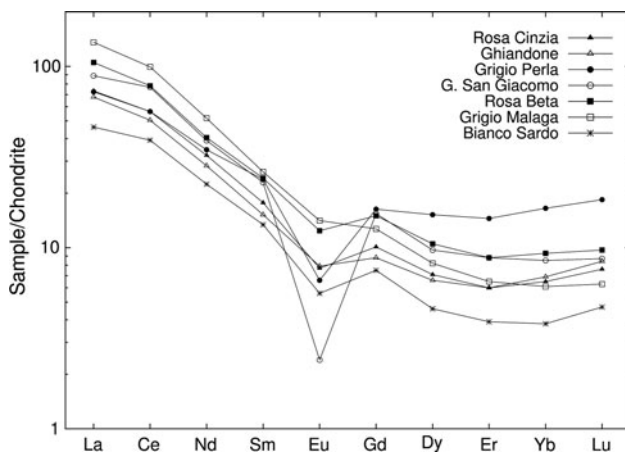


Fig. 3 Chondrite normalized REE patterns of the seven granite dimension stones analyzed

were chosen, far from the sides of the outcrop and from man-made constructions. The portable NaI(Tl) detector was placed on bare rocks with no soil cover or vegetation. The measurements were never performed immediately after rainfalls and since the detector was placed on bare rocks the interference of moisture was considered negligible. The ²³⁸U and ²³²Th activity concentrations were calculated assuming secular equilibrium in the decay series.

The activity concentrations of ⁴⁰K, ²³⁸U and ²³²Th obtained from in situ surveys were compared with those measured in individual samples of each commercial granite using inductively coupled plasma mass spectrometry (ICP-MS) and HPGe spectrometry (Table 2). The elemental composition measurements were performed at Activation

Laboratories Ltd. using a Perkin Elmer SCIEX ELAN 9000 ICP/MS with a combination of analysis packages Code 4B (lithium metaborate/tetraborate fusion ICP whole rock) and Code 4B2 (trace element ICP-MS), in which the fused sample is diluted and analyzed using ICP-MS. The detection limits of these methods for K₂O, U and Th were 0.01 % (2.6 Bq/kg), 0.1 µg/g (1.2 Bq/kg) and 0.1 µg/g (0.4 Bq/kg), respectively. The ICP-MS method permits not only to crosscheck in situ measurements, but it also provides information on the major and trace element composition necessary for the geochemical characterization of different granites (see Sect. 3).

The activity concentrations were measured on a 180 cm³ sample using the MCA_Rad system (Xhixha et al. 2013). The fully automatic spectrometer consists of two 60 % relative efficiency coaxial p-type HPGe gamma-ray detectors, with an energy resolution of ~1.9 keV at 1332.5 keV (⁶⁰Co). The absolute full energy peak efficiency of the MCA_Rad is calibrated using certified standard point sources (¹⁵²Eu and ⁵⁶Co). The overall uncertainty in the efficiency calibration is estimated to be <5 %.

Results and discussion

Statistical analysis

The latter measurements were used to determine the radiological hazard of 7 types of commercial granites. The distributions of the ⁴⁰K, ²³⁸U and ²³²Th activity concentration of these two classes of data are reported in Figs. 4,

Table 2 Median values of the log-normal distributions of ^{40}K , ^{238}U and ^{232}Th activity concentration with 1σ asymmetrical uncertainty, based on 21 in situ measurements (NaI:Tl). For each commercial granite, a measurement was performed with HPGe detectors and ICP-

MS. In the fourth row are reported data published in the literature (in brackets the number of samples). The activity concentration index (ACI) and default dose categories are indicated in the last two columns

Commercial brand	Quarries/HPGe analysis/bibliography	^{40}K (Bq/kg)	^{238}U (Bq/kg)	^{232}Th (Bq/kg)	ACI	Category
<i>Rosa Beta</i>	NaI:Tl (20 quarries)	$1,144^{+126}_{-114}$	$42.3^{+7.7}_{-6.6}$	$55.0^{+6.8}_{-9.6}$	$0.78^{+0.06}_{-0.06}$	A1
	HPGe	1059 ± 19	37.4 ± 2.0	55.1 ± 2.9		A2
	ICP-MS ^a	1,020	64	52		
	(Tzortzis et al. 2003; Al-Saleh and Al-Berzan 2007; Aydarous et al. 2010; Carrera et al. 1996; SR 2012) (9 data)	897–1,221	18.2–45.2	32.0–69.0		
<i>Ghiandone</i>	NaI:Tl (20 quarries)	$1,092^{+215}_{-181}$	$56.3^{+14.1}_{-11.4}$	$68.9^{+11.2}_{-9.6}$	$0.88^{+0.11}_{-0.09}$	A1/B1
	HPGe	953 ± 21	49.6 ± 2.4	50.8 ± 3.1		A2
	ICP-MS	840	49	58		
	(Tzortzis et al. 2003; SR 2012) (5 data)	736–1,047	33.3–57.0	59.1–89.0		
<i>G. San Giacomo</i>	NaI:Tl (13 quarries)	$1,335^{+142}_{-128}$	$50.1^{+15.7}_{-11.9}$	$61.9^{+10.1}_{-8.7}$	$0.91^{+0.10}_{-0.08}$	A1/B1
	HPGe	1284 ± 25	53.2 ± 2.6	55.0 ± 3.6		A2
	ICP-MS	1,257	28	62		
	(SR 2012) (2 data)	919–1,019	19.8–58.6	47.5–58.0		
<i>Rosa Cinzia</i>	NaI:Tl (2 quarries)	$1,313^{+66}_{-63}$	$56.0^{+7.2}_{-6.5}$	$69.4^{+3.5}_{-3.3}$	$0.95^{+0.04}_{-0.04}$	A1/B1
	HPGe	$1,296 \pm 25$	46.2 ± 2.4	60.2 ± 3.5		A2
	ICP-MS	1,205	44	63		
	(SR 2012) (1 data)	1,023	34.0	56.1		
<i>Grigio Malaga</i>	NaI:Tl (8 quarries)	848^{+130}_{-113}	$34.5^{+5.0}_{-4.3}$	$61.1^{+5.8}_{-5.3}$	$0.66^{+0.05}_{-0.05}$	A1
	HPGe	711 ± 18	29.2 ± 2.0	52.8 ± 3.2		A2
	ICP-MS (Barbey et al. 2008)	970	25	61		
	(SR 2012) (1 data)	748	22.9	51.2		
<i>Grigio Perla</i>	NaI:Tl (7 quarries)	$1,222^{+165}_{-145}$	$39.1^{+5.6}_{-4.9}$	$60.6^{+6.0}_{-5.5}$	$0.81^{+0.06}_{-0.06}$	A1
	HPGe	$1,270 \pm 25$	52.3 ± 2.6	61.0 ± 3.6		A2
	ICP-MS	1,140	38	69		
	(Carrera et al. 1996; SR 2012) (2 data)	1,039–1,208	33.7–37.0	45.3–58.0		
<i>Bianco Sardo</i>	NaI:Tl (3 quarries)	$1,269^{+66}_{-63}$	$44.8^{+7.6}_{-6.5}$	$51.6^{+7.8}_{-6.8}$	$0.82^{+0.05}_{-0.05}$	A1
	HPGe	$1,355 \pm 25$	40.8 ± 2.3	50.5 ± 3.1		A2
	ICP-MS (Barbey et al. 2008)	1,255	25	45		
	(Carrera et al. 1996) (1 data)	1,137	48	95		

^a Conservatively, an accuracy of 10 % for ICP-MS results was assumed

5, and 6. The variances of the commercial granite data are slightly smaller than those of the data collected at scattered locations on outcrops of the C-SB. Both classes generally have non-normal distributions. The distribution of ^{40}K in non-commercial (commercial) granites shows negative skewness of -1.1 (-0.7), while the distributions of ^{238}U and ^{232}Th show positive skewness of 1.3 (1.2) and 0.8 (0.1), respectively. The distributions are well fitted with a log-normal probability function (Ahrens 1954) (as reported in footnotes in Fig. 4, 5, and 6 the reduced χ^2 is <2 with exception to the case of ^{40}K in non-commercial C-SB granites where it is 4.3), which was used to calculate the asymmetrical (geometric) standard deviation (Table 2).

These results are used to calculate the absorbed dose rate in outdoor air and the ACI, when the combined asymmetric uncertainties were estimated by Monte Carlo method (Huang et al. 2012; JCGM 2008). In particular, 10^5 pseudo-random samples for each input (^{40}K , ^{238}U and ^{232}Th) are generated according to the specific distribution parameters (median and 1σ uncertainty). The distributions of the absorbed dose rate and the ACI were estimated by repeating the process over a cycle of iterations and the median and combined asymmetric uncertainties are evaluated. This improved analysis accounts for the non-normal distribution of elements in igneous rocks. By adopting a log-normal distribution as the universal form of the

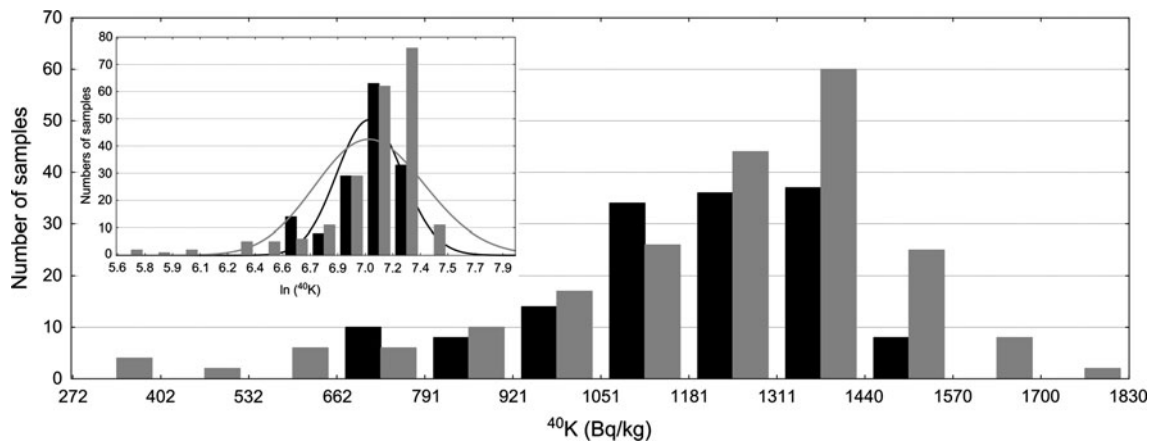


Fig. 4 Distribution of the activity concentration of ^{40}K in Bq/kg. The 210 measures of non-commercial C-SB granitic rocks (in gray), and 147 measures of commercial granitic rocks (in black) are fitted with log-normal distributions showing, respectively, a reduced χ^2 of 4.3 and 1.8

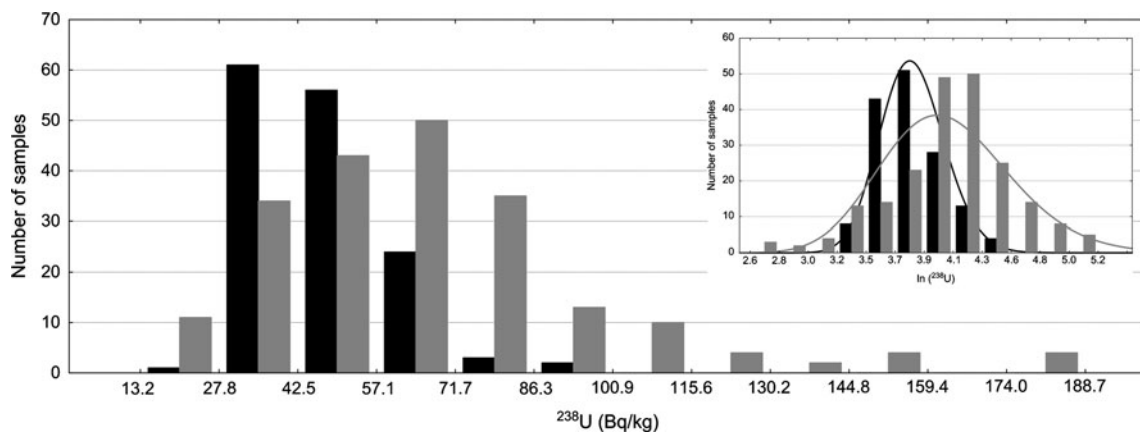


Fig. 5 Distribution of the activity concentration of ^{238}U in Bq/kg. The 210 measures of non-commercial C-SB granitic rocks (in gray), and 147 measures of commercial granitic rocks (in black) are fitted with log-normal distributions showing, respectively, a reduced χ^2 of 1.6 and 0.7

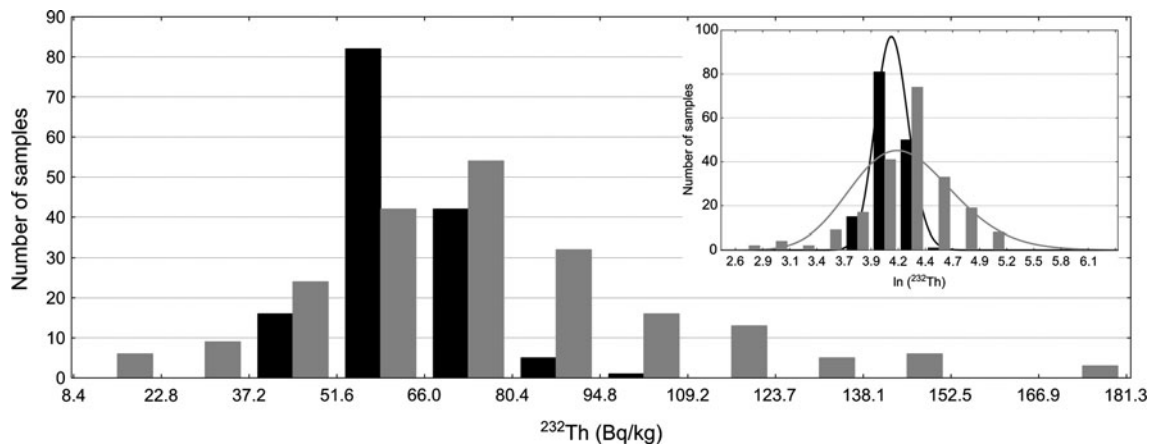


Fig. 6 Distribution of the activity concentration of ^{232}Th in Bq/kg. The 210 measures of non-commercial C-SB granitic rocks (in gray), and 147 measures of commercial granitic rocks (in black) are fitted with log-normal distributions showing, respectively, a reduced χ^2 of 1.6 and 0.8

abundance distribution, the incidence of high values in the tails of the distribution is increased. Based on the statistical meaning of a 1σ uncertainty, we are able to quantify the probability of exceeding a given absorbed dose rate and/or ACI.

Radiological characterization of the C-SB granitic rocks

The radioactivity concentrations of the C-SB granitic plutons are generally higher than those typical for the upper continental crust (Rudnick and Gao 2003). The activity concentrations of ^{40}K , ^{238}U and ^{232}Th (at 1σ uncertainty) are $1,177^{+408}_{-304}$, 60^{+36}_{-23} and 69^{+38}_{-25} Bq/kg, respectively. The abundances of ^{238}U and ^{232}Th are comparable to those in the upper portion of the continental crust at the 1σ level, while the ^{40}K content is $\sim 2\sigma$ higher. The relatively high concentration of radioelements in the C-SB crust could be related to the origin of the extensive HT-LP province established in the Variscan belt during the Carboniferous–Permian transition, as discussed in (Lexa et al. 2011; Schulmann et al. 2008). The wide spread of the measurements made on outcrops in the Sardinian sector of the Batholith is a consequence of a coalescence of many calc-alkaline plutons (see Sect. 2). The Sardinian Batholith crust has a lower average abundance ratio of K/U and Th/U values of 7.8×10^3 and 3.5, respectively.

The absorbed dose rate in air from external gamma radiation at 1 m above ground level due to the presence of natural radionuclides in measured outcrops is calculated as (UNSCEAR 2000)

$$D \text{ (nGy h}^{-1}\text{)} = 0.0417 C_{\text{K}} + 0.462 C_{\text{U}} + 0.604 C_{\text{Th}},$$

where C_{K} , C_{U} , C_{Th} are the activity concentrations (in Bq/kg) of ^{40}K , ^{238}U (^{226}Ra) and ^{232}Th . In the C-SB, the outdoor absorbed dose rate at 1σ uncertainty is 124^{+33}_{-26} nGy/h (the maximum and minimum calculated values are 28 and 256 nGy/h). This dose is 3σ higher than the population-weighted average absorbed dose rate in outdoor air from terrestrial gamma radiation (60 nGy/h). However, only 3.3 % of our measurements exceed the upper limit of the worldwide typical range of variability of 10–200 nGy/h (UNSCEAR 2000).

The radiological hazard is evaluated using the annual effective dose rate (expressed in mSv/y). Adopting a conversion factor of 0.7 (Sv/Gy) (UNSCEAR 2000), which accounts for the dose biological effectiveness in causing damage to human tissue and an outdoor time occupancy factor of 20 %, was calculated the annual effective dose rate of the population living in the C-SB area. The obtained annual outdoor effective dose rate of $0.15^{+0.04}_{-0.03}$ mSv/y is 3σ higher than the worldwide annual effective dose value of 0.07 mSv/y reported by UNSCEAR (2000).

For each commercial granite, a measurement was performed with HPGe detectors and ICP-MS. In the fourth row are reported data published in the literature (in brackets the number of samples). The ACI (ACI) and default dose categories are indicated in the last two columns.

ACI of commercial granites

The radiological characterization of the seven commercial granites is reported in Table 2. The abundances of ^{40}K and ^{232}Th exceed those in the upper continental crust by more than 1σ for all of the granites except *Grigio Malaga* and *Bianco Sardo*. The ^{238}U abundance is comparable to that in the upper continental crust at the 1σ level for all except *Ghiandone* and *Rosa Cinzia*. However, the spreads of the distributions are narrower than those for the C-SB pluton outcrops: for ^{40}K and ^{232}Th , 68.3 % of the data lie within 12 % of the median value. The higher variance ($\langle \sigma \rangle \sim 20\%$) of the ^{238}U measurements is comparable to the systematic uncertainty of the NaI(Tl) detector. In general, the distributions of the *Rosa Cinzia* and *Bianco Sardo* are narrower, and these considering the number of quarries investigated, respectively, 2 and 3, is an evidence on the reliability of the measures representing the variability of commercial granites quarried in C-SB area.

The radiological hazard of rocks used as building materials can be evaluated using the ACI (ACI), proposed by EC (2011):

$$\text{ACI} = \frac{C_{\text{Ra}}}{300} + \frac{C_{\text{Th}}}{200} + \frac{C_{\text{K}}}{3,000},$$

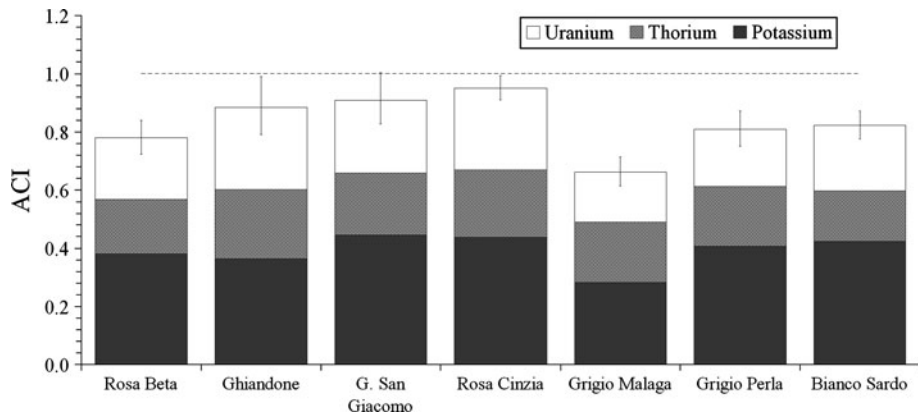
where C_{Ra} , C_{Th} and C_{K} are the activity concentrations in Bq/kg for ^{226}Ra (equivalent to ^{238}U under secular equilibrium conditions), ^{232}Th and ^{40}K , respectively. Following EC (2011), the radiological hazard is classified into four categories. The first category of materials is appropriate for use in bulk quantities, while the second category of materials is limited to superficial or other restricted use (Table 3). The contribution to the ACI index of the median radioactivity content for potassium, uranium and thorium is shown in Fig. 7. It shows that $\sim 50\%$ of the ACI index comes from ^{40}K .

The ACI varies from $0.66^{+0.05}_{-0.05}$ for *Grigio Malaga* to $0.95^{+0.04}_{-0.04}$ for *Rosa Cinzia*. Because they have ACIs < 6 within the reported standard deviation, these rocks are categorized as A2 (suitable for being used as surface materials without restriction). The ACIs of *Rosa Beta*, *Grigio Malaga*, *Grigio Perla* and *Bianco Sardo* are more than 2σ below unity and, therefore, these materials can be classified as A1 (suitable for being used as bulk materials without restriction). However, *Rosa Cinzia*, *Giallo san Giacomo* and *Ghiandone* have ACIs within 1σ of unity. In

Table 3 Categories based on the default dose according to the ACI (ACI) criteria defined in EC (2011)

Category (corresponding default dose)	Type 1 Materials used in bulk amounts e.g. concrete, bricks etc.	Type 2 superficial and other materials with restricted use e.g. tiles, boards etc.
A (≤ 1 mSv/y)	For ACI ≤ 1 category A1	For ACI ≤ 6 category A2
B (>1 mSv/y)	For ACI > 1 category B1	For ACI > 6 category B2

Fig. 7 The ACI (ACI) calculated for each commercial granite using the median values for ^{40}K , ^{238}U and ^{232}Th



these cases, it is reported the classification A1/B1 (Table 2) to emphasize a potential radiological hazard in bulk utilization of these commercial granites, and recommend further ad hoc controls.

The activity concentrations measured with NaI:Tl and HPGe spectrometry are comparable at the 1σ level; however, the data collected in situ are more robust since they are supported by more observations. Although some of the ICP-MS data are 2σ away (only for *Bianco Sardo* was found a discrepancy at 3σ for ^{238}U activity concentration) from the median of the in situ investigations, there is general agreement between the ^{40}K , ^{238}U and ^{232}Th abundances measured using the three different methods. However, the laboratory measurements are based on the assumption that the samples are representative of the entire dimension stone. This hypothesis is weak, and may increase the discrepancies with respect to the in situ data. In the case of the granitic rocks of the C-SB, the in situ measurements provide a suitable method of investigation, as indicated by previously published data (Table 2).

Summary and conclusions

An extensive in situ survey was performed for the first time in the C-SB area using a portable NaI(Tl) scintillation detector for the determination of the radioactivity concentration of ^{40}K , ^{238}U and ^{232}Th on 210 intrusive granite outcrops. Moreover, the radioactivity content of the main seven commercial granites quarried in 73 extractive sites in this area was investigated by means of 147 in situ

measurements. This approach made it possible to collect a large statistics of samples while minimizing time and costs, and optimizing the spectral analysis through FSA-NNLS. The large number of measurements permitted to perform an accurate analysis of the data based on assumed log-normal distributions of the radioelements. The propagation of asymmetrical uncertainties was treated using a Monte Carlo method instead of assuming Gaussian errors, increasing the quality of the radiological characterization of the rocks.

The in situ measurements on granitoid outcrops of the C-SB showed activity concentrations of $1,177^{+408}_{-304}$, 60^{+36}_{-23} and 69^{+38}_{-25} Bq/kg for ^{40}K , ^{226}Ra (^{238}U) and ^{232}Th , respectively. These data are found to be comparable at the 1σ level to those in the upper continental crust for uranium and thorium, whereas the potassium content is $\sim 2\sigma$ higher. These results were used to assess the outdoor absorbed dose rate, which is 124^{+33}_{-26} nGy/h (ranging between 28 and 256 nGy/h), and exceeding the reported UNSCEAR (2000) population-weighted average absorbed dose rate (60 nGy/h) by more than 3σ . However, only 3.3 % of our measurements exceed the upper limit of the worldwide typical range of variability of 10–200 nGy/h. The corresponding annual outdoor effective dose rate for the population living in the C-SB area is calculated to be $0.15^{+0.04}_{-0.03}$ mSv/y.

The ^{40}K , ^{238}U and ^{232}Th activity concentrations of commercial granites measured in 73 quarries show good agreement (at 2σ level) compared to data from representative samples using ICP-MS and HPGe spectrometry. The ACI of the seven traded varieties was found to range between $0.66^{+0.05}_{-0.05}$ for *Grigio Malaga* and $0.95^{+0.04}_{-0.04}$ for

Rosa Cinzia. All of these granites are categorized with 3σ confidence as A2 material, permitting their utilization as superficial materials without restrictions. *Rosa Beta*, *Grigio Malaga*, *Grigio Perla* and *Bianco Sardo* are categorized with 2σ confidence as A1 materials, and may, therefore, also be used in bulk quantities without restriction. However, *Ghiandone*, *Giallo San Giacomo* and *Rosa Cinzia* have activity concentration indices within 1σ of the limiting value, and further ad hoc controls are, therefore, recommended for their utilization in bulk quantities.

Acknowledgments The authors are grateful to G. P. Bezzon, C. Brogini, G. P. Buso, A. Caciolli, L. Carmignani, T. Colonna, S. De Bianchi, G. Fiorentini, M. Gambaccini, Y. Huang, W. F. McDonough, R. Menegazzo, L. Mou, R. L. Rudnick, M. Shyti and A. Zanon for useful comments and discussions. This work was funded by the Banco di Sardegna Foundation (G. Oggiano grant) and Sardinia Government grant L.R. 7/2007—no CRP2_104 (L. Casini and S. Cuccuru) and was partially supported by National Institute of Nuclear Physics, INFN (Italy).

References

- Ahrens LH (1954) The lognormal distributions of the elements. (A fundamental law of geochemistry and its subsidiary). *Geochim Cosmochim Acta* 5:49–73
- Al-Saleh FS, Al-Berzan B (2007) Measurements of natural radioactivity in some kinds of marble and granite used in Riyadh region. *J Nucl Rad Phys* 2:25–36
- Anjos RM, Veiga R, Soares T, Santos AMA, Aguiar JG, Frascá MHBO, Brage JAP, Uzêda D, Mangia L, Fature A, Mosquera B, Carvalho C, Gomes PRS (2005) Natural radionuclide distribution in Brazilian commercial granites. *Radiat Meas* 39:245–253
- Aydarous ASH, Zeghib S, Al-Dughmah M (2010) Measurements of natural radioactivity and the resulting radiation doses from commercial granites. *Radiat Prot Dosim* 142:363–368
- Barbey P, Gasquet D, Pin C, Bourgeix AL (2008) Igneous banding, schlieren and mafic enclaves in calc-alkaline granites: the Budduso pluton (Sardinia). *Lithos* 104:147–163
- Bralia A, Ghezzi C, Guasparri G, Sabatini G (1981) Aspetti genetici del batolite sardo-corso. *Rend Soc Ital Miner Petrol* 38:701–764
- Caciolli A, Baldoncini M, Bezzon GP, Brogini C, Buso GP, Callegari I, Colonna T, Fiorentini G, Guastaldi E, Mantovani F, Massa G, Menegazzo R, Mou L, Rossi Alvarez C, Shyti M, Xhixha G, Zanon A (2012) A new FSA approach for in situ γ ray spectroscopy. *Sci Total Environ* 414:639–645
- Carrera G, Garavaglia M, Magnoni S, Valli G, Vecchi R (1996) Natural radioactivity and radon exhalation in stony materials. *J Environ Radioactiv* 34:149–159
- Casini L (2012) A MATLAB-derived software (geothermMOD1.2) for one-dimensional thermal modeling, and its application to the Corsica-Sardinia batholith. *Comput Geosci* 45:82–86
- Casini L, Cuccuru S, Maino M, Oggiano G, Tiepolo M (2012) Emplacement of the Arzachena Pluton (Corsica-Sardinia Batholith) and the geodynamics of incoming Pangaea. *Tectonophysics* 544:31–49
- Cherchi GP (2005) Prospezione e caratterizzazione di rocce granitoidi della Sardegna settentrionale: indicazioni per l'ottimizzazione del processo estrattivo e della mitigazione degli impatti. PhD. Thesis (in Italian), University of Sassari
- Cocherie A, Fouillac R, Vidal AM (1994) Crust and mantle contributions to granite genesis—an example from the Variscan batholith of Corsica, France, studied by trace element and Nd–Sr–O-isotope systematics. *Chem Geology* 115:173–211
- Cocherie A, Rossi P, Fanning CM, Guerrot C (2005) Comparative use of TIMS and SHRIMP for U–Pb zircon dating of A-type granites and mafic tholeiitic layered complexes and dykes from the Corsican Batholith (France). *Lithos* 82:185–219
- Cuccuru S, Gamboni A, Casini L (2011) The Mt. Mazzolu quarry: a new mineralogic locality *Plinius* 37:304
- Cuccuru S, Casini L, Oggiano G, Cherchi GP (2012) Can weathering improve the toughness of a fractured rock? A case study using the San Giacomo Granite. *Bull Eng Geol Environ* 71(3):557–567
- European Commission (EC) (2011) Draft presented under Article 31 Euratom Treaty for the opinion of the European Economic and Social Committee: laying down basic safety standards for protection against the dangers arising from exposure to ionising radiation. COM(2011) 593, Brussels. http://ec.europa.eu/energy/nuclear/radiation_protection/doc/com_2011_0593.pdf. Accessed 26 Oct 2011
- Faure M, Cocherie A, Bé Mézème E, Charles N, Rossi P (2010) Middle carboniferous crustal melting in the Variscan Belt: new insights from U–Th–Pb total monazite and U–Pb zircon ages of the Montagne Noire Axial Zone (southern French Massif Central). *Gondwana Res* 18(4):653–673
- Ferrè EC, Leake BE (2001) Geodynamic significance of early orogenic high-K crustal and mantle melts: example of the Corsica-Sardinia Batholith. *Lithos* 59:47–67
- Gaggero L, Oggiano G, Buzzi L, Slejko F, Cortesogno L (2007) Post-Variscan mafic dykes from the late orogenic collapse to the Tethyan rift: evidence from Sardinia. *Ophioliti* 32:15–37
- Gamboni A, Gamboni T (2006) Gallura, tesori nel granito, i minerali delle pegmatiti granitiche. Webber, Sassari
- Ghezzi C, Orsini J-B (1982) Lineamenti strutturali e composizionali del batolite ercinico sardo corso in Sardegna. In: Guida alla geologia del Paleozoico Sardo, Soc Geol Ita, Roma, pp 88–102
- Huang Y, McDonough WF, Mantovani F (2012) Propagation of uncertainties in geochemistry by Monte Carlo simulation. *Chem Geol* (Submitted)
- Joint Committee for Guides in Metrology (JCGM) (2008) Evaluation of measurement data—supplement 1 to the “guide to the expression of uncertainty in measurement”—propagation of distributions using a Monte Carlo method (1st edn). JCGM 101, p 90
- Lexa O, Schulmann K, Janoušek V, Stipská P, Guy A, Racek M (2011) Heat sources and trigger mechanisms of exhumation of HP granulites in Variscan orogenic root. *J Metamorphic Geol* 29:79–102
- Oggiano G, Cherchi G P, Aversano A, Di Pisa A, Ulzega A, Orrù P, Pintus C (2005) Note illustrative della Carta Geologica d'Italia, Arzachena
- Oggiano G, Casini L, Rossi P H, Mameli P (2007) Long lived dextral strike-slip tectonics in the southern Variscan Belt: evidence from two syn-kynematic intrusions in north Sardinia, vol 2. In: *Geologie de la France, Meeting on Mechanics of Variscan Orogeny: a modern view on orogenic research*, Orleans, Sept. 13–15, p 141
- Paquette J-L, Ménot R-P, Pin C, Orsini J-B (2003) Episodic and short-lived granitic pulses in a post-collisional setting: evidence from precise U–Pb zircon dating through a crustal cross-section in Corsica. *Chem Geol* 198:1–20
- Poggi D, Lazzarini L (2005) Il granito sardo: cave e cavatura. Usi, diffusione e aspetti archeometrici. *Marmora* 1:49–68
- Regione Autonoma della Sardegna (RAS) (2007) Piano Regionale delle Attività Estrattive: riepilogo dei principali dati, Cagliari

- Renna MR, Tribuzio R, Tiepolo M (2006) Interaction between basic and acid magmas during the latest stages of the post-collisional Variscan evolution: clues from the gabbro–granite association of Ota (Corsica–Sardinia batholith). *Lithos* 90:92–110
- Rogers JJW, Ragland PC (1961) Variation of thorium and uranium in selected granitic rocks. *Geochim Cosmochim Acta* 25:99–109
- Rossi P, Oggiano G, Cocherie A (2009) A restored section of the “southern Variscan realm” across the Corsica-Sardinia micro-continent. *Comp Rend Geosci* 341:224–238
- Rudnick R L, Gao S (2003) Composition of the Continental Crust, vol 3. In: Holland H D, Turekian K K (eds) *Treatise on geochemistry: meteorites, comets and planets*, vol 1, Elsevier Ltd., Oxford, pp 59–659
- Salas HT, Nalini HA Jr, Mendes JC (2006) Radioactivity dosage evaluation of Brazilian ornamental granitic rocks based on chemical data, with mineralogical and lithological characterization. *Environ Geol* 49:520–526
- Sardegna Ricerche (SR) (2012) Progetto Cluster “radioattività nei materiali da costruzione”. http://www.sardegna ricerche.it/documenti/13_116_20110114161302.pdf. Accessed 1 Aug 2012
- Schulmann K, Lexa O, Štípská P, Racek M, Tahčmanová L, Konopásek J, Edel J-B, Peschler A, Lehmann J (2008) Vertical extrusion and horizontal channel flow of orogenic lower crust: key exhumation mechanisms in large hot orogens? *J Metamorphic Geol* 26:273–297
- Tzortzis M, Tsertos H, Christofides S, Christodoulides G (2003) Gamma radiation measurements and dose rates in commercially-used natural tiling rocks (granites). *J Environ Radioactiv* 70:223–235
- UNI (Ente Nazionale Italiano di Unificazione). Natural stone—denomination criteria. UNI-EN 12440:2008
- United Nations Scientific Committee on the Effects of Atomic Radiation (UNSCEAR) (2000) *Exposures from Natural Radiation Sources*. UN, New York
- Whitfield JM, Rogers JJW, Adams JAS (1959) The relationship between the petrology and the thorium and uranium contents of some granitic rocks. *Geochim Cosmochim Acta* 17:248–271
- Xhixha G, Bezzon GP, Broggin C, Buso GP, Caciolli A, Callegari I, De Bianchi S, Fiorentini G, Guastaldi E, Mantovani F, Massa G, Menegazzo R, Mou L, Pasquini A, Rossi Alvarez C, Shyti M, Xhixha Kaçeli M (2013) The worldwide NORM production and a fully automated gamma-ray spectrometer for their characterization. *J Radioanal Nucl Chem* 295:445–457

FIRST CHARACTERISATION OF NATURAL RADIOACTIVITY IN BUILDING MATERIALS MANUFACTURED IN ALBANIA

G. Xhixha^{1,2,3,*}, A. Ahmeti³, G. P. Bezzon¹, M. Bitri³, C. Broggin⁴, G. P. Buso¹, A. Cacioli^{1,4}, I. Callegari⁵, F. Cfarku⁶, T. Colonna⁵, G. Fiorentini^{1,2,7}, E. Guastaldi⁵, F. Mantovani^{2,7}, G. Massa⁵, R. Menegazzo⁴, L. Mou¹, D. Prifti⁸, C. Rossi Alvarez⁴, Dh. Sadiraj Kuqi⁹, M. Shyti^{2,7}, L. Tushe⁹, M. Xhixha Kaçeli¹⁰ and A. Zyfi³

¹Istituto Nazionale di Fisica Nucleare (INFN), Legnaro National Laboratory, Via dell'Università, 2, Legnaro, Padova 35020, Italy

²Physics Department, University of Ferrara, Via Saragat, 1, Ferrara 44100, Italy

³Faculty of Forestry Science, Agricultural University of Tirana, Kodër Kamëz, Tirana 1029, Albania

⁴Istituto Nazionale di Fisica Nucleare (INFN), Padova Section, Via Marzolo 8, Padova 35131, Italy

⁵Center for GeoTechnologies, University of Siena, Via Vetri Vecchi, 34, San Giovanni Valdarno, Arezzo 52027, Italy

⁶Faculty of Natural Sciences, Centre of Applied Nuclear Physics, University of Tirana, PO Box 85, Tirana, Albania

⁷Istituto Nazionale di Fisica Nucleare (INFN), Ferrara Section, Via Saragat, 1, Ferrara 44100, Italy

⁸Antea Cement Sh.A., Boka e Kuqe, Burizanë, Krujë, Albania

⁹Polytechnic University of Tirana, Square Nënë Tereza, 4, Tirana, Albania

¹⁰Botanical, Ecological and Geological Sciences Department, University of Sassari, Piazza Università 21, Sassari 07100, Italy

*Corresponding author: xhixha@fe.infn.it

Received August 17 2012, revised December 21 2012, accepted December 22 2012

This study focuses on the radiological characterisation of building materials manufactured in Albania by using a high-resolution gamma-ray spectrometer. The average activity concentrations of ^{40}K , ^{226}Ra and ^{232}Th were, respectively, 644.1 ± 64.2 , 33.4 ± 6.4 and 42.2 ± 7.6 Bq kg⁻¹ in the clay brick samples and 179.7 ± 48.9 , 55.0 ± 5.8 and 17.0 ± 3.3 Bq kg⁻¹ in the cement samples. The calculated activity concentration index (ACI), varied from 0.48 ± 0.02 to 0.63 ± 0.04 in the clay brick samples and from 0.29 ± 0.03 to 0.37 ± 0.02 in the cement samples. Based on the ACI, all of the clay brick and cement samples were categorised as A1 materials. The authors can exclude (at 3σ level) any restriction of their use as bulk materials.

INTRODUCTION

An important contribution to public radioactive exposure is made by external terrestrial radiation, principally due to uranium and thorium decay chains, and by ^{40}K , which is present in the Earth's crust. According to the United Nations Scientific Committee on the Effects of Atomic Radiation⁽¹⁾, this contribution corresponds to $\sim 20\%$ (ranging between 0.3 and 1.0 mSv y⁻¹) of the average worldwide radiation exposure (2.4 mSv y⁻¹). Considering an indoor occupancy factor of 0.8 , the average indoor-to-outdoor ratio of the contribution of external terrestrial radiation is roughly 6 .

Building materials contain naturally occurring radionuclides; therefore, they are potential sources contributing to excesses in external and internal radiation exposure due to their final uses in dwellings. According to the European recommendations^(2, 3), building materials are classified as suitable for use by regulating an upper external radiation exposure limit of 1.0 mSv y⁻¹.

Scientific interest in studying the radioactivity content of various building materials has increased in the last decade^(4–6). Moreover, industrial waste/by-products (e.g. fly ash, red mud and phosphogypsum) have recently been adapted and used as additives in various building materials^(7–9). This industrial waste and these by-products are themselves subject to regulations⁽¹⁰⁾ because of the potential increase of naturally occurring radioactive materials (NORMs) due to technological processes⁽¹¹⁾.

Clay bricks and cements are the principal building materials manufactured in Albania, constituting an important proportion of the domestic construction industry, as well as being exported to several foreign countries^(12, 13). However, there is a lack of data about the natural radioactivity content in these building materials.

The aim of this study was to characterise the concentrations of ^{40}K , ^{226}Ra and ^{232}Th in the clay brick and cement samples manufactured in Albania using a high-resolution gamma-ray spectrometer. These data

were further used to evaluate the absorbed dose rate of indoor external gamma radiation due to exposure to natural radionuclides. Recent criteria, based on the activity concentration index (ACI)⁽³⁾, were used to assess the potential radiological hazards associated with the final use of these materials in dwellings. Finally, these data were compared with the values reported in the similar studies performed in those countries that are economic partners of Albania.

EXPERIMENTAL METHODS

Sampling and sample preparation

The Albanian industries of clay brick and cement have become heavily developed over the last few decades, offering quality products for the European market. More than 80 % of the clay bricks and cements commercialised in Albania are produced, respectively, by 9 and 3 manufacturers located across the country (Figure 1). For each of these 12 manufacturers, 5 different samples were collected to obtain a homogeneous data set of 60 samples.

The samples of clay brick were crushed and milled into fine powders with the particle size of <2 mm, while the samples of cement were directly processed because they were already in a powder form. To remove the moisture content, all of the samples were dried in a temperature-controlled furnace at 110°C for at least 24 h (or until constant weight). After cooling in a moisture-free atmosphere, each sample was transferred for measurement to a cylindrical PVC container (with the dimensions of diameter of 7.5 cm × 4.5 cm of height and an effective volume of 180 cm³) and was then weighted. The hermetically sealed containers were stored for at least 4 weeks prior to measurement to allow ²²⁶Ra and its short-lived decay products to reach the secular equilibrium. Each box contained materials coming from the different stocks of clay bricks and cement samples collected in the period from 2010 to 2012.

The same protocol was applied to the three certified reference materials (95% confidence interval)⁽¹⁴⁾, prepared in a powder matrix (240 mesh) containing 4940 ± 30 Bq kg⁻¹ of ²³⁸U (diluted uranium ore BL-5), 3250 ± 90 Bq kg⁻¹ of ²³²Th (diluted thorium ore OKA-2) in a secular equilibrium and 14 000 ± 400 Bq kg⁻¹ of ⁴⁰K (high-purity K₂SO₄). These certified reference materials were used to calibrate the gamma-ray spectrometer^(15, 16).

High-resolution gamma-ray spectrometry calibration and measurements

The natural radioactivity content of the building materials was investigated using a fully automated high-resolution gamma-ray spectrometry system, called the MCA_Rad system⁽¹⁷⁾. This equipment is

composed of two coaxial high-purity germanium p-type detectors with a 60 % relative efficiency, having an energy resolution of 1.9 keV at 1332.5 keV (⁶⁰Co).

The certified International Atomic Energy Agency reference materials, prepared in a standard geometry, were measured to study the efficiency of the MCA_Rad system. A self-absorption correction, due to variations in the density and the composition between the samples and the reference materials, was performed, considering the approach discussed in detail by Bolivar *et al.*⁽¹⁷⁾ and by Cutshall *et al.*⁽¹⁸⁾. According to this approach, the self-attenuation correction factor (Eq. 1) is given as a function of the sample density and of the energy of the gamma ray investigated. The ratio of the self-attenuation factor in a reference material (C_{SA}^{ref}) to that of the sample (C_{SA}^s) allows for the definition of the self-attenuation correction factor (C_{SA}),

$$C_{SA} = \frac{C_{SA}^{ref}}{C_{SA}^s} \quad (1)$$

or

$$C_{SA} = \frac{1 + a_1 E^{-a_2}}{\exp[\rho_s(a_3 + a_4 \ln E + a_5 \ln E^2)]} \quad (2)$$

where E is the gamma-ray energy (in keV), ρ_s is the sample density (in g/cm³) and a_n are arbitrary parameters. An average mass attenuation coefficient⁽¹¹⁾ was parameterised in the energy range of 200–3000 keV and used to calculate the best fit of the C_{SA} functions, fixing the following coefficients as $a_1 = 8.8443$, $a_2 = 0.5157$, $a_3 = 1.2609$, $a_4 = -0.2547$ and $a_5 = 0.0134$ ⁽¹¹⁾.

The activity concentration of the samples (A_s in Bq kg⁻¹) is then calculated by using the formula:

$$A_s = \frac{[R_s / (m_s \cdot C_\epsilon)]}{C_{SA}} \quad (3)$$

where R_{ref} and R_s are the count rates (in cpm); A_{ref} and A_s are the activity concentrations (in Bq kg⁻¹) and m_{ref} and m_s are the masses (in kg) for, respectively, in the reference materials and the samples. In Table 1 the values of the conversion coefficient [$C_\epsilon = R_{ref} / (A_{ref} m_{ref})$] for the principal gamma-ray energies investigated are reported.

RESULTS AND DISCUSSION

Activity concentrations

Measuring for 1 h the activity concentration of isotopes mentioned in Table 1, the activity concentrations of ²²⁶Ra, ²³²Th and ⁴⁰K in 60 samples were determined. In appendix A, the results and overall

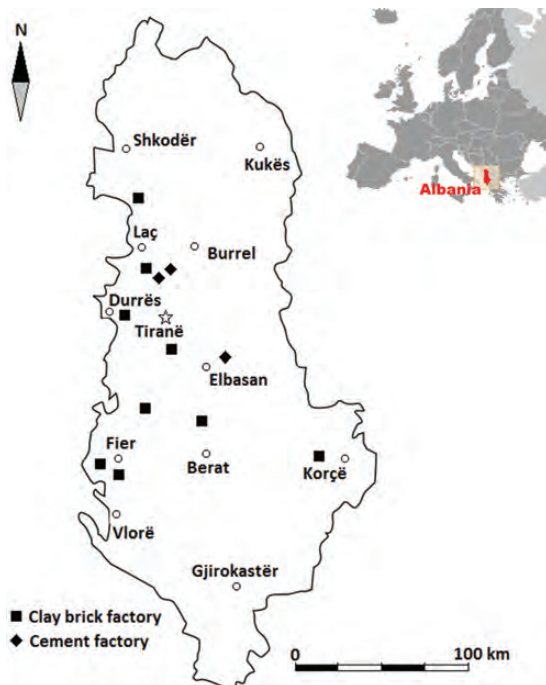


Figure 1. The location of the clay brick (rectangles) and cement (rhombi) factories investigated in this study.

Table 1. The fixed conversion coefficients C_e (obtained as described in Eq. 3), used for measuring the elements reported in column two, calculated for the principal photopeaks with energy E and having the highest gamma yield I .

Parent isotope	Daughter isotope	E (keV)	I (%)	$C_e \pm \sigma$ (cpm Bq ⁻¹)
²³⁸ U	^{234m} Pa	1001	0.84	0.0153 (2)
	²¹⁴ Bi	609	44.8	0.9634 (59)
²³² Th	²¹⁴ Pb	352	35.8	1.2714 (78)
	²²⁸ Ac	911	26.6	0.4850 (134)
	²¹² Pb	238	43.3	1.9019 (527)
	²¹² Bi	727	6.58	0.1505 (42)
⁴⁰ K	²⁰⁸ Tl	583	84.5	0.6478 (180)
	—	1460	11.0	0.1437 (42)

measurement uncertainties (Supplementary data, Table A1) are reported. The authors note that the radioactivity contents from each manufacturer were homogeneous. Because the standard deviation of the mean for the five samples was comparable to the measurement uncertainty, in Table 2 the mean and combined errors were reported for each manufacturer. The combination of uncertainties was estimated by the Monte Carlo simulation⁽¹⁹⁾. In particular, to obtain the standard deviation of the mean, matrices

were generated with the 10^5 pseudo-random values, using the individual measurement parameters (K, U and Th measures $\pm 1\sigma$). The activity concentrations of K, U and Th in the clay brick samples were found to be lower than or comparable within 1σ to that of the typical activity concentrations of 670, 50 and 50 Bq kg⁻¹ for ⁴⁰K, ²²⁶Ra and ²³²Th, respectively⁽²⁾.

Radiological hazard indexation

The radiological hazards of the building materials were calculated by adopting the following ACI, which is widely used at the investigation level for practical monitoring purposes⁽²⁰⁾:

$$ACI = \frac{C_{Ra}}{300} + \frac{C_{Th}}{200} + \frac{C_K}{3000}, \quad (4)$$

where C_{Ra} , C_{Th} and C_K are the activity concentrations in Bq kg⁻¹ for radium (equivalent to uranium under the secular equilibrium conditions), thorium and potassium, respectively. Following ref. (3), the radiological hazard could be classified into four classes, leading to two categories of materials used in bulk amounts and materials with superficial or restricted uses (Table 3).

Table 2. For each manufacturer, ID, the specific activity (mean $\pm 1\sigma$) calculated for ^{40}K , ^{226}Ra and ^{232}Th (in Bq kg^{-1}), the ACI, the absorbed gamma dose rate indoors (D^{indoor}) and the AEDE are reported.

Manufacturer ID	^{40}K (Bq kg^{-1})	^{226}Ra (Bq kg^{-1})	^{232}Th (Bq kg^{-1})	ACI	D^{indoor} (nGy h^{-1})	AEDE (mSv y^{-1})
Clay brick						
A	723.7 ± 65.8	40.5 ± 4.6	50.1 ± 4.7	0.63 ± 0.04	92.4 ± 8.5	0.45 ± 0.04
B	671.1 ± 58.0	42.1 ± 5.8	44.4 ± 3.8	0.59 ± 0.03	83.3 ± 8.2	0.41 ± 0.04
C	644.2 ± 50.4	29.0 ± 2.2	37.4 ± 3.0	0.50 ± 0.02	61.4 ± 5.6	0.30 ± 0.03
D	608.1 ± 75.2	32.6 ± 5.1	38.4 ± 9.4	0.50 ± 0.06	62.8 ± 12.9	0.31 ± 0.06
E	672.3 ± 29.9	33.8 ± 2.2	42.6 ± 3.0	0.57 ± 0.02	79.2 ± 4.5	0.39 ± 0.02
F	566.5 ± 37.2	31.2 ± 2.8	45.4 ± 7.4	0.52 ± 0.04	66.0 ± 9.1	0.32 ± 0.04
G	613.9 ± 21.2	28.7 ± 2.2	35.1 ± 3.4	0.48 ± 0.02	56.2 ± 4.6	0.28 ± 0.02
H	642.8 ± 45.1	28.0 ± 4.7	39.1 ± 5.6	0.50 ± 0.04	62.2 ± 8.4	0.30 ± 0.04
I	654.3 ± 25.0	34.4 ± 5.8	47.6 ± 4.7	0.57 ± 0.03	78.3 ± 7.7	0.38 ± 0.04
Cement						
J	157.0 ± 49.1	49.8 ± 7.4	15.1 ± 3.7	0.29 ± 0.03	17.0 ± 8.8	0.08 ± 0.04
K	227.3 ± 19.7	58.0 ± 3.9	19.8 ± 2.2	0.37 ± 0.02	35.3 ± 4.6	0.17 ± 0.02
L	154.9 ± 12.3	57.2 ± 1.9	16.2 ± 2.0	0.32 ± 0.01	24.8 ± 3.0	0.12 ± 0.01

The uncertainties associated with ACI, D^{indoor} and AEDE were calculated, propagating the errors of specific activities.

Table 3. The scheme for the association of the default dose, according to the ACI criteria defined in European commission recommendation^(2,3).

Category (corresponding default dose)	Type 1: materials used in bulk amounts, e.g. concrete, bricks etc.	Type 2: superficial and other materials with restricted use, e.g. tiles, boards, etc.
A ($\leq 1 \text{ mSv y}^{-1}$)	For ACI ≤ 1 category A1	For ACI ≤ 6 category A2
B ($> 1 \text{ mSv y}^{-1}$)	For ACI > 1 category B1	For ACI > 6 category B2

In Table 2 the ACIs varied from 0.48 ± 0.02 to 0.63 ± 0.04 in the clay brick samples and from 0.29 ± 0.03 to 0.37 ± 0.02 in the cement samples. An ACI of < 1 within 3σ standard deviations categorised these building materials as A1 and therefore suitable for use in bulk amounts without restrictions. Applying the default dose criteria recommended by the European Union (EU) for building materials, the investigated clay brick and cement samples met, within 3σ , the exemption for the annual effective dose criterion of $< 1 \text{ mSv y}^{-1}$ (Table 2).

Estimation of the absorbed gamma dose rate and the annual effective dose equivalent

The total external absorbed dose rates (D^{indoor} in nGy h^{-1}) in the indoor air, due to gamma rays emitted by ^{226}Ra , ^{232}Th and ^{40}K , was estimated

according to refs (2, 21), using the absorbed dose conversion coefficients (0.92, 1.10 and 0.08 for ^{226}Ra , ^{232}Th and ^{40}K , respectively and expressed in $\text{nGy h}^{-1}/\text{Bq kg}^{-1}$) determined by the Monte Carlo simulation, with a standard room model of $4 \text{ m} \times 5 \text{ m} \times 2.8 \text{ m}$ with the thicknesses of the walls, floor and ceiling and the density of the structures of 20 cm and density of 2350 kg m^{-3} (concrete). The resulting external absorbed dose rates in the indoor air, due to gamma rays emitted by the ^{226}Ra , ^{232}Th and ^{40}K , was estimated using the formula:

$$D^{\text{indoor}} = 0.08C_{\text{K}} + 0.92C_{\text{Ra}} + 1.10C_{\text{Th}} \quad (5)$$

where C_{Ra} , C_{Th} and C_{K} are the activity concentrations in Bq kg^{-1} for radium (equivalent to uranium under the secular equilibrium conditions), thorium and potassium, respectively. The excess in the external absorbed dose rates in the indoor air was estimated by subtracting the 'background' outdoor average absorbed dose rate of $58 \text{ nGy h}^{-1(1)}$. In Table 2, the absorbed dose rates in the indoor air are reported, which varied from 56.2 ± 4.6 to $92.4 \pm 8.5 \text{ nGy h}^{-1}$ in the clay brick samples and from 17.0 ± 8.8 to $35.3 \pm 4.6 \text{ nGy h}^{-1}$ in the cement samples. The listed values were lower or comparable (within 1σ) to that of the published world average dose rate of $84 \text{ nGy h}^{-1(1)}$.

To assess the annual effective dose equivalent (AEDE) rate, the conversion coefficient from absorbed doses in the air to the effective dose received by an adult must be considered as 0.7 Sv Gy^{-1} , published in the UNCREAR⁽²²⁾, and the

Table 4. The mean activity concentrations ($\pm 1\sigma$) and, when available, the respective minimum and maximum values (in brackets) for the 45 clay brick samples and 15 cement samples measured in this study and compared with reported bibliographic results.

Author of the study	Country	^{40}K (Bq kg $^{-1}$)	^{226}Ra (Bq kg $^{-1}$)	^{232}Th (Bq kg $^{-1}$)	ACI ^a
Clay brick					
This study	Albania	644.1 \pm 64.2 (490.6–820.3)	33.4 \pm 6.4 (20.8–51.9)	42.2 \pm 7.6 (29.2–55.1)	0.54 \pm 0.05
Trevisi <i>et al.</i> ⁽²⁰⁾	EU	598 (12–1169)	47 (2–148)	48 (2–164)	0.59
Xinwei ⁽²³⁾	China	713.9 \pm 8.2	58.6 \pm 4.7	50.4 \pm 3.5	0.70 \pm 0.04
Zhao <i>et al.</i> ⁽²⁴⁾	China	846 \pm 67 (745–961)	46 \pm 4 (39–53)	56 \pm 7(48–66)	0.70 \pm 0.07
Turhan <i>et al.</i> ⁽²⁵⁾	Turkey	775.8 \pm 149.6 (587.3–1092.0)	31.2 \pm 7.2 (24.7–49.0)	37.2 \pm 7.8 (26.6–51.2)	0.54 \pm 0.11
Baykara <i>et al.</i> ⁽²⁶⁾	Turkey	201.4 \pm 4.4	15.7 \pm 1.1	3.8 \pm 0.9	0.16 \pm 0.01
Krstić <i>et al.</i> ⁽²⁷⁾	Serbia	579 \pm 104 (488–700)	34 \pm 4 (29–38)	43 \pm 8 (35–53)	0.51 \pm 0.08
Cement					
This study	Albania	179.7 \pm 48.9 (107.3–250.8)	55.0 \pm 5.8 (40.9–61.4)	17.0 \pm 3.3 (11.5–22.9)	0.33 \pm 0.03
Trevisi <i>et al.</i> ⁽²⁰⁾	EU	216 (4–846)	45 (4–422)	31 (3–266)	0.40
Xinwei ⁽²³⁾	China	173.8 \pm 8.6	68.3 \pm 3.6	51.7 \pm 5.4	0.57 \pm 0.04
Zhao <i>et al.</i> ⁽²⁴⁾	China	310 \pm 76 (219–385)	52 \pm 3 (49–55)	103 \pm 25 (80–133)	0.71 \pm 0.12
Turhan <i>et al.</i> ⁽²⁵⁾	Turkey ^b	316.5 \pm 88.1 (196.1–475.7)	39.9 \pm 18.0 (17.8–81.6)	26.4 \pm 9.8 (7.8–48.8)	0.39 \pm 0.15
Baykara <i>et al.</i> ⁽²⁶⁾	Turkey	2493.1 \pm 78.9	24.7 \pm 1.6	20.7 \pm 1.5	1.02 \pm 0.04

^aACI calculated for the reported mean $\pm \sigma$ values.

^bReported Pozzolana additive of <3 %.

indoor occupancy factor is ~ 0.8 . The AEDE is given by the following equation:

$$\text{AEDE} = D^{\text{indoor}} \times 10^6 \times 8760 \times 0.8 \times 0.7 \quad (6)$$

The corresponding average AEDEs are given in Table 2 and include values varying from 0.28 ± 0.02 to 0.45 ± 0.04 mSv y $^{-1}$ in the clay brick samples and from 0.08 ± 0.04 to 0.17 ± 0.02 mSv y $^{-1}$ in the cement samples. Considering the average world AEDE from the indoor terrestrial gamma radiation of 0.41 mSv y $^{-1}$ (corresponding to an indoor absorbed gamma dose rate of 84 nGy h $^{-1}$), the estimated doses were lower or comparable within 1σ .

According to the INSTAT⁽¹³⁾, Albania in 2010 had an export/import trading rates of ‘construction materials and metals’ of 19.8 and 16.0%, respectively. Albania’s main economic partners are EU member states (Italy, Greece, Switzerland, Spain, Germany) and Kosovo, Turkey, China, Serbia and Montenegro, with roughly 85% of exports and 65% of imports. In Table 4 the available bibliographic results found in the similar studies in the EU and in particular in the aforementioned countries are reported to acquire a broader perspective of the building materials used in Albania. It was emphasised that the reported bibliographic values of activity concentrations of building materials in specific

studies are only indicative and should not be used to characterise the respective country levels.

These data show that Albanian construction materials have the average concentrations of radioactivity, in the clay brick and cement samples, comparable within 1σ to those reported for EU member states, respectively, for ^{40}K , ^{226}Ra and ^{232}Th . In general, other countries of economic interest report values that are 1σ below the limit value of ACI=1, with the exception of one case in which the cements studied, in Turkey, showed ACIs slightly higher, ranging within 1σ around the limit value. On the basis of this study, it is clear that the clay brick and cement industries in Albania produce building materials of low activity concentrations, as characterised according to the European recommendations.

CONCLUSIONS

The radioactivity content of ^{40}K , ^{226}Ra and ^{232}Th were measured in 45 clay brick and 15 cement samples manufactured in Albania and then were compared with the results from other countries. The average activity concentrations of ^{40}K , ^{226}Ra and ^{232}Th were, respectively, 644.1 ± 64.2 , 33.4 ± 6.4 and 42.2 ± 7.6 Bq kg $^{-1}$ in the clay brick samples and 179.7 ± 48.9 , 55.0 ± 5.8 and 17.0 ± 3.3 Bq kg $^{-1}$ in the cement samples. These activity concentrations were found to be comparable within 1σ to the

measurements from EU member states. These results were useful for the assessment of the radiological hazards due to the final use of these materials as building materials. Adopting the 'new' ACI, these samples can be categorised within a 3σ uncertainty as A1 materials, i.e. suitable for use in bulk amounts without any restrictions. The external absorbed dose rates in the indoor air, due to natural radioactivity, in such building materials was estimated to be in the range from 56.2 ± 4.6 to 92.4 ± 8.5 nGy h⁻¹ in the clay brick samples and from 17.0 ± 8.8 to 35.3 ± 4.6 nGy h⁻¹ in the cement samples and was comparable, at close to a 1σ level, to the average world dose rate of 84 nGy h⁻¹. This level corresponds to an AEDE varying from 0.28 ± 0.02 to 0.45 ± 0.04 mSv y⁻¹ in the clay brick samples and from 0.08 ± 0.04 to 0.17 ± 0.02 mSv y⁻¹ in the cement samples. These data are comparable with the average world AEDE from the indoor terrestrial gamma radiation of 0.410 mSv y⁻¹. The clay bricks and cements manufactured in Albania do not pose a significant radiological hazard when used for building construction.

SUPPLEMENTARY DATA

Supplementary data are available at *Radiation Protection Dosimetry*.

ACKNOWLEDGEMENTS

The authors are grateful for useful discussions and valuable comments with L. Carmignani, B. Duka, M. Gambaccini, S. Grazhdani, Y. Huang, A. Marku, W. F. McDonough, T. Mulaj, G. Oggiano, R. L. Rudnick, V. Tabaku, G. Xhixha and A. Zanon.

FUNDING

This work was partially supported by Istituto Nazionale di Fisica Nucleare (INFN), Italy and by Fondazione Cassa di Risparmio di Padova e Rovigo in collaboration with Albanian Society of Radioecology.

REFERENCES

1. UNSCEAR (United Nations Scientific Committee on the Effects of Atomic Radiation). *Exposures from Natural Radiation Sources*. United Nations (2008).
2. EC (European Commission). *Radiological protection principles concerning the natural radioactivity of building materials*, European Commission. Radiation Protection 112. Directorate General, Environment Nuclear Safety and Civil Protection (1999).
3. EC (European Commission). *Draft presented under Article 31 Euratom Treaty for the opinion of the European Economic and Social Committee: laying down basic safety standards for protection against the dangers arising from exposure to ionising radiation*, 2011/0254 (NLE). European Commission (2011) <http://eur-lex.europa.eu/LexUriServ/LexUriServ.do?uri=CELEX:52011PC0593:EN:NOT>.
4. Markkanen, M. *Challenges in harmonising controls on the radioactivity of building materials within the European Union*. *Sci. Total Environ.* **272**, 3–7 (2001).
5. Hewamanna, R., Sumithrarachchi, C. S., Mahawatte, P., Nanayakkara, H. L. C. and Ratnayake, H. C. *Natural radioactivity and gamma dose from Sri Lankan clay bricks used in building construction*. *Appl. Radiat. Isot.* **54**, 365–369 (2001).
6. El-Taher, A., Makhluif, S., Nossair, A. and Abdel Halim, A. S. *Assessment of natural radioactivity levels and radiation hazards due to cement industry*. *Appl. Radiat. Isot.* **68**, 169–174 (2010).
7. Beretka, J. and Mathew, P. J. *Natural radioactivity of Australian building materials, industrial wastes and byproducts*. *Health Phys.* **48**, 87–95 (1985).
8. Kovler, K. *Radiological constraints of using building materials and industrial by-products in construction*. *Construct. Build. Mater.* **23**, 246–253 (2009).
9. Somlai, J., Jobbágy, V., Kovács, J., Tarján, S. and Kovács, T. *Radiological aspects of the usability of red mud as building material additive*. *J. Hazard. Mater.* **150**, 541–545 (2008).
10. IAEA (International Atomic Energy Agency). *International Basic Safety Standards for protection against ionizing radiation and for the safety radiation sources*. Safety Series No. 115. IAEA (1996).
11. Xhixha, G. et al. *The worldwide NORM production and a fully automated gamma-ray spectrometer for their characterization*. *J. Radioanal. Nucl. Chem* (2012). doi: 10.1007/s10967-012-1791-1.
12. Dodona, A. *Estimation of the natural radioactivity of the Albanian clays*. *J. Balkan Geophys. Soc.* **3**, 7–12 (2000).
13. INSTAT (Instituti i Statistikës, Republika e Shqipërisë). *Tregtia e jashtme (Foreign trade) 2006–2010* (2011). http://www.instat.gov.al/graphics/doc/downloads/tregti_jashtme/Tregtia%20e%20jashtme%202010.pdf.
14. IAEA (International Atomic Energy Agency). *Preparation and certification of IAEA gamma spectrometry reference materials, RGU-1, RGTh-1 and RGK1*. Report-IAEA/RL/148. International Atomic Energy Agency (1987).
15. Nir-El, Y. *Application of reference materials in the accurate calibration of the detection efficiency of a low-level gamma-ray spectrometry assembly for environmental samples*. *J. Radioanal. Nucl. Chem.* **227**, 67–74 (1998).
16. Anjos, R. M. et al. *Natural radionuclide distribution in Brazilian commercial granites*. *Radiat. Meas.* **39**, 245–253 (2005).
17. Bolivar, J. P., Garcia-Leon, M. and Garcia-Tenorio, R. *On self-attenuation corrections in gamma-ray spectrometry*. *Appl. Radiat. Isot.* **48**, 1125–1126 (1997).
18. Cutshall, N. H., Larsen, I. L. and Olsen, C. R. *Direct analysis of Pb-210 in sediment samples: self-absorption corrections*. *Nucl. Instrum. Methods* **206**, 309–312 (1983).

RADIOACTIVITY IN ALBANIAN BUILDING MATERIALS

19. JCGM (Joint Committee for Guides in Metrology). *Evaluation of measurement data—Supplement 1 to the ‘Guide to the expression of uncertainty in measurement’—propagation of distributions using a Monte Carlo method*, first edition. JCGM **101**, 90 (2008).
20. Trevisi, R., Risica, S., D’Alessandro, M., Paradiso, D. and Nuccetelli, C. *Natural radioactivity in building materials in the European Union: a database and an estimate of radiological significance*. J. Environ. Radioact. **105**, 11–20 (2012).
21. Markkanen, M. *Radiation dose assessments for materials with elevated natural radioactivity*. Radiation and Nuclear Safety Authority—STUK. Report STUK-B-STO 32. Finnish Centre for Radiation and Nuclear Safety (1995).
22. UNSCEAR (United Nations Scientific Committee on the Effects of Atomic Radiation). *Exposures from natural radiation sources*. United Nations (2000).
23. Xinwei, L. *Natural radioactivity in some building materials of Xi’an, China*. Radiat. Meas. **40**, 94–97 (2005).
24. Zhao, C., Lu, X., Li, N. and Yang, G. *Natural radioactivity measurements of building materials in Baotou, China*. Radiat. Prot. Dosim. (2012). doi: 10.1093/rpd/ncs054.
25. Turhan, Ş., Baykan, U. N. and Şen, K. *Measurement of the natural radioactivity in building materials used in Ankara and assessment of external doses*. J. Radiol. Prot. **28**, 83–91 (2008).
26. Baykara, O., Karatepe, Ş. and Doğru, M. *Assessments of natural radioactivity and radiological hazards in construction materials used in Elazığ, Turkey*. Radiat. Meas. **46**, 153–158 (2011).
27. Krstić, D., Nikizić, D., Stefanović, N. and Vučić, D. *Radioactivity of some domestic and imported building materials from South Eastern Europe*. Radiat. Meas. **42**, 1731–1736 (2007).

The worldwide NORM production and a fully automated gamma-ray spectrometer for their characterization

G. Xhixha · G. P. Bezzon · C. Brogini · G. P. Buso · A. Cacioli ·
I. Callegari · S. De Bianchi · G. Fiorentini · E. Guastaldi · M. Kaçeli Xhixha ·
F. Mantovani · G. Massa · R. Menegazzo · L. Mou · A. Pasquini ·
C. Rossi Alvarez · M. Shyti

Received: 1 April 2012 / Published online: 29 April 2012
© Akadémiai Kiadó, Budapest, Hungary 2012

Abstract Materials containing radionuclides of natural origin and being subject to regulation because of their radioactivity are known as Naturally Occurring Radioactive Material (NORM). By following International Atomic Energy Agency, we include in NORM those materials with an activity concentration, which is modified by human made processes. We present a brief review of the main categories of non-nuclear industries together with the

levels of activity concentration in feed raw materials, products and waste, including mechanisms of radioisotope enrichments. The global management of NORM shows a high level of complexity, mainly due to different degrees of radioactivity enhancement and the huge amount of worldwide waste production. The future tendency of guidelines concerning environmental protection will require both a systematic monitoring based on the ever-increasing sampling and high performance of gamma-ray spectroscopy. On the ground of these requirements a new low-background fully automated high-resolution gamma-ray spectrometer MCA_Rad has been developed. The design of lead and copper shielding allowed to reach a background reduction of two order of magnitude with respect to laboratory radioactivity. A severe lowering of manpower cost is obtained through a fully automation system, which enables up to 24 samples to be measured without any human attendance. Two coupled HPGe detectors increase the detection efficiency, performing accurate measurements on small sample volume (180 cm³) with a reduction of sample transport cost of material. Details of the instrument calibration method are presented. MCA_Rad system can measure in less than one hour a typical NORM sample enriched in U and Th with some hundreds of Bq kg⁻¹, with an overall uncertainty less than 5 %. Quality control of this method has been tested. Measurements of three certified reference materials RGK-1, RGU-2 and RGTh-1 containing concentrations of potassium, uranium and thorium comparable to NORM have been performed. As a result, this test achieved an overall relative discrepancy of 5 % among central values within the reported uncertainty.

G. Xhixha (✉) · S. De Bianchi · G. Fiorentini · F. Mantovani ·
M. Shyti
Dipartimento di Fisica, Università di Ferrara, Polo Scientifico
e Tecnologico Via Saragat, 1, 44100 Ferrara, Italy
e-mail: xhixha@fe.infn.it

G. Xhixha · G. Fiorentini · F. Mantovani · M. Shyti
Ferrara Section, Istituto Nazionale di Fisica Nucleare (INFN),
Via Saragat, 1, 44100 Ferrara, Italy

G. Xhixha
Faculty of Forestry Science, Agricultural University of Tirana,
Kodër Kamëz, 1029 Tiranë, Albania

G. P. Bezzon · G. P. Buso · G. Fiorentini
Legnaro National Laboratory, Istituto Nazionale di Fisica
Nucleare (INFN), Via dell'Università, 2, 35020 Legnaro,
Padua, Italy

C. Brogini · A. Cacioli · R. Menegazzo · C. R. Alvarez
Padova Section, Istituto Nazionale di Fisica Nucleare (INFN),
Via Marzolo 8, 35131 Padua, Italy

A. Cacioli · I. Callegari · E. Guastaldi · G. Massa ·
L. Mou · A. Pasquini
Center for GeoTechnologies, University of Siena, Via Vetri
Vecchi, 34, 52027 San Giovanni Valdarno, Arezzo, Italy

M. Kaçeli Xhixha
Botanical, Ecological and Geological Sciences Department,
University of Sassari, Piazza Università 21, 07100 Sassari, Italy

Keywords HPGe · Gamma-ray spectrometry · Industrial waste/by-product · NORM · Non-nuclear industry · Reference materials

Introduction

Materials containing radionuclides of natural origin and being subject to regulation because of their radioactivity are known as NORM (Naturally Occurring Radioactive Material). By following IAEA, we include in NORM those materials with an activity concentration altered by human made processes¹ [37, 40]. In the last decades the large production of NORM and the potential long-term radiological hazards, due to long-lived radionuclides, represented an increasing level of concern. The development of instruments devoted to the measurements of NORM concentrations is a crucial task for the evaluation of the radiological impact on both workers and public members.

NORM are found as products, by-products and/or wastes of industrial activities, such as production of non-nuclear fuels (e.g. coal, oil and gas), mining and milling of metalliferous and nonmetalliferous ores (e.g. aluminum, iron, copper, gold and mineral sand), industrial minerals (e.g. phosphate and clays), radioisotope extraction and processing, as well as water treatments [38].

The most important sources of natural radioactivity are due to the presence of ²³⁸U, ²³²Th and ⁴⁰K in the Earth. Generally ²³⁵U and ⁸⁷Rb and other trace elements are negligible. The decay chain of ²³⁸U (²³²Th) includes 8 (6) alpha decays and 6 (4) beta decays respectively, which are often associated with gamma transitions. The detection of these radioactivity sources can be performed through a wide set of methods, such as gamma-ray spectroscopy, alpha spectroscopy, neutron activation analysis (NAA), inductively-couple plasma mass-spectroscopy (ICP-MS), inductively coupled plasma atomic emission spectroscopy (ICP-AES), X-ray fluorescence spectroscopy (XRF) and liquid scintillation counting (LSC) [39]. The choice of the methodology for determining radioactive content of NORM depends on many factors, especially the economic character and prompt measurement of the individual samples.

Usually, in NORM ²³⁸U and ²³²Th decay chains are not in secular equilibrium. It means that in ²³⁸U decay chain, some long-lived radionuclides (²³⁸U, ²²⁶Ra, ²¹⁰Pb) represent the head of decay chain segments, which can reach the secular equilibrium in less than one year: the gamma-ray spectrometry, therefore, is the suitable technique for measuring the abundance of these radionuclides and for checking the secular equilibrium among the respective chain segments. NORM can be enriched in ²³⁰Th and ²¹⁰Po, which can be out of chain segments: the activities of ²³⁰Th can be determined by gamma-spectrometry directly, while the suitable technique for quantifying ²¹⁰Po

concentration is alpha spectrometry. In ²³²Th decay chain the two chain segments, having on head ²²⁸Ra and ²²⁸Th, reach the secular equilibrium in about one month. By measuring the gamma transitions in each chain segment, one can determine ²²⁸Ra and ²²⁸Th abundances; while XRF, NAA, ICP-AES, ICP-MS are suitable techniques for measuring ²³²Th content.

By using high-resolution gamma-ray spectrometry, all radioisotopes of ²³⁸U and ²³²Th decay chains, with the exception of ²³²Th and ²¹⁰Po, can be investigated simultaneously. The radioactivity characterization of NORM may require a massive amount of measures of samples. For this purpose we designed and built up a low-background high-resolution gamma-ray spectrometry system, which allows an autonomous investigation of the radioactivity content on a large amount of samples, without any human attendance.

An empirical method for the characterization of the absolute efficiency of this instrument is presented in detail. Along with the instrument calibration, a quality test of this method was carried out. We tested the performances of the instrument by using three reference materials RGK-1, RGU-1 and RGTh-1 certified by IAEA and containing radioactive concentration comparable to NORM values.

Industrial processes producing NORM: an overview

Non-nuclear fuels extraction and processing

Oil and gas industry

Most hydrocarbons are trapped within porous reservoirs (known as oil/tar sand and oil shale deposits) by impermeable rocks above: the rock formations holding the oil also contain U and Th at the order of some ppm, corresponding to a total specific activity of some tens² of Bq kg⁻¹. Oil and gas reservoirs contain a natural water layer (formation water) that lies under the hydrocarbons: U and Th do not go into solution, but the formation water tends to reach a specific activity of the same order of the rock matrix [50] due to dissolution of ²²⁶Ra and ²²⁸Ra radium as radium chloride [33]. Additional heated water is often injected into the reservoirs to achieve maximum oil recovery. This process disturbs the cation/anion ratio and alters the solubility of various sulfate salts, particularly BaSO₄ and RaSO₄: radium co-precipitates with barium as sulfates forming scale within the oil pipes [41]. The solids,

¹ Sometimes these materials are known in the literature as TENORM (technologically enhanced naturally occurring radioactive material).

² The U and Th abundances vary for different rock types: e.g. in considering shale, the range of U and Th abundances reported by [17] are 2.4–3.4 and 8.5–14.3 ppm respectively. We remind that the specific activity of 1 ppm U (Th) corresponds to 12.35 (4.06) Bq/kg.

Table 1 Range of specific activity concentrations of ^{226}Ra and ^{228}Ra in scale and sludge, as reported by different authors for various geographic regions

Authors of the study	Country	^{226}Ra (10^4 Bq kg^{-1})		^{228}Ra (10^4 Bq kg^{-1})	
		Scale	Sludge	Scale	Sludge
Godoy and Cruz [31]	Brazil	1.91–32.3	0.036–36.7	0.421–23.5	0.025–34.3
Gazineu et al. [29]	Brazil	12.1–95.5	0.24–350	13.1–79.2	205
Gazineu and Hazin [28]	Brazil	7.79–211	0.81–41.3	10.2–155	0.94–11.8
Shawky et al. [70]	Egypt	0.754–14.3	0.0018	3.55–66.1	1.33
Abo-Elmaged et al. [1]	Egypt	49.3–51.9	0.527–0.886	3.20–5	0.1–0.19
Bakr [9]	Egypt	0.0016–0.0315	0.00055–0.179	0.00007–0.0177	0.00007–0.0885
Omar et al. [55]	Malaysia	0.055–43.4	0.0006–0.056	0.09–47.9	0.0004–0.052
Lysebo et al. [46]	Norway	0.03–3.23	0.03–3.35	0.01–0.47	0.01–0.46
Al-Saleh and Al-Harshan [6]	Saudi Arabia	0.00008–0.00015	0.00068–0.00594	0.000014–0.00031	0.00063–0.00476
Al-Masri and Suman [5]	Syria	14.7–105	47–100	4.3–18.1	35.9–66
Jonkers et al. [43]	USA	0.01–1500	0.005–80	0.005–280	0.05–50
Zielinski et al. [85]	USA	1.88–489	2.04–6.38	0.118–19	0.241–0.574

Remind that the exemption level recommended by [36] is 10^4 Bq kg^{-1} for both ^{226}Ra and ^{228}Ra

which are dissolved in crude oil and in the produced water, precipitate forming the sludge, which is a mixture of oil, carbonates and silicates sediments, as well as corrosion products that accumulate inside piping and in the bottom of storage tanks. The contribution to the radioactivity content in the sludge comes mainly from the precipitates of hard insoluble radium sulfate and possibly from radioactive silts and clays [33]. The specific activity of scales and sludges can vary enormously and generally it is of several orders of magnitude more than formation water. As reported in Table 1, the high variability, often among the samples collected in the same area, shows that a frequent and dense sampling of these NORM may be required.

Coal-fired power plant

Coal is a combustible sedimentary rock formed through the anaerobic process of the decomposed dead plants accumulated at the bottom of basins of some marsh land, lake or sea: the coalification process yields a product rich in carbon and hydrogen [65]. The organic matter plays an important role in the uranium concentrations at syngenetic, epigenetic and diagenetic stages of the sedimentary cycle [54]. The complexation and reduction of uranium are considered the main geochemical processes of the fixation of uranium on organic matter from very dilute solutions. The complexation of uranium involves the uranyl cation (UO_2^{2+}) producing a UO_2 complex through a dehydrogenation process of organic matter. During the reduction of the soluble UO_2^{2+} , the insoluble UO_2 is produced precipitating as uraninite [45]. The efficiency of these processes depends on the chemistry of the organic matter and on the temperature of reaction, producing U concentrations ranged

over a couple orders of magnitude: the typical range of radionuclide activity concentrations of ^{238}U , ^{232}Th and ^{40}K in coal can be 10–600, 10–200 and 30–100 Bq kg^{-1} respectively [10]. The geological processes over the time increase the grade of coal transforming the organic material from peat to graphite. In low-grade coal the secular equilibrium between ^{238}U and ^{232}Th and their decay products is not expected while in the high-grade coal it may exist [74]. The volatilization–condensation process of particles during coal combustion breaks the secular equilibrium and increases the radionuclide concentrations with decreasing of particle size: the maximum enrichment has been measured in particles with diameters of about 1 μm . ^{210}Pb and ^{210}Po exhibit the greatest enrichment, as much as a factor of 5, while maximum enrichment for uranium isotopes is about a factor of 2, and for ^{226}Ra a factor of around 1.5. In some samples of fly ash the ^{210}Pb and ^{226}Ra activity exceeds thousands of Bq kg^{-1} [27].

According to the World Coal Institute [84] 40 % of the world's electricity in 2003 is generated by coal: in the same year the world coal consumption reached $48.4 \times 10^{11} \text{ kg}$ [80]. After the combustion of the bituminous coal containing an average ash of 12 %, coal by-products are composed by some 70 % of fly ash and by some 30 % of the bottom ash and boiler slag. A large fraction (more than 95 %) of these small particles can be removed from gas stream, by usually applying electrostatic precipitator and fabric filters: in 2003 the estimated worldwide fly ash production was $3.9 \times 10^{11} \text{ kg}$ [53]. In 2003 the US and EU fly ash production was about $0.6 \times 10^{11} \text{ kg}$ and $0.4 \times 10^{11} \text{ kg}$ respectively. In US and UE about 39 and 48 % of this amount was recycled respectively [2, 25]. According to [80] the world coal consumption in 2035 is

projected to reach 93.8×10^{11} kg, corresponding to an estimated fly ash production of 7.5×10^{11} kg. This large amount of NORM is required to be measured and monitored with accuracy, by developing fast and ad hoc methods: the MCA_Rad system presented in “MCA_Rad system” section has been designed as a response to this increasing demand.

Metal mineral extraction and processing

Bauxite extraction and alumina production

In metal mining and waste processing, the radioactive content varies from 10^{-2} kBq kg⁻¹, for the large volume industry, to 10^2 kBq kg⁻¹ for rare earth metals [38]. In massive metal extraction, the amount of NORM produced by bauxite processing is relevant.

Bauxites generally contain concentrations of Th and U greater than the Earth’s crustal average: in a multi-methodological study published by Adams and Richardson [3] based on 29 samples of bauxites from different locations, the reported specific activities of U and Th are in the range 33–330 and 20–532 Bq kg⁻¹ respectively. These values can be compared with the typical concentration in bauxite: 400–600 Bq kg⁻¹ for U and 300–400 Bq kg⁻¹ for Th [79].

The parent rocks affect the U and Th abundances in the bauxites: in particular the bauxites derived from acid igneous rocks show a concentration higher than those extracted from basic igneous rocks, whereas the bauxites mined from deposits of shales and carbonates rocks are characterized by intermediate concentrations. The process of lateritization during bauxite formation contributes to increase the ratio Th/U, which is generally more than 4 [3].

Bayer process is used for refining bauxite to smelting grade alumina, the aluminum precursor: it involves the digestion of crushed bauxite in a concentrated sodium hydroxide solution at temperatures up to 270 °C. Under these conditions, the majority of the species containing aluminum is dissolved in solution in the ore, while the insoluble residues are filtered making a solid waste called “red mud”. The alumina is obtained by the hydroxide solution after the processes of precipitation and calcination [34]. Finally, by using the Hall–Heroult electrolytic process, alumina is reduced to aluminum metal.

The fact that thorium and radium in a hydroxide medium are practically insoluble [73] could disturb especially the secular equilibrium of the uranium chain, as it has been observed in some measurements [62]. However, some “results indicate that the chemical processing of the bauxite ore has not significant consequences in the secular equilibrium of either the uranium or thorium series” [18]. In the process of extracting alumina from bauxite, over

Table 2 Activity concentration in red mud reported in the literature (a) the range indicated correspond to the maximum and minimum value measured for different samples and in (b) the uncertainties of measurement results. The activities quoted are assumed equal to ²²⁸Ac in (1), equal to ²²⁸Th in (2) and equal to ²³⁸U in (3)

Authors of the study	Country	Activities (Bq kg ⁻¹)	
		²²⁶ Ra	²³² Th
Papathodorou et al. [56] ^(a)	Greece	13–185	15–412
Philipsborn and Kuhnast [60] ^{(b),(1)}	Germany	122 ± 18	183 ± 33
Pinnock [61] ^(a)	Jamaica	370–1047	328–350
Somlai et al. [73] ^(a)	Hungary	225–568	219–392
Akinci and Artir [4] ^(b)	Turkey	210 ± 6	539 ± 18
Jobbágy et al. [42] ^(a)	Hungary	102–700	87–545
Cooper et al. [18] ^{(b),(2)}	Australia	310 ± 20	1350 ± 40
Turhan et al. [78] ^(a)	Turkey	128–285	342–357
Pontikes et al. [62] ^{(b),(2)}	Greece	379 ± 43	472 ± 23
Beretka and Mathew [12]	Australia	326	1129
Georgescu et al. [30]	Romania	212	248
Döring et al. [23] ^(b)	Germany	190 ± 30	380 ± 50
Ruyters et al. [66] ⁽³⁾	Belgium	550	640

70 % of the thorium and radium are concentrated in the red mud [3].

In 2009 the worldwide production of bauxite and alumina was 199×10^9 and 123×10^9 kg respectively. Considering that the worldwide ratio bauxite/alumina, averaged in the period 1968–2009, is 2.7 ± 0.1 , we expect that 1.7 ± 0.1 kg of red mud is generated per kg of alumina [83]. By assuming that at least 70 % of the radioisotopes in bauxite accumulate in the red mud, the increasing factor of radioactivity content in the red mud varies in a range of 1.1–1.6. Using these estimated enrichments for bauxite we encompass a large portion of the radium and thorium activities of the red mud reported in literature (Table 2).

Based on recent statistics, more than 70×10^9 kg of red mud is discharged annually in the world: it constitutes the most important disposal problem of the aluminum industry. The mud is highly basic (pH > 10) and its storage on huge area can cause environmental pollution, soil basification, paludification, surface water and groundwater pollution as well as resource pollution. The safe treatment of this NORM is an increasing social problem. Moreover, a considerable attention has been given to additional uses of bauxite wastes: they include metallurgical extractions, building materials productions and the development of new ceramics and catalytic materials. Gamma-ray spectrometers are able to process thousands of measurements in order to perform environmental monitoring and to control the

recycled by-products. The MCA_Rad system described in “MCA_Rad system” section could be extremely helpful for processing these measurements by significantly diminishing manpower costs.

Mineral sand and downstream productions

The extraction of mineral sand ore is important for the production of heavy minerals (with densities heavier than 2.8 g cm^{-3}) like titanium, tin and zirconium bearing minerals and rare earth elements³ (REEs) The deposits of hard minerals, which do not undergo erosion and transport processes, mainly occur when they have been concentrated by marine, alluvial and/or wind processes. These placer deposits can be found also in vein deposits, mostly disseminated in alkaline intrusions in hard rocks. The radioactivity concentration of mineral sand can be of the order of a few hundreds Bq kg^{-1} , depending on the placer geology. In heavy minerals we can often find high content of radioactivity, sometimes of the order of hundreds kBq kg^{-1} .

The process involved in heavy mineral extraction includes two main phases of separation. The first phase separates the heavy mineral concentration, by using either dry operation or dredging of the slurried ore: this produces high amount of residues with a radionuclide concentration of the same order of mineral sand [59]. During the second phase, the heavy mineral concentration is further separated mainly by combining dry magnetic and electrostatic processes. This allows the concentration of various minerals, such as titanium bearing minerals (ilmenite, leucoxene, rutile), zircon bearing minerals (zircon, baddeleyite) and REEs bearing minerals (monazite, xenotime). The products of this second phase generally show a high content of radioisotopes.

Titanium bearing minerals are used mainly to produce TiO_2 pigment. The radioactivity concentration in these minerals varies in rutile ($400\text{--}2900 \text{ Bq kg}^{-1}$ Th and $250\text{--}500 \text{ Bq kg}^{-1}$ U) and ilmenite ($400\text{--}4100 \text{ Bq kg}^{-1}$ Th and $250\text{--}750 \text{ Bq kg}^{-1}$ U) [38, 48, 76]. The higher production efficiency is obtained by rutile: it is directly processed through the chloride route producing TiO_2 pigment/waste with a ratio of 5/1 [81]. Since the radioisotopes follow the liquid waste stream, the radioactivity concentration in the waste is very high due to the severe mass reduction.

Ilmenite requires a pre-processing in order to produce synthetic rutile: the product/waste ratio is 10/7. The synthetic rutile is further processed through the chloride route in order to produce TiO_2 pigment with a product/waste ratio of 5/6, showing a light enhancement of radioactivity concentration in waste of ilmenite processing [38].

In TiO_2 pigment production the most relevant NORM are made by the chloride treatment of rutile. The worldwide production of TiO_2 in 2010 was about $5.7 \times 10^9 \text{ kg}$ when the mineral extraction ratio is 1/10 for rutile/ilmenite [38, 82]: about 2 % of the total waste which has been generated can show a strong enhancement in radioactivity concentration.

The most common zirconium bearing minerals are zircon and baddeleyite: in 2010 the world extraction of these minerals was about $1.2 \times 10^9 \text{ kg}$ [82]. Mineral sands containing zircon are commonly used in ceramic and refractory industries. The zircon crystal lattice host uranium and thorium: their activities in zircon bearing minerals are in the range of $1\text{--}5 \text{ kBq kg}^{-1}$ for U and of $0.5\text{--}1 \text{ kBq kg}^{-1}$ for Th respectively [64].

The manufacture of zirconia is mainly performed by fusion of feedstock with coke near to zirconium molten temperatures. It causes the dissociation of mineral in ZrO_2 and SiO_2 : during the fusion U and Th end up almost at the same concentration in zircon product, while ^{226}Ra tends to end up in silica, causing the disequilibrium of U decay chain. The subsequent caustic fusion process at $600 \text{ }^\circ\text{C}$ increases the purity of zirconia. During the chemical dissolution, zircon crystal structure is destroyed, yielding nearly 100 % of uranium recovery in the form of sodium uranate [14]. The performances of MCA_Rad system completely fit the need of measuring radioactivity content in this kind of NORM.

The main minerals used as sources of REEs can be extracted by placer deposits (monazite and xenotime) and by hard rocks (bastnaesite, coperite and pyrochlore). Monazite minerals are characterized by high activity concentration of U ($25\text{--}75 \text{ kBq kg}^{-1}$) and Th ($41\text{--}575 \text{ kBq kg}^{-1}$). The chemical attack of the mineral based on NaOH separates sodium phosphate from a mixture called “cake I”, which is rich in heavy minerals. Cake I is further filtered, given that it yields a concentration of rare earth chlorides and a mixture called “cake II” containing most of thorium and uranium originally present in monazite feedstock [58]. The decay chain of U and Th are not in secular equilibrium in cake II: thorium precipitates while radium remains in solution. The latter can reach very high activities (7 and 10 MBq kg^{-1} for ^{226}Ra and ^{228}Ra respectively) [59]. In 2010, the extraction of monazite has been $1.3 \times 10^8 \text{ kg}$ [82] and its processing has made 10 % of cake II waste [57]. This large amount of highly enhanced radioactivity NORM requires scrupulous monitoring and control.

³ REEs contain 16 chemical elements, including those with atomic numbers 57 (lanthanum) through 71 (lutetium), as well as yttrium (atomic number 39), which has similar chemical properties.

Industrial minerals extraction and processing

Phosphate fertilizer industry

The main phosphate-rock (phosphorite) deposits are both of igneous and sedimentary origin and they are part of the apatite group. They are commonly encountered as fluorapatite and francolite respectively. A specific characteristic of phosphate rocks consists in a low ratio Th/U, in general <0.5 , which is mainly due to relative high concentrations of uranium commonly between 370 and 2470 Bq kg⁻¹ and sometimes higher than 12.35 kBq kg⁻¹. Uranium and thorium decay chains are generally found to be in secular equilibrium [49].

Phosphorite is mainly processed through the so-called “wet process”, which includes chemical treatments, mostly by using sulfuric acid: the products are phosphoric acid (PA) and an insoluble calcium sulfate salt called phosphogypsum (PG), with a ratio PG/PA = 5 [75]. PA and PG are usually separated by filtration and reactor off-gas and vapors. These processes concentrate the trace elements in PA or PG in various amounts causing secular disequilibrium in U and Th decay chains. In PG is found approximately 80–90 % of the ²²⁶Ra along with a high content of ²¹⁰Pb and ²¹⁰Po [11, 15], as a consequence of the similar chemistry [11, 32]. About 80–85 % of the uranium [11, 63] and about 70 % of thorium [75] concentrate in PA. As a consequence of these processes, we expect a relevant enhancement of U concentration in PA and an abundance of Ra in PG comparable with that in phosphate-ore (Table 3). The high production of phosphogypsum requires constant controls in order to make a secure stockage and reutilization of such material. These controls must be extended to PA and phosphate fertilizers: the MCA_Rad system described in the next section has been designed to deal with automatic gamma-ray measurements on large amounts of PA and PG samples.

MCA_Rad system

An accurate radiological characterization of NORM requires careful investigation on a case-by-case basis. Indeed the NORM issue shows high levels of complexity mainly due to the huge amount of worldwide waste production perturbed by the different geochemical composition of raw materials and the effective concentration of a wide range of industrial processes. Most of current studies show that determining the content of ²²⁶Ra, ²²⁸Ra and ⁴⁰K radioisotopes in NORM is mandatory for radiation protection. High-resolution gamma-ray spectrometry is a frequently used non-destructive technique, which provides an accurate identification and quantitative determination of such radioisotopes.

A strategic approach to the NORM issue consists in constructing systematic monitoring programs. However, this approach is often limited by funding and manpower capacities of a laboratory. Indeed, when a laboratory deals with random measurements, the main costs are determined by the instrument investment program; instead, for a routine monitoring program the substantial costs are due to the manpower involved. The MCA_Rad system introduces an innovative configuration of a laboratory high-resolution gamma-ray spectrometer featured with a complete automation measurement process. Two HPGe detectors allow to achieve both good statistical accuracy in a short time and ad hoc approach to low-background shielding construction design. This self-constructed instrument drastically minimizes measurement and manpower costs.

Set-up design and automation

The core of the MCA_Rad system is made of two 60 % relative efficiency coaxial p-type HPGe gamma-ray detectors, which possess an energy resolution of about 1.9 keV at 1332.5 keV (⁶⁰Co). Both detectors are controlled by individual integrated gamma spectrometers for

Table 3 Studies on activities of phosphate rock (PR) and phosphogypsum (PG) in different countries

Authors of the study	Country	²³⁸ U (Bq kg ⁻¹)		²²⁶ Ra (Bq kg ⁻¹)	
		PR	PG	PR	PG
Mazilli et al. [47]	Brazil			130–1445	93–729
Silva et al. [71]	Brazil	434–1128	66–140	407–1121	228–702
Saueia et al. [69]	Brazil	14–638	<2–61	53–723	24–700
Santos et al. [67]	Brazil	102–1642	32–69	239–862	307–1251
Saueia et al. [68]	Brazil	158–1868	40–58	139–1518	122–940
EM Afifi et al. [26]	Egypt	916	140	890	459
Azouazi et al. [8]	Morocco	2100–2450	–	1850–2320	1420
Carvalho [15]	Portugal	1003	26–156	1406	950–1043
Hull and Burnett [35]	USA (Central Florida)	848–1980	45–368	882–1980	505–1353
	USA (Northern Florida)	242–982	23–452	230–883	270–598

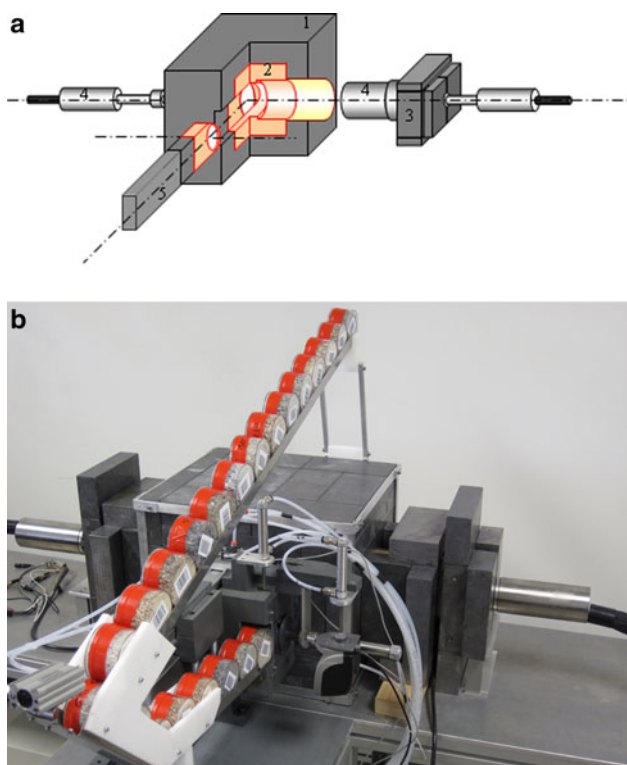


Fig. 1 **a** Schematic design of the MCA_Rad system. (1) The main lead shielding construction (20 cm × 25 cm × 20 cm). (2) The core copper shielding (10 cm × 15 cm × 10 cm). (3) Rear lead shielding construction. (4) HPGe semiconductor detectors. (5) The mechanical sample changer. **b** View of the MCA_Rad system

the digital signal processing. The new cooling technology, which employs mechanical coolers, allows to simplify the management of the system. The detectors are accurately shielded and positioned facing each other 5 cm apart (Fig. 1a).

The background spectrum of a gamma-ray spectrometer is mainly due to the combination of cosmic radiation, environmental gamma radiation and the radioactivity produced by radio-impurities both in the shielding materials and in the detector. In order to effectively reduce the environmental gamma radiation, an adequate shielding construction is needed.

In the MCA_Rad a 10 cm thick lead house shields the detector assembly, leaving an inner volume around the detectors of about 10 dm³ (Fig. 1a, b). The lead used as shielding material adds some extra background due to the presence of ²¹⁰Pb, produced by ²³⁸U decay chain. This isotope, which has an half life of 22.3 years, is revealed by a gamma energy of 46.5 keV and a *bremsstrahlung continuum* from beta decay of its daughter ²¹⁰Bi extending from low energy up to 1162 keV. Furthermore, when a gamma-ray strikes the lead surface, characteristic lead X-rays may escape and hit the detector [72].

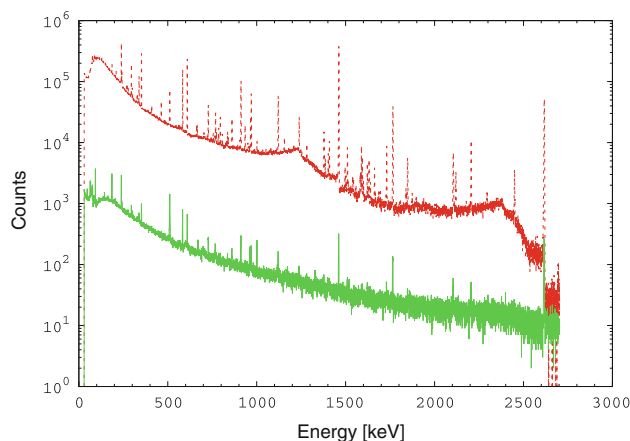


Fig. 2 The MCA_Rad system background spectra (acquisition live time 100 h) with (continuous line) and without (dashed line) shielding. Spectra are obtained by summing the single detector background after rebinning with 0.33 keV/channel

The inner volume is occupied by 10 cm thick oxygen free copper house, which allows to host the sample under investigation. In order to reduce the X-rays coming from the sample, the end-cup windows of the detectors is further shielded with a tungsten alloy sheet of 0.6 mm. A 10 mm thick bronze cylinders and walls of about 10 cm of lead are also shielding the rear part of the system (Fig. 1a, b). The final intrinsic background is reduced by two order of magnitude compared to other unshielded detectors (see Fig. 2).

As a good practice of gamma-ray spectrometry analysis, information concerning background spectra is required both to detect any potential residual contaminations and for background corrections. A background measurement with acquisition time of several days is performed regularly. The final sensitivity of the measurements can be evaluated by using the detection limit (L_D) described in [19], assuming the Gaussian probability distribution of the number of counts in the background (B) and rejecting the data not included in a range of 1.645σ (95 % confidence level):

$$L_D = 2.71 + 4.65\sqrt{B} \approx 4.65\sqrt{B} \tag{1}$$

where the approximation is admitted for high number of counts. The minimum detectable activity (MDA) for the background is calculated using the L_D , according to the formula:

$$MDA = \frac{L_D}{\epsilon I_\gamma t} \tag{2}$$

where ϵ is the absolute efficiency (calculated as described below), I_γ is the gamma line intensity and t is the acquisition live time. In Table 4 we report the typical one hour acquisition live time background counts and the sensitivity of the measurement expressed by L_D and MDA for the

Table 4 MCA_Rad system characterization of typical one hour (live time) background (B in counts) for the most important energies and the corresponding detection limit L_D and minimum detectable activity (MDA) [19] for 95 % confidence interval (CI)

Parent isotope	Daughter isotope	Energy (keV)	B (counts)	L_D (counts)	MDA (Bq)
^{238}U	$^{234\text{m}}\text{Pa}$	1001.0	8 ± 1	21	22.16
	^{214}Pb	351.9	31 ± 2	49	0.50
	^{214}Bi	609.3	44 ± 1	32	0.49
^{232}Th	^{228}Ac	911.2	27 ± 1	27	0.94
	^{212}Pb	238.6	100 ± 2	62	0.46
	^{212}Bi	727.3	10 ± 1	31	3.00
	^{208}Tl	583.2	42 ± 1	33	0.71
^{40}K	^{40}K	1460.8	151 ± 1	19	5.53

main gamma lines used to calculate the radionuclide concentrations in NORM.

The sample material is contained in a cylindrical polycarbonate box of 75 mm in diameter, 45 mm in height and 180 cm^3 of useful volume, labeled by a barcode. Up to 24 samples can be charged in a slider moving by gravity and further introduced at the inner chamber through an automatic “arm” made of copper, lead and plastic closing the lateral hole of the housing (Fig. 1b). The mechanical automation consists on a barcode scanner and a set of compressed air driven pistons. This mechanism not only makes the sample identification possible, but is also able to introduce/expel the samples. All operations, including measurements, are controlled by a PC by means of a dedicated software.

The program receives by the operator an input file with relevant information about the slot of samples: acquisition live time, spectra file name, sample weight, sample description and barcode. The procedure is repeated until the barcode reader detects samples. A new batch command file is generated to be successively employed in spectrum analysis. In order to complete the automation of the MCA_Rad system, a user-friendly software has been developed for spectra analysis. The code adopts ANSI No. 42 [7] standard specification for the peak analysis.

Calibration and data analysis

For each measurement, the final spectrum is obtained by adding, after rebinning, the two simultaneously measured spectra: for this purpose an accurate energetic calibration of the system, along with a periodical check, is required. When a shift larger than 0.5 keV is observed, the energy calibration procedure is repeated.

The absolute photopeak efficiency (ε_p) for the MCA_Rad system has been determined by using standard point sources method, and producing the calibration curve. Two low activity point sources with complex decay schemes are used [22]: a certified ^{152}Eu source, with an activity of 6.56 kBq in 1995, known with an uncertainty of

1.5 % and a ^{56}Co home made source, that has been normalized relative to ^{152}Eu by calculating the activity of the 846.8 keV (^{56}Co) gamma line. The ^{56}Co source is used in order to extend the efficiency calibration for gamma energies up to 3,000 keV.

The spectra obtained are corrected for: (1) coincidence summing, C_{CS} , on each individual detector, produced by the complex decay scheme of the sources, (2) differences between the geometry of the point sources and the sample shape, C_G and (3) self-attenuation, C_A , of gamma-rays within the sample volume.

The correction due to coincidence summing is studied by following the method described in [21] and obtained as a relationship between the single total efficiency (ε_t), the single apparent absolute photopeak efficiency ($\varepsilon_p^{\text{app}}$) and isotope decay data. The single total efficiency is obtained by estimating the peak-to-total ratio (P/T) using the empirical approach described by [16] and recalling the relationship $\varepsilon_p^{\text{app}}/\varepsilon_t = P/T$. The decay coefficients for ^{152}Eu were calculated from decay data taken from [52], while those for ^{56}Co were taken from [24, 77]. Finally, the absolute efficiency, $\varepsilon_p(E)$, of the MCA_Rad system is given by the sum of single HPGe detector contribution corresponding to the characteristic gamma energies (E_i) of the standard calibration sources used.

$$\varepsilon_p(E_i) = \varepsilon_p^{\text{app}}(E_i)C_{CS}(E_i) \quad (3)$$

Then the absolute efficiency is obtained for the energetic range from 200 to 3,000 keV by fitting them using the function given by [44] (Fig. 3):

$$\varepsilon (\%) = (b_0E/E_0)^{b_1} + b_2 \exp(-b_3E/E_0) + b_4 \exp(-b_5E/E_0) \quad (4)$$

where E (keV) is the gamma-ray energy; $E_0 = 1$ keV is introduced to make dimensionless the argument of the exponential dimensionless and b_i are the fitting parameters (where $b_0 = 1.38$, $b_1 = 1.41$, $b_2 = 22.97$, $b_3 = 5.43$, $b_4 = 6.61$ and $b_5 = 0.44$).

The effect of volume geometry can be described in terms of the effective solid angle developed analytically by [51] within less than 2 % of uncertainty between numerical

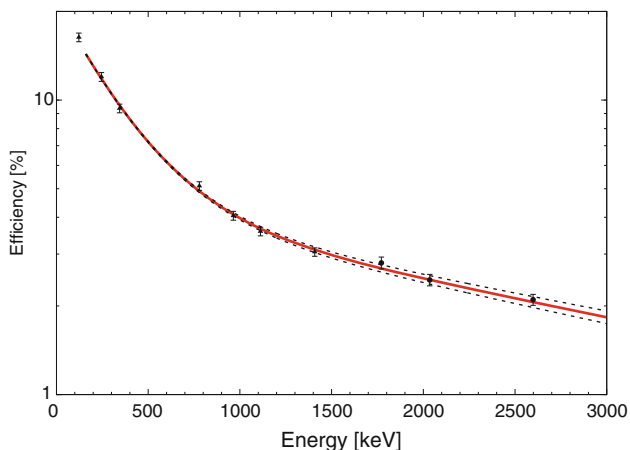


Fig. 3 Absolute efficiency curve of MCA_Rad system. It is obtained by fitting ¹⁵²Eu (triangle) and ⁵⁶Co (circle) energies with Eq. 2 performing the best fit. Dashed curves represent ± one sigma uncertainty interval

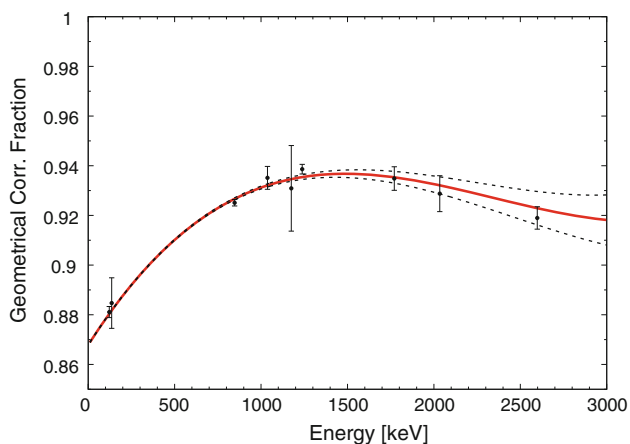


Fig. 4 The geometrical correction factor due to differences between calibration (point source) and measurement geometry (cylinder of 75 mm of diameter and 45 mm of height), which is obtained by fitting nine photopeaks of ⁵⁶Co and ⁵⁷Co with a third order polynomial. Dashed curves represent ± one sigma uncertainty interval

and experimental calculations. The geometrical factor (Fig. 4) for MCA_Rad system is deduced from a set of measurements using a ⁵⁶Co and ⁵⁷Co point sources placed at different radial distances (center, middle and lateral) from the detector axis at different planes, reconstructing the sample geometry using the formula:

$$C_G(E_i) = \frac{\bar{\Omega}_x}{\Omega_{ref}} \approx \frac{1}{R_{ref}(E_i)} \sum_{j=1}^N \frac{[R_x(E_i)]_j}{N} \tag{5}$$

where $R_x(E_i)$ is the net count rate in the standard spectrum collected in different positions (j) and $R_{ref}(E_i)$ is the net count rate in the standard spectrum collected in the reference positions (center). The geometrical correction factor is obtained as a function of energy by fitting a third order polynomial as a function of energy (Fig. 4):

$$C_G(E) = \sum_{i=0}^4 a_i \left(\frac{E}{E_0}\right)^i \tag{6}$$

where $E_0 = 1$ keV is introduced to make the argument dimensionless and a_i are the fitting coefficients ($a_0 = 0.8678$, $a_1 = 0.1098$, $a_2 = -0.0541$, $a_3 = 0.0077$).

The gamma-ray attenuation correction C_{SA} is calculated for different kind of samples taking into account their differences in density by a simplified expression deduced by [13, 20]:

$$C_{SA} = \frac{1 - \exp(-\mu t)}{\mu t} \tag{7}$$

where $\mu_1 = \mu\rho$ (cm^{-1}) is the linear mass attenuation coefficient, μ ($\text{cm}^2 \text{g}^{-1}$) is the mass attenuation coefficient, ρ (g cm^{-3}) is the sample density and t (cm) is the sample effective thickness (which in our case is the half thickness of the sample container). The mass attenuation coefficient is strongly Z dependent in the energy range below few hundred keV while for higher energies the trend is smoother and it depends mainly on energy. These features can be used, since NORM characterization, especially concerning ²²⁶Ra, ²²⁸Ra and ⁴⁰K, requires the investigation of gamma-rays with energies higher than hundreds keV. We can parameterize the mass attenuation coefficient as a function of energy. We used XCOM 3.1 database, which is available on-line and developed by the Nuclear Institute of Standards and Technology (NIST). It is calculated by using for various rocks forming minerals, the average mass attenuation coefficient was deduced with a standard deviation of less than 2 % in the energetic range 200–3,000 keV.

$$\bar{\mu}(E) = \sum_{i=0}^2 a_i [\ln(E)]^i \tag{8}$$

where a_i ($a_0 = 0.5593$, $a_1 = -0.1128$, $a_2 = 0.0590$) are coefficients determined by fitting this function with a reduced χ^2 of $\chi^2_v = 1.12$. Finally the self-attenuation correction factor was given as a function of gamma-ray energy and sample density through the relationship:

$$C_{SA}(E, \rho_s) = \exp \left[b_0 + b_1 \ln(E) + b_2 \ln(E)^2 \right] \rho_s \tag{9}$$

Table 5 Uncertainty budgeted for absolute efficiency determination

Uncertainty source	Relative uncertainty (%)
Certified standard source uncertainty	1.5 ^a
Coincidence summing correction factor	<2
Geometrical correction factor	<2
Self-attenuation correction factor	<2

^a 95 % of confidence level

Table 6 In the sixth column we report the activity concentrations (in Bq kg⁻¹) calculated for the main energetic lines used for ²³⁸U and ²³²Th decay chains and for ⁴⁰K together with respective statistical uncertainties

Parent isotope	Daughter isotope	<i>E</i> (keV)	<i>C</i> _{CS} [*]	<i>C</i> _{SA}	Activity (Bq kg ⁻¹)	Certified reference material activity (Bq kg ⁻¹)
²³⁸ U	^{234m} Pa	1001.0	1.000	1.24	4875 ± 48	4940 ± 30
	²¹⁴ Bi	609.3	1.190	1.32	4872 ± 4	
	²¹⁴ Pb	351.9	1.002	1.42	4773 ± 3	
²³² Th	²²⁸ Ac	911.2	1.024	1.24	3092 ± 4	3250 ± 90
	²¹² Pb	238.6	0.990	1.48	3246 ± 2	
	²¹² Bi	727.3	1.056	1.27	3389 ± 9	
	²⁰⁸ Tl	583.2	1.298	1.31	3342 ± 4	
⁴⁰ K		1460.8		1.21	14274 ± 71	14000 ± 400

The reference material activities certificated by IAEA are shown in seventh column. The correction coefficients *C*_{CS}^{*} and *C*_{SA} are referred to coincidence summing and self-absorption respectively

where *b*₁ (*b*₀ = 1.2609, *b*₁ = -0.2547, *b*₂ = 0.0134) are coefficients determined by fitting this function.

The uncertainty budget for the calibration procedure is reported in Table 5. Considering the uncertainties due to geometrical and self-attenuation correction factors as systematic errors, the overall uncertainty about the absolute efficiency of the MCA_Rad system is estimated to be <5 %.

Measurement of reference materials

The applicability of the MCA_Rad system as well as the method quality control was cross checked using certified reference materials containing concentrations comparable to NORM values. Three reference materials certified within 95 % of confidence level prepared in powder matrix (240 mesh) containing ²³⁸U (IAEA RGU-1) 4,940 ± 30 Bq kg⁻¹, ²³²Th (IAEA RGTh-1) 3,250 ± 90 Bq kg⁻¹ in secular equilibrium and ⁴⁰K (IAEA RGK-1) 14,000 ± 400 Bq kg⁻¹ are used. The sample boxes were filled with the reference materials, after were dried at 60 °C temperature, hermetically sealed and then left undisturbed for at least 3 weeks in order to establish radioactive equilibrium in ²²⁶Ra decay chain segment prior to be measured.

In Table 6 we report the specific activity calculated for the principal gamma lines used to estimate the isotopes of uranium and thorium decay chain and for potassium using the formula:

$$A \text{ (Bq/kg)} = \frac{R}{\varepsilon I_{\gamma} m} C_{SA} C_G C_{CS}^* \quad (10)$$

where *R* is the measured count rate (background corrected), *ε* is the absolute efficiency, *I*_γ is the gamma line intensity, *m* is the mass of the sample, *C*_{SA} is the correction factors for self-absorption, *C*_G is the geometrical correction factor and *C*_{CS}^{*} is the coincidence summing correction factor

(calculated using the same approach as described above for the specific decay chains of the uranium and thorium). The results have an overall relative discrepancy of less than 5 % among certified central values within the reported uncertainty.

Conclusions

We presented a summary of the main categories of non-nuclear industries together with the levels of activity concentration in feeding raw materials, products, by-products/waste and the possible enhancement mechanisms. The main chemical and physical processes that disturb the secular equilibrium of uranium and thorium decay chains have been reported. The degree of radioactivity enhancement is studied along with the radioactivity level in feeding raw material and the industrial process involved. A refined estimation of radioactivity concentrations of ²²⁶Ra, ²²⁸Ra and ⁴⁰K in NORM is almost impossible in such a wide range of industrial activities: the strategy that we propose consist in a systematic monitoring and continuous checking based on high-resolution gamma-ray spectroscopy.

For this purpose an innovative approach to the configuration of a laboratory low-background high-resolution gamma-ray spectrometer, MCA_Rad system, was developed and featured with fully automated measurement processes. It presents the following advantages.

- The new design of lead and copper shielding configuration allowed to reach a background reduction of two order of magnitude respect to laboratory radioactivity.
- A severe lowering of manpower cost is obtained by a fully automation system which permits to measure up to 24 samples without any human attendance.
- The two HPGe detectors offer higher detection efficiency: confronting the MDA of the system with typical

NORM values, it can be deduced that measurements in less than one hour are realized with uncertainties of less than 5 %.

- Accurate measurements are performed on small sample volume (180 cm³) with a reduction of material transport costs.
- A user-friendly software has been developed in order to analyze a high number of spectra, possibly with automatic procedure and customized output.

An empirical efficiency calibration method using multi-gamma standard point sources is discussed. The correction factors affecting the measured spectra (coincidence summing, sample shape, sample gamma-ray self-attenuation) are given with respective procedures. As a result of this procedure the absolute efficiency is estimated to have an overall uncertainty of less than 5 %. A test of the applicability of the instrument as well as the method quality control using certified reference materials showed an overall relative discrepancy of less than 5 % among certified central values within the reported uncertainty.

We, therefore, conclude that the MCA_Rad system shows efficacy in the face of the NORM issue, by increasing the capacities of a laboratory and offering accurate results with a reduction of manpower costs.

Acknowledgments We are grateful for useful comments and discussions to P. Altair, M. Baldoncini, E. Bellotti, L. Carmignani, L. Casini, V. Chubakov, T. Colonna, M. Gambaccini, Y. Huan, W. F. McDonough, G. Oggiano, R. L. Rudnick and R. Vannucci. This work was partially supported by INFN (Italy) and by Fondazione Cassa di Risparmio di Padova e Rovigo.

References

1. Abo-Elmagd M, Soliman HA, Salman KhA, El-Masry NM (2010) Radiological hazards of TENORM in the wasted petroleum pipes. *J Environ Radioact* 101:51–54
2. ACAA (American Coal Ash Association) (2003) 'Fly Ash facts for highway engineers'. Federal Highway Association Report FHWA-IF-03-019
3. Adams JAS, Richardson KA (1960) Thorium, uranium and zirconium concentration in bauxite. *Econ Geol* 55:1653–1675
4. Akinci A, Artir R (2008) Characterization of trace elements and radionuclides and their risk assessment in red mud. *Mater Charact* 59:417–421
5. Al-Masri MS, Suman H (2003) NORM waste management in the oil and gas industry: The Syrian experience. *J Radioanal Nucl Chem* 256:159–162
6. Al-Saleh FS, Al-Harshan GA (2008) Measurements of radiation level in petroleum products and wastes in Riyadh City Refinery. *J Environ Radioact* 99:1026–1031
7. ANSI No. 42.14 (1999) American national standard for calibration and use of germanium spectrometers for the measurement of gamma-ray emission rates of radionuclides
8. Azouazi M, Ouahidi Y, Fakhi S, Andres Y, Abbe JCh, Benmansour M (2001) Natural radioactivity in phosphates, phosphogypsum and natural waters in Morocco. *J Environ Radioact* 54:231–242
9. Bakr WF (2010) Assessment of the radiological impact of oil refining industry. *J Environ Radioact* 101:237–243
10. Beck HL (1989) Radiation exposures due to fossil fuel combustion. *Int J Radiat Appl Instrum, Part C. Radiat Phys Chem* 34:285–293
11. Beddow H, Black S, Read D (2006) Naturally occurring radioactive material (NORM) from a former phosphoric acid processing plant. *J Environ Radioact* 86:289–312
12. Beretka J, Mathew PJ (1983) Natural Radioactivity of Australian building material wastes and by-products. *Health Phys* 48:87–95
13. Bolivar JP, Garcia-Leon M, Garcia-Tenorio R (1997) On self-attenuation corrections in gamma-ray spectrometry. *Appl Radiat Isot* 48:1125–1126
14. Brown AEP, Costa EC (1972) Processing of a uraniferous zirconium ore. IEA Publication N. 274
15. Carvalho FP (1995) ²¹⁰Pb and ²¹⁰Po in sediments and suspended matter in the Tagus estuary, Portugal. Local enhancement of natural levels by wastes from phosphate ore processing industry. *Sci Total Environ* 159:201–214
16. Cesana A, Terrani M (1989) An empirical method for peak-to-total ratio computation of a gamma-ray detector. *Nuclear Instrum Methods Phys Res A* 281:172–175
17. Condie KC (1993) Chemical composition and evolution of the upper continental crust: Contrasting results from surface samples and shales. *Chem Geol* 104:1–37
18. Cooper MB, Clarke PC, Robertson W, Mcpharlin IR, Jeffrey RC (1995) An investigation of radionuclide uptake into food crops grown in soils treated with Bauxite mining residues. *J Radioanal Nucl Chem* 194:379–387
19. Currie LA (1986) Limits for Qualitative Detection and Quantitative Determination Application to Radiochemistry. *Anal Chem* 40:586–593
20. Cutshall NH, Larsen IL, Olsen CR (1983) Direct analysis of Pb-210 in sediment samples: self-absorption corrections. *Nuclear Instrum Methods* 206:309–312
21. De Felice P, Angelini P, Fazio A, Biagini R (2000) Fast procedures for coincidence-summing correction in gamma-ray spectrometry. *Appl Radiat Isot* 52:745–752
22. DeFelice P, Fazio A, Vidmar T, Korun M (2006) Close-geometry efficiency calibration of p-type HPGe detectors with a Cs-134 point source. *Appl Radiat Isot* 64:1303–1306
23. Döring J Beck T, Beyermann M, Gerler J, Henze G, Mielcarek J, Schkade (2007) Exposure and radiation protection for work areas with enhanced natural radioactivity NORM V (Proc. Conf. Seville, Spain 2007)
24. Dryák P, Kovář P (2009) Table for true summation effect in gamma-ray spectrometry. *J Radioanal Nucl Chem* 279:385–394
25. ECOBA (European Coal Combustion Products Association) (2003) CCP Production & Use Survey-EU 15
26. El Afifi EM, Hilal MA, Attallah MF, EL-Reefy SA (2009) Characterization of phosphogypsum wastes associated with phosphoric acid and fertilizers production. *J Environ Radioact* 100:407–412
27. Flues M, Camargo IMC, Silva PSC, Mazzilli BP (2006) Radioactivity of coal and ashes from Figueira coal power plant in Brazil. *J Radioanal Nucl Chem* 270:597–602
28. Gazineu MHP, Hazin CA (2008) Radium and potassium-40 in solid wastes from the oil industry. *Appl Radiat Isot* 66:90–94
29. Gazineu MHP, Araújo AA, Brandão YB, Hazin CA, Godoy JM (2005) Radioactivity concentration in liquid and solid phases of scale and sludge generated in the petroleum industry. *J Environ Radioact* 81:47–54
30. Georgescu D, Aurelian F, Popescu M, Radulescu C (2004) Sources of TENORM—Inventory of phosphate fertilizer and aluminum industry, NORM IV (Proc. Conf. Szczryk

31. Godoy JM, Cruz RP (2003) ^{226}Ra and ^{228}Ra in scale and sludge samples and their correlation with the chemical composition. *J Environ Radioact* 70:199–206
32. Guimond RJ, Hardin JM (1989) Radioactivity released from phosphate-containing fertilizers and from gypsum. *Radiat Physics Chem* 34:309–315
33. Heaton B, Lambley J (1995) TENORM in the oil, gas and mineral mining industry. *Appl Radiat Isot* 46:577–581
34. Hind AR, Bhargava SK, Grocott SC (1999) The surface chemistry of Bayer process solids: a review. *Coll Surf A: Physico-chemical Engineering aspects* 146:359–374
35. Hull CD, Burnett WC (1996) Radiochemistry of Florida phosphogypsum. *J Environ Radioact* 32:213–238
36. IAEA (International Atomic Energy Agency) (1996) International basic safety standards for protection against ionizing radiation and for the safety radiation sources. safety series no. 115. IAEA, Vienna
37. IAEA (International Atomic Energy Agency) (2003) Radioactive waste management glossary. IAEA, Vienna
38. IAEA (International Atomic Energy Agency) (2003) Extent of environmental contamination by naturally occurring radioactive material (NORM) and technological options for mitigation. technical reports series no. 419. IAEA, Vienna
39. IAEA (International Atomic Energy Agency) (2006) Assessing the need for radiation protection measures in work involving minerals and raw materials. safety reports series no. 49. IAEA, Vienna
40. IAEA (International Atomic Energy Agency) (2008) Naturally occurring radioactive material (NORM V), proceedings series. IAEA, Vienna
41. Jerez Vegueria SF, Godoy JM, Miekeley N (2002) Environmental impact studies of barium and radium discharges by produced waters from the “Bacia de Campos” oil-field offshore platforms, Brazil. *J Environ Radioact* 62:29–38
42. Jobbágy V, Somlai J, Kovács J, Szeiler G, Kovács T (2009) Dependence of radon emanation of red mud bauxite processing wastes on heat treatment. *J Hazard Mater* 172:1258–1263
43. Jonkers G, Hartog FA, Knaepen AAI, Lancee PFJ (1997) Characterization of NORM in the oil and gas production (E&P) industry, Radiological problems with natural radioactivity in the non-nuclear industry In: Proc. Int. Symp., Amsterdam
44. Knoll GF (1999) Radiation detection and measurements, 3rd edn. Wiley, New York
45. Landais P (1996) Organic geochemistry of sedimentary uranium ore deposits. *Ore Geol Rev* 11:33–51
46. Lysebo I, Birovljev A, Strand T (1996) NORM in oil production—occupational doses and environmental aspects. In: Proceedings of the 11th Congress of the Nordic Radiation Protection Society, Reykjavik, Iceland
47. Mazzilli B, Palmiro V, Saueia C, Nisti MB (2000) Radiochemical characterization of Brazilian phosphogypsum. *J Environ Radioact* 49:113–122
48. McNulty GS (2007) Production of titanium dioxide. In: Proc. Conf. Seville, Spain
49. Menzel RG (1968) Uranium, radium, and thorium content in phosphate-rocks and their possible radiation hazard. *J Agric Food Chem* 16:231–234
50. Metz V, Kienzler B, Schüßler W (2003) Geochemical evaluation of different groundwater–host rock systems for radioactive waste disposal. *J Contam Hydrol* 61:265–279
51. Moens L, De Donder J, Xi-lei L, De Corte F, De Wespelaere A, Simonits A, Hoste J (1981) Calculation of the absolute peak efficiency of gamma-ray detectors for different counting geometries. *Nuclear Instrum Methods* 187:451–472
52. Monographie BIPM-5 (2004) Table of Radionuclides, vol 2. Bureau International des Poids et Mesure. ISBN 92-822-2207-1
53. Mukherjee AB, Zevenhoven R, Bhattacharya P, Sajwan KS, Kikuchi R (2008) Mercury flow via coal and coal utilization by-products: a global perspective. *Resour Conserv Recycl* 52:571–591
54. Nakashima S (1992) Complexation and reduction of uranium by lignite. *The Sci Total Environ* 117(118):425–437
55. Omar M, Ali HM, Abu MP, Kontol KM, Ahmad Z, Ahmad SHSS, Sulaiman I, Hamzah R (2004) Distribution of radium in oil and gas industry wastes from Malaysia. *Appl Radiat Isot* 60:779–782
56. Papatheodorou G, Papaefthymiou H, Maratou A, Ferentinos G (2005) Natural radionuclides in bauxitic tailings (red-mud) in the Gulf of Corinth, Greece. *Radioprotection* 1(40):549–555
57. Paschoa AS (1993) Overview of environmental and waste management aspects of the monazite cycle. *Radiat Prot Australia* 11:170–173
58. Paschoa AS (1997) Potential Environmental and Regulatory Implications of Naturally Occurring Radioactive Materials (NORM). *Appl Radiat Isotopes* 49:189–196
59. Paschoa AS (2008) NORM from the Monazite cycle and from the oil and gas industry: problems and tentative solutions. International conference on radioecology and environmental radioactivity. In: Proc. Conf. Bergen, Norway
60. Philipsborn HV, Kuhnast E (1992) Gamma spectrometric characterization of industrially used African and Australian bauxites and their red mud tailings. *Radiat Prot Dosimetry* 45:741–744
61. Pinnock W (1991) Measurements of radioactivity in Jamaican building materials and gamma dose equivalents in a prototype red mud house. *Health Phys* 61:647–651
62. Pontikes Y, Vangelatos I, Boufounos D, Fafoutis D, Angelopoulos GN (2006) Environmental aspects on the use of Bayer’s process bauxite residue in the production of ceramics. *Adv Sci Technol* 45:2176–2181
63. Poole AJ, Allington DJ, Baxter AJ, Young AK (1995) The natural radioactivity of phosphate ore and associated waste products discharged into the eastern Irish Sea from a phosphoric acid production plant. *Sci Total Environ* 173(174):137–149
64. Righi S, Andretta M, Bruzzi L (2005) Assessment of the radiological impacts of a zircon sand processing plant. *J Environ Radioact* 82:237–250
65. Rubio Montero MP, Durán Valle CJ, Jurado Vargas M, Botet Jiménez A (2009) Radioactive content of charcoal. *Appl Radiat Isot* 67:953–956
66. Ruyters S, Mertens J, Vassilieva E, Dehandschutter B, Poffijn A, Smolders E (2011) The red mud accident in Ajka (Hungary): plant toxicity and trace metal bioavailability in red mud contaminated soil. *Environ Sci Technol* 45:1616–1622
67. Santos AJG, Mazzilli BP, Fávoro DIT, Silva PSC (2006) Partitioning of radionuclides and trace elements in phosphogypsum and its source materials based on sequential extraction methods. *J Environ Radioact* 87:52–61
68. Saueia CHR, Mazzilli BP (2006) Distribution of natural radionuclides in the production and use of phosphate fertilizers in Brazil. *J Environ Radioact* 89:229–239
69. Saueia CH, Mazzilli BP, Fávoro DIT (2005) Natural radioactivity in phosphate rock, phosphogypsum and phosphate fertilizers in Brazil. *J Radioanal Nucl Chem* 264:445–448
70. Shawky S, Amer H, Nada AA, El-Maksoud TMA, Ibrahiem NM (2001) Characteristics of NORM in the oil industry from eastern and western deserts of Egypt. *Appl Radiat Isot* 55:135–139
71. Silva NC, Fernandes EAN, Cipriani M, Taddei MHT (2001) The natural radioactivity of Brazilian phosphogypsum. *J Radioanal Nucl Chem* 249:251–255
72. Smith ML, Bignell L, Alexiev D, Mo L, Harris J (2008) Evaluation of lead shielding for a gamma-spectroscopy system. *Nuclear Instrum Methods Phys Res A* 589:275–279

73. Somlai J, Jobbàgy V, Kovács J, Tarján S, Kovács T (2008) Radiological aspects of the usability of red mud as building material additive. *J Hazard Mater* 150:541–545
74. Tadmor J (1986) Radioactivity from coal-fired power plants: a review. *J Environ Radioact* 4:177–204
75. Tayibi H, Choura M, López FA, Alguacil FJ, López-Delgado A (2009) Environmental impact and management of phosphogypsum. *J Environ Manage* 90:2377–2386
76. Timmermans CWM, van der Steen J (1996) Environmental and occupational impacts of natural radioactivity from some non-nuclear industries in The Netherlands. *J Environm Radioact* 32:97–104
77. Tomarchio E, Rizzo S (2011) Coincidence-summing correction equations in gamma-ray spectrometry with p-type HPGe detectors. *Radiat Phys Chem* 80:318–323
78. Turhan S, Arikan IH, Demirel H, Güngör N (2011) Radiometric analysis of raw materials and end products in the Turkish ceramics industry. *Radiat Phys Chem* 80:620–625
79. UNSCEAR (2000) (United Nations Scientific Committee on the Effects of Atomic radiation) Sources and effects of ionizing radiation. Report to the General Assembly of the United Nations with Scientific Annexes, United Nations Sales Publication E.00.IX.3, New York
80. US EIA/IOE (2010) US Energy Information Administration/International Energy Outlook
81. USGS MCS (1996) US Geological Survey Mineral Commodities Summary
82. USGS MCS (2011) US Geological Survey Mineral Commodities Summary
83. USGS US Geological Survey Data Series 140, Kelly T, Buckingham D, DiFrancesco C, Porter K, Goonan T, Sznoppek J, Berry C, Crane M (2002) Historical statistics for mineral commodities in the United States. US Geological Survey open-file report 01-006, minerals.usgs.gov/minerals/pubs/of-01-006/
84. WCI World Coal Institute (2005) Coal facts 2005 edition
85. Zielinski RA, Otton JK, Budahn JR (2001) Use of radium isotopes to determine the age and origin of radioactive barite at oil-field production sites. *Environ Pollut* 113:299–309